August 2020

Understanding Mechanochemical Processes on Surfaces Measured in Ultrahigh Vacuum

Resham Rana
University of Wisconsin-Milwaukee

UNDERSTANDING MECHANOCHEMICAL PROCESSES ON SURFACES MEASURED IN ULTRAHIGH VACUUM

by

Resham Rana

A Dissertation Submitted in

Partial Fulfillment of the

Requirements for the Degree of

Doctor of Philosophy

in Chemistry

at

The University of Wisconsin-Milwaukee

August 2020

ABSTRACT

UNDERSTANDING MECHANOCHEMICAL PROCESSES ON SURFACES MEASURED IN ULTRAHIGH VACUUM

by

Resham Rana

The University of Wisconsin-Milwaukee, 2020
Under the Supervision of Professor Wilfred T. Tysoe

Tribology is the study of friction and wear and of the energy dissipated when two surfaces slide against each other. A recent DOE report shows that improved lubricants could save ~103 exaJoules (1 exaJoule = 10^{18} joules) per year, equivalent to 20% of the world's total energy consumption. The focus of this work is to understand the surface chemistry and tribological reactions of model sulfur-, carbon-, and phosphorus-based lubricant additives to understand the mechanisms by which they operate. Previous work has shown that lubricant additives react by a novel mechanochemical process in which the force acting on the adsorbate accelerates the rate of reaction and can lead to new metastable materials.

The tribochemical reactions are studied using a tungsten carbide pin sliding against a planar substrate in ultrahigh vacuum where the reaction is followed by

detecting gas-phase products and analyzing the rubbed region using Auger spectroscopy.

The tribochemistry of dimethyl disulfide (DMDS) on copper has been studied previously. Here, reaction is initiated by the decomposition of adsorbed methyl thiolate species to form small gas-phase hydrocarbons, followed by a process in which the surface sulfur penetrates the bulk of the copper to produce a metastable copper sulfide film. This work aims at further understanding the second step in this process, namely, the surface-to-bulk transport of sulfur into copper by studying the effect of coverage and the crystallinity of the copper substrate on the transport kinetics. These kinetic studies were supplemented by electron microscopy if the subsurface region of samples that had been prepared by fast-ion beam methods.

These studies explored the effect of binding to the substrate. As a consequence, work was also carried out to investigate how binding of the reactive molecule to the tungsten carbide pin might influence the tribochemistry. This work is carried out using unsaturated carboxylic and saturated carboxylic acids, where the carboxylate group has been shown to anchor strongly to the copper substrate, and where the C=C species are expected to bind to the tungsten carbide counterface and thus influence the reactivity. The adsorbed carboxylic acids were found to decompose during sliding by rapid cleavage of the bond between the carboxylate and the hydrocarbon groups. Difference in the surface chemistry was found, but was

traced to difference in the reactivity of the hydrocarbon.

In addition to the sulfides investigated above, phosphorus-containing molecules, notably phosphite esters, have been found to be good lubricants for iron. The surface tribochemistry model lubricant additives, triethyl phosphite, and trimethyl phosphite were studied on iron oxide (Fe_3O_4) by both experimental and theoretical approaches, where the molecules were found to decompose by sequential removal of alkoxide species to form friction-reducing iron phosphate films.

Dedicated To:

The people we have lost to COVID-19

TABLE OF CONTENTS

List of Figures **xiii**

List of Tables **xxxiii**

Acknowledgements **xxxvi**

1 Introduction **1**

1.1 Tribology: Friction and Wear 1

1.2 Tribo/Mechanochemistry 7

1.3 Overview of this work described in this thesis 7

References 11

2 Experimental Methods **13**

2.1 Introduction 13

2.2 Vacuum Pumps 14

2.2.1 Rotatory/Mechanical Pump 14

2.2.2 Diffusion Pump 16

2.2.3 Turbomolecular Pump 17

2.2.4 Ion Pump 19

2.3 Gas Handling Line and Chemical Purification 20

2.4 Design, Construction, and Operation of a UHV Chamber 22

2.5 UHV Tools and Techniques 23
2.5.1 Sample Manipulators 24
2.5.2 Sample Preparation, Mounting and Cleaning 25
2.5.3 Mass Spectrometer 26
2.5.4 Temperature-Programmed Desorption 28
2.5.5 Cylindrical Mirror Analyzer 30
2.5.6 Auger Electron Spectroscopy 32
2.5.7 X-ray Photoelectron Spectroscopy 34
2.5.8 Scanning Electron Microscopy 36
2.5.9 UHV-compatible Tribometer and Tribology System 39
2.5.10 Aluminum Evaporation Source 47
2.5.11 Scanning Transmission Electron Microscopy 48
2.6 Non-UHV Tools 50
2.6.1 Nano Indenter 50
References 53

3 Kinetic Mechanism for the Mechanochemical Formation of Metastable Phases from the Reaction between Sulfur and Copper 56

3.1 Introduction 56
3.2 Experimental 61
3.3 Modified Rigney Model for Interfacial Mixing at a Sliding Interface . . . 65

3.4 Results 68
3.4.1 Mechanical Properties and Structure of Annealed Copper Samples 70
3.4.2 Analysis of the Surface of the Tribopin 75
3.4.3 Measurement of the Kinetics of Sulfur Surface-to-Bulk Transport in Copper as a Function of Sample Annealing Temperature . . . 77
3.4.4 Subsurface Structure and Composition of Copper Samples after Rubbing in Dimethyl Disulfide as a Function of Sample Annealing Temperature 81
3.5 Discussion 88
3.6 Conclusions 94
References 97

4 Reaction between Dimethyl Disulfide and Copper by Sliding Graphitic Carbon Covered Tungsten Carbide Tribopin: Influence of the Counterface on Mechanochemistry 109

4.1 Introduction 109
4.2 Experimental 111
4.3 Results 115
4.3.1 Analysis of the surface of the tribopin 115
4.3.2 Methyl thiolate decomposition rate on copper samples annealed at 500, 850, and 1020 K with graphitic carbon-covered tribopin . . 116

4.3.3 Friction coefficient and average roughness of copper samples . . 118
4.3.4 Measurement of the kinetics of surface-to-bulk sulfur transport with graphitic carbon-covered tribopin 121
4.4 Discussion 124
4.5 Conclusions 127
References 128

5 Tribochemical Reaction Pathways of Carboxylic Acid Monolayers on Copper in Ultrahigh Vacuum 131

5.1 Introduction 131
5.2 Experimental 134
5.3 Results 137
5.3.1 Surface Structure Determination 137
5.3.2 Thermal Decomposition of Carboxylic Acids on Copper 140
5.3.3 Tribochemical Reactions of Carboxylic Acids on Copper 146
5.3.4 Frictional Behavior of Carboxylic Acids on Copper 157
5.3.5 Surface-to-Bulk Transport of Carbon into the Copper Subsurface Region 162
5.4 Discussion 164
5.5 Conclusions 168
References 169

6 Tribochemical Mechanisms of Trimethyl and Triethyl Phosphite on Oxidized Iron in Ultrahigh Vacuum **175**

6.1 Introduction 175

6.2 Experimental Section 177

6.3 Results 179

6.3.1 Formation, Characterization and Friction of Iron Oxide Films on Clean Iron 179

6.3.2 Surface Chemistry of Trimethyl Phosphite on Fe_3O_4 Films on Iron 183

6.3.3 Surface Chemistry of Triethyl Phosphite on Fe_3O_4 Films on Iron . 192

6.3.4 Gas-Phase lubrication of Fe_3O_4 Films on Iron by Triethyl Phosphite 198

6.4 Discussion 199

6.5 Conclusions 205

References 207

7 Adsorption and Reaction of Trimethyl and Triethyl Phosphites on Fe_3O_4 by Density Functional Theory **215**

7.1 Introduction 215

7.2 Theoretical Method 216

7.3 Results 219

7.3.1 Adsorption of Trimethyl Phosphite on Fe_3O_4 219

7.3.2 Adsorption of Triethyl Phosphite on Fe_3O_4 223

7.4 Discussion 226

7.5 Conclusions 230

References 232

Curriculum Vitae **236**

LIST OF FIGURES

1.1 A drawing in a grotto at El Bersheh, circa 1880 BC [4, 5]. Liquid being poured in front of the colossus from a jar. 2

1.2 Stribeck curve: the relationship between the Hersey number, $\frac{\eta N}{P}$, where η is viscosity, N is the speed of the fluid and P is the normal load per length of tribological contact, and the friction coefficient μ at different lubrication regimes: i) hydrodynamic lubrication, ii) mixed lubrication, and iii) boundary lubrication [8]. 5

2.1 Rotary pump operation stages. 15

2.2 Schematic of the diffusion pump. 17

2.3 Schematics of turbomolecular pump. 18

2.4 Schematics of ion pump. 20

2.5 Schematics of gas handling line attached with UHV chamber. 21

2.6 Schematics of typical UHV chamber. 23

2.7 Schematics of sample manipulator. 24

2.8 Schematics of mass spectrometer. 27

2.9 Schematics of TPD system. 29

2.10 a. Outline of typical cylindrical mirror analyzer (CMA) b. Internal optics of double pass CMA. 31

2.11 Auger process a. ejection of K electron by the impact of incident electron beam b. generation of auger electron after internal transition [8]. 33
2.12 XPS process a. incident photon b. ejection of K electron followed by X-ray emission. 35
2.13 Schematics of twin X-ray source. 36
2.14 a. SEM Optical alignment system b. Beam size vs Beam current. 37
2.15 SEM schematics for locating wear track for AES analysis. 38
2.16 Schematics of tribo-arm and mounted sample. 40
2.17 Tribological system with SEM microfocus e-gun used during S-transport experiments for AES analysis of wear track. 41
2.18 Tribological system with UTi 100 mass spectrometer for gas phase product analysis during tribochemical experiments. 43
2.19 Tribological system with Al evaporation cell. The wear track created Cu foils during the DMDS exposure are coated with Al protective layer using this configuration for STEM analysis of FIBed samples taken from inside the wear track. 44
2.20 Schematics of tribology vacuum system configured for carboxylic acid experiments for measuring the C-removal rate. The figure in the rectangular inset is a design of a Knudsen dosing cell used for dosing carboxylic acids. 45

2.21 a) Circuit diagram for e-beam heating of tungsten carbide tribopin b) Auger spectra of the tungsten carbide tribopin: untreated and e-beam heated. 46

2.22 a. Schematic diagram of Al evaporation source mounted on power supply feedthrough b. surface source evaporation geometry for film thickness calculation. 48

2.23 Schematic diagram of STEM showing the different elements. 49

2.24 a. Indentation and Residual impression b. Residual impression from a Berkovich indenter. 51

3.1 Optical microscope images of a copper foil showing the variation in grain size with increasing annealing temperature. Image a) shows a 700 μm × 520 μm image of the initial, unannealed foil, image b) shows a 2600 μm × 2000 μm image that has been annealed at 500 K and image c) shows a 4000 μm × 3000 μm image that has been annealed at 850 K. Images d) to e) show the depth profile electron microscope images of FIBed samples of copper that had been annealed to various temperatures and the rubbed at a load of 0.44 N at a sliding speed of 4×10^{-3} m/s in a background pressure of 5×10^{-8} Torr of DMDS for 80 cycles: d) a High-angle annular dark-field (HAADF) image of a sample annealed at 500 K (200 keV, 160000 magnification), where the red square indicates the analyzed regions shown in Fig. 3.11, e) a HAADF TEM image of a sample annealed at 850 K (200 keV, 200000 magnification) and f) FIB SEM image of a sample annealed at 1020 K (5 keV, 6500 magnification). Figure a, b, and c courtesy of Yufu Xu, Hefei University of Technology, China. 69

3.2 Plots of hardness of the sample measured using a Berkovich tip as a function of depth into the sample for copper foils that had been annealed at (a) 500, (b) 850 and (c) 1020 K and after having been rubbed at a load of 0.44 N at a sliding speed of 4×10^{-3} m/s in a background pressure of 1×10^{-8} Torr of DMDS for 80 cycles for the same annealing temperatures (d-f). 73

3.3 Measured values of hardness for copper foils that had been annealed at 500, 850, and 1020 K (■) and after having been rubbed at a load of 0.44 N at a sliding speed of 4×10^{-3} m/s in a background pressure of 1×10^{-8} Torr of DMDS for 80 cycles (●), summarizing the data shown in Fig. 3.2. 74

3.4 Measured values of elastic modulus E^* for copper foils that had been annealed at 500 (■), 850 (●), and 1020 (▲) K and after having been rubbed at a load of 0.44 N at a sliding speed of 4×10^{-3} m/s in a background pressure of 1×10^{-8} Torr of DMDS for 80 cycles. 76

3.5 Analyses of the surface of the tungsten carbide tribopin. Figure A, lower trace shows an Auger spectrum of the initially contaminated pin showing predominantly carbon on the surface and the upper trace shows the effect of e-beam heating now revealing the presence of tungsten. Figure B shows an Al K_α X-ray photoelectron spectrum of the tungsten carbide pin that has been Argon ion bombarded. Figure B courtesy of Jules Galipaud and Thierry LeMogne, Ecole Centrale de Lyon, France. 77

3.6 Plot of the relative sulfur to copper (S/Cu) Auger ratio measured inside the wear track as a function of the number of times that the copper samples had been rubbed in a background pressure of 1×10^{-8} Torr of DMDS at an applied normal load of 0.44 N and a sliding speed of 4×10^{-3} m/s after being cleaned and annealed at 500 (●), 850 (▲), and 1020 (■) K . Shown for comparison are the results obtained previously for a sample that had been heated to 850 K [23]. 79

3.7 A 100 nm × 50 nm EDX image of a copper foil that had been cleaned and annealed in UHV at 1020 K and then reacted while rubbing at an applied normal load of 0.44 N and a sliding speed of 4×10^{-3} m/s in 5×10^{-8} Torr of DMDS. The interface between the copper and the aluminum capping layer is at the top of the image and the X-ray spectra are displayed for various points in the image as indicated by colored arrows. 83

3.8 Plot of the intensity of the sulfur K_α X-ray signal at 2307 eV as a function of distance from the surface of a copper foil that had been cleaned and annealed in UHV at 1020 K and then reacted while rubbing at an applied normal load of 0.44 N and a sliding speed of 4×10^{-3} m/s in 5×10^{-8} Torr of DMDS, where the origin of the abscissa represents the surface, where negative values are within the copper sample (■). The line through the data is a fit to the theoretical depth profile [28] which has been broadened by 1 nm to take account of the spatial resolution of the instrument. 84

3.9 A 200 nm × 100 nm EDX image of a copper foil that had been cleaned and annealed in UHV at 850 K and then reacted while rubbing at an applied normal load of 0.44 N and a sliding speed of 4×10^{-3} m/s in 5×10^{-8} Torr of DMDS. The interface between the copper and the aluminum capping layer is at the top of the image and the X-ray spectra are displayed for various points in the image as indicated by colored arrows. 86

3.10 Plot of the intensity of the sulfur K_α X-ray signal at 2307 eV as a function of distance from the surface of a copper foil that had been cleaned and annealed in UHV at 850 K and then reacted while rubbing at an applied normal load of 0.44 N and a sliding speed of 4×10^{-3} m/s in 5×10^{-8} Torr of DMDS, where the origin of the abscissa represents the surface, where negative values are within the copper sample (■). The line through the data is a fit to the theoretical profile [28] which has been broadened by 1 nm to take account of the spatial resolution of the instrument. 87

3.11 A 480 nm × 320 nm EDX image of a copper foil that had been cleaned and annealed in UHV at 500 K and then reacted while rubbing at an applied normal load of 0.44 N and a sliding speed of 4×10^{-3} m/s in 5×10^{-8} Torr of DMDS. The interface between the copper and the aluminum capping layer is at the top of the image and is dedicated by a white line and the X-ray spectra are displayed for various points in the image as indicated by colored arrows. The inset to the spectra shows the predicted depth profile [28] which has been broadened by 1 nm to take account of the spatial resolution of the instrument. 89

3.12 Plot of the rate constant for the shear-induced transport of sulfur into the subsurface region of copper, $k_2^{'}$, as a function of the strain-rate sensitivity for samples modified by heating the copper sample to various temperatures. 92

3.13 Plot of the rate constant for the shear-induced transport of sulfur into the subsurface region of copper, $k_2^{'}$, as a function of dislocation density for samples modified by heating the copper sample to various temperatures. 93

4.1 Comparison of the Auger spectra of the tribopin; the red (top) spectrum is collected after e-beam heating and the black (lower spectrum) is for the untreated tibopin. Less W is detected in untreated tribopin and graphitic carbon is profoundly dominant in the untreated tribopin. . 114

4.2 The desorption of methane from a methyl thiolate overlayer (formed from 5 L exposure to DMDS) on copper that had been annealed to 1020 K. The inset shows a plot of ln(Methane Yield) versus $n-1$, where n is the number of passes, indicative of a first-order reaction. 117

4.3 Plot of the relative friction coefficient measured with 10 Langmuir of DMDS on the copper samples that had been rubbed at an applied normal load of 0.44 N and a sliding speed of 4×10^{-3} m/s after being cleaned and annealed at 500 (■), 850 (●), or 1020 (▲) K. 118

4.4 Plot of the relative friction coefficient measured at 5^{th} scan with 1, 2, 5, and 10 Langmuir of DMDS exposure on the copper samples that had been rubbed at an applied normal load of 0.44 N and a sliding speed of 4×10^{-3} m/s after being cleaned and annealed at 500 (■), 850 (●), or 1020 (▲) K. 119

4.5 Plot of average roughness (Ra) measured on copper samples after being cleaned and annealed at 500, 850, or 1020 K measured using a confocal laser microscope (♦). 120

4.6 Plot of the relative sulfur to copper (S/Cu) Auger ratio measured inside the wear track as a function of the number of times that the copper samples had been rubbed at an applied normal load of 0.44 N and a sliding speed of 4×10^{-3} m/s after being cleaned and annealed at 500 (■), 850 (●), and 1020 (▲) K. 122

4.7 Plot of the relative sulfur to copper (S/Cu) Auger ratio measured inside the wear track as a function of the number of times that the copper samples had been rubbed at an applied normal load of 0.44 N and a sliding speed of 4×10^{-3} m/s after being cleaned and annealed at 500 (■), 850 (●), and 1020 (▲) K. 123

5.1 Reflection-absorption infrared spectra of (a) 7-octenoic acid and (b) octanoic acid adsorbed on a Cu(100) single crystal surface at room temperature. Courtesy of Robert Vincent Bavisotto, UW-Milwaukee, USA. . . . 138

5.2 Structures of various carboxylic acids adsorbed on a Cu(100) surface in a (2×2) units cell, assuming that the carboxylic acids adsorb on the surface via the carboxylate group as suggested by infrared spectroscopy (Figure 5.1). Courtesy of Robert Vincent Bavisotto, UW-Milwaukee, USA. 139

5.3 Analyses of the surface of the tungsten carbide tribopin. Figure A shows the initially contaminated pin showing predominantly carbon on the surface and the upper trace shows the effect of e-beam heating now revealing the presence of tungsten. Figure B shows an Al K_α X-ray photoelectron spectrum of the tungsten carbide pin that has been Argon ion bombarded. Figure B courtesy of Jules Galipaud and Thierry LeMogne, Ecole Centrale de Lyon, France. 141

5.4 Temperature-programmed desorption profiles of 6.3×10^{-6} Torr.s of 7-octenoic acid adsorbed on a copper foil at 300 K monitored at various masses using a heating rate of 2.9 K/s, where the monitored masses are displayed adjacent to the corresponding spectrum. 142

5.5 Temperature-programmed desorption profiles of 1.8×10^{-5} Torr.s of octanoic acid adsorbed on a copper foil at 300 K monitored at various masses using a heating rate of 2.9 K/s, where the monitored masses are displayed adjacent to the corresponding spectrum. 143

5.6 Temperature-programmed desorption profiles of 8.7×10^{-6} Torr.s of 6-heptenoic acid adsorbed on a copper foil at 300 K monitored at various masses using a heating rate of 2.9 K/s, where the monitored masses are displayed adjacent to the corresponding spectrum. 144

5.7 Temperature-programmed desorption profiles of 1.05×10^{-5} Torr.s of heptanoic acid adsorbed on a copper foil at 300 K monitored at various masses using a heating rate of 2.9 K/s, where the monitored masses are displayed adjacent to the corresponding spectrum. 145

5.8 Plot of the C/Cu Auger ratio in the wear track of a saturated overlayer of 7-octenoic acid on a copper foil as a function of the number of passes at a normal load of 0.44 N and a sliding speed of 4×10^{-3} m/s, for 7-octenoic acid on a clean surface (■) and after a second dose of 7-octanoic acid on the previously rubbed surface. 147

5.9 Plot of the initial (indicated as 0 scan) and final (indicated as 50 scans) carbon to copper Auger ratio measured in the wear track after rubbing a copper surface saturated with 7-octenoic acid at a normal load of 0.44 N at a sliding speed of 4×10^{-3} m/s. Neither the copper surface nor the tungsten carbide pin was cleaned between scans so that each consecutive scan is for an interface that includes the accumulated carbon from previous scans. 149

5.10 Plot of the C/Cu Auger ratio in the wear track of a saturated overlayer of octanoic acid on a copper foil as a function of the number of passes at a normal load of 0.44 N and a sliding speed of 4×10^{-3} m/s, for octanoic acid on a clean surface (■) and after a second dose of octanoic acid on the previously rubbed surface. 151

5.11 Plot of the initial (indicated as 0 scan) and final (indicated as 50 scans) carbon to copper Auger ratio measured in the wear track after rubbing a copper surface saturated with octanoic acid at a normal load of 0.44 N at a sliding speed of 4×10^{-3}. Neither the copper surface nor the tungsten carbide pin was cleaned between scans so that each consecutive scan is for an interface that includes the accumulated carbon from previous scans. 152

5.12 Plot of the C/Cu Auger ratio in the wear track of a saturated overlayer of 6-heptenoic acid on a copper foil as a function of the number of passes at a normal load of 0.44 N and a sliding speed of 4×10^{-3} m/s, for 6-heptenoic on a clean surface (■) and after a second dose of 6-heptenoic on the previously rubbed surface. 153

5.13 Plot of the initial (indicated as 0 scan) and final (indicated as 50 scans) carbon to copper Auger ratio measured in the wear track after rubbing a copper surface saturated with 6-heptenoic acid at a normal load of 0.44 N at a sliding speed of 4×10^{-3} m/s. Neither the copper surface nor the tungsten carbide pin was cleaned between scans so that each consecutive scan is for an interface that includes the accumulated carbon from previous scans. 154

5.14 Plot of the C/Cu Auger ratio in the wear track of a saturated overlayer of heptanoic acid on a copper foil as a function of the number of passes at a normal load of 0.44 N and a sliding speed of 4×10^{-3} m/s, for heptanoic on a clean surface (■) and after a second dose of heptanoic on the previously rubbed surface. 155

5.15 Plot of the initial (indicated as 0 scan) and final (indicated as 50 scans) carbon to copper Auger ratio measured in the wear track after rubbing a copper surface saturated with heptanoic acid at a normal load of 0.44 N at a sliding speed of 4×10^{-3} m/s. Neither the copper surface nor the tungsten carbide pin was cleaned between scans so that each consecutive scan is for an interface that includes the accumulated carbon from previous scans. 156

5.16 Plot of the O/Cu Auger ratio in the wear track of a saturated overlayer of 7-octenoic acid (■), octanoic acid (●), 6-heptenoic acid (▲), and heptanoic acid (▼) as a function of the number of passes at a normal load of 0.44 N and a sliding speed of 4×10^{-3} m/s. 158

5.17 Plot of the evolution in the friction coefficient of a 7-octenoic acid overlayer on copper rubbed at a normal load of 0.44 N and a sliding speed of 4×10^{-3} m/s for an overlayer formed on a clean surface (■) and on a surface that has been dosed and rubbed six times (●). 159

5.18 Plot of the evolution in the friction coefficient of a octanoic acid overlayer on copper rubbed at a normal load of 0.44 N and a sliding speed of 4×10^{-3} m/s for an overlayer formed on a clean surface (■) and on a surface that has been dosed and rubbed six times (●). 160

5.19 Plot of the evolution in the friction coefficient of a 6-heptenoic acid overlayer on copper rubbed at a normal load of 0.44 N and a sliding speed of 4×10^{-3} m/s for an overlayer formed on a clean surface (■) and on a surface that has been dosed and rubbed six times (●). 161

5.20 Plot of the evolution in the friction coefficient of a heptanoic acid overlayer on copper rubbed at a normal load of 0.44 N and a sliding speed of 4×10^{-3} m/s for an overlayer formed on a clean surface (■) and on a surface that has been dosed and rubbed six times (●). 162

5.21 C CKK Auger profiles across a wear track for a tribochemical reaction of 6-heptenoic acid on copper following 50 scans over the surface for six doses of 6-heptenoic acid (black line) showing the Auger signal of the 6-heptenoate overlayer outside the rubbed region and the reduction in Auger signal in the rubbed region due to the tribochemical reaction. The sample was then Argon ion bombarded to remove the majority of the surface carbon (blue line) and the sample was then heated to 790 K to cause any subsurface carbon to diffuse to the surface once again (red line). 165

6.1 O 1s X-ray photoelectron spectrum of an iron foil oxidized in a background pressure of 5×10^{-7} Torr of oxygen at 800 K for various times. The reaction times are indicated adjacent to the corresponding spectrum. 180

6.2 Friction coefficient (●) and contact resistance (■) of an oxide film grown on iron as a function of the number of passes at a sliding speed of 4×10^{-3} m/s at a normal load of 0.29 N. 182

6.3 63 amu TPD profiles as a function of exposure, in Langmuirs, of trimethyl phosphite on a Fe_3O_4 film on iron collected using a heating rate of 4.2 K/s. The trimethyl phosphate exposures are indicated adjacent to the corresponding spectrum. 184

6.4 TPD data collected at 31 amu as a function of exposure, in Langmuirs, of trimethyl phosphite on a Fe_3O_4 film on iron collected using a heating rate of 4.2 K/s. The trimethyl phosphite exposures are indicated adjacent to the corresponding spectrum. 185

6.5 TPD data collected at various masses (indicated adjacent to the corresponding spectrum) following the exposure of 4 L of trimethyl phosphite on oxidized iron at 180 K. 186

6.6 C 1s XPS spectra collected at various temperatures (indicated adjacent to the corresponding spectrum) following the exposure of 30 L of trimethyl phosphite on Fe_3O_4 at 180 K. 188

6.7 P 2p XPS spectra collected at various temperatures (indicated adjacent to the corresponding spectrum) following the exposure of 30 L of trimethyl phosphite on Fe_3O_4 at 180 K. 189

6.8 Proportion of phosphate and phosphite species on oxidized iron as a function of temperature following the exposure of 30 L of trimethyl phosphite at 180 K. 191

6.9 TPD data collected at 31 amu function of exposure, in Langmuirs, of triethyl phosphite on a Fe_3O_4 film on iron collected using a heating rate of 4.2 K/s. The triethyl phosphate exposures are indicated adjacent to the corresponding spectrum. 193

6.10 TPD data collected at various masses (indicated adjacent to the corresponding spectrum) following the exposure of 4 L of triethyl phosphite on oxidized iron at 180 K. 194

6.11 C 1s XPS spectra collected at various temperatures (indicated adjacent to the corresponding spectrum) following the exposure of 30 L of triethyl phosphite on oxidized iron at 180 K. 195

6.12 P 2p XPS spectra collected at various temperatures (indicated adjacent to the corresponding spectrum) following the exposure of 30 L of triethyl phosphite on oxidized iron at 180 K. 196

6.13 Proportion of phosphate (●) and phosphite (■) species on oxidized iron as a function of temperature following the exposure of 30 L of triethyl phosphite at 180 K. Reduction in friction during gas-phase lubrication of oxidized iron at various temperatures (▲, see text). 197

6.14 Friction reduction of a Fe_3O_4 film formed by heating an iron foil at 800 K for 90 mins in 5×10^{-7} Torr of oxygen at a normal load of 0.29 N at a sliding speed of 4×10^{-3} m/s in the presence of 1×10^{-7} Torr of triethyl phosphite at sample temperatures of (a) 300, (b) 420 and (c) 650 K. 199

6.15 Plot of the formation activation energies for the removal of the second and third alkyl groups for trialkyl phosphites on Fe_3O_4 for trimethyl, triethyl and tributyl phosphite [15] as a function of the number of carbon atoms in the alkyl chain. Activation energies are obtained using the Redhead equation [28] by assuming a pre-exponential factor of $1\times10^{13}s^{-1}$, and using the experimental heating rate of 4.2 K/s for this work and a value of 10 K/s for tributyl phosphite. 204

7.1 a) Top and b) side views of the Fe_3O_4 slab used for adsorption of phosphite ester molecules, where the bottom shaded part of the iron oxide slab is constrained. 217

7.2 Geometric models of a) trimethyl phosphite, b) dimethyl phosphite and c) monomethyl phosphite. 217

7.3 Geometric models of a) triethyl phosphite, b) diethyl phosphite and c) monoethyl phosphite. 218

7.4 Geometric models of adsorbed trimethyl phosphite (a - top view, d - magnified section of side view), dimethyl phosphite (b - top view, e - magnified section of side view), and monomethyl phosphite (c - top view, f - magnified section of side view) on Fe_3O_4. 220

7.5 Geometric models of adsorbed triethyl phosphite (a - top view, d - magnified section of side view), diethyl phosphite (b - top view, e - magnified section of side view), and monoethyl phosphite (c - top view, f - magnified section of side view) on Fe_3O_4. 224

7.6 Bronsted-Evans-Polanyi plot for alkoxy group removal elementary reaction (thermally induced) of TMPi (■) and TEPi (●), the change in P-O bond scission activation energies (E_{act}) are estimated from Redhead analysis from the experimental results and enthalpy changes (ΔH) are calculated from the DFT calculated adsorption energies. 227

7.7 DFT calculated adsorption energy profiles of TMPi (top) and TEPi (bottom), where activation energy (†E_{act}), adsorption energy (E_{ads}) and reaction enthalpy (ΔH) are shown for the reaction sequence found on Fe_3O_4 slab. 229

LIST OF TABLES

3.1 Parameters for copper annealed and cleaned in vacuo at various temperatures. *Values estimated from the Hall-Petch equation. †Measured from electron microscope images in Figures 3.1 (d-f). 72

4.1 Rate constants for shear-induced methyl thiolate decomposition on copper. 117

4.2 Friction coefficients measured for first 5 scans after dosing with 1, 2, 5, or 10 Langmuir of DMDS on the copper samples that had been rubbed at an applied normal load of 0.44 N and a sliding speed of 4×10^{-3} m/s after being cleaned and annealed at 500, 850, or 1020 K. 121

5.1 The number of scans at a load on 0.44 N at a sliding speed of 4×10^{-3} m/s to decrease the C KLL Auger intensity to 1/e of its original value for the adsorption of each of the carboxylic acids on copper, compared with the initial friction coefficient of the saturated overlayer of each compound. . 157

5.2 The proportion of carbon on the surface after Rubbing and TPD experiments. 167

7.1 Adsorption energies of trimethyl phosphite, dimethyl phosphite and monomethyl phosphite adsorbed on Fe_3O_4 calculated by implementing the Vienna ab initio simulation package, VASP, density functional theory (DFT). The structures include van der Waals (VDW) forces. 221

7.2 Grid-based Bader charge analysis of P and Fe atoms calculated for trimethyl phosphite, dimethyl phosphite and monomethyl phosphite in vacuum and when adsorbed on Fe_3O_4. 221

7.3 Grid-based Bader charge analysis of O and C atoms calculated for trimethyl phosphite, dimethyl phosphite and monomethyl phosphite in vacuum and when adsorbed on Fe_3O_4. 222

7.4 Grid-based Bader charge analysis of P and Fe atoms calculated for triethyl phosphite, diethyl phosphite, and monmethyl phosphite in vacuum and when adsorbed on Fe_3O_4. 225

7.5 Grid-based Bader charge analysis of O, C1 and C2 atoms calculated for a for triethyl phosphite, diethyl phosphite, and monoethyl phosphite on Fe_3O_4. 225

7.6 Activation energies estimated by Redhead analysis from experimentally observed data [Chapter 6] and the calculated change in enthalpy (ΔH) trialkyl phosphite, dialkyl phosphite, and monoalkyl phosphite adsorbed on Fe_3O_4 calculated by implementing Vienna ab initio simulation package, VASP, density functional theory (DFT). The structures are converged by considering Van der Waals (VDW) forces. 226

ACKNOWLEDGEMENTS

It was a great opportunity of mine to have Prof. Wilfred T. Tysoe as my advisor who helped and guided me in every step of my graduate studies. It was my immense pleasure to be a student of a true scientist, he has won a place in my heart; I will always offer him great respect throughout my life for his contribution to science.

I would like to thank my dissertation committee members Prof. Andrew Pacheco, Prof. Mark Dietz, Prof. Jorg Woehl, Prof. Alan Schwabacher, and Dr. Peter Kotvis for their constructive help and suggestions.

I would like to thank my mother Nanu Maya Rana and late father Him Bahadur Rana who helped me on paving a path to the school-to-college-to-university. I would like to thank my wife Malati Thapa who always supported and helped me on accomplishing my academic dream. I would like to thank my sisters: Bhuwani Rana, Gita Rana, Madhu Rana, Amrita Rana, and brother Indra Bahadur Rana who always supported me in pursuing my academic dream. I would like to thank my late maternal grandmother Nanda Kala Rana for her immense love and care that she gave to me. I would like to thank my cousin Purnima Rana and Roshan Rana for their love and support.

During the time I have been here at UW-Milwaukee, I met enthusiastic and encouraging people who have been dedicating valuable times of their beautiful life to the research. I would like to thank Dustin Olson, a man with eager, who was always there to help and encourage me. I would like to thank Heather Loren Adams who trained me operating the UHV-tribometer, it was pleasing to see her in the lab even after her graduation to help me. I appreciate her very much for the help she provided. I would like to thank Nicholas Hopper who shared his computational skills with me. I would like to thank Alejandro Boscoboinik, Robert Bavisotto, Sree Roy, and Kaiming Hou for their help and suggestions. Also, I would like to thank senior graduate colleagues Ted Thuening, Mausumi Mahapatra, and Rasha Abuflaha.

I would like to thank Dr. Anna Benko and Dr. Holger Frosteling for helping me to check the purity of chemicals by GCMS/LCMS and NMR. I would like to thank Neal Korfhage for helping me in glass blowing jobs and I would like to thank Elise Nicks, Wendy Grober, Shelley Hagen, and Kevin Blackburn for the clerical advice they provided to me.

I would like to thank my all teachers who taught me in school, college, and the university. I would like to thank all my kith and kin who helped and encouraged me to move forward in every step of my life.

I would like to express unconditional love to my son, Martin Rana.

Chapter 1

Introduction

1.1 Tribology: Friction and Wear

The word tribology is derived from the Greek word tribos, which means to rub, so that tribology is the study of contacting interfaces or the science of friction and wear. Tribology has a major economic significance for a range of areas from metalworking equipment to space lubrication. Significant economic savings can arise by reducing friction and wear processes [1, 2]. Regarding its benefit to humankind, research work should lead to applications that are beneficial to human civilization. Interfacial chemistry has a profound influence on friction and wear through the formation of a film on surfaces by the reaction of lubricant additives, emphasizing the importance of understanding the surface interactions occurring during tribological processes. This is the subject of ongoing research work around the globe of the research described in this thesis.

The first practical application of friction was its use for lighting fires by frictional heating of rubbed pieces of wood. Looking back on the history of tribology, lubricated wheels have been used since 3500 BC to reduce the friction for moving objects and

wheeled harvesters were used in the past [3]. Around 1880 BC, Egyptians used sledges to transport heavy statues, moving them with a force of ~ 600 KN along lubricated wooden tracks (Figure 1.1) [4].

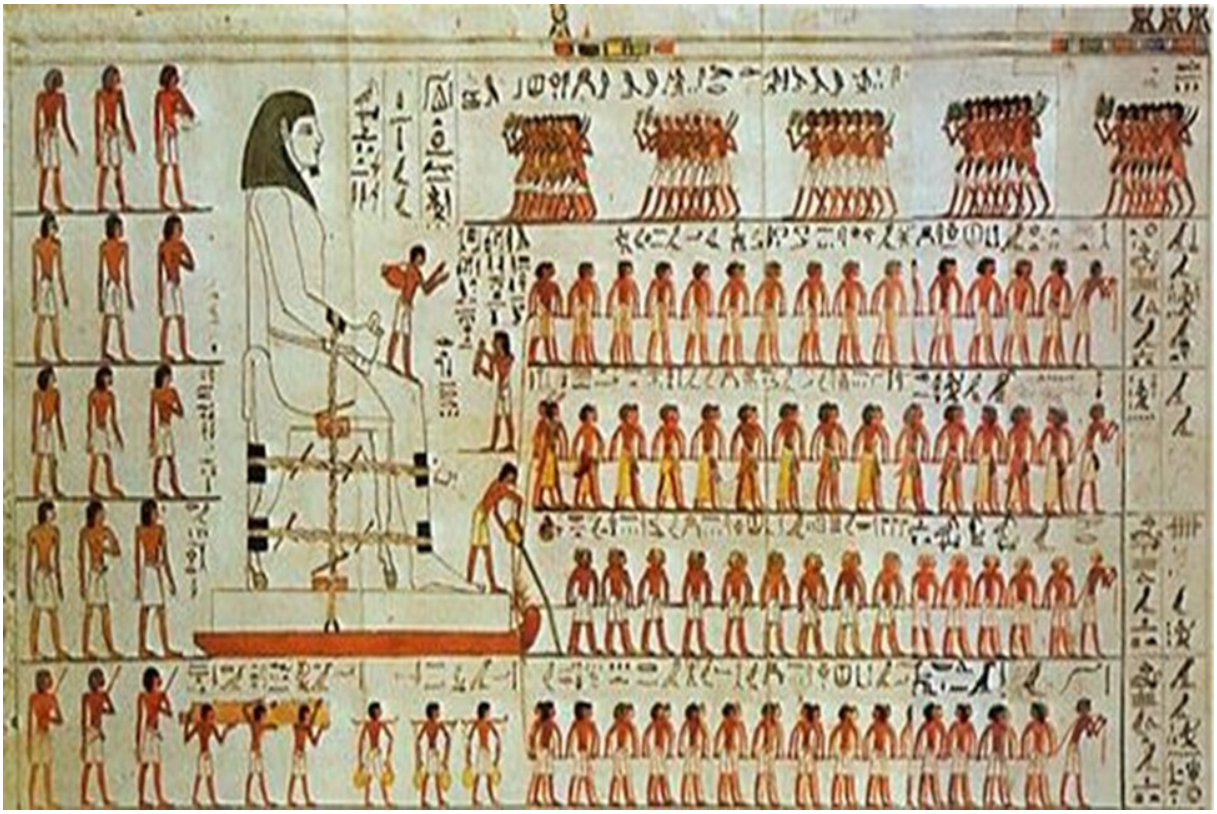

FIGURE 1.1: A drawing in a grotto at El Bersheh, circa 1880 BC [4, 5]. Liquid being poured in front of the colossus from a jar.

Da Vinci, around the 15^{th} century, introduced the concept of coefficient of friction as the ratio of friction force to normal force from experimental studies on a rectangular block sliding over a flat surface. In general, nowadays, the Coulomb friction approximation is used for calculating frictional force, where Coulomb's law of friction states that kinetic friction is independent of the sliding velocity. For two objects moving

relative to each other, the relationship between the coefficient of kinetic friction (μ_k), friction force (F_k) and normal force (F_n) is:

$$F_k = \mu_k F_n \tag{1.1}$$

Over the past decades, cutting-edge tribology research has developed the fundamental understanding of tribology that has been used to understand friction of tribological equipment from the macro to the nanoscale to save billions of dollars and exaJoules (EJ) of wasted energy per year [1]. A recent study on the impact of tribology on energy use shows that 20% (~ 103 EJ) of the world's total energy is lost to friction [2]. In tribological systems, contact occurs between the counterfaces, where the length scale of the contact ranges from a single to multiple asperities. In micro/nanoelectromechanical systems (MEMS/NEMS), where few or only a single asperity is dominant, low loads, ranging from μg to mg are important, and negligible wear takes place. In conventional or macrotribology, higher loads are important, where wear is inevitable and bulk properties of the material are important.

The concept of wear and friction are central subjects for understanding tribological systems. The nature of the materials and experimental conditions influence the wear and friction. The metallurgical compatibility, in other words, metal-metal solubility is also an important factor to be considered for understanding friction and wear of

contacting bodies. The increasing degree of metallurgical compatibility results in high friction and wear [6]. Principally identical contacting pair must be avoided to avoid high friction and wear.

The friction and wear mechanisms cannot be explained by a single approach because friction and wear depend on various conditions viz, the compatibility of the materials pair, the chemical environment, grain sizes, surface roughness, etc. To lower friction and wear, lubricants are applied between the contacting pair of surfaces. The lubricating substances can be solids (thin or powdered film), liquids, or gases. Lubrication is mainly divided into two types: solid lubrication and fluid (liquid or gaseous) film lubrication. These lubricants are intended not only to decrease friction but can also be used to decrease the wear.

The lubrication regimes depend on the sliding conditions and can be categorized as hydrodynamic or elastodynamic, mixed, and boundary lubrication. As shown in Figure 1.2 known as the Stribeck curve [7], the hydrodynamic regime is the condition where the thickness of lubricant film, h, is greater than the average roughness Ra of the contacting surface so that there is always a fluid film at the interface. In the second regime known as mixed lubrication, h is approximately equal to the surface roughness so that asperities on the surfaces start to come into contact. Finally, in the so-called boundary regime, the film is much thinner than the surface roughness so that the sliding surfaces are in intimate contact. Most of the friction-related work performed in this

dissertation is carried out under boundary lubrication condition.

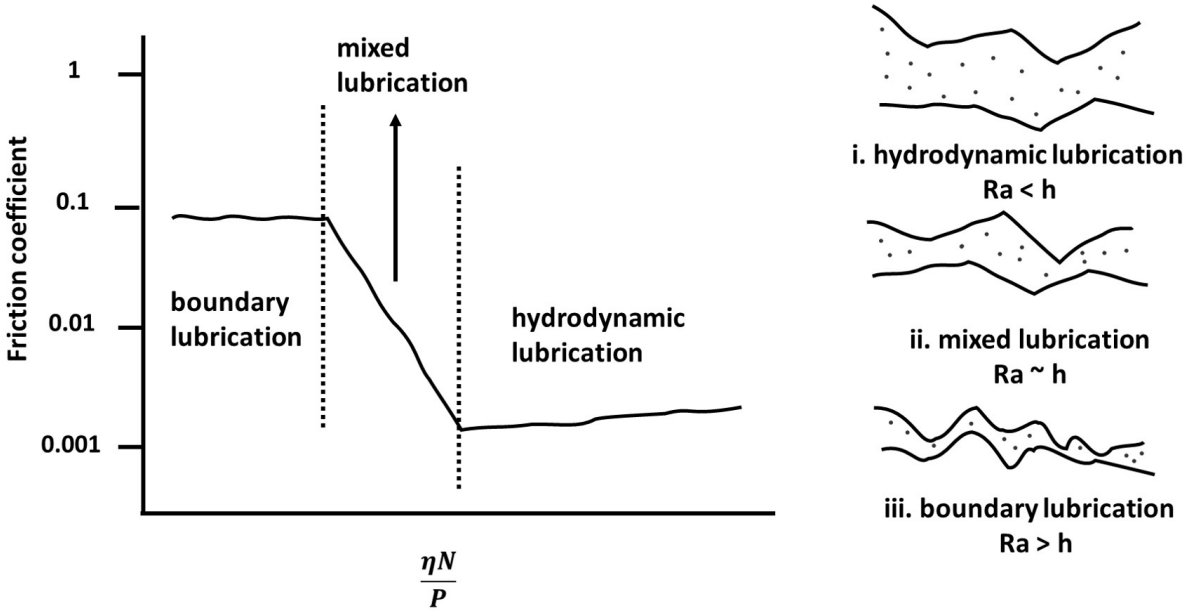

FIGURE 1.2: Stribeck curve: the relationship between the Hersey number, $\frac{\eta N}{P}$, where η is viscosity, N is the speed of the fluid and P is the normal load per length of tribological contact, and the friction coefficient μ at different lubrication regimes: i) hydrodynamic lubrication, ii) mixed lubrication, and iii) boundary lubrication [8].

As shown in Figure 1.2. iii, boundary lubrication occurs when the two contacting bodies are only separated by a thin layer of molecules so that the average roughness of the contacting interface is greater than the thickness of the layer of molecules in the contact. In this lubrication regime, direct contact between the surfaces is dominant, so that significant wear and deformation can occur in the rubbing pair. To protect the contacting surfaces and to minimize friction and wear, boundary lubricating films are formed by physisorption, chemisorption, or by chemical reactions at the sliding interface. Among these three types of surface layers, the chemisorbed layer and reactively

formed films are more stable and durable than the physisorbed layer. Polar molecules can bind strongly to the solid surface to provide a strong interaction between the rubbing surfaces and molecules [3] and such boundary layers are generally good lubricant. The chemical activity of the sliding surface also influences the bonding and reactivity of the boundary film for providing a durable and stable lubricant film. Over the past few decades, there has been a significant improvement in the quality of lubricants because of active additives that are included in the lubricant, which enhances the role of film formation by chemically reacting with the sliding surface.

The substances which are added to the base oil and interact with the rubbing pair to produce a protective film or tribofilm are known as lubricant additives. Additives are mainly of three types: low-friction, anti-wear, and extreme-pressure additives. The most commonly used additives often contain long-chain carbon atoms ($C_n > 12$), such as fatty acids, alcohols, etc. The most widely used anti-wear additive is zinc dialkyal dithiophosphate (ZDDP), a phosphate-based compound that works by forming a protective film during sliding. Phosphate or phosphite esters like trimethyl and triethyl phosphates/phosphites and organo-sulfur compound like dimethyl disulfide (DMDS) are also used as lubricant additives. Both types of P and S-based additives react to form a thin protective anti-wear film of metal-phosphate and metal-sulfide/sulfate during the tribological process. The surface and tribological properties of these compounds are investigated as part of this work.

1.2 Tribo/Mechanochemistry

Under the influence of shear at a sliding interface, chemical changes can take place at the interface between the sliding pair caused by the work carried out during sliding, known as mechanochemistry. These effects have been known for millennia, and in ancient Greece, there are reports of rubbing mercuric sulfide (cinnabar) with vinegar in copper mortar and pestle to yield mercury [9]. Shearing can modify the rate of a chemical reaction by changing the structure of the molecule, which in turn modifies its electronic configuration and can then lower the energy barrier of the chemical reaction. Such mechanochemical phenomena can be observed for several processes such as mechanical alloying, solid-state synthesis, etc. [10]. As will be shown below, tribo- or mechanochemical processes can also lead to the formation of a protective anti-wear film, can yield gas-phase reaction products [11], and induce the transport of atoms on the surface into the bulk of the sample [12].

1.3 Overview of this work described in this thesis

The surface-to-bulk transport kinetics of sulfur is studied on copper samples that have been cleaned and annealed at 500, 850, and 1020 K during the sample cleaning procedure in ultrahigh vacuum (UHV) to influence their crystallite sizes and mechanical properties. The annealed copper samples were rubbed for a number of cycles by a

tungsten carbide tribopin on a copper surface dosed with dimethyl disulfide (DMDS), where it reacts to form a methyl thiolate overlayer. The rate of methyl thiolate decomposition was measured on the different copper samples and the results showed that the methyl thiolate decomposition rates change with changed DMDS coverage. It is also found that the kinetics of sulfur transport depends on the nature of tribopin, i.e. whether it is graphitic covered or cleaned. It is found that the rate of shear-induced surface-to-bulk transport of sulfur is influenced by the presence of grain boundaries and dislocations. To further understand the transport mechanism, samples prepared using focused-ion beam (FIB) technique were extracted from the rubbed region formed on copper foils annealed at different temperatures after having been exposed to DMDS while rubbing. The sample were imaged by electron microscopy and the elemental distribution analyzed by Energy Dispersive X-Ray (EDX) images. It was found that the surface-to-bulk sulfur transport rates depend upon the grain sizes in the copper that are microstructurally developed during the sample annealing.

The mechanochemistry of saturated and unsaturated carboxylic acids viz, 6-heptenoic, 7-octenoic, heptanoic and octanoic acids were studied on annealed copper samples. The carboxylic-acid-dosed copper samples were rubbed a tungsten carbide tribopin that had been cleaned by e-beam heating. The mechanochemical reaction rates measured inside the wear track by monitoring the carbon Auger signal as a function of the number of times that the sample was rubbed shows that the interaction between

the terminus of the hydrocarbon chain and the moving counterface (the pulling point) influenced the tribochemical reaction rate. It is expected that the reaction kinetics is controlled by the tribochemical decomposition of the hydrocarbon fragment that is formed.

The surface chemistry of model lubricant additives, trimethyl phosphite (TMPi) and triethyl phosphite (TEPi), was studied on oxidized iron in UHV and the results compared with the gas-phase lubrication of TEPi on oxidized iron in a UHV tribometer. Oxide films are grown on a polycrystalline iron substrate and characterized by X-ray photoelectron spectroscopy (XPS). It reveals that on heating, the phosphite esters convert to phosphate species. Gas-phase lubrication experiments in the presence of 1×10^{-7} Torr of gas-phase TEPi show that the friction coefficient is significantly reduced, where the friction reduction is found to increase with increasing reaction temperature. The friction reduction correlates well with the proportion of phosphate product formed in the film and indicates that the formation of phosphate tribofilm is primarily responsible for reducing friction [13].

In the final section of this work, the adsorption energies of phosphite ester molecules and their fragments are calculated using the Vienna ab initio simulation package (VASP) density functional theory (DFT) method, where the results show that trimethyl phosphites are slightly more strongly adsorbed than triethyl phosphites on Fe_3O_4 surface and the phosphite esters molecule adsorb on top of the octahedral Fe^{3+} atom. The

adsorption energies calculated by DFT also scale linearly with the activation energies for the sequential removal of alkoxide groups from the phosphite esters measured experimentally using temperature-programmed desorption, and thus obey a linear-free energy relationship proposed by Evans and Polanyi [14, 15].

References

[1] K. Holmberg and A. Erdemir, "Influence of tribology on global energy consumption, costs and emissions," *Friction*, vol. 5, no. 3, pp. 263–284, 2017.

[2] K. Holmberg and A. Erdemir, "The impact of tribology on energy use and CO_2 emission globally and in combustion engine and electric cars," *Tribology International*, vol. 135, pp. 389–396, 2019.

[3] B. Bhushan, *Principles and applications of tribology*. John Wiley & Sons, 1999.

[4] A. H. Layard, *Discoveries in the Ruins of Nineveh and Babylon: with Travels in Armenia, Kurdistan and the Desert*. John Murray, 1853.

[5] C. S. C. Davison, "Transporting sixty-ton statues in early *A*ssyria and *E*gypt," *Technology and Culture*, pp. 11–16, 1961.

[6] E. Rabinowicz, "Surface interactions," *Friction and Wear of Materials. Second Edition, A Wiley-Interscience Publication*, 1995.

[7] M. Furey and J. Appeldoorn, "The effect of lubricant viscosity on metallic contact and friction in a sliding system," *ASLE Transactions*, vol. 5, no. 1, pp. 149–159, 1962.

[8] M. D. Hersey, "The laws of lubrication of horizontal journal bearings," *Journal of the Washington Academy of Sciences*, vol. 4, no. 19, pp. 542–552, 1914.

[9] Z. Goffer, *Archaeological Chemistry: A Source Book on the Applications of Chemistry to Archaeology*. John Wiley and Sons, 1980.

[10] J. J. Gilman, "Mechanochemistry," *Science*, vol. 274, no. 5284, pp. 65–65, 1996.

[11] H. L. Adams, M. T. Garvey, U. S. Ramasamy, Z. Ye, A. Martini, and W. T. Tysoe, "Shear-induced mechanochemistry: pushing molecules around," *The Journal of Physical Chemistry C*, vol. 119, no. 13, pp. 7115–7123, 2015.

[12] O. J. Furlong, B. P. Miller, and W. T. Tysoe, "Shear-induced surface-to-bulk transport at room temperature in a sliding metal–metal interface," *Tribology Letters*, vol. 41, no. 1, pp. 257–261, 2011.

[13] R. Rana and W. Tysoe, "Tribochemical mechanisms of trimethyl and triethyl phosphite on oxidized iron in ultrahigh vacuum," *Tribology Letters*, vol. 67, no. 3, p. 93, 2019.

[14] H. Eyring and M. Polanyi, "Über einfache gasreaktionen," *Z. Phys. Chem. B*, vol. 12, pp. 279–311, 1931.

[15] R. A. Van Santen, M. Neurock, and S. G. Shetty, "Reactivity theory of transition-metal surfaces: a brønsted- evans- polanyi linear activation energy- free-energy analysis," *Chemical Reviews*, vol. 110, no. 4, pp. 2005–2048, 2009.

Chapter 2

Experimental Methods

2.1 Introduction

Most of the work presented in this dissertation was carried in an ultrahigh vacuum (UHV) chamber where pressures in the range of 1.0×10^{-9} – 1.0×10^{-12} Torr are categorized as being in the UHV regime. Performing surface-science experiments in a UHV chamber has some advantages. The key feature for performing experiments in UHV is that clean and well-defined surfaces can be obtained and kept free from contaminants for times that are sufficient to allow experiments to be performed [1]. Another advantage of carrying out experiments in UHV is that electron-based spectroscopic techniques, which are inherently surface sensitive because of the small mean-free path of electrons in solids, can operate inside the chamber. From the kinetic theory of gases, if every molecule that collides with a surface sticks, a monolayer coverage can be obtained with a pressure of $\sim 1.0 \times 10^{-6}$ Torr during a period of one second. Therefore, pressures much better than 1.0×10^{-6} Torr are required to perform surface-science experiments, and generally pressures of $\sim 2.0 \times 10^{-10}$ Torr are needed for extensive experiments and most of the experiments performed for this thesis work were done under

a vacuum of ~ 2.0×10^{-10} Torr unless specifically indicated. The vacuum systems and UHV tools used for this work are described in the following sections.

2.2 Vacuum Pumps

The use of various pumps are required to reach the UHV pressure range by using several sequential pumping stages to obtain ultrahigh vacuum inside the chamber. First, a mechanical pump is used to initially pump systems from atmospheric pressure, which leads to pressures up to a medium vacuum of ~ 2.0×10^{-3} Torr. Second, turbomolecular pumps can be used which reduce the pressure to ~ 2.0×10^{-8} Torr (high vacuum) and finally, ion pumps are used to reach the UHV range of ~ 2.0×10^{-10} Torr after baking the system as explained in the section describing the UHV chambers. In cases in which high gas throughputs are required, diffusion pumps can be used, but were not required during the course of this work. However, for pumping the gas-handling lines, two pumping systems are used. First, a mechanical pump is used to obtain a medium vacuum and a diffusion pump is used to obtain a high vacuum in the gas line.

2.2.1 Rotatory/Mechanical Pump

The working principle of the rotary pump is based on the use of pump oil with the help of a rotating vane to pressurize and expel the gas, where the pump oil also works

as both a lubricant and sealant. The vane slides into and out of the rotor and seals on all edges, so that during this process the vane traps the gas coming from the inlet section and forces it out from the outlet section as shown in the Figure 2.1. This vane operates at a steady speed and creates vacuum a in the mTorr range [2]. Although the mechanical pump cannot create a high vacuum, it has a high throughput and is used as a backing pump to diffusion and turbomolecular pumps and for initially pumping the chamber from atmospheric pressure.

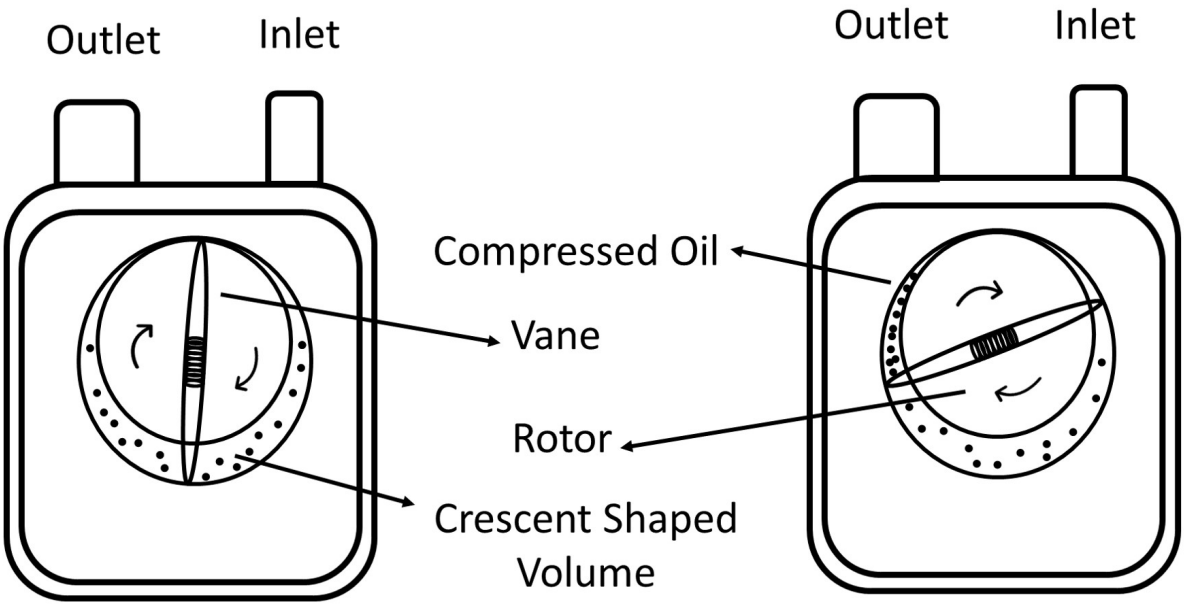

FIGURE 2.1: Rotary pump operation stages.

2.2.2 Diffusion Pump

The diffusion pump, also called the gas-jet pump, uses a high speed of vapor to direct gas molecules down into the bottom of the pump towards the outlet. In other words, oil gas molecules traveling upward through the jet assembly are directed downward and forced to exit through the outlet, where a rotary pump is connected to finally remove the gas from the system. Oil having a low vapor pressure is used for producing the gas-jet. The diffusion pump does not work alone for pumping and it must be continuously backed by the mechanical pump via the outlet throughout its operation. A schematic of diffusion pump is shown in the Figure 2.2.

A diffusion pump contains vertically stacked jet assemblies inside a glass or stainless steel container, where a gas-jet is produced by heating the oil bath via an oil heater which is attached to the bottom of the chamber [2, 3]. The diffusion pump is equipped with cooling system which minimizes back streaming of the oil into the gas handling line/UHV chamber and condensed the oil in the outset, thus leaving the pressurized gas to be pumped away by the rotary pump. Depending on the make, for cooling the oil vapor, a water coil or air fan is used and backstreaming can be prevented by using a or cryotrap. Despite the back-streaming problem, these pumps are cost-effective.

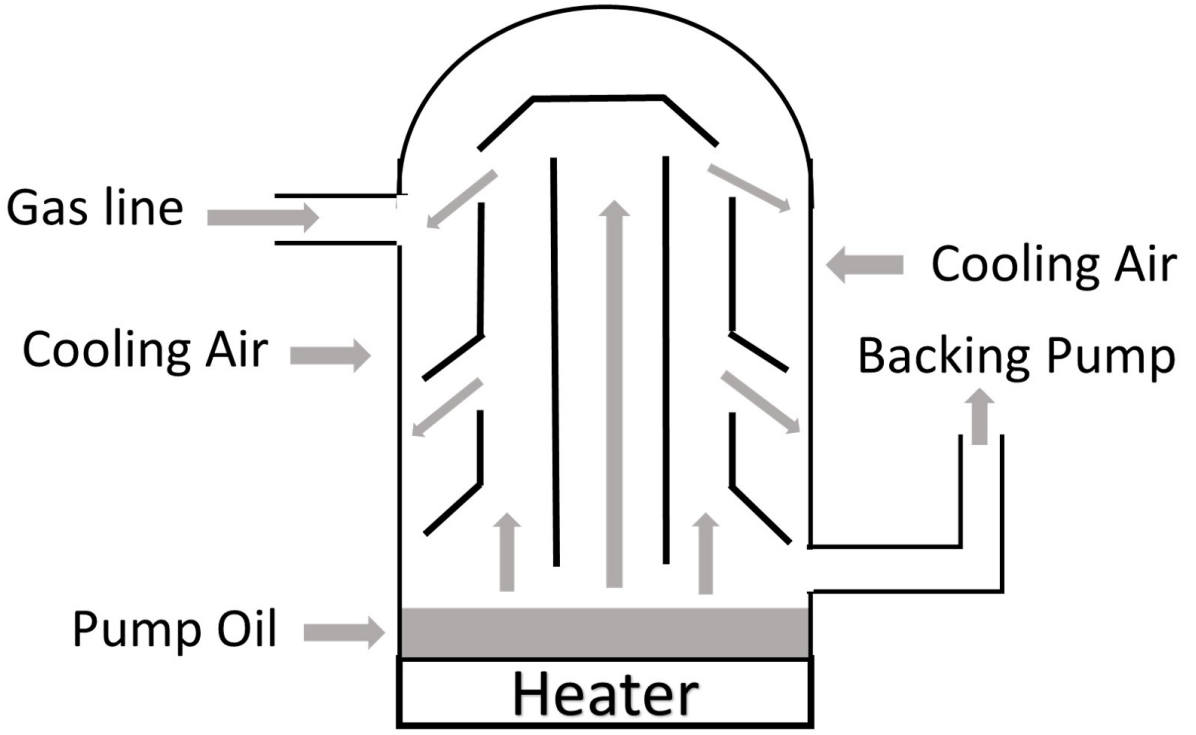

FIGURE 2.2: Schematic of the diffusion pump.

2.2.3 Turbomolecular Pump

The turbomolecular pump operates by the use of a very rapidly spinning turbine. The multiple stages of the turbine (rotor) and stator blades are organized in series to give momentum to the gas molecules and push them towards the outlet end of the pump, which is connected to backing pump. Repeated collision of gaseous molecules with a set of rotor/stator blades arranged in series occurs when angled blades rotate up to speeds of ~75 krpm. The spinning rotor blades transfer energy to the gas molecules and these gas molecules enter the stator to exit a first set of rotor and stator blades.

Again, these gas molecules collide with second set of rotor blades and enter the stator blades, and this process continues until the gas molecules are forced out from the end of the pump to exit the chamber [2, 4]. Figure 2.3 shows the arrangement of rotor and stator blades in the pump.

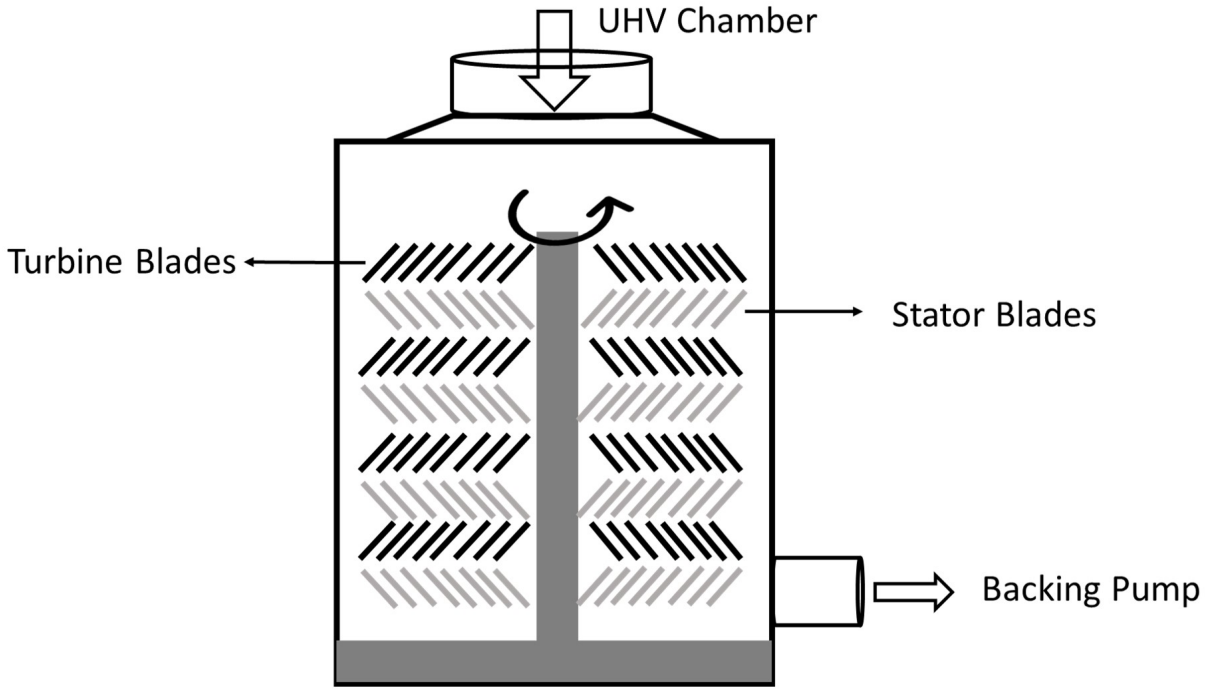

FIGURE 2.3: Schematics of turbomolecular pump.

Since the rotating speed of blade is high (75 krpm/1350 Hz at normal operation), it is required to maintain the blade thickness to withstand the high pressure. Friction builds up heat due to the high speed, therefore the pump is air-cooled by a fan attached to the end of the pump. To reduce the deformation of rotor blades, stiff materials are used to build them. To minimize the friction, magnetic bearings are used, and these

bearings also help to eliminate oil contamination. Turbomolecular pump can be used over wide range of high vacuum pressures and it can achieve a vacuum of ~ 1.0×10^{-8} Torr. Depending upon the size of pump, the turbomolecular pump is fitted to the UHV chamber with Conflat® flange and backed continuously up by a mechanical pump.

2.2.4 Ion Pump

Ion pump is the primary pump for achieving UHV, where incoming gaseous molecules are ionized within the chamber by an electric discharge. An electrical potential of between 3 to 7 kV is maintained between the ion pump electrodes, which accelerates the ions into the cathode and helps to trap the ions or sputter the cathode to produce a newly exposed surface. The electric discharge creates a swirling electron cloud which ionizes the incoming gaseous molecules. The gas ions formed during this process accelerate towards the titanium/tantalum cathode to become buried, and the pumping effect occurs. The incoming ions are either chemisorbed or physisorbed onto the cathode [2].

As shown in the Figure 2.4, a strong magnetic field of 800 - 2000 G is applied parallel to the anodes to guide the electrons in a spiral trajectory, which increases the ionization probability. The ion pump can operate when the pressure of the chamber reaches ~ 1.0×10^{-5} Torr and can reach a vacuum of ~ 1.0×10^{-10} Torr after the chamber has been baked. Once it reaches the optimum vacuum, this pump does not require a backing

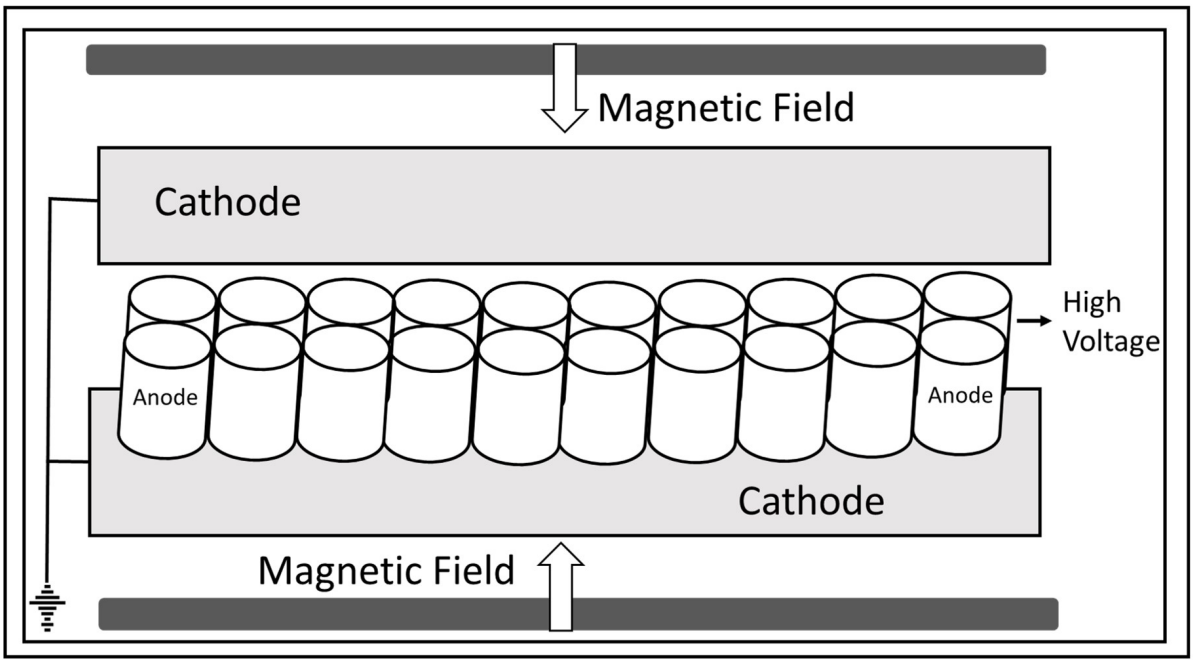

FIGURE 2.4: Schematics of ion pump.

pump. This pump is also vibration free but, because the gases are trapped in the pump, cannot be used when the gas loads are high.

2.3 Gas Handling Line and Chemical Purification

A gas-handling is used to store gases and volatile liquids for introduction into the UHV chamber via a high-precision leak valve. The line is built from glass tubes, where several valves are fitted to attach gas cylinders or vials for liquids, and is connected to rotary and diffusion pumps to ultimately produce a vacuum in the 1.0×10^{-7} Torr range. A schematic diagram of a typical gas-handling line and its attachment to the UHV

chamber is shown in Figure 2.5. A diaphragm manometer is fitted to the gas-handling line to monitor the gas pressure inside it. The arms of the gas lines are connected to the

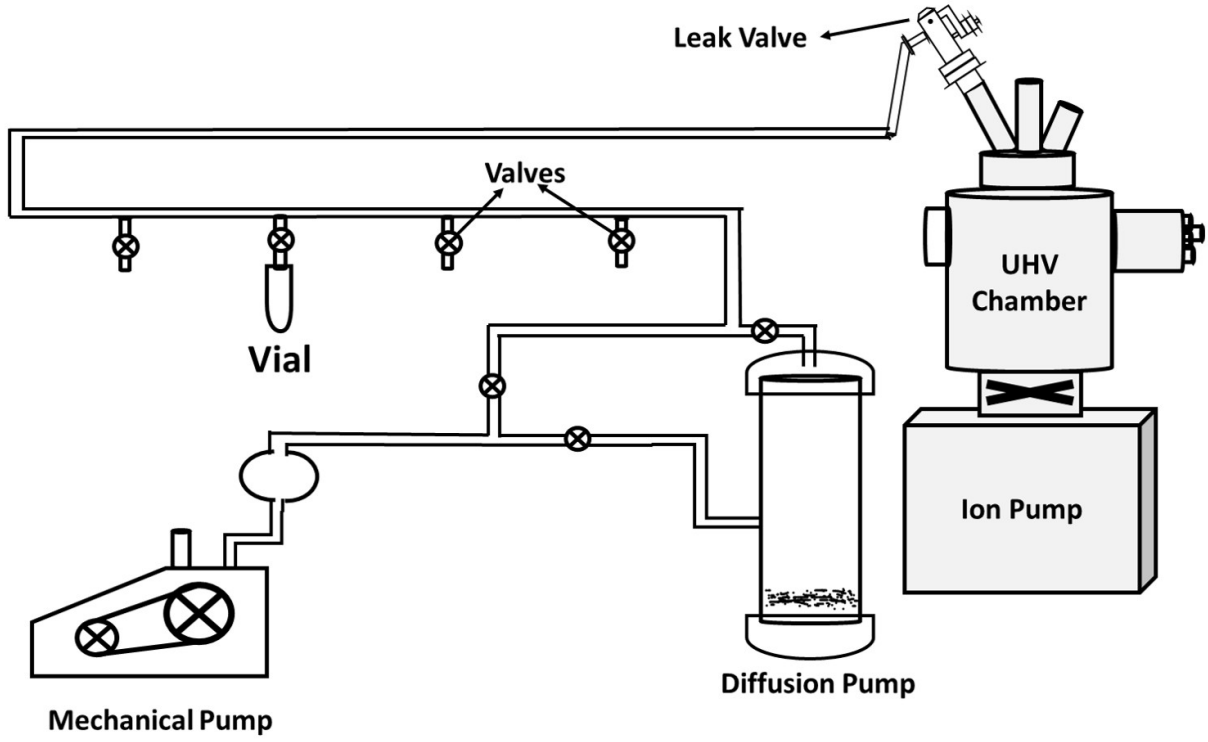

FIGURE 2.5: Schematics of gas handling line attached with UHV chamber.

UHV chamber through high-precision leak valves to introduce various gaseous chemicals into the vacuum chamber. For example, these can be Ar for argon-ion sputter cleaning of samples, N_2 for back-filling the chamber, and gaseous chemicals of interest for dosing onto the sample. A small glass bottle or vial containing the chemical of interest is attached through a valve to introduce the chemical into the gas line. The liquid chemicals in the vial can be cleaned by freeze-pump-thaw cycles using pumps connected to the gas line to remove any dissolved volatile contaminants.

2.4 Design, Construction, and Operation of a UHV Chamber

The chambers used in these experiments consisted of a 304 stainless-steel vessel having a 6.0" (tribochamber) or 8.0" (X-ray photoelectron spectroscopy chamber) diameter, machined with several sized ports that are terminated by Conflat® flanges on the outside of the vacuum vessel in order to mount UHV-based spectroscopic or non-spectroscopic tools to allow a wide range of experiments to be performed. Several windows are mounted on the Conflat® flanges and are used to see inside the chamber while manipulating the sample. A schematic diagram of a typical UHV chamber is shown in Figure 2.6. Once the mechanical, turbomolecular and ion pumps are operated to create a vacuum, the chamber is required to be baked out to remove water vapor and other volatile contaminants from the wall of the chamber that can limit the ultimate pressure of the system, and to enable pressures in UHV range to be attained. Heating tapes are mounted on the external walls of the chamber and it is covered by aluminum foil which insulates the chamber by trapping a layer of air and also helps to heat the chamber evenly. Normally chambers are baked for ~36-42 hours at 100-200^{o}C. After baking the chamber, before the chamber cools to room temperature, it is necessary to outgas any filaments of UHV-based equipment inside the chamber which helps to attain a better vacuum.

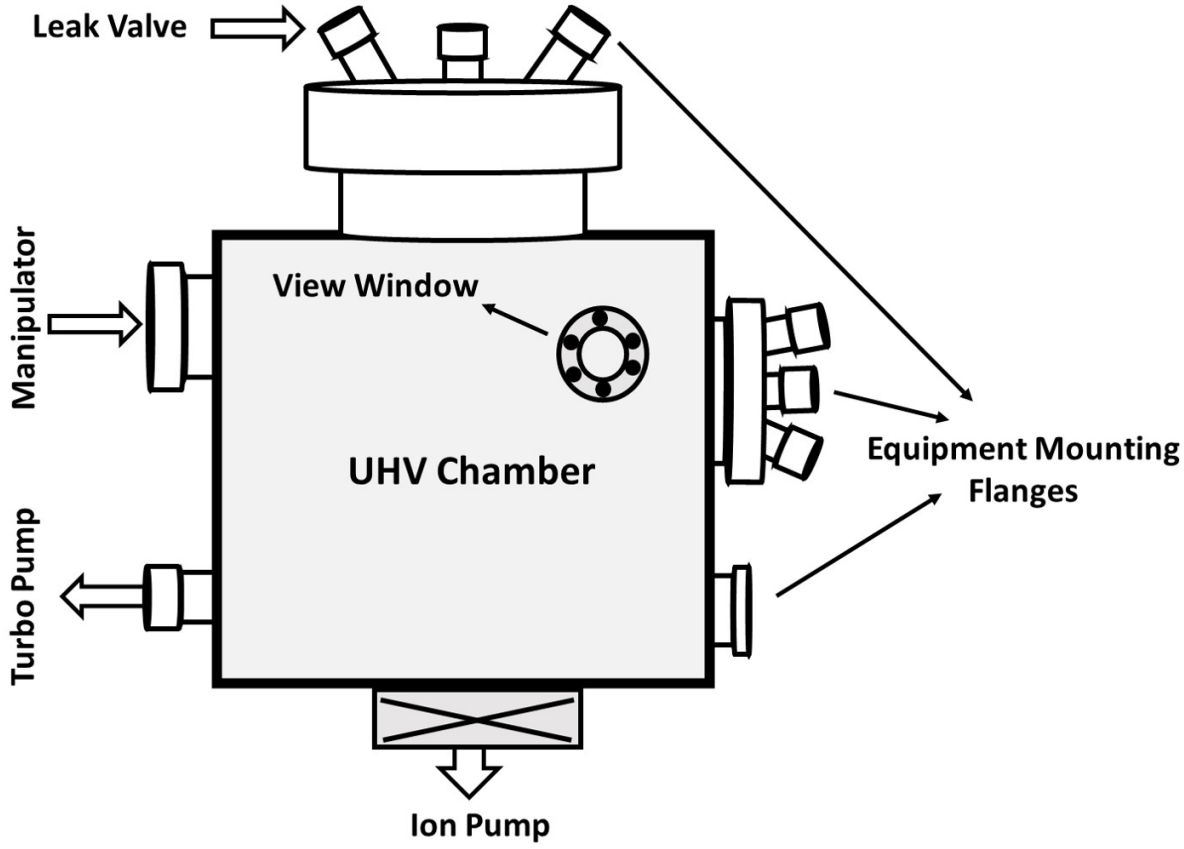

FIGURE 2.6: Schematics of typical UHV chamber.

2.5 UHV Tools and Techniques

To build a fully functioning UHV system, it is necessary to have several UHV-based analytical and experimental tools mounted inside the chamber. The equipment and techniques used during the work presented in this dissertation are described below.

2.5.1 Sample Manipulators

In order to conduct experiments in the vacuum chamber, it is generally necessary to move samples in vacuum to various positions to either clean or analyze the sample or to perform other experiments. This is accomplished by a sample manipulator which is mounted on 6.0″-diameter flange. It can move the sample in the X, Y and Z directions with precision of 0.002 mm over a maximum distance of 25.0 mm in either direction.

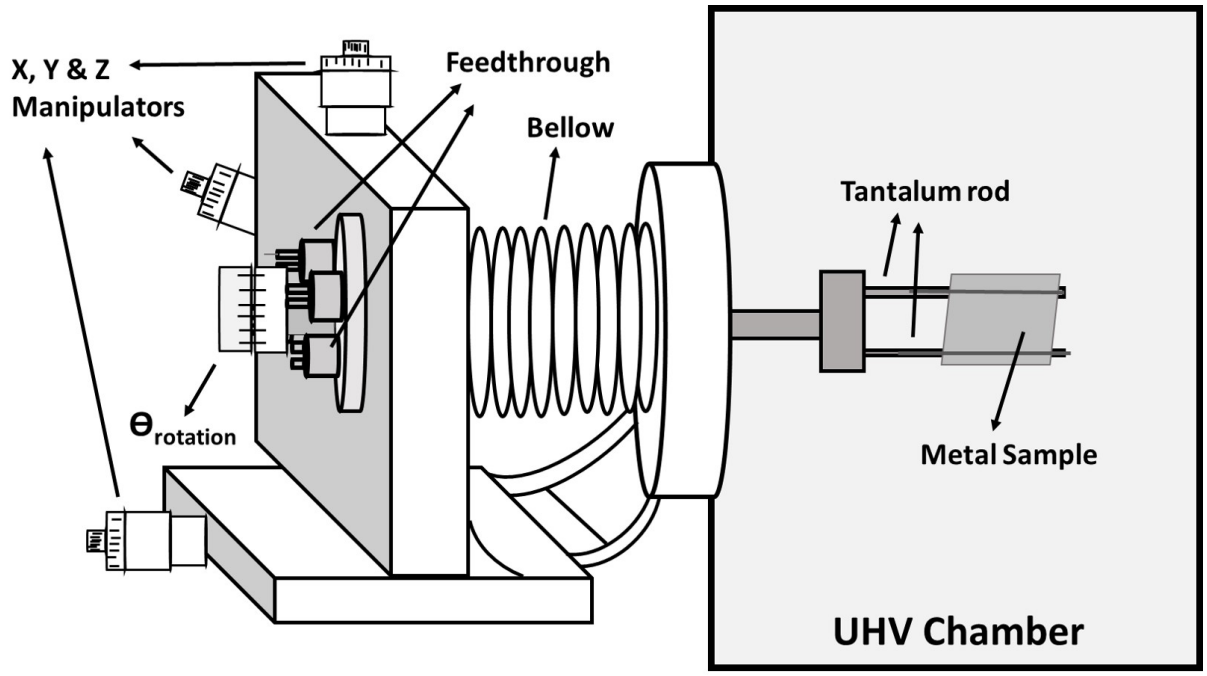

FIGURE 2.7: Schematics of sample manipulator.

Also, sample can be rotated around the main axis (see Figure 2.7) by 360^o. On the manipulator flange, 1⅓″ Conflat® flanges are used to mount feedthroughs which can

be used, for example, for resistive heating of the sample, installing a (K-type) thermocouple for monitoring sample temperature or for introducing refrigerants to cool the sample.

2.5.2 Sample Preparation, Mounting and Cleaning

Two different polycrystalline metal samples were used in this work. Iron samples were used for temperature-programmed desorption (TPD), X-ray photoelectron spectroscopy (XPS) and tribological measurements. For these experiments, 0.1 mm thick iron foils (99.999%) with ~17 mm x 17 mm dimension were cut, and spot welded over a 0.45 mm steel base after polishing the iron foil with 1.0 μm diamond paste to give it a mirror finish. The sample comprising the iron on a steel base was mounted by spot welding to tantalum rods attached to the manipulator. Iron foils were cleaned by a number of annealing and sputtering cycles, where foils were heated to ~ 1000 K and Ar ion bombarded using a 2.0-keV beam energy with a 3.5 $\mu A/cm^2$ sample current. The cleanliness of the iron sample was monitored using Auger spectroscopy (see section 2.5.6).

Another type of sample used in this work was a polycrystalline copper foil, where surface-to-bulk sulfur transport, methyl thiolate decomposition and carbon removal or carbon transport rates were measured. The 1.0-mm thick copper foils with a dimension of ~17 mm x 17 mm were polished with silicon grit and diamond paste, where 1.0-μm

diamond paste was used as a final step to give a mirror finish. Then the sample was cleaned with acetone and mounted to the tantalum rods by spot welding. These copper foils were cleaned at different temperatures i.e. 500, 850, or 1020 K with 1.0 keV ion-beam energies with a 2.0 $\mu A/cm^2$ sample current. The cleanliness of both iron and copper samples were monitored by Auger electron spectroscopy (see section 2.5.6).

2.5.3 Mass Spectrometer

The mass spectrometers used in this work are Ametek Dycor and UTi quadrupole gas analyzers. These mass spectrometers were used for checking the purity of gaseous chemicals, leak checking the vacuum system, and residual gas analysis during the tribological experiments in the vacuum chamber. The Ametek Dycor was used for TPD analysis and the UTi mass spectrometer was used for measuring the rates of product evolution during shear-induced methyl thiolate decomposition. A mass spectrometer head mainly consists of an ion source, analyzer, and detector. The ion source generates the ions, where a hot filament generates electrons with a kinetic energy of 70 eV which are used to ionize the gas molecules. These ions are then accelerated towards the entrance of the quadrupole analyzer, where the applied combined AC and DC voltages between the quadrupoles helps to differentiate the ions with respect to their charge-to-mass (m/z) ratios and allows the mass-filtered ions to reach the detector to read and record the ions current as a function of the mass of the fragment. The detectors can

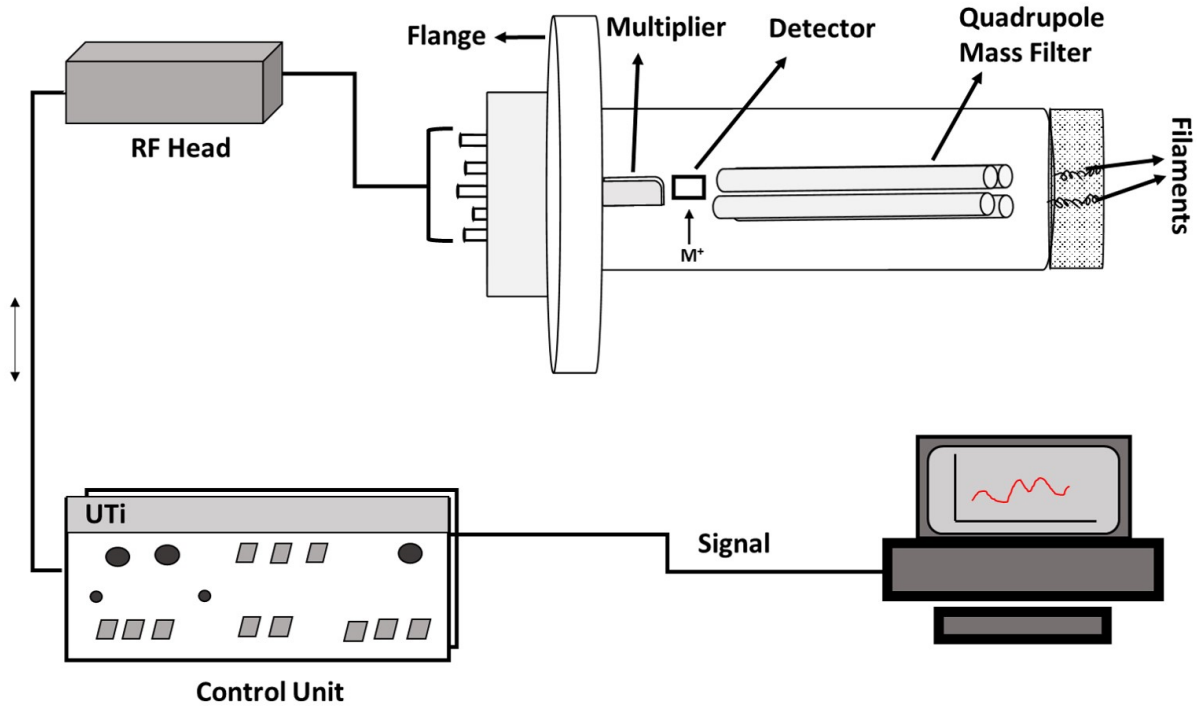

FIGURE 2.8: Schematics of mass spectrometer.

either be a Faraday cup or an electron multiplier, where the detector of interest can be used depending upon the nature of experimental design. The Faraday cup is less sensitive than the electron multiplier and is used in cases in which the gas pressures are high. Data were collected by using LabView software to plot the ion intensity versus its mass or to monitor the intensity of a particular fragment mass as a function of time. A schematic of a quadrupole mass spectrometer is given in Figure 2.8.

2.5.4 Temperature-Programmed Desorption

The temperature-programmed desorption (TPD) experiments for the 7-octenoic acid, octanoic acid, 6-heptenoic acid and heptanoic acid were carried out on copper sample. The carboxylic acids were exposed to cleaned copper foil via a Knudsen dosing source at room temperature. A sample heating rate of 2.9 K/s was maintained, and the sample temperature was ramped to ~815 K and intensities of six different mass-fragments were collected. The TPD experiments for triethyl and trimethyl phosphites were carried out on the iron sample. The cleaned iron sample was cooled to ~ 180 K and dosed with 0.5, 1, 2, or 4 Langmuir exposures of the phosphite ester as explained in Chapter 6. Liquid nitrogen for sample cooling an iron sample was supplied from a 5 L liquid-nitrogen filled Dewar. A sample heating rate of 4.2 K/s was used for the TPD experiments of phosphite esters. A LabView program was used for controlling the temperature ramp of the sample to a maximum of ~950 K and for collecting six different mass spectrometer fragments.

The liquid samples used for the TPD experiments were transferred to glass bottles and attached to the gas-handling systems of the vacuum chambers, where it was subject to several freeze-pump-thaw cycles.

The TPD results were analyzed using a Redhead analysis, where the desorption activation energy of an adsorbed compound could be calculated [5] using the equation:

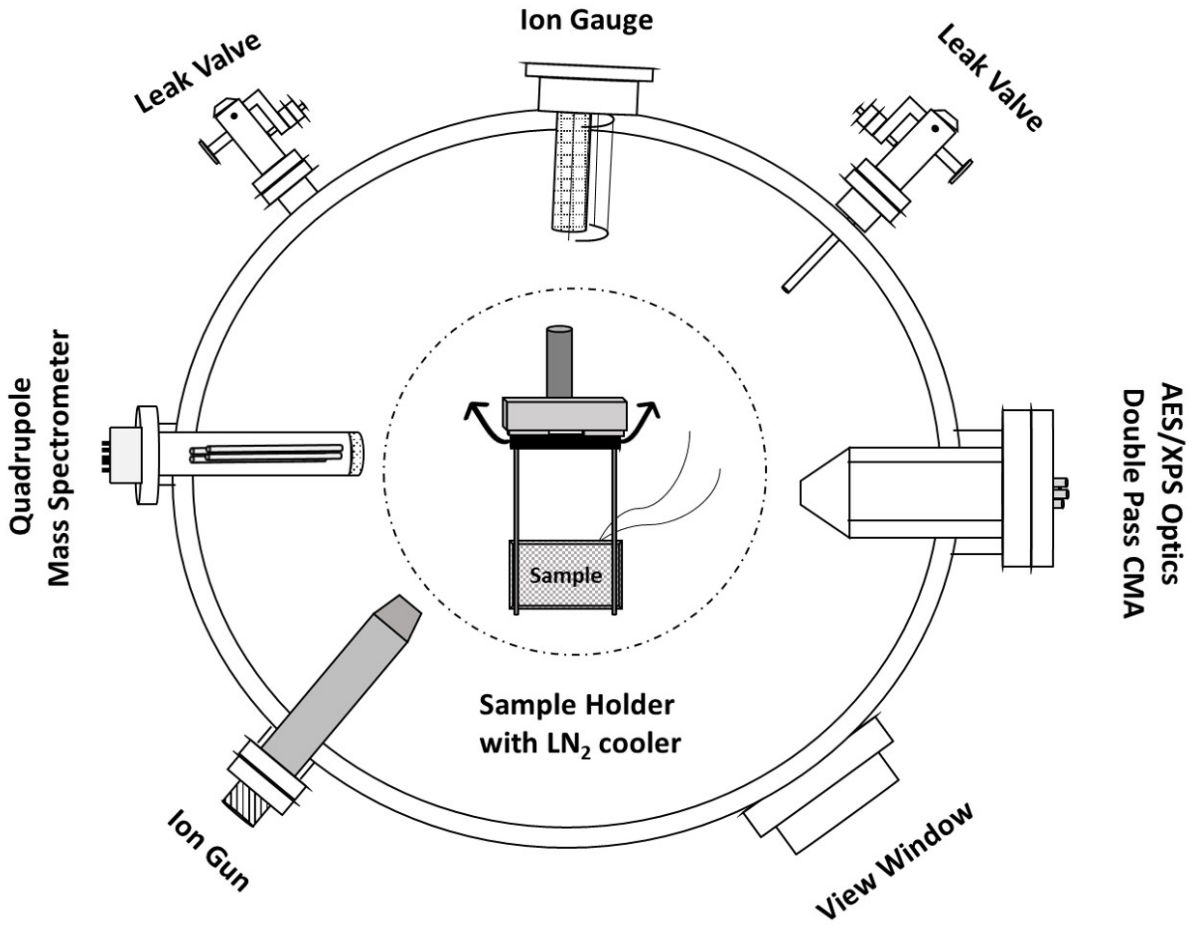

FIGURE 2.9: Schematics of TPD system.

$$E_d = RT_p\left[ln\left(\frac{AT_p}{\beta}\right) - 3.64\right] \tag{2.1}$$

where, E_d is activation energy of desorption, R is gas constant, A is pre-exponential factor, T_p is sample temperature and β is heating rate [K/s].

The TPD system was also equipped with an X-ray photoelectron spectroscopy (XPS)

system (see Section 2.5.7), where the base pressure of ~ 2.0×10^{-10} Torr can be obtained after baking. Leak valves were connected to the gas-line for dosing reactants, and contained an ion gun for sample cleaning, a LN_2 sample cooling system that allowed the sample to be cooled to ~100 K, and a Dycor quadrupole mass spectrometer for collecting TPD data, leak checking and gas analysis. The design of the TPD system is shown in Figure 2.9.

2.5.5 Cylindrical Mirror Analyzer

The cylindrical-mirror analyzer (CMA) is an electron analyzer and is used to measure the number of electrons as a function of the kinetic energy for measuring photoelectron and Auger spectra. The CMA consists of two concentric cylinders arranged one inside the other, where the inner cylinder is at ground potential and outer cylinder is at some negative potential. The potential applied across the cylinders allows the passage of impinging electrons having a specific kinetic energy, which depends linearly on the potential energy difference between the inner and the outer cylinder, and to reach the detector [6]. The electron gun is placed coaxially, and an electron detector or channeltron is placed behind an aperture in line with the focal plane of the CMA. Electrons ejected from samples enter the entrance slit of the analyzer and reach the channeltron, where secondary electrons are generated to create a current pulse. The CMA has the

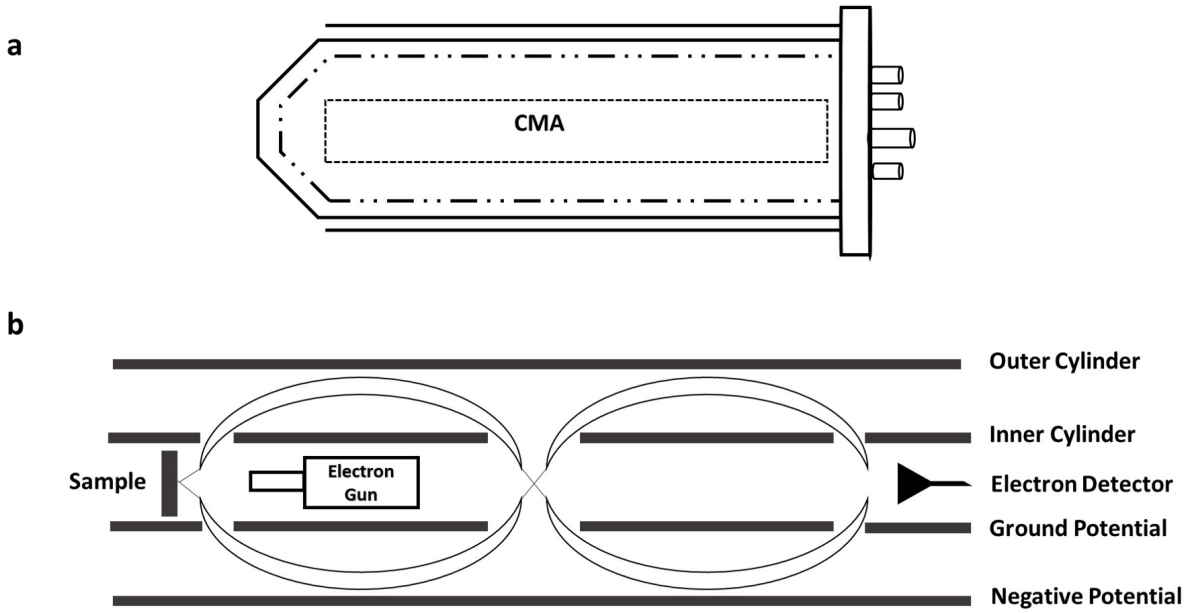

FIGURE 2.10: a. Outline of typical cylindrical mirror analyzer (CMA) b. Internal optics of double pass CMA.

geometrical advantage of collecting electrons uniformly around a 360^o azimuth. As indicated above, the kinetic energy of the electrons that pass through the CMA is directly proportional to the potential energy difference between the outer and inner cylinder. However, the energy resolution of the CMA is also proportional to the kinetic energy of the electrons. High-resolution detection is not required for Auger spectroscopy (see Section 2.5.6), but is needed for XPS (see Section 2.5.7). Consequently, Auger spectra are collected by varying the potential energy difference between the inner and outer cylinders. However, to collect XPS data, the CMA is operated as an energy filter with a constant potential energy difference between the inner and outer cylinders. The fixed kinetic energy of the electrons traversing the CMA is known as the pass energy, E_P,

and effectively allows the spectral resolution to be tuned. To obtain a spectrum, a retarding voltage E_R is applied to the CMA to decelerate the electrons so that electrons with a kinetic energy E_K given by $E_K = E_P + E_R$ can reach the detector. The spectrum is collected by varying E_R.

The schematics shown in Figure 2.10 is of double-pass CMA design. In this work, both single- and double-pass CMAs were used. For the experiments carried out in the XPS or TPD chambers, a double-pass CMA was used, while for the experiments carried out in tribometer chamber a single-pass CMA was used.

2.5.6 Auger Electron Spectroscopy

Auger electron spectroscopy (AES) is a surface-sensitive technique, which can probe approximately the top five layers of the surfaces of solids [7]. Auger electrons are produced when a high-energy electron beam hits the surface of the material. During the Auger process, as shown in Figure 2.11, an electron hole is created by the impact of high-energy electrons while, at the same time, the electron hole is filled by an electron from a higher energy level. During the process of the electron transition from a higher energy level to a lower energy level, energy is released, and this released energy ejects a third or Auger electron from the higher energy level. For example, if first electron is ejected from a K shell and the second and third electrons are from higher-energy L_2

and L_3 shells, this Auger process is labeled KL_2L_3. The measured Auger electron intensities at different kinetic energies are useful to identify the different types of atoms because different elements have different characteristic Auger kinetic energies. For this spectroscopic technique, the suggested background vacuum pressure is lower than $\sim 5.0 \times 10^{-8}$ Torr. In this work, two types of electron gun were used as a source of the

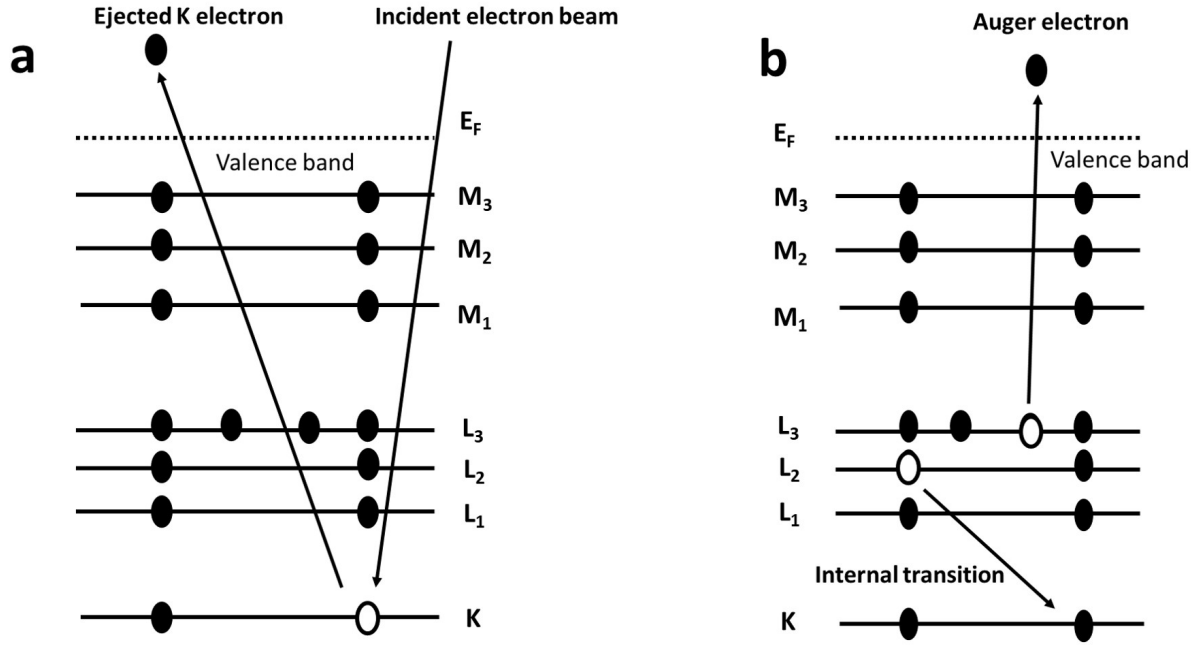

FIGURE 2.11: Auger process a. ejection of K electron by the impact of incident electron beam b. generation of auger electron after internal transition [8].

electron beam. For monitoring the cleanliness of samples, an electron gun mounted inside the CMA was used. Another type of high spatial-resolution electron gun was used for measuring the surface-to-bulk sulfur and carbon transport rates. This electron gun was a Staib model EK050M2 Microfocus electron gun, which can produce a ~100 μm electron beam spot size with a relatively high beam current for collecting Auger

spectra, or small beams spots with lower currents for obtaining scanning electron microscopy images of the sample surface. This sized spot was necessary for analyzing the wear track during the tribological experiments.

2.5.7 X-ray Photoelectron Spectroscopy

X-ray photoelectron spectroscopy (XPS) is a surface-sensitive technique that can be used to characterize and analyze a sample to a depth of ~2 - 10 nm. XPS requires high vacuum to operate and a vacuum of ~5.0 $\times 10^{-8}$ Torr or less must be maintained because this vacuum level allows the electron to travel to the detector. To produce X-rays, high-energy source electrons are produced from a hot filament to strike an anode to produce X- rays. The X-rays incident on the sample surface ejects photoelectrons [9] from the atoms in the sample as shown in the Figure 2.12. The intensities of these photoelectrons are measured as a function of the binding energy of the electrons in the sample which is characteristic of the type of element and nature of the chemical binding if the atoms in the surface region of the sample and can detect all elements except H and He. The equation for calculating the binding energy $E_{binding}$ from the electron kinetics energy measured by the double-pass CMA, $E_{kinetic}$ is [6].

$$E_{binding} = h\nu - (E_{kinetic} + \phi) \tag{2.2}$$

where, ϕ is the work function difference between the sample and spectrometer and $h\nu$ is the X-ray photon energy.

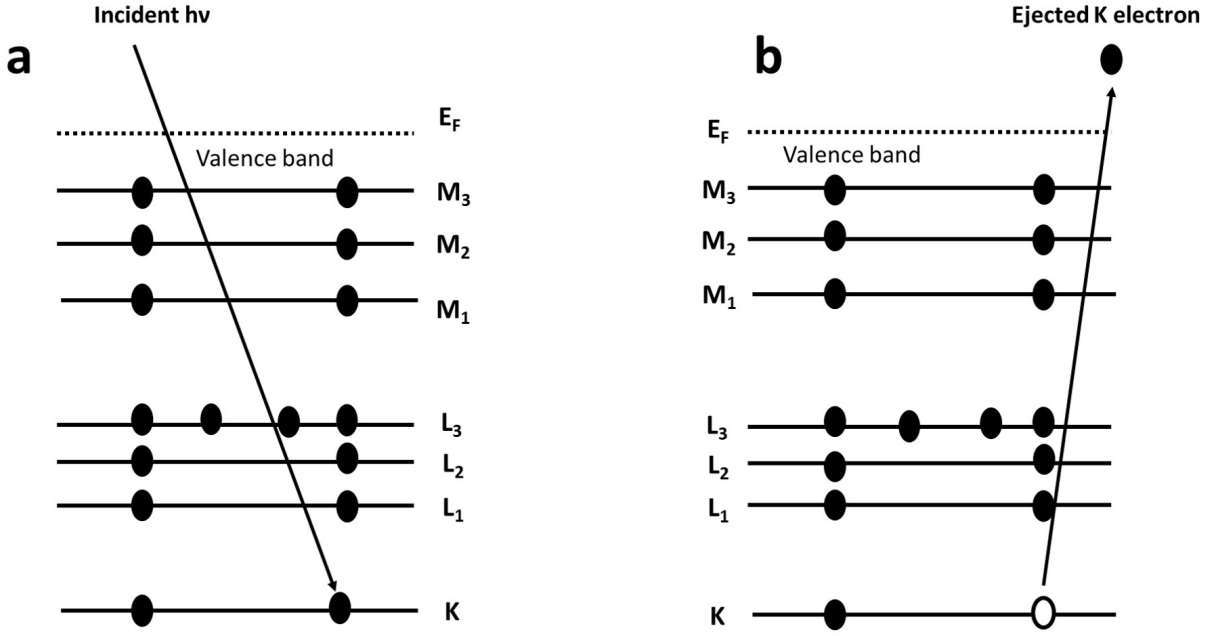

FIGURE 2.12: XPS process a. incident photon b. ejection of K electron followed by X-ray emission.

For generating X-rays, a twin anode X-ray source, as shown in Figure 2.13, is used, which has aluminum (to produce AlKα radiation at 1486.6 eV) and magnesium (to produce MgKα radiation at 1253.6 eV) twin anodes. The heated thoria-coated iridium filaments emit electrons, and these electrons are accelerated towards the anode to produce X-rays. A large amount of power is dissipated by the anode during the X-ray production, so that the anodes are water-cooled. A thin aluminum window of 0.2 μm in thickness is used to prevent secondary electrons from being emitted from the X-ray

source and reaching the analyzer.

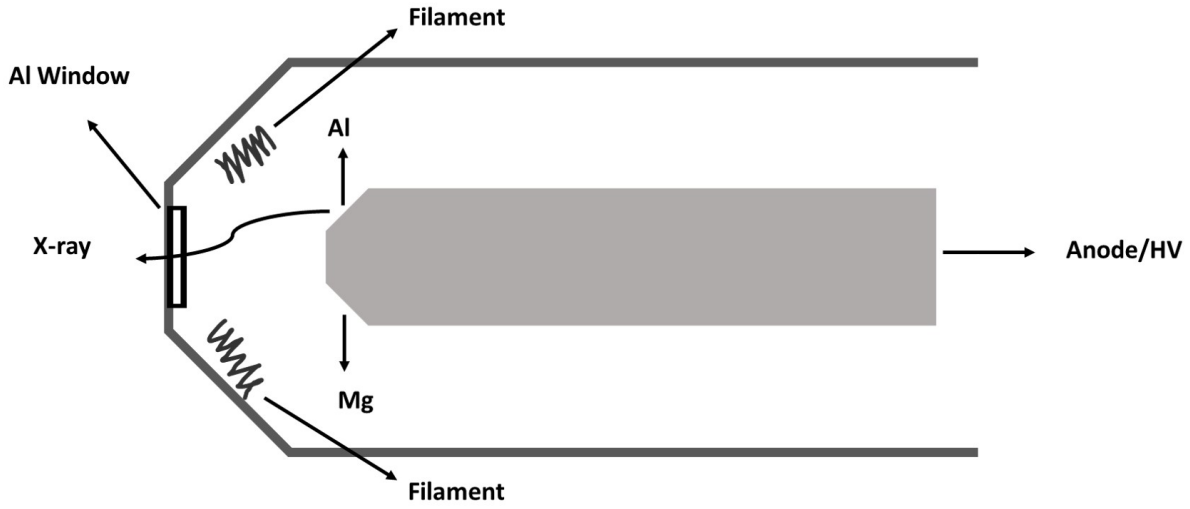

FIGURE 2.13: Schematics of twin X-ray source.

For the work described in this thesis, the X-ray source control was a SPECS XRC 1000 system. The XPS data were collected using an X-ray power of 250 W (12.5 kV × 20 mA) and a 100 eV pass energy for the CMA. The sample was positioned approximately with a 45^o glancing angle to the CMA while operating the XPS system.

2.5.8 Scanning Electron Microscopy

In this work, the purpose of using secondary electron microscopy (SEM) is to precisely locate the wear track by imaging the sample and to then use a microfocused electron beam for Auger analysis of the wear track. The microfocused electron beam is generated by the optical Staib EK050M2 electron gun which has an alignment and focusing

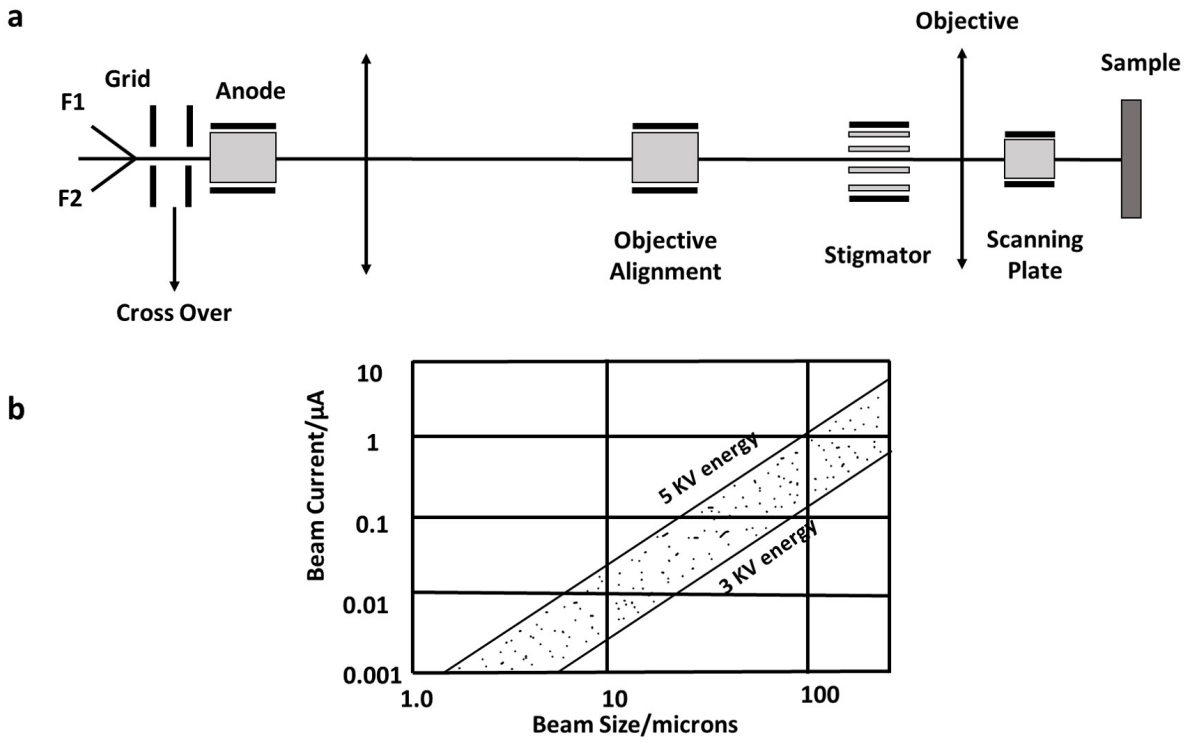

FIGURE 2.14: a. SEM Optical alignment system b. Beam size vs Beam current.

system as shown in Figure 2.14 (a) [10]. The hairpin type W filament is heated by a current of 1.7 A to emit the electrons and the electron beam can be demagnified in the range from 3/1 down to a 1/10 ratio. The spot size of the beam can be adjusted from 50 μm to 3 μm and the beam current ranges between 10 μA to 0.1 nA. A typical variation in beam current with spot sizes is shown in Figure 2.14 (b) and there is a clear compromise between spatial resolution (spot size) and sensitivity (beam current). For the sulfur and carbon surface-to-bulk transport experiments, a TV screen was used to display SEM images of the surface of the sample and was used to locate the wear track. The SEM gun was mounted on the top of the tribometer chamber which was slightly

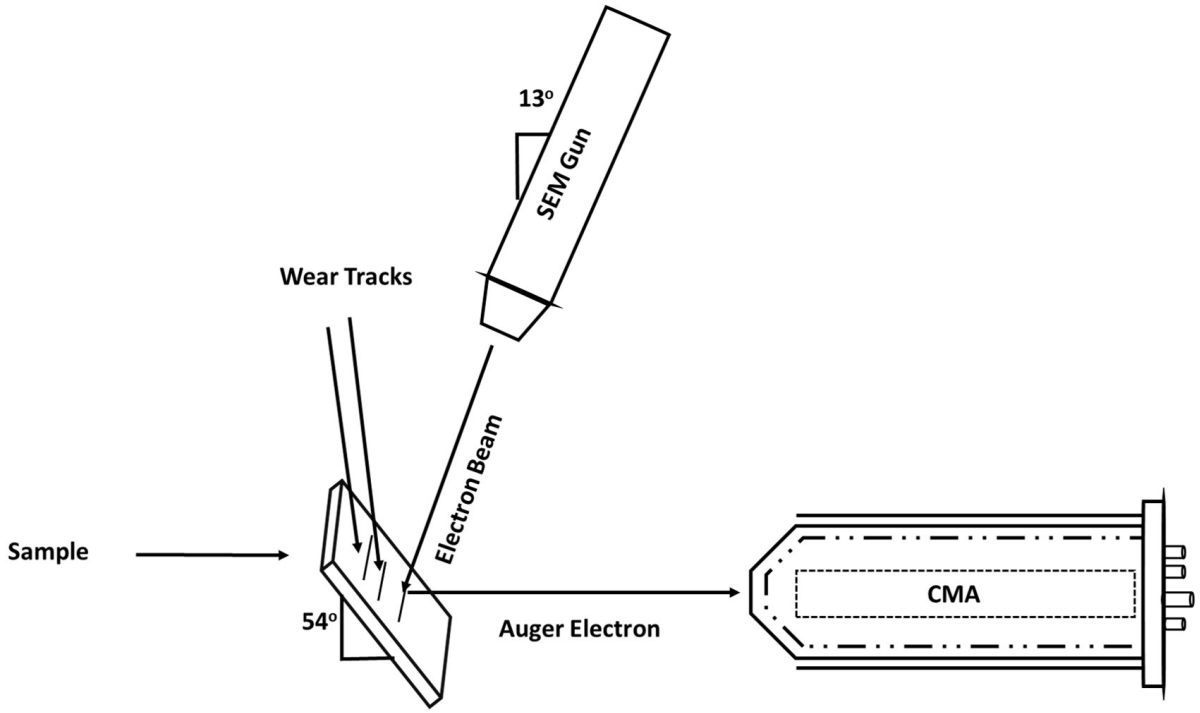

FIGURE 2.15: SEM schematics for locating wear track for AES analysis.

tilted towards the CMA by 13^{o} from the normal position as shown in Figure 2.15. For locating and analyzing the wear track, the sample was rotated horizontally towards the CMA by ~54^{o}. It was essential to adjust the SEM e-gun position by using the bellows stage in order to exactly direct the electron beam at the wear track created at a tribopin position of X = -19.5 mm. Secondary electrons that we used to provide the SEM images, which were collected using a channeltron placed close to the sample.

2.5.9 UHV-compatible Tribometer and Tribology System

An instrument to measure the friction coefficient, a so-called tribometer, was used in this work and is pin-and-flat type tribometer, where a moving pin (comprising a spherical ball) is attached to an arm that slides against the stationary flat sample during the experiment. The pin was moved using an arm that contained strain gauges to enable the normal and lateral forces to be measured. The position of the tip of the UHV-compatible tribometer is controlled by micro-stepper motors, which can move linearly for locating pin at a desired rubbing position on the flat sample. It slides reciprocally during the rubbing experiments, and for unidirectional sliding experiments, it has to be started repeatedly with a set value of 1 stroke per step for a desired number of passes. This tribometer is equipped with spherical tungsten carbide tribopin with ball diameter of 1.27×10^{-2} m. Tungsten carbide was selected because it is very hard and will not wear between experiments. For all experiments in this work, a sliding speed of 4.0×10^{-3} m/s was used but could be varied if necessary. Also, the tribo-arm assembly can be rotated so that it faces towards an ion gun for Ar^{+} bombardment or the CMA to acquire Auger spectra of the tribopin. This tribometer is also capable of measuring the contact resistance between the pin and the sample and a schematic diagram of triboarm is shown in Figure 2.16.

The UHV-compatible tribometer was mounted to a 2¾″ flange and it was fitted

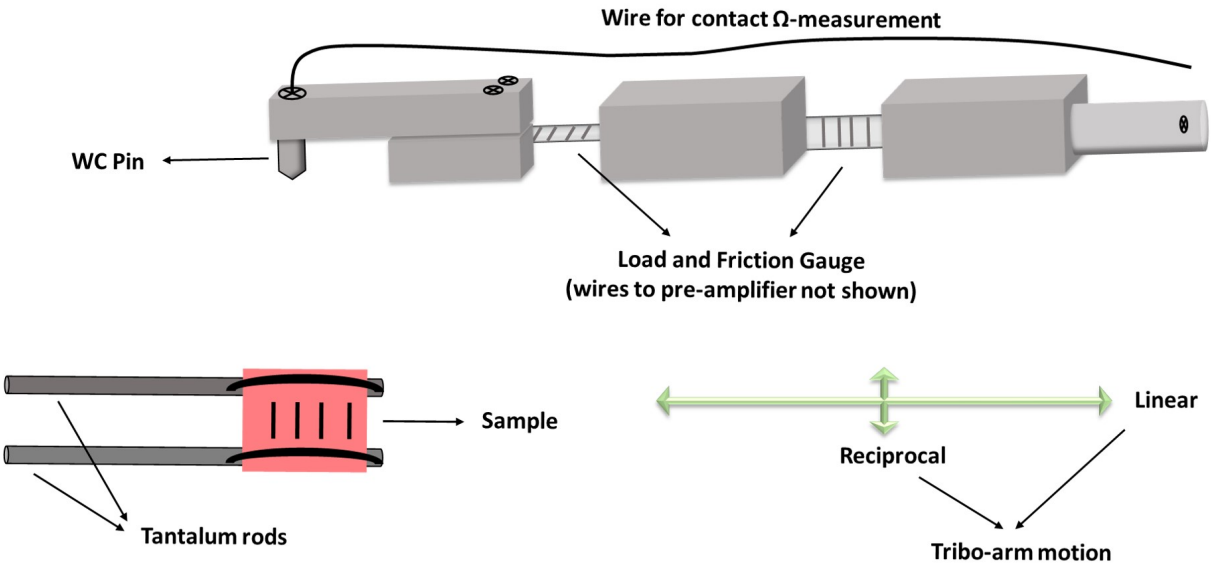

FIGURE 2.16: Schematics of tribo-arm and mounted sample.

with an axial rotator so it can be manually rotated to face the CMA or the ion gun. The planar sample can also be manipulated in the X, Y and Z directions and can be rotated by 360^0. The tribometer chamber was also equipped with single-pass CMA, which was used for characterizing the surface of the tungsten carbide tribopin, to monitor cleanliness of the samples and to analyze the wear track created on the flat sample. This tribology system also includes a leak valve for dosing sample and for introducing gaseous chemicals into the chamber. In addition, a Knudsen dosing source was used for dosing chemicals with lower vapor pressures.

Other tools incorporated into tribology system were a UTi mass spectrometer, a SEM electron-gun paired with secondary-electron detector and an aluminum evaporation source used to deposit a protective aluminum layer on wear tracks created on a Cu

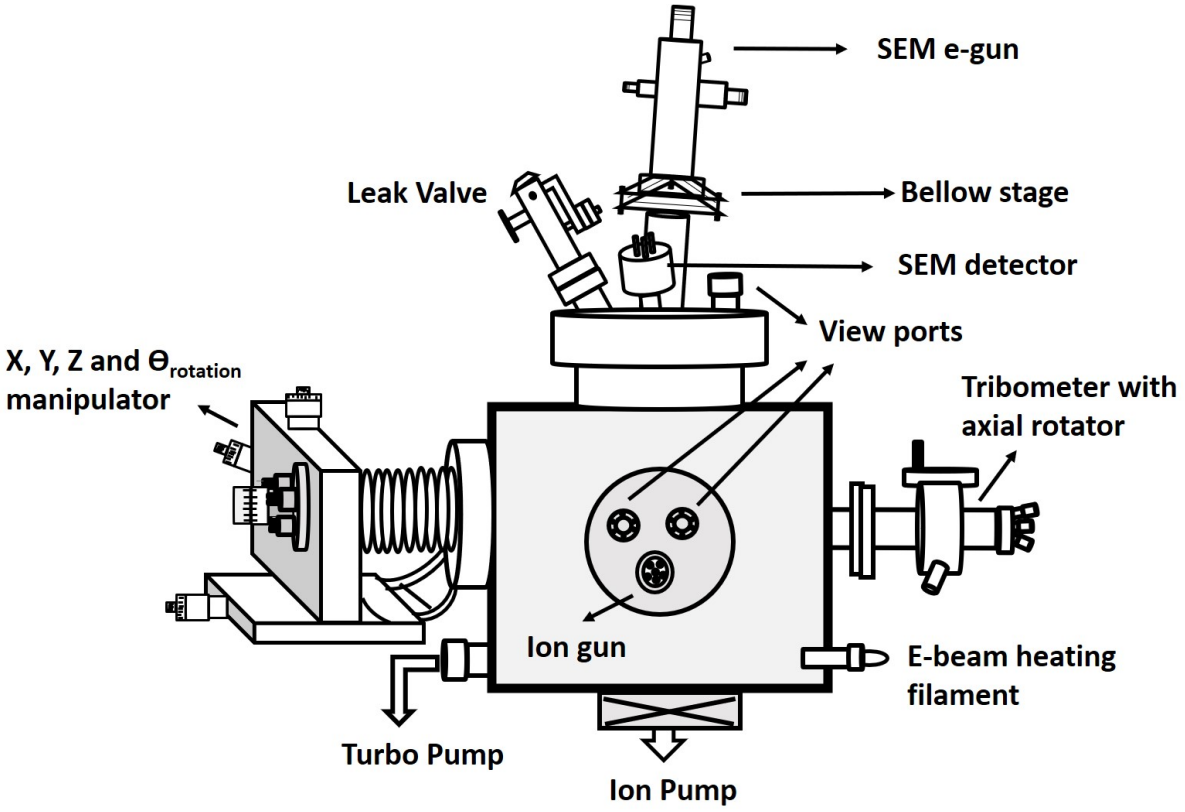

FIGURE 2.17: Tribological system with SEM microfocus e-gun used during S-transport experiments for AES analysis of wear track.

foil for preparing focused-ion beam (FIB) samples for scanning transmission electron microscopy (STEM) analysis at the Sandia National Laboratory. Depending upon the experiment, the system was reconfigured from time to time. For example, to analyze the wear track, it was required to mount the SEM microfocus e-gun and secondary-electron detector on the top of the UHV chamber on a four-port flange and ion gun (opposite to the CMA) on the front of the chamber at three-port flange as shown in Figure 2.17. Also, this type of configuration was used for measuring friction and contact

resistance during the experiments with phosphite esters. Using this set of experimental tools, S- and C-surface-to-bulk transport rates were measured during the tribological experiments. The SEM microfocus e-gun was adjusted in such a way that the wear track created by tribopin at a position of X = -19.5 mm could be focused under an electron beam to collect elemental information only from the wear track. For precisely locating the wear track, the SEM image was displayed on a TV screen and a bellows stage mount for the microfocus e-gun was adjusted whenever necessary to direct the electron beam at the wear track.

In the second type of configuration, a UTi mass spectrometer was mounted on the front of the chamber using a 6.0" flange (opposite the CMA), and a ion-gun was mounted on the top of the chamber on a four-port flange. This configuration was used for analyzing the gas-phase products formed during rubbing of adsorbate-covered samples. A leak valve was always mounted on the top of the tribo-chamber on the four-port flange as depicted in Figure 2.18. A third configuration of the tribology system was used for coating protective aluminum layers on the Cu foil after creating the wear track for subsequent STEM analysis of FIBed samples. For coating a sample by depositing a thin aluminum layer on a foil containing wear tracks created on the copper sample, an evaporation cell containing an aluminum evaporation source was used. During the Al vapor deposition, the gate valve placed between the transfer arm and main chamber was closed, so that no Al could enter the tribology chamber. An O-ring

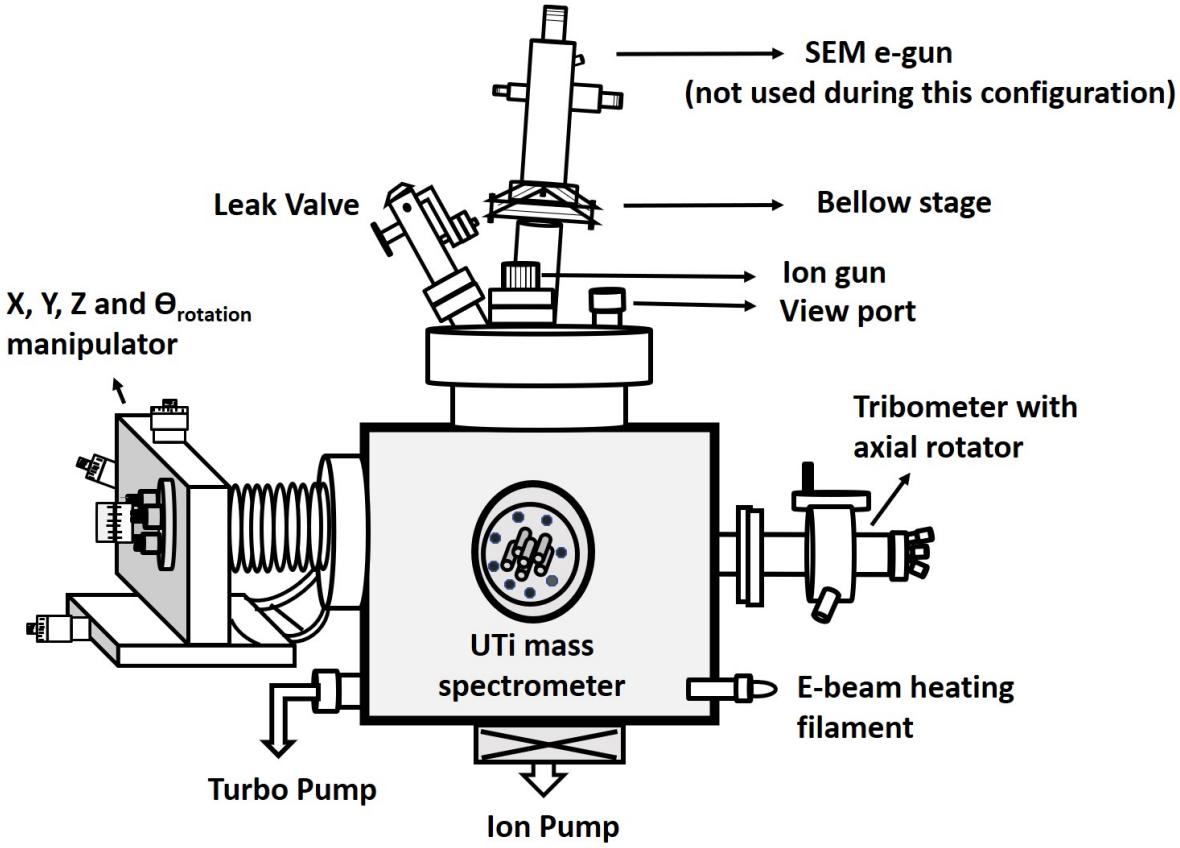

FIGURE 2.18: Tribological system with UTi 100 mass spectrometer for gas phase product analysis during tribochemical experiments.

seal is located between the bellow region of transfer arm and the Al vaporization cell as shown in Figure 2.19 to allow the transfer arm to be moved between the main UHV chamber and the cell used for aluminum coating. The evaporation cell with the transfer arm are attached to the main tribology chamber by a Conflat® flange coupled by a flexible bellow. An angle valve was fitted at the end of flexible bellow to separate the transfer arm and vaporization cell whenever necessary.

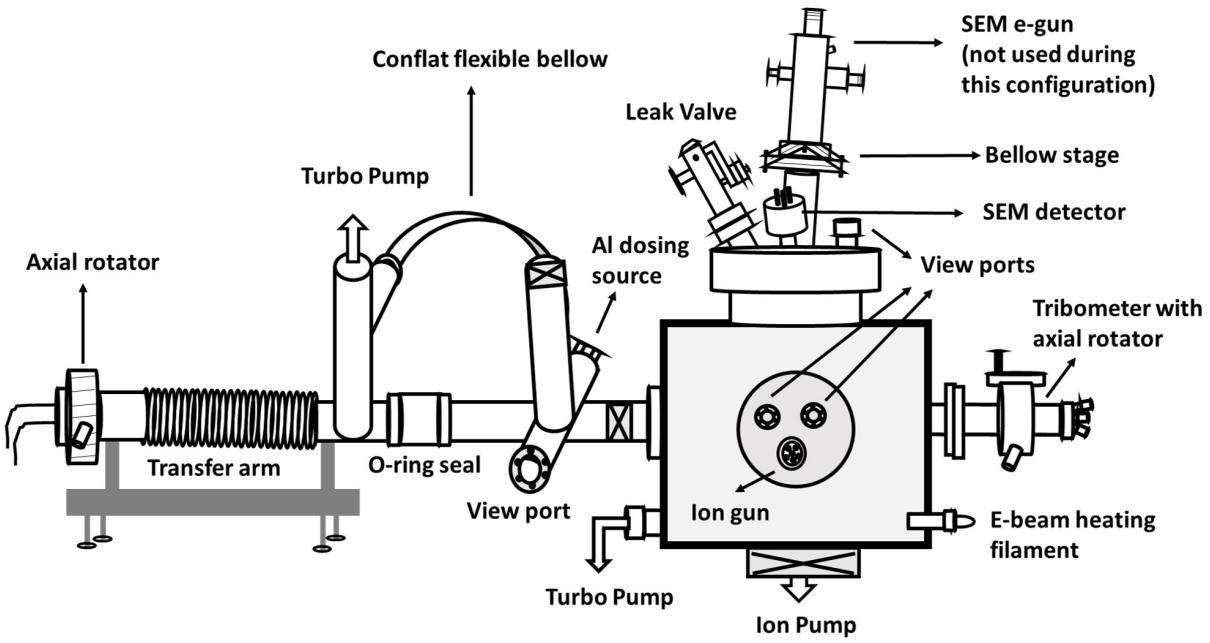

FIGURE 2.19: Tribological system with Al evaporation cell. The wear track created Cu foils during the DMDS exposure are coated with Al protective layer using this configuration for STEM analysis of FIBed samples taken from inside the wear track.

The fourth type of configuration used for tribological-based experiments was similar to first type of configuration (Figure 2.17). Here an additional Knudsen dosing cell was mounted on the top right port of the three-port-flange, above the ion gun, as shown in the Figure 2.20. This configuration was used for the experiments performed with carboxylic acids for measuring the tribochemistry and C-surface-to-bulk transport rates on copper.

During the wear track analysis experiments (both S-transport and C-transport), the sample's Y-axis (across the manipulator to tribometer arm) motion was restricted to avoid backlash effects. It was essential to precisely repeatedly rub over the same spot

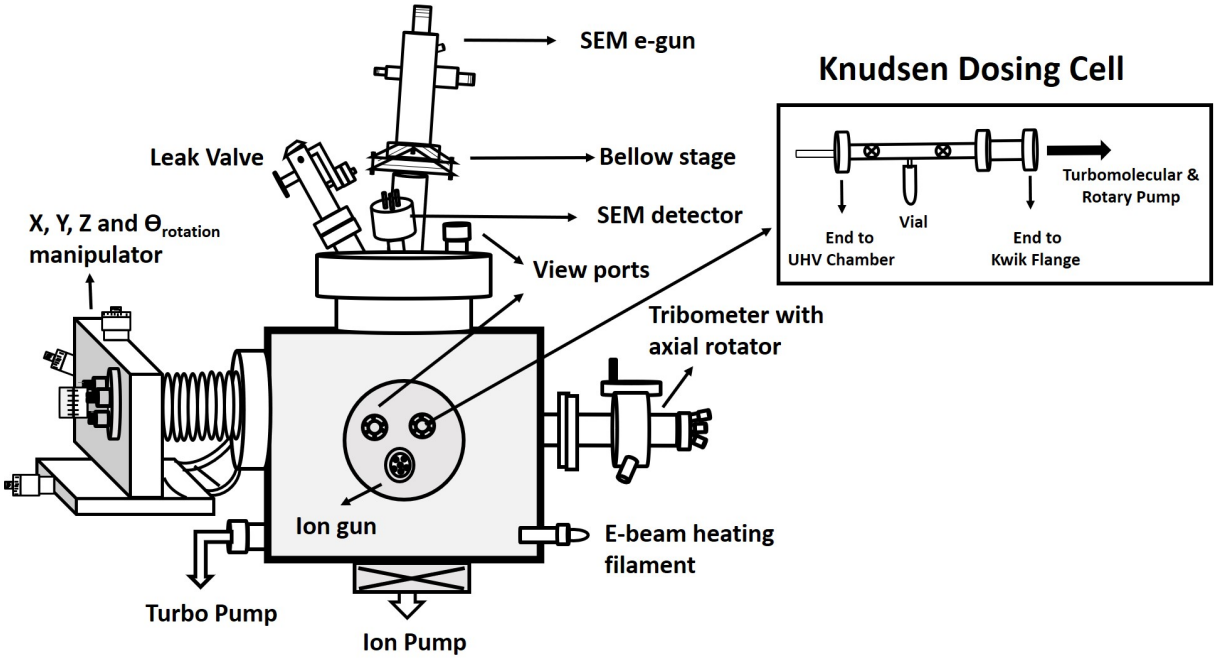

FIGURE 2.20: Schematics of tribology vacuum system configured for carboxylic acid experiments for measuring the C-removal rate. The figure in the rectangular inset is a design of a Knudsen dosing cell used for dosing carboxylic acids.

or on the same wear track and to collect the Auger spectra only from the wear track. The X, Z and $\Theta_{rotation}$ motions were adjusted to allow the sample to face towards the CMA for Auger analysis and to be able to move back to the rubbing position for additional rubbing cycles. During these experiments, the sample remains flat when rubbing, but is tilted by ~ 54^o from horizontal such that it faces towards the CMA and the microfocus e-gun when the Auger spectrum is collected from the wear track, as shown in Figure 2.15.

For performing surface-to-bulk transport experiments under shear, using a tungsten carbide tribopin on a copper surface, the tribopin was cleaned by e-beam heating

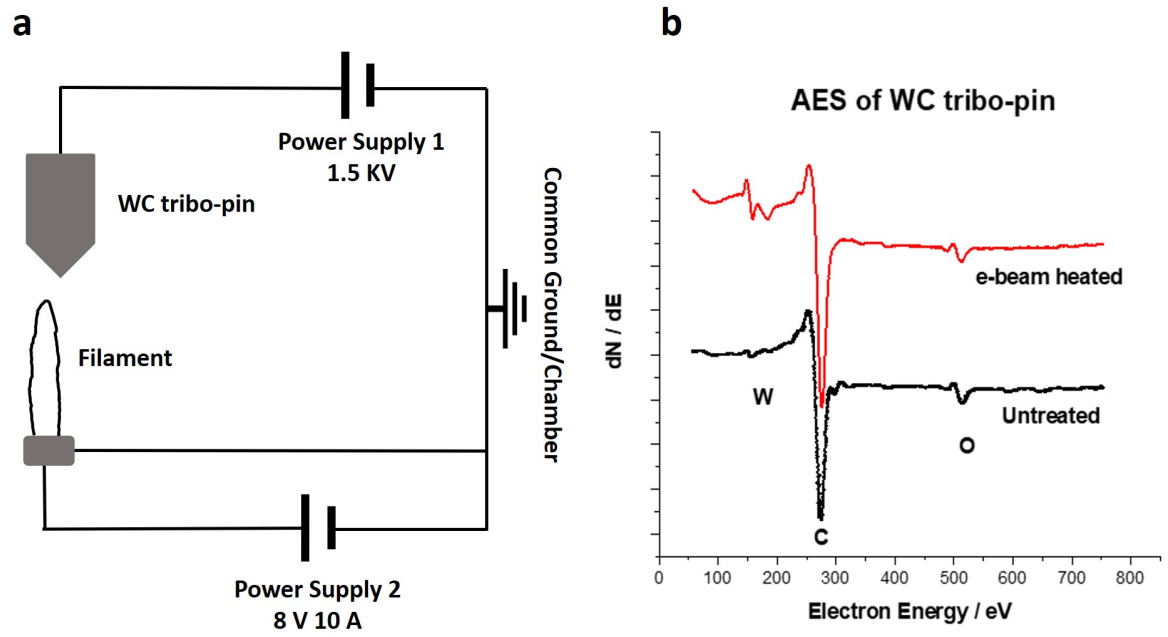

FIGURE 2.21: a) Circuit diagram for e-beam heating of tungsten carbide tribopin b) Auger spectra of the tungsten carbide tribopin: untreated and e-beam heated.

before the experiment to remove any carbon contamination. The e-beam heating was performed by supplying 1.2 kV (from a Keithley 247 high voltage power supply) between the tribopin and ground (UHV Chamber), and another power supply (0-8 V, 0-10A) was used to heat the filament which was located close to and below the tungsten carbide tribopin for generating the electron beam. E-beam heating was carried for 7-12 minutes until the tribopin showed a dull red color. Figure 2.21 (a) shows the circuit diagram of e-beam heating and Figure 2.21 (b) shows the AES spectra of tungsten carbide tribopin before and after e-beam heating. In order to acquire the AES spectra of tungsten carbide tribopin, it was positioned at X = -18.6 mm (note that this could change if

tribometer fitting position is changed) and Z = 0.0 mm by using the tribometer-control-software, and the triboarm was rotated by 90^o to face the CMA. Then the tribopin was moved towards CMA by using the "JOG" function of the tribometer-control software to adjust the value of Z to be -2.5 mm to collect an Auger spectrum of the pin. After collecting the Auger spectrum of the tungsten carbide tribopin, the following three steps were performed; i) JOG the pin position back to Z = 0.0, ii) rotate the tribo-arm back to 0^o and, iii) retract tribo-arm to position of ~X = 19.00 mm so that the tribo-arm can be safely parked after completing these three steps.

2.5.10 Aluminum Evaporation Source

For coating a thin aluminum protective layer on the Cu foils prepared for scanning transmission electron microscopy (STEM) analysis of the wear track on FIBed samples, an evaporation source was designed. Two 1-mm thick Mo wires were twisted together to hold a graphite crucible to contain the aluminum as shown in Figure 2.22 (a). The aluminum was vaporized by heating the source resistively in a cell located between transfer arm and main chamber which was separated by a gate-valve from tribometer chamber, as shown in Figure 2.19. The required mass of aluminum for coating the desired film thickness was placed inside the crucible and it was heated until all the aluminum had evaporated. The required mass of the aluminum for developing a thin film was calculated by using the equation 2.3 [11].

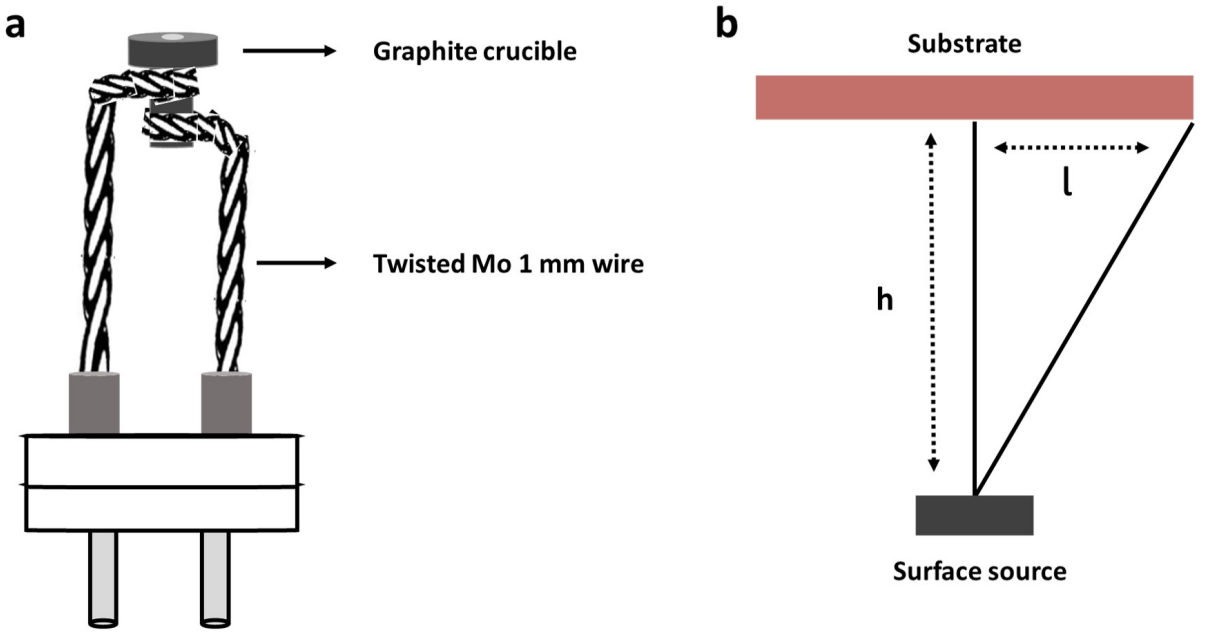

FIGURE 2.22: a. Schematic diagram of Al evaporation source mounted on power supply feedthrough b. surface source evaporation geometry for film thickness calculation.

$$d = \frac{M_{Al} h^2}{\pi (h^2 + l^2)^2 \rho_{Al}} \tag{2.3}$$

where h is distance between substrate and source in m (3.5×10^{-2} m for this work), l is half the length of sample in m (1.0×10^{-2} m for this work), ρ is density of Al in g/m^3, d is the resulting film deposition thickness in meters, M_{Al} is mass of aluminum in grams.

2.5.11 Scanning Transmission Electron Microscopy

Principally, in scanning transmission electron microscopy (STEM), an electron source emits a finite-sized e-beam which is steered through the condenser lenses which are aligned in series. Scans coils are placed in the beam path to raster the atomic-sized

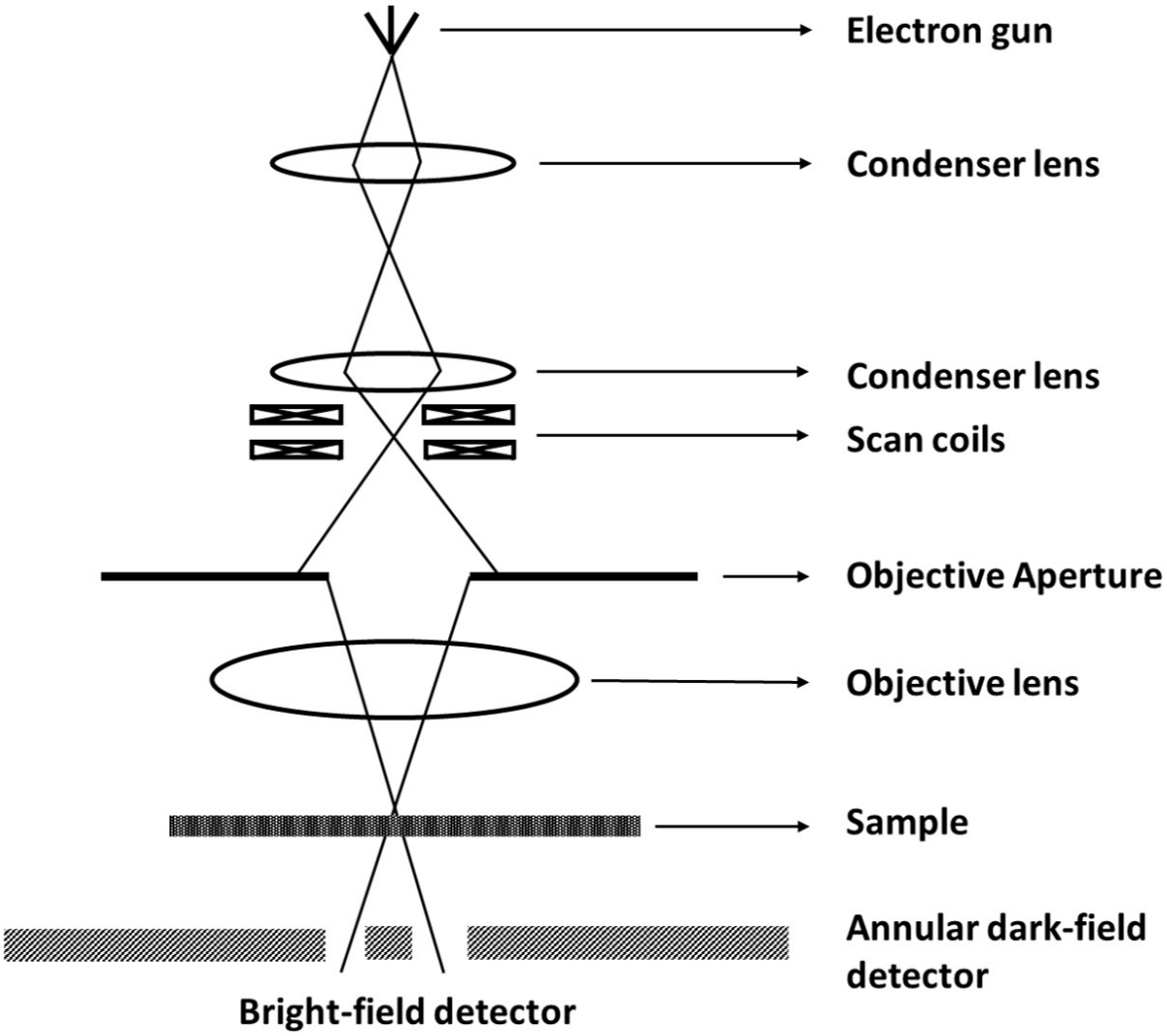

FIGURE 2.23: Schematic diagram of STEM showing the different elements.

e-beam. During this process, scattered electrons are detected; a magnified image is produced when the scattered signals are plotted with respect to probe position [12, 13]. Figure 2.23 shows the optical configuration of STEM. The wear track created on the copper samples had been annealed to 500-, 850- or 1020-K during tribological experiments by reaction with gas-phase DMDS were coated with a protective Al layer for

STEM analysis. The atomic-resolution imaging and nanoscale elemental analysis of the wear track created on copper samples were analyzed by STEM on FIB-prepared samples. This work was carried out by Daniel Long and Paul Kotula who prepared the FIB samples and collected the STEM images and carried out the EDX analyses at Sandia National Laboratory.

2.6 Non-UHV Tools

The various non-UHV tools and techniques which were used in this work are described below.

2.6.1 Nano Indenter

For the mechanical characterization of copper foils that had been annealed to different temperatures (500, 850, or 1020 K) during cleaning in UHV, instrumented-indented testing (IIT) was carried out by using an Agilent G200 nano-indenter. In this testing method, indents can be positioned within ~1 μm which provides the ability to map the spatial distribution of surface mechanical properties with good resolution. For example, mechanical properties can be mapped within the wear track of width of ~200 μm or less.

During the nanoindentation experiment, the indenter tip is driven into the material. Both elastic and plastic deformation during the motion of the tip cause the formation of indentation to some contact depth conforming to the shape of the indenter. A Berkovich geometry nanoindenter tip [14–17] was used for the characterization of the copper samples, and this type of tip is generally preferred for the measurement of hardness. This tip has a three-sided pyramidal structure that produces plasticity at very low loads and minimizes the influence of friction. The indenter's tip has a radius of ≤ 20 nm when newly supplied. The residual impression of the Berkovich tip on the sample leaves a three-sided pyramidal residual shape as shown in Figure 2.24 [18].

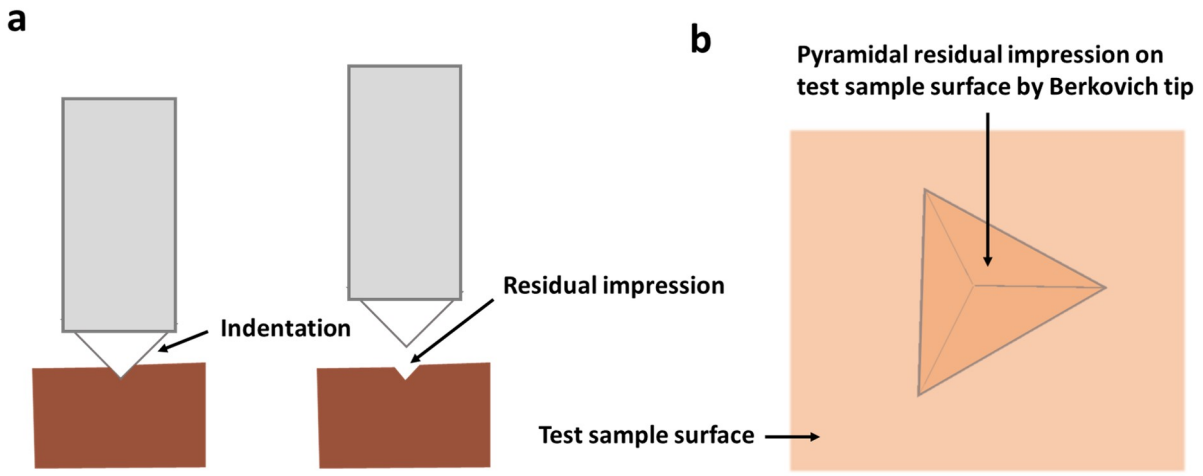

FIGURE 2.24: a. Indentation and Residual impression b. Residual impression from a Berkovich indenter.

The hardness of the test surface (H) is determined using the equation-

$$H = \frac{P}{A} \tag{2.4}$$

where, P is the load applied to the test surface and, A is the projected contact area at that load.

References

[1] D. P. Woodruff, *Modern techniques of surface science*. Cambridge university press, 2003.

[2] M. H. Hablanian, *High-vacuum technology: a practical guide*. Routledge, 2017.

[3] W. Gaede, "Die diffusion der gase durch quecksilberdampf bei niederen drucken und die diffusionsluftpumpe," *Annalen der Physik*, vol. 351, no. 3, pp. 357–392, 1915.

[4] R. M. Besançon, "Vacuum techniques," *Van Nostrand Reinhold, New York*, pp. 1278–1284, 1990.

[5] P. Redhead, "Thermal desorption of gases," *vacuum*, vol. 12, no. 4, pp. 203–211, 1962.

[6] S. Hüfner, *Photoelectron spectroscopy: principles and applications*. Springer Science & Business Media, 2013.

[7] C. C. Chang, "Auger electron spectroscopy," *Surface Science*, vol. 25, no. 1, pp. 53–79, 1971.

[8] P. Auger, "Sur l'effet photoélectrique composé," *Journal de Physique et le Radium*, vol. 6, no. 6, pp. 205–208, 1925.

[9] P. Van der Heide, "X-ray photoelectron spectroscopy," *An Introduction to Principles and Practices*, 2011.

[10] *Instruction Manual Microfocus Electron Gun Model EK050M2*. STAIB INSTRUMENTE, 2002.

[11] L. Holland and W. Steckelmacher, "The distribution of thin films condensed on surfaces by the vacuum evaporation method," *Vacuum*, vol. 2, no. 4, pp. 346–364, 1952.

[12] S. J. Pennycook and P. D. Nellist, *Scanning transmission electron microscopy: imaging and analysis*. Springer Science & Business Media, 2011.

[13] P. W. Hawkes and J. C. Spence, *Springer Handbook of Microscopy*. Springer Nature, 2019.

[14] R. D. Dukino and M. V. Swain, "Comparative measurement of indentation fracture toughness with berkovich and vickers indenters," *Journal of the American Ceramic Society*, vol. 75, no. 12, pp. 3299–3304, 1992.

[15] H. Bei, E. P. George, J. Hay, and G. M. Pharr, "Influence of indenter tip geometry on elastic deformation during nanoindentation," *Physical Review Letters*, vol. 95, no. 4, p. 045501, 2005.

[16] N. Sakharova, J. Fernandes, J. Antunes, and M. Oliveira, "Comparison between

berkovich, vickers and conical indentation tests: A three-dimensional numerical simulation study," *International Journal of Solids and Structures*, vol. 46, no. 5, pp. 1095–1104, 2009.

[17] A. C. Fischer-Cripps, "The sharpness of a berkovich indenter," *Journal of Materials Research*, vol. 25, no. 5, pp. 927–934, 2010.

[18] *User's Guide G200*. Agilent Technologies, 2009.

Chapter 3

Kinetic Mechanism for the Mechanochemical Formation of Metastable Phases from the Reaction between Sulfur and Copper

3.1 Introduction

Mechanochemical processes are often induced either by agitation in a ball mill or by shock waves to induce novel solid-state reactions and, in particular, the formation of metastable materials that are not accessible through thermal processes [1–5]. Indeed, such solid-state reactions have long been known and the mechanical reduction of cinnabar to mercury in a copper pestle and mortar was reported by Theophrastus of Eresos in ~315 BC [6], and Michael Faraday studied the mechanochemistry of solids in the 19^{th} century [7]. Little is known about the mechanism by which such solid-state mechanochemical reactions occur and the way in which metastable materials are

formed, but it has been suggested that they are caused by the energy dissipated at collision sites that increase local temperatures, through the formation of defect sites [8–11] or by a dislocation glide mechanism [12–14]. Significant structural changes have also been found for sheared copper-copper interfaces, which form nanocrystalline structures in the subsurface region [15–21].

Part of the lack of progress in understanding solid-state mechanochemical reaction mechanisms arises from a lack of simple, well-characterized model systems of sliding interfaces that produce metastable phases. This is addressed in the following by investigating the mechanically induced reaction between dimethyl disulfide (DMDS) and copper in ultrahigh vacuum. In the absence of an external force, DMDS reacts stoichiometrically with copper at room temperature via S–S bond scission to form adsorbed methyl thiolate species, which are thermally stable at room temperature. However, two distinct mechanochemical processes are induced by rubbing the methyl thiolate-covered surface with a tungsten carbide ball. The first is the decomposition of the stable, adsorbed methyl thiolate species to form small gas-phase hydrocarbons [22–28]. The second shear-induced process, relevant to the study of the mechanochemical formation of novel phases, is the surface-to-bulk transport of the adsorbed sulfur to produce a metastable CuS_x phase. Note that the sliding conditions for these experiments are sufficiently mild that the temperature rise is negligible ($\ll 1$ K), thus allowing the influence of thermal effects to be excluded [23]. In this case, the adsorbed sulfur formed

by methyl thiolate decomposition was lost from the surface by being transported into the subsurface region of the copper substrate to form a metastable phase. The sulfide phase was shown to be metastable by demonstrating that the subsurface sulfur diffused to the surface once again when the sample was heated [23, 28].

The first-order rate constants for the elementary-step reactions have been measured and used to construct a kinetic model that accurately predicts the variation in friction as a function of the number of rubbing cycles for the gas-phase reaction of DMDS with copper measured in vacuum. Note that this reaction could be viewed as either a mechanocatalytic reaction or a tribochemical processes depending on whether the focus is on the formation of gas-phase products or the deposition of a friction reducing film [29]. In addition to being able to reproduce the evolution in friction force as a function of the number of passes, the model correctly predicts both the depth profile of the sulfur in the bulk of the sample and the variation in the total amount of sulfur in the bulk of the copper [28]. Here, the surface-to-bulk transport kinetics were modeled by assuming that the distance that an initial, adsorbed layer of sulfur moves into the copper substrate is proportional to the number of times that it has been rubbed. This produces an effectively first-order rate constant for the sulfur surface-to-bulk transport [27]. This result is consistent with molecular dynamics (MD) simulations of sliding interfaces which reveal shear-induced vortices in the surface region, allowing surface atoms to be transported into the bulk [30, 31]. The resulting patterns formed in the

near-surface region of the sample resemble those produced in shear by classical Kelvin-Helmholtz (K-H) instabilities, despite the differences in effective viscosity values [32–37]. The resulting crystalline subsurface structures of copper depend on the sliding condition and can lead to surprisingly low friction of metal-metal sliding [3, 38, 39].

An analytical model proposed by Karthikeyan and Rigney [40] described a sliding metal interface by assuming a material flow law given by the Herschel-Bulkley model, where the shear stress $\tau_{xy} = \tau_o + C\left(\frac{du}{dy}\right)^m$ [41], where, τ_o and C are parameters of the model, m is strain-rate sensitivity, which can take values between 0 and 1, and $\frac{du}{dy}$ is the shear strain rate. The Karthikeyan-Rigney model showed that the time dependence t of the variation in the characteristic width of the deformed zone, y^*, depends critically on the value of m. However, metals and, in particular copper, have $m \ll 1$ [42, 43], leading to $y^* \propto t$ (see below). Since, at a constant sliding speed and load, the contact time is proportional to the number of passes p, this suggests that the intermixing should depend linearly on the number of times that the sample has been rubbed, in accord with experiment.

As also demonstrated below, the value of y^* also depends on the strain-rate sensitivity, m which, for metals in general, and for copper in particular, often decreases with the size of the nanocrystallites [2, 19, 42–47]. However, the initial crystallite size of the copper sample will also depend on the temperature at which it had been annealed during the cleaning process (see Experimental section). If the size of the crystallites

formed during rubbing correlate with the size of the initial crystallites, the surface-to-bulk transport kinetics will depend on the initial crystallite size. Since the hardness also depends on crystallite size through the Hall-Petch effect [48, 49], this postulate implies that the surface-to-bulk transport kinetics should correlate with the hardness of the copper sample. This idea is tested in the following by measuring the nanohardness of copper samples that had been annealed at different temperatures (500, 850, and 1020 K) during cleaning in UHV. Hardness measurement made in regions on the sample with and without rubbing, reveal that the hardness in regions that had been rubbed does depend on the initial hardness and therefore the temperature at which the copper had been heated. The postulate that the surface-to-bulk transport kinetics depend on the strain-rate sensitivity is tested by measuring the rate of shear-induced transport of sulfur into the copper bulk. The surface-to-bulk transport mechanism is explored by studying the depth profile of focused-ion-beam (FIBed) prepared samples that had been rubbed in the presence of DMDS to identify whether the sulfur was located at grains (in which case, the transport is grain-boundary mediated) or uniformly distributed throughout the sample (in which case, the mechanically induced transport kinetics are mediated by dislocations).

3.2 Experimental

Tribological measurements were carried out in a stainless-steel, ultrahigh vacuum (UHV) chamber operating at a base pressure of ~2×10^{-10} Torr following bakeout, which has been described in detail elsewhere [50]. Briefly, the chamber was equipped with a UHV-compatible tribometer, which simultaneously measures normal load, lateral force and the contact resistance between the tip and substrate. All tribological measurements were made using a sliding speed of ~4×10^{-3} m/s at a normal load of 0.44 N. Previous work has shown that the maximum interfacial temperature rise for a copper sample under these conditions is much less than 1 K [23]. The spherical tribopin (~1.27×10^{-2} m diameter) was made from tungsten carbide containing some cobalt binder and could be heated by electron bombardment in vacuo or by Argon ion bombardment in order to clean it. The pin was attached to an arm that contained strain gauges to enable the normal and lateral forces to be measured. The arm was mounted to a rotatable Conflat® flange to allow the pin to be rotated to face a cylindrical-mirror analyzer (CMA) to enable Auger spectra of the pin surface to be obtained. Additional experiments were carried out by analyzing the tungsten carbide pin by X-ray photoelectron spectroscopy (XPS) after Argon ion bombardment using a spectrometer containing a hemispherical analyzer built by ThermoFisher (220i) with a focused Al Kα monochromatic X-Ray source.

The copper samples (Alfa Aesar, 99.99% pure, 1 mm thick) were polished to a mirror finish using 1 µm diamond paste and then rinsed with deionized water and degreased ultrasonically in acetone before mounting in the UHV chamber. The copper was cleaned using a standard procedure which consisted of Argon ion bombardment (~1 kV, ~2 μA/cm^2) and annealing cycles up to ~500, 850, or 1020 K to result in different mechanical properties of the sample. The cleanliness of the samples was monitored using Auger spectroscopy.

The samples were either mounted in UHV either to a precision x, y, z manipulator for measuring the sulfur depth profiles across a rubbed region of the sample, or to a transfer arm that allowed the sample to be moved from the UHV chamber to a small cell attached to the main UHV chamber, which was isolated by a gate valve [51]. The transfer arm slid though a differentially pumped seal and the copper sample was attached to the end of the transfer arm and could be resistively heated and the temperature measured via thermocouple attached to the sample. A 1-μm thick film of aluminum was deposited to coat the surface of the copper sample when enclosed in the cell to protect it from atmospheric contamination during transport to Sandia National Laboratories for additional analysis.

The tribometer chamber contained a single-pass CMA for Auger analysis, and an Argon ion bombardment source for sample cleaning and depth profiling. Auger spectra were either collected using the coaxial electron gun in the CMA with an electron

beam energy of 3 kV or with a Staib model EK050M2 Microfocus electron gun. The chamber is also equipped with a channeltron secondary electron detector which allowed scanning electron microscopy (SEM) images of the wear scar to be collected using the high-resolution electron gun. Auger elemental profiles were obtained across the rubbed regions to measure the loss of sulfur from the surface as a function of the number of times that the sample had been rubbed. In order to ensure that the sulfur signal was being measured only in the rubbed region and did not include signals from the unrubbed part of the sample, calibration experiments were carried out to focus the electron beam on a 100 μm-diameter silver wire and by detecting Auger signals due only to silver. Concentration profiles across the rubbed region were measured either by moving the sample laterally by translating the precision manipulator to which the copper sample was mounted, or by deflecting the electron beam by using capacitor plates incorporated in the high-resolution electron gun. Both methods yielded identical results for the variation in Auger signal as a function of the number of times that it had been rubbed. Finally, the chamber also included a quadrupole mass spectrometer for leak checking and for gauging reactant purity. Nanoindentation measurements were made using a Nanoindenter G200 (KLA/Agilent) with a ~130 nm Berkovich tip.

All experiments were performed by initially rubbing the tribopin against the clean copper sample (~1.7×1.7 cm^2 by ~1 mm thick) until a constant friction coefficient was obtained. This resulted in the formation of a wear track. DMDS was dosed through a

leak valve connected to a dosing tube (with an internal diameter of 4×10^{-3} m) directed towards the sample so that the pressure at the sample is enhanced compared to the background pressure, which was set at $\times10^{-8}$ Torr during DMDS dosing (pressures are not corrected for ionization gauge sensitivity).

In the first experiment, the loss of sulfur from a saturated overlayer of methyl thiolate formed by dosing the rubbed sample with DMDS was measured by Auger spectroscopy as a function of the number of times that it had been rubbed for samples that had been cleaned by annealing to 500, 850, or 1020 K.

In a second experiment, samples were prepared by rubbing copper sample that had been annealed at 500, 850, or 1020 K during the cleaning process in a background pressure of $5\sim10^{-8}$ Torr of DMDS for 80 cycles at a load of 0.44 N to cause sulfur to continually penetrate the subsurface region. The sulfur depth distribution for this gas-phase lubrication experiment has been measured by angle-resolved XPS and compared with the kinetic model described above [28]. This protocol provided high subsurface sulfur concentrations for subsequent ex-situ analyses at Sandia National Laboratories. Electron-transparent lamella (11 μm $\times$ 6.7 μm $\times$ 16 μm deep) were prepared from these aluminum-coated copper samples at the Center for Integrated Nanotechnologies (CINT) at Sandia National Laboratories using a Thermo Scientific Scios 2 Dual-Beam focused-ion beam (FIB) apparatus. Scanning-transmission electron microscopy (STEM) and energy-dispersive X-ray spectroscopy (EDXS) were done with a FEI (now

Thermo Fisher Scientific) Titan G2 80-200 electron microscope equipped with a spherical aberration corrector on the probe-forming optics and four silicon-drift X-ray detectors operating at 200 kV electron energy.

The DMDS (Aldrich, 99.0% purity) was transferred to a glass bottle and attached to the gas-handling system of the vacuum chamber, where it was subjected to several freeze-pump-thaw cycles. The purity of the DMDS was monitored using mass spectroscopy.

3.3 Modified Rigney Model for Interfacial Mixing at a Sliding Interface

The following outlines a modification of the analysis by Karthikeyan-Rigney [40] for the mixing at a sliding interface to specifically investigate the dependence on strain-rate sensitivity. The model assumes that the flow properties of copper are described by the Herschel-Bulkley model [41] where:

$$\tau_{xy} = \tau_o + C\left(\frac{du}{dy}\right)^m \tag{3.1}$$

where τ_o and C are strength parameters, and m is the strain-rate sensitivity. Writing $u(y,t) = U(\lambda)$ where, $\lambda = yt^{\alpha}$ where $\alpha = -\frac{1}{m+1^2}$, and using the Cauchy's equation of

motion gives the following differential equation for the velocity $U\lambda$ as:

$$\lambda\left(\frac{dU}{d\lambda}\right)^{2-m} = -\left(\frac{Cm(1+m)}{\rho}\right)\frac{d^2U}{d\lambda^2} \tag{3.2}$$

where ρ is the density. We derive a solution for the case in which $m \ll 1$, typical of a metal such as copper [17, 21, 43, 44, 52, 53], so that $\lambda = yt^{-1}$ so that equation (3.2) simplifies to:

$$\lambda\left(\frac{dU}{d\lambda}\right)^{2} = -\left(\frac{Cm}{\rho}\right)\frac{d^2U}{d\lambda^2} \tag{3.3}$$

A general solution to this equation is given by:

$$U(\lambda) = c_2 - \sqrt{\frac{2A}{c_1}}\arctan\left(\frac{\lambda}{\sqrt{2Ac_1}}\right) \tag{3.4}$$

where $A = \frac{Cm}{\rho}$ and c_1 and c_2 are constants of integration, which are determined from the boundary conditions. Using the no-slip boundary conditions of Karthikeyan and Rigney [40] at $\lambda = 0$ gives $U(0)$=0, so that c_2=0, and at $\pm\infty$ give $U(\pm\infty) = \pm U$ and $\frac{dU(\lambda)}{d\lambda} = 0$. The second condition is automatically obeyed from the form of the function in Eqn. 4. Applying the first boundary condition gives:

$$\sqrt{\frac{2A}{c_1}} = -\frac{2U}{\pi} \tag{3.5}$$

where $\sqrt{2A}c_1 = \frac{\pi A}{U} = \frac{C\pi m}{\rho U} \equiv B$, to give the full solution as:

$$U(\lambda) = \frac{2U}{\pi} \arctan\left(\frac{\lambda}{B}\right) \tag{3.6}$$

However, the sliding conditions for copper in the experiments carried out in this work involve a stationary copper substrate and a pin sliding at a velocity U. This now gives boundary conditions $\lambda = 0$, $U(0) = U$, and at $+\infty$, $U = 0$ and $\frac{dU(\lambda)}{d\lambda} = 0$, so that now:

$$U(\lambda) = U - \frac{2U}{\pi} \arctan\left(\frac{\lambda}{B}\right) \tag{3.7}$$

The slope at the origin is given by:

$$\frac{dU}{d\lambda}\Big|_{\lambda=0} = -\frac{2U}{\pi B} \tag{3.8}$$

Taking the average value of λ^* to be that at which the linear extrapolation of $U(\lambda)$ becomes zero gives:

$$1 - \frac{2U}{\pi B}\lambda^* = 0 \tag{3.9}$$

Substituting $\lambda^* = \frac{y^*}{t}$ gives: $y^* \propto mt$, and predicts that the surface layer moves a constant distance per pass is constant as found experimentally [23, 24, 26–28] and that it is proportional to the strain-rate sensitivity, m. Since the strain-rate sensitivity and hardness depend on crystallite size [54], the hardness of the copper samples is measured

after heating to various temperatures to control the crystallite size, and the results correlated with the surface-to-bulk transport kinetics of sulfur to form a metastable copper sulfide.

3.4 Results

In order to explore the proposed dependence of the shear-induced formation kinetics of a metastable copper sulfide phase on the mechanical properties of the copper, the nanohardness was measured on the rubbed and unrubbed areas of the samples. The nature of the tribopin surface and the effect of e-beam heating and Argon ion bombardment are then discussed. The hardness data are then compared with the surface-to-bulk transport kinetics measured for copper samples annealed at 500, 850, or 1020 K using a pin that has been electron-beam heated to form a predominantly tungsten carbide surface. Note that repeated rubbing forms a graphitic surface for which the surface to bulk-to-transport properties are different and will be reported elsewhere. A correlation is found between the surface-to-bulk transport rate and the strain-rate sensitivity (m) and dislocation density of the copper samples that are prepared at different temperatures. These samples are further analyzed by imaging the subsurface structure and measuring the composition of the FIB-prepared samples that have been heated to 500, 850, or 1020 K and rubbed in the presence of a DMDS atmosphere to investigate how the sulfur penetration depends on the annealing temperature and mechanical

properties of the copper.

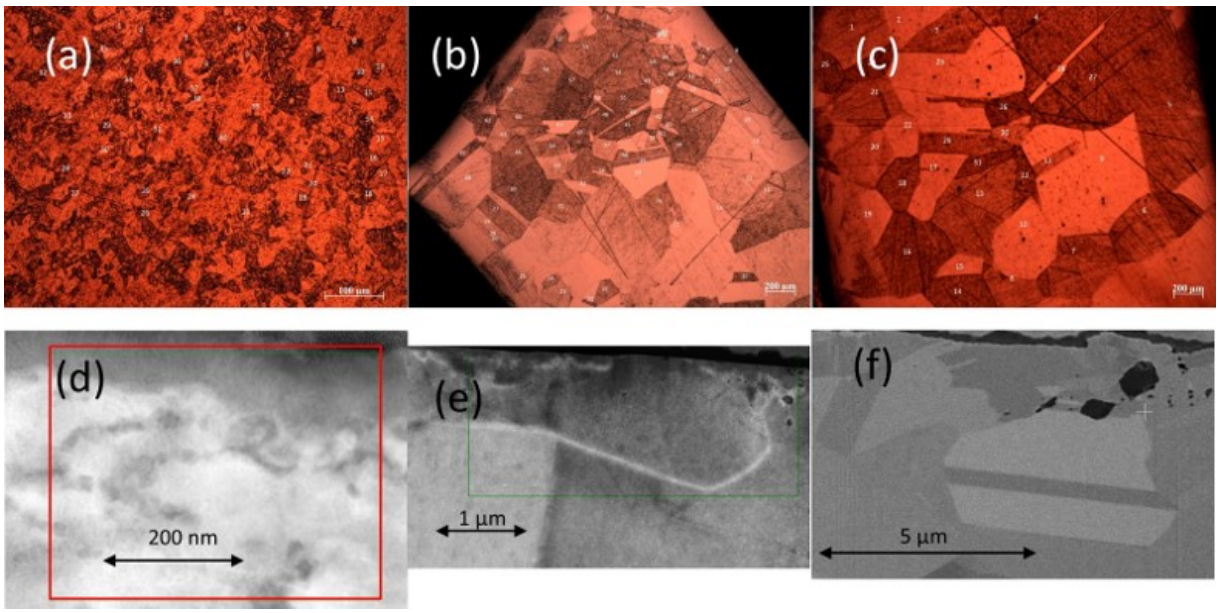

FIGURE 3.1: Optical microscope images of a copper foil showing the variation in grain size with increasing annealing temperature. Image a) shows a 700 μm × 520 μm image of the initial, unannealed foil, image b) shows a 2600 μm × 2000 μm image that has been annealed at 500 K and image c) shows a 4000 μm × 3000 μm image that has been annealed at 850 K. Images d) to e) show the depth profile electron microscope images of FIBed samples of copper that had been annealed to various temperatures and the rubbed at a load of 0.44 N at a sliding speed of 4×10^{-3} m/s in a background pressure of 5×10^{-8} Torr of DMDS for 80 cycles: d) a High-angle annular dark-field (HAADF) image of a sample annealed at 500 K (200 keV, 160000 magnification), where the red square indicates the analyzed regions shown in Fig. 3.11, e) a HAADF TEM image of a sample annealed at 850 K (200 keV, 200000 magnification) and f) FIB SEM image of a sample annealed at 1020 K (5 keV, 6500 magnification). Figure a, b, and c courtesy of Yufu Xu, Hefei University of Technology, China.

3.4.1 Mechanical Properties and Structure of Annealed Copper Samples

Experiments were carried out on pure copper foils that had been cleaned and annealed at 500, 850, or 1020 K to modify their grain sizes. This is illustrated in Figures 3.1 (a)-(c) which show optical images of an as-received etched copper sample (Fig. 3.1(a)) and after heating to 500 (Fig. 3.1(b)) and 850 (Fig., 3.1(c)) K. This reveals that, as expected, cleaning and annealing the samples at higher temperatures increases the size of the crystallites. Since the differences in crystal size are expected to influence the mechanical properties [48, 49], the copper hardness was measured as function of depth inside and outside the rubbed region using a Berkovich tip diameter of ~130 nm. The results are displayed in Figure 3.2, where the measurements taken outside the rubbed regions are shown in Figs. 3.2A (500 K), 3.2B (850 K) and 3.2C (1020 K). This shows a variation in the nano-indentation hardness with indentation depth. Such behavior has been observed previously and modeled by Nix and Gao [55] in which the hardness varies with depth as:

$$H = H_o\sqrt{1 + \frac{h_o}{h}} \tag{3.10}$$

where H_o is the limiting hardness at large depths and h_o is a scale parameter that depends on the statistically stored dislocation density. The data fit reasonably well to

the Nix/Gao model, except for depths where there are positive excursions from the Nix/Gao formula, ascribed to crystallites in the sample that are of the order of the size of the Berkovich tip [56], which are particularly apparent for samples annealed at 500 K. The resulting hardness values are summarized in Fig.3.3 (■), which shows that samples annealed at higher temperatures have hardness values close to that of single-crystal copper, consistent with larger crystals having formed at higher annealing temperatures.

Similar measurements were made in regions of the sample that had been annealed at various temperatures and that had also been rubbed in a background of DMDS (Figs. 3.2 D-E) where the variation of hardness with depth is also analyzed by the Nix and Gao model. This results in an increase in a hardness of the rubbed regions (Fig. 3.3 (●)). The hardness of the rubbed regions depends on the temperature at which the sample had been heated during the cleaning cycle. This is proposed to be due to the Hall-Petch effect because of the shear-induced formation of smaller crystallites. In order to test this idea, the grain sizes were estimated from the limiting hardness H_0 from the equation:

$$H = H_o = \frac{K}{\sqrt{d}} \tag{3.11}$$

where H_r is the limiting hardness for infinitely large crystals and K is a constant [54, 57].

This leads to estimated grain sizes of ~115, ~250, and ~1400 nm for samples that had been annealed at 500, 850, and 1020 K, and these values are summarized, along with the hardness values in Table 3.1.

Annealing Temperature/K	H/GPa	Estimated Grain Size*/nm	Measured Grain Size†/nm	h^*/nm	Dislocation Density/m^2 $\times 10^{13}$	k_2/pass
500	1.35±0.02	115	97±13	284	3.95	4±1
850	1.15±0.05	250	350±70	465	2.4	2.5±0.2
1020	0.72±0.01	1400	1200±120	1178	0.95	0.051±0.004

TABLE 3.1: Parameters for copper annealed and cleaned in vacuo at various temperatures. *Values estimated from the Hall-Petch equation. †Measured from electron microscope images in Figures 3.1 (d-f).

These results are compared with the images of similar copper samples that had been annealed at 500, 850, or 1020 K that have been rubbed in a background pressure of DMDS for which FIBed samples had been removed from the rubbed region and the results are shown in Fig. 3.1(d-f). The crystallite sizes were estimated from the images by simply counting the number of crystallites that intersected a line of a given length measured using ImageJ [58] and by dividing the line length by the number of crystals. This process was repeated several times and the results are also displayed in Table 3.1 and the values are in reasonable agreement with those obtained from the mechanical properties.

It has also been proposed that the total dislocation density of the samples annealed at various temperatures can be estimated from the value of h^* [59] using:

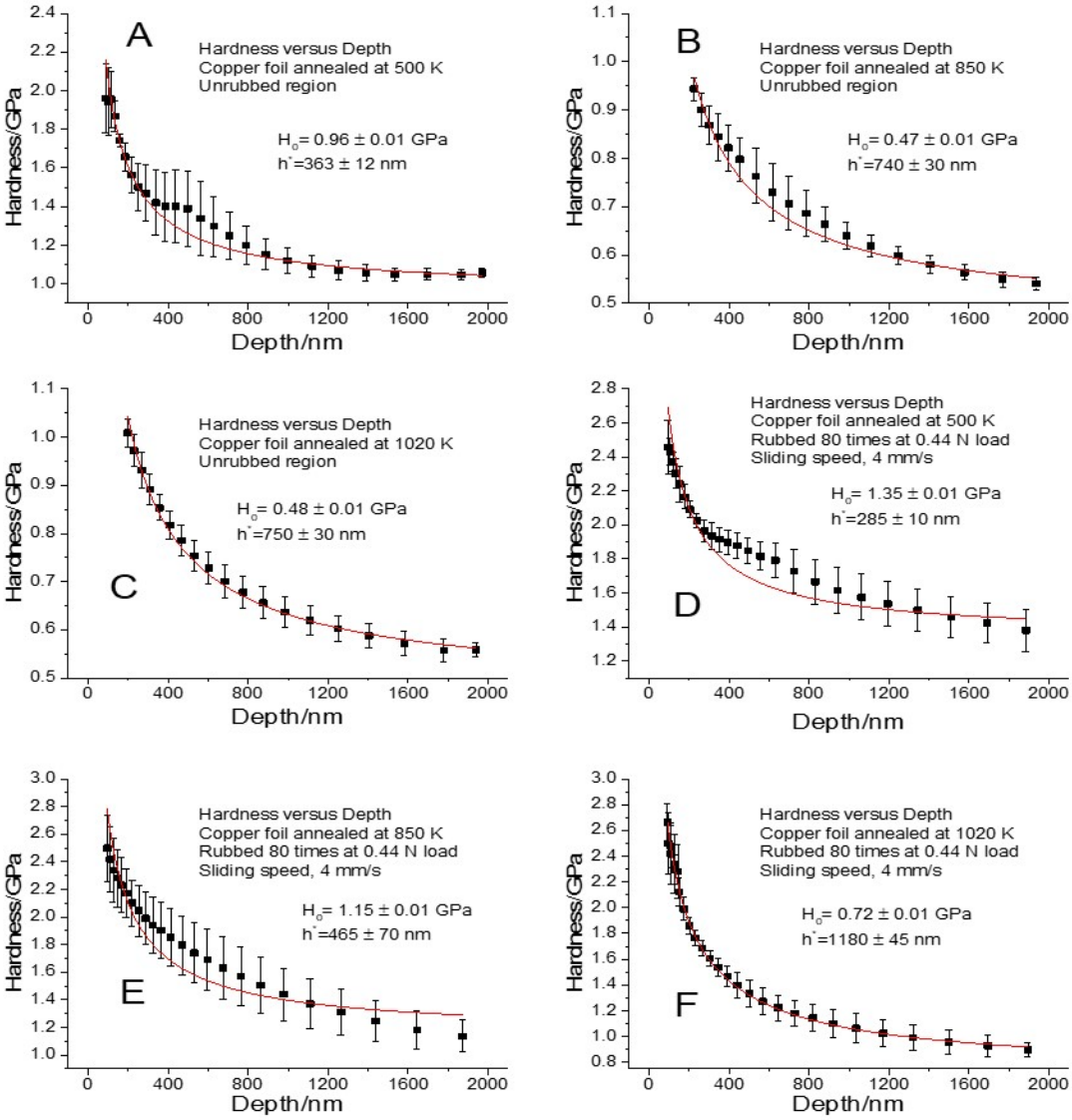

FIGURE 3.2: Plots of hardness of the sample measured using a Berkovich tip as a function of depth into the sample for copper foils that had been annealed at (a) 500, (b) 850 and (c) 1020 K and after having been rubbed at a load of 0.44 N at a sliding speed of 4×10^{-3} m/s in a background pressure of 1×10^{-8} Torr of DMDS for 80 cycles for the same annealing temperatures (d-f).

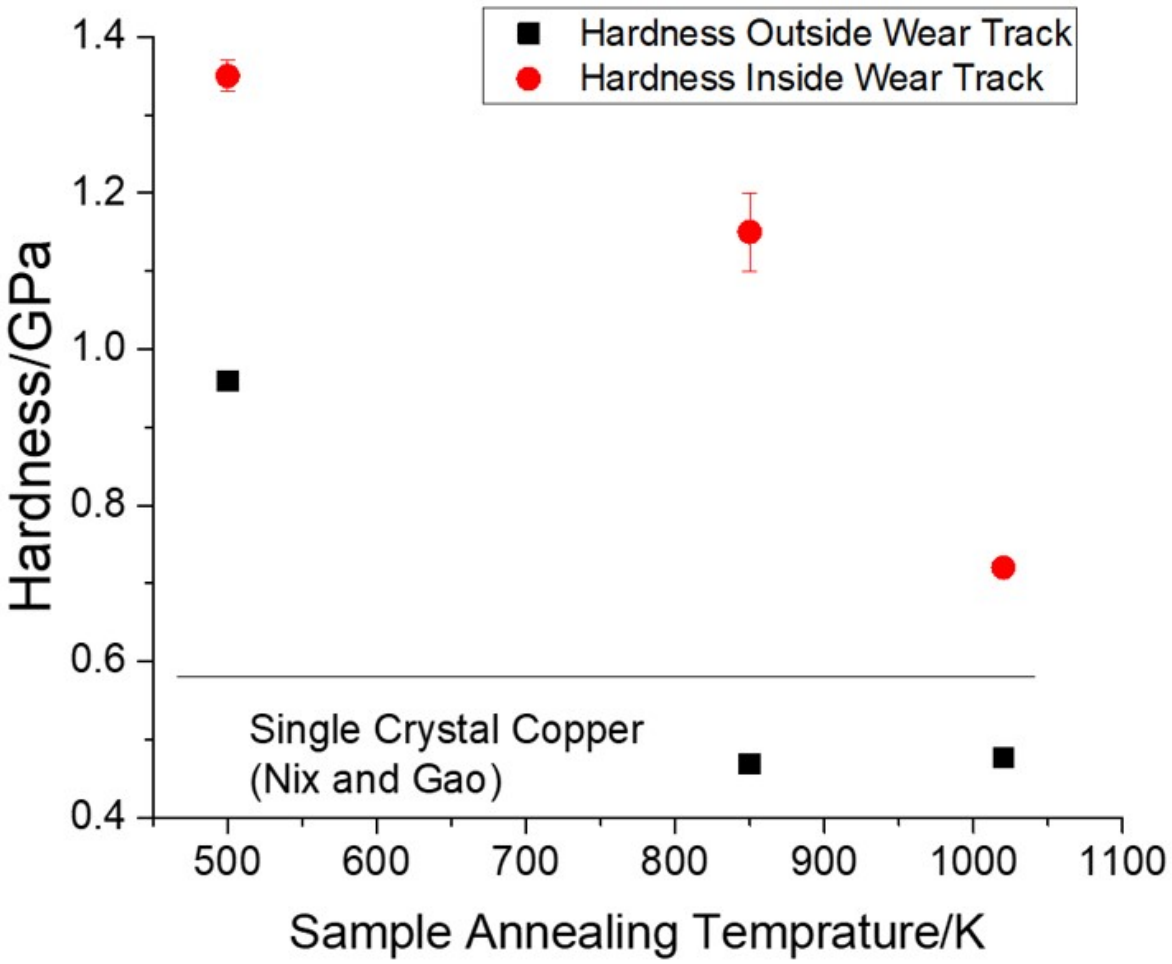

FIGURE 3.3: Measured values of hardness for copper foils that had been annealed at 500, 850, and 1020 K (■) and after having been rubbed at a load of 0.44 N at a sliding speed of 4×10^{-3} m/s in a background pressure of 1×10^{-8} Torr of DMDS for 80 cycles (●), summarizing the data shown in Fig. 3.2.

$$\rho_S = \frac{3\tan^2\theta}{2f^3bh^*} \tag{3.12}$$

where ρ_S is the density of dislocations, θ is the angle between the surface of the material

and the surface of the indenter, b is the Burgers vector and f is a correction factor for the size of the plastic zone (taken to be 1.9). For a Berkovich tip, $\tan^2\theta = 0.128164$, and $b = 2.5$ nm for copper [60], and Eqn. 12 yields dislocation densities that are given in Table 3.1, where the value for the sample annealed at 1020 K is close to that previously measured for single crystal copper [61], although higher values dislocation densities have been reported for copper at high strain rates [62, 63].

Values of the elastic modulus E^* for the various samples annealed at 500, 850, and 1020 K were also measured, and the results are summarized in Fig. 3.4. This reveals that, although the hardness of the copper in influenced by rubbing, the elastic modulus is not strongly affected.

3.4.2 Analysis of the Surface of the Tribopin

The tungsten carbide pin is routinely cleaned by electron-beam heating using a filament located inside the UHV chamber. It can also be cleaned by Argon ion bombardment, although the latter strategy may also change the surface microstructure. The effect of e-beam heating on the pin is illustrated in Fig. 3.5A, which shows an Auger spectrum of the pin indicating that the untreated pin is covered by carbon immediately after inserting it into the UHV chamber. Heating briefly until the sample glows red causes a change in the Auger spectrum and the appearance of features due to tungsten, and is consistent with the presence of tungsten carbide in the pin [64]. Note that

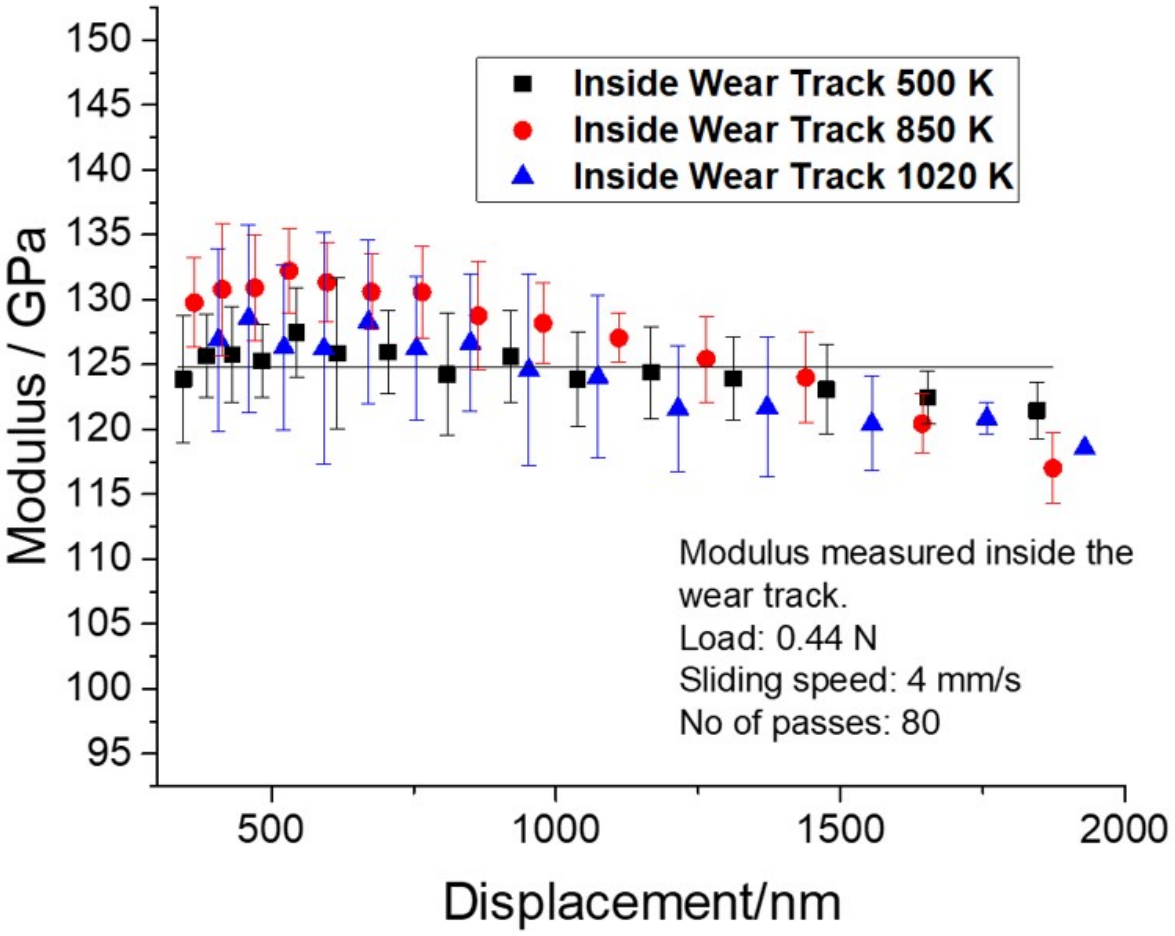

FIGURE 3.4: Measured values of elastic modulus E^* for copper foils that had been annealed at 500 (■), 850 (●), and 1020 (▲) K and after having been rubbed at a load of 0.44 N at a sliding speed of 4×10^{-3} m/s in a background pressure of 1×10^{-8} Torr of DMDS for 80 cycles.

repeatedly rubbing the copper surface in DMDS causes the eventual deposition of carbon on the sample to produce an Auger spectrum similar to that in Fig. 3.5A. The presence of tungsten carbide was confirmed from the XPS spectrum in Fig. 3.5B, obtained after ion bombarding, which shows peaks characteristic of tungsten carbide. Cobalt has a characteristic feature at ~800 eV binding energy [65] and no features are

detected at this energy in the spectrum indicating that there is little cobalt binder on the surface of the pin.

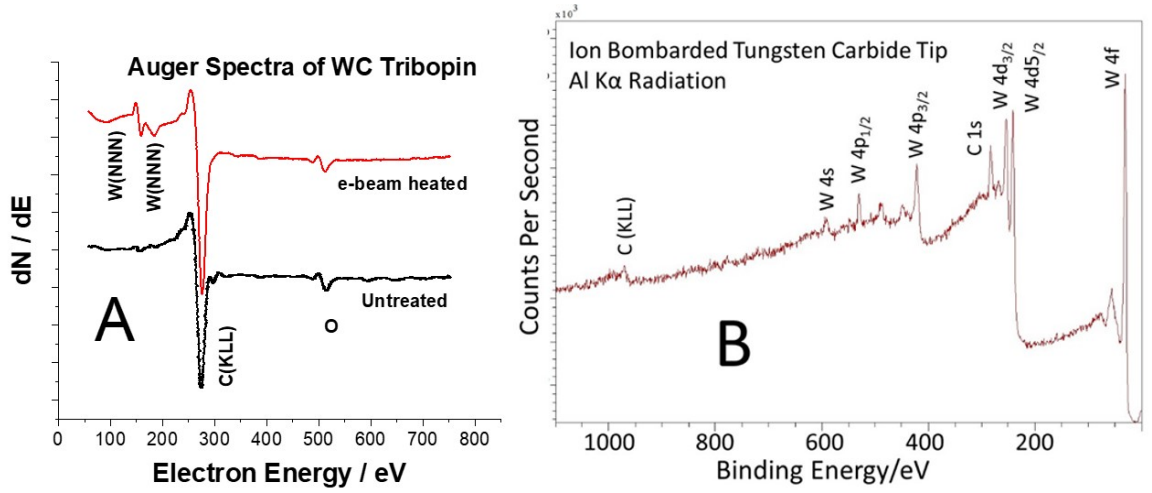

FIGURE 3.5: Analyses of the surface of the tungsten carbide tribopin. Figure A, lower trace shows an Auger spectrum of the initially contaminated pin showing predominantly carbon on the surface and the upper trace shows the effect of e-beam heating now revealing the presence of tungsten. Figure B shows an Al K_α X-ray photoelectron spectrum of the tungsten carbide pin that has been Argon ion bombarded. Figure B courtesy of Jules Galipaud and Thierry LeMogne, Ecole Centrale de Lyon, France.

3.4.3 Measurement of the Kinetics of Sulfur Surface-to-Bulk Transport in Copper as a Function of Sample Annealing Temperature

The rate of surface-to-bulk transport was measured for copper samples that had been annealed at 500, 850, or 1020 K. The concentration of sulfur on the surface was obtained by using a small-spot size electron gun that enabled the variation in the sulfur Auger signal to be measured as a function of position in the wear track [66]. However, this signal includes contributions from the methyl thiolate species and adsorbed sulfur as

well as subsurface sulfur [27]. Disentangling these contributions requires a measurement of the rate of shear-induced methyl thiolate decomposition, which is obtained from the rate of methane formation during sliding [26].

In all experiments, a wear track was initially created by rubbing the clean sample 50 times to ensure that the contact conditions remained the same for subsequent scans. During this process, the friction coefficient dropped from an initial value of ~0.8 to a final, constant value of ~0.45 [24]. The surface, including the wear track, was then dosed with DMDS at a sample temperature of 300 K to form a saturated methyl thiolate overlayer [67]. An Auger signal profile was obtained by scanning the electron beam across the wear track while monitoring the S KLL Auger signal at 151 eV kinetic energy. The full Auger spectrum was collected within the wear track and the amount of sulfur on the surface was gauged from the ratio of the peak-to-peak intensities of the S KLL to the Cu LMM Auger features. The surface was then rubbed several times under a normal load of 0.44 N at a sliding speed of 4×10^{-3} m/s. Auger spectra were collected at various sliding intervals until no sulfur was detected on the surface. The resulting plots of the normalized S/Cu Auger ratios as a function of the number of passes are displayed in Fig. 3.6 for samples that had been annealed to 500 (●), 850 (▲), or 1020 (■) K, The experiments were repeated several times and were very reproducible and show that there are significant differences in the rate at which sulfur is lost from the surface. Shown for comparison are the results obtained previously for a sample that had been

heated to 850 K (▼) [23], where the agreement with the current results is good.

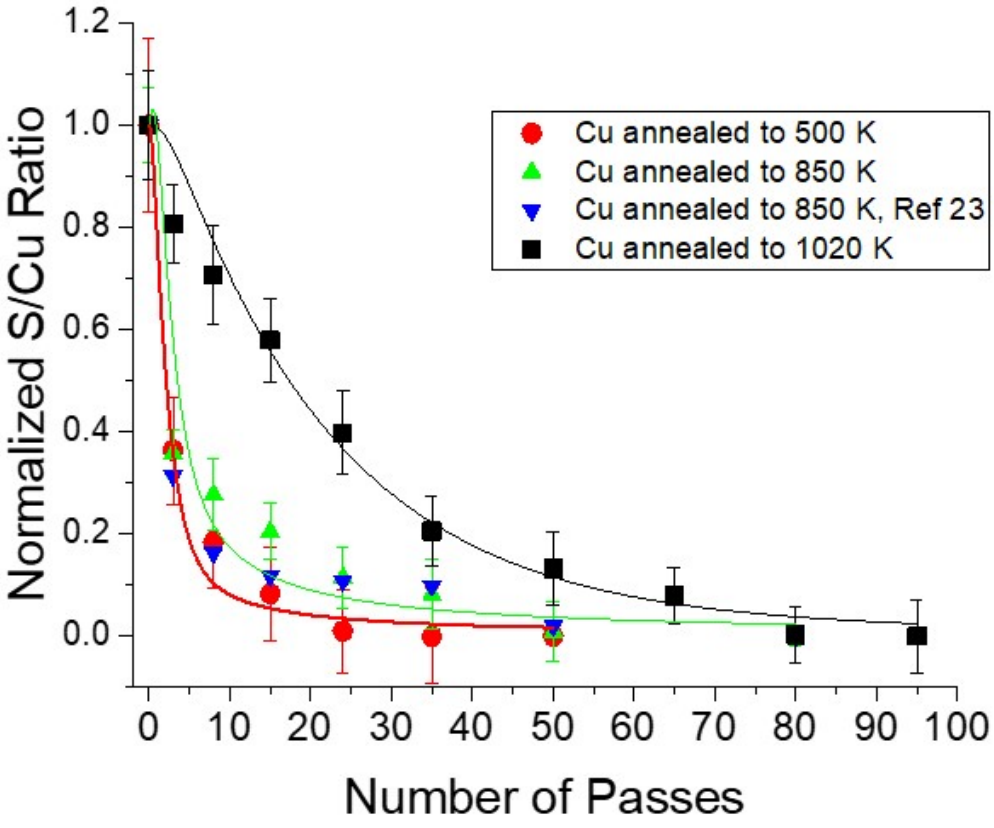

FIGURE 3.6: Plot of the relative sulfur to copper (S/Cu) Auger ratio measured inside the wear track as a function of the number of times that the copper samples had been rubbed in a background pressure of 1×10^{-8} Torr of DMDS at an applied normal load of 0.44 N and a sliding speed of 4×10^{-3} m/s after being cleaned and annealed at 500 (●), 850 (▲), and 1020 (■) K . Shown for comparison are the results obtained previously for a sample that had been heated to 850 K [23].

Previous work has shown that methyl thiolate species react by two distinct shear-induced processes, the first being C–S bond scission, with a first-order rate constant k_1 and a second process, investigated in this work, consists of sulfur surface-to-bulk

transport with a first-order rate constant k_2. These rate constants have been used to construct a kinetic model that reproduces the experimental reaction kinetics [27, 28, 68]. Because the time that the tip stays in contact with the surface is not precisely known, reaction rates are not described as function of reaction time, but more conveniently described as a function of the number of passes over the surface, which for the surface-to-bulk transport is given by $k_2^{'}$. The results in Fig. 3.6 are analyzed to yield values of $k_2^{'}$ for samples that had been annealed to various temperatures and the resulting fits are shown as solid lines through the data. The resulting best-fit values of $k_2^{'}$ are given in Table 3.1. The value of $k_2^{'}$ also controls the characteristic distance that the sulfur penetrates the bulk of the sample. In the case of the experiments carried out in this work, the distance over which the sulfur concentration is predicted to decrease to ~50% of the value at the surface is very small (~0.3 nm) for the sample annealed to ~1020 K with the largest crystallites, increasing to ~10 nm for a sample heated to 850 K, and ~35 nm for a sample heated to 500 K. The values of $k_2^{'}$ can also be used to calculate a sulfur subsurface sulfur depth profile for gas-phase lubrication of copper by DMDS and to analyze the electron microscopy data described below.

3.4.4 Subsurface Structure and Composition of Copper Samples after Rubbing in Dimethyl Disulfide as a Function of Sample Annealing Temperature

Similar experiments were carried out in which an initial wear track was created during a run-in period of 50 scans. The previously rubbed portion of the surface was then rubbed repeatedly at an applied normal load of 0.44 N and a sliding speed of 4×10^{-3} m/s while the sample was continuously exposed to gas-phase DMDS from a dosing tube with a background pressure of 5×10^{-8} Torr for a total of 80 scans. The samples were then coated with a film of aluminum to provide a protective layer and FIB samples were extracted from the rubbed regions and analyzed. Figures 3.1(d-e) show high-angle annular dark-field (HAADF) transmission electron microscopy (TEM) images, and Fig. 3.1(f) shows a FIB scanning electron microscope (SEM) image, of the subsurface regions of the copper samples and show crystallite sizes that are in accord with the Hardness measurements (Table 3.1).

Energy-dispersive X-ray (EDX) spectral images (comprising a full X-ray spectrum at each pixel in an array) were acquired from selected areas of each sample close to the surface of the copper to investigate the depth distribution and location of sulfur in the subsurface region of the sample. Fig. 3.7 shows a 100 nm × 50 nm region of a sample that had been cleaned and annealed at 1020 K and then reacted in DMDS while

rubbing. The X-ray spectral images were analyzed with Sandia's Automated eXpert Spectral Image Analysis (AXSIA) software [69, 70]. The results of this analysis produce an image of the component distribution (the location and quantity are shown in a color overlay) and the corresponding X-ray spectra, which indicate which elements are present at a particular location. The component image and corresponding spectral shape matrices then represent a reduced-rank and de-noised model of the original spectral image. The X-ray energies of the lines are indicative of the elements present in the sample, where copper has a characteristic K_α energy at 8.040 keV, a K_β energy at 8.905 keV and an L_α energy at 0.928 keV, and is clearly evident in the Cu component spectral shape (red) and is uniformly distributed throughout the sample as seen in the color overlay with corresponding Cu component image in red. The dark region at the top of the image is the aluminum capping layer (component spectral shape not shown). Sulfur is clearly evident in the Cu–S spectral shape (green) from the K_α peak at 2.307 keV, and is localized at the copper surface, consistent with the small $k_2^{'}$ value (Table 3.1). A small amount of oxygen contamination is evident in the Cu–S component from its characteristic K_α energy at 0.525 keV.

The large crystallite size for the sample that had been annealed to 1020 K (Table 3.1) leads to a low rate of surface-to-bulk transport (Figure 3.6) and a small value of $k_2^{'}$. This rate constant is proportional to the distance that the sulfur moves into the subsurface region per pass, and the kinetic model for the reaction of DMDS with copper can be

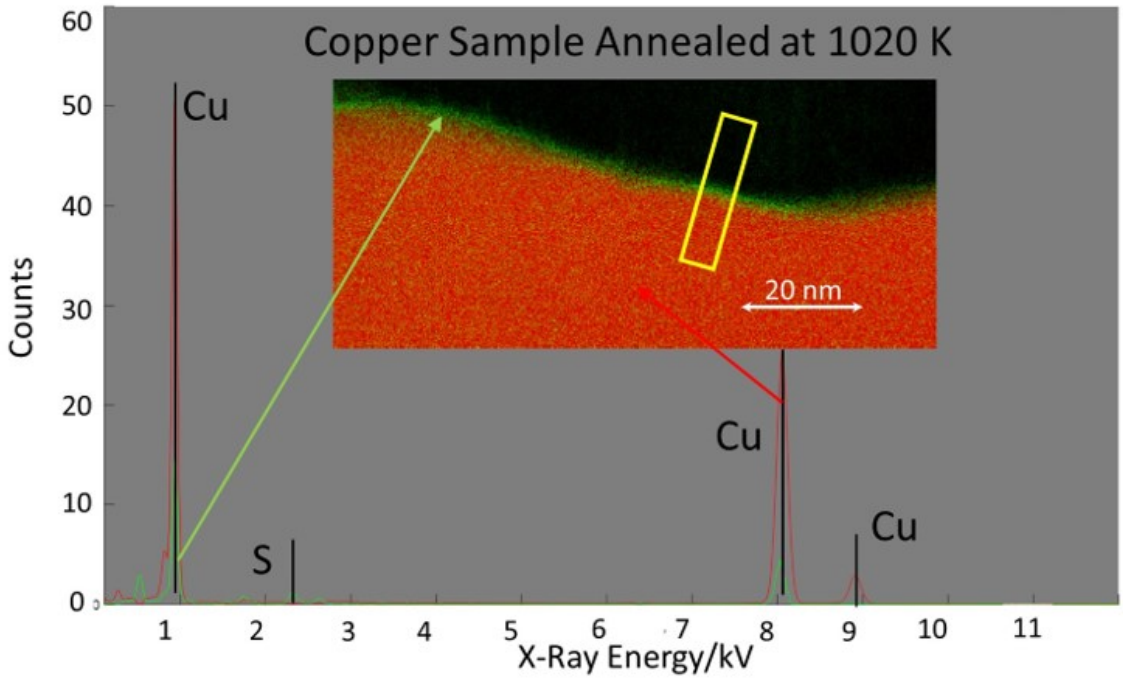

FIGURE 3.7: A 100 nm × 50 nm EDX image of a copper foil that had been cleaned and annealed in UHV at 1020 K and then reacted while rubbing at an applied normal load of 0.44 N and a sliding speed of 4×10^{-3} m/s in 5×10^{-8} Torr of DMDS. The interface between the copper and the aluminum capping layer is at the top of the image and the X-ray spectra are displayed for various points in the image as indicated by colored arrows.

analyzed to yield the sulfur depth distribution as a function of the number of passes [28]. Such an analysis predicts that the sulfur should only penetrate a few Ångstroms into the subsurface of a sample annealed at 1020 K, consistent with the narrow sulfur-containing band seen in Fig. 3.7. An integrated profile of the sulfur signal as a function of distance into the sample, collected from region defined by the yellow box in Fig. 3.7, is displayed in Fig 3.8 (■) and has a width of ~2 nm, with a maximum at ~0.5 nm below the surface. This implies that the spatial resolution of the instrumental and experimental configuration is ~1 nm primarily due to broadening of the electron beam (initially

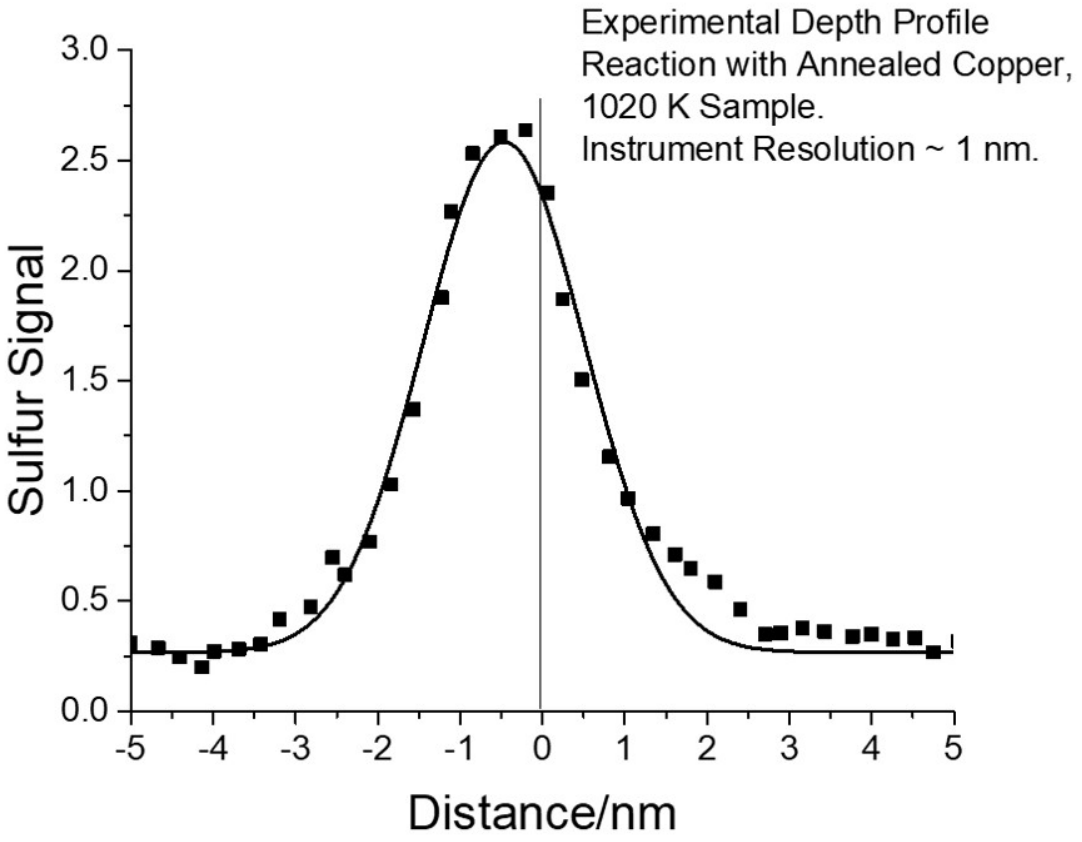

FIGURE 3.8: Plot of the intensity of the sulfur K_α X-ray signal at 2307 eV as a function of distance from the surface of a copper foil that had been cleaned and annealed in UHV at 1020 K and then reacted while rubbing at an applied normal load of 0.44 N and a sliding speed of 4×10^{-3} m/s in 5×10^{-8} Torr of DMDS, where the origin of the abscissa represents the surface, where negative values are within the copper sample (■). The line through the data is a fit to the theoretical depth profile [28] which has been broadened by 1 nm to take account of the spatial resolution of the instrument.

smaller than ~0.12 nm) as it interacts with the sample. The solid line through the data in Figure 3.8 show the theoretically predicted profile broadened by numerically convoluting it with a 1-nm wide Gaussian function using Origin software, leading to good agreement with the experimental profile.

Similar results are presented in Figure 3.9 for a sample that had been cleaned and annealed at 850 K and then reacted with DMDS while rubbing. In this case, the crystallite size is ×250 nm, on the same order as the 200 nm × 100 nm field of view of the X-ray spectral image acquired here. Again the green component X-ray spectrum shows the presence of copper and sulfur, where the sulfur is located near the surface of the sample (indicated by the green component in the color overlay), but penetrates further into the bulk than the sample annealed at 1020 K (Fig. 3.8), in accord with the larger value of $k_2^{'}$ for a sample annealed to 850 K (Fig. 3.6 and Table 3.1). The sulfur intensity for the near-surface region is larger for the sample annealed to 850 K than one heated to 1020 K. Note that the sample consists predominantly of a single copper grain over the analyzed region in Fig. 3.9 so that the larger penetration for this sample cannot be dominated by grain-boundary diffusion [71–73].

An integrated profile of the Cu–S EDXS signal is shown plotted as a function of distance into the sample for a localized region defined by the yellow rectangle in Fig. 3.9 and the results are displayed in Fig. 3.10 (■). Here the sulfur signal peaks at ~4 nm below the surface but penetrates 10's of nanometers into the bulk. Note that previous angle-resolved XPS results measured for a sample that had been annealed at 850 K and reacted for various times in DMDS yielded results that were in excellent agreement with the depth profile calculated using the kinetic model described above [28]. A sulfur depth profile calculated using the kinetic model using $k_2^{'} = 2.5/\text{scan}$ (Table 3.1) that was

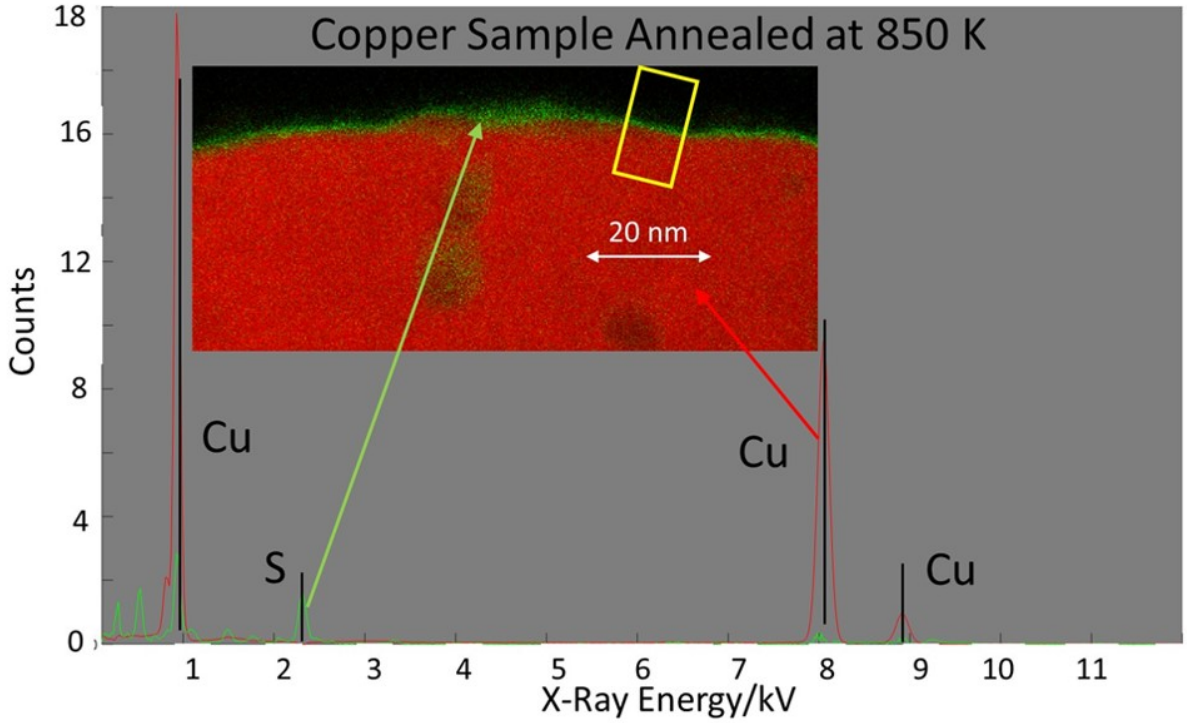

FIGURE 3.9: A 200 nm × 100 nm EDX image of a copper foil that had been cleaned and annealed in UHV at 850 K and then reacted while rubbing at an applied normal load of 0.44 N and a sliding speed of 4×10^{-3} m/s in 5×10^{-8} Torr of DMDS. The interface between the copper and the aluminum capping layer is at the top of the image and the X-ray spectra are displayed for various points in the image as indicated by colored arrows.

broadened by convoluting it with a 1-nm wide Gaussian is plotted as a solid line in Fig. 3.10. The agreement with the experiment is reasonable, although there are significant differences between theory and experiment, likely due to local concentration variations due to the small sampling region. In addition, the sample surface may not be exactly parallel to the electron beam due to roughness.

A similar spectral image analysis is shown for a sample that had been cleaned and annealed at 500 K in Figure 3.11. In this case the image size is 480 nm × 320 nm, while

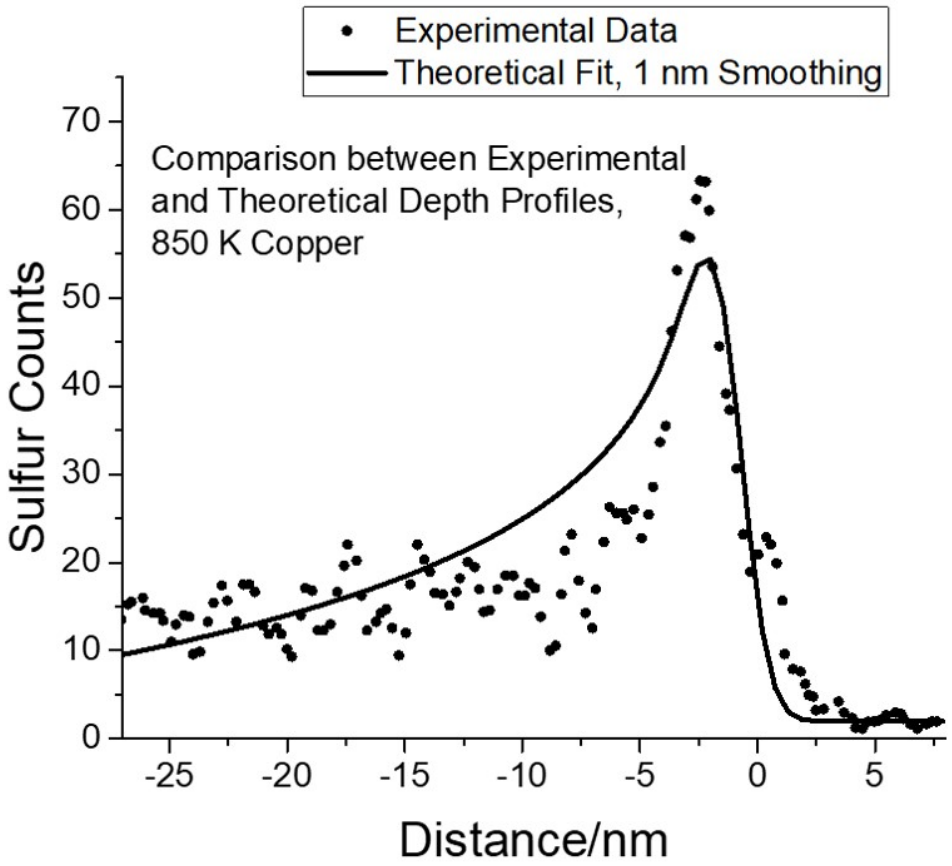

FIGURE 3.10: Plot of the intensity of the sulfur K_α X-ray signal at 2307 eV as a function of distance from the surface of a copper foil that had been cleaned and annealed in UHV at 850 K and then reacted while rubbing at an applied normal load of 0.44 N and a sliding speed of 4×10^{-3} m/s in 5×10^{-8} Torr of DMDS, where the origin of the abscissa represents the surface, where negative values are within the copper sample (■). The line through the data is a fit to the theoretical profile [28] which has been broadened by 1 nm to take account of the spatial resolution of the instrument.

the crystallite size for this sample is ~100 nm (Table 3.1). A line is included in the image to indicate the location of the surface and a calculated sulfur depth profile is shown as an inset to the figure. The spectral image shows a region adjacent to the surface that is rich in sulfur over a distance of ~65 nm from the surface, but with less sulfur at

larger distances away from it. This region is somewhat heterogeneous and will thus yield depth profiles that will depend significantly on the measurement position. However, the depth profile calculated using k_2'= 4.0/scan (Table 3.1) is shown as an inset to the figure and indicates that the width of the sulfur-rich region near the surface is in agreement with the theoretically predicted value. These results indicate that the experimental variation in the sulfur depth distribution with sample annealing temperature is in agreement with the calculated depth profiles using the measured surface-to-bulk transport rate constants (Fig. 3.6). In particular, the sulfur depth profiles and surface-to-bulk transport rate constants correlate with dislocation densities (Table 3.1).

In addition. however, there are linear sulfur-rich regions deeper into the sample that are separated by ~100 nm, close to the grain size in the sample. Fig. 3.1(d) shows a HAADF TEM image of this sample, where the red square highlights the region analyzed in Fig. 3.11, indicating that the linear sulfur-rich regions correspond to grain boundaries and this result implies that sulfur transport along grain boundaries can also facilitate the surface-to-bulk transport of sulfur in copper [71–73].

3.5 Discussion

The modified Karthikeyan-Rigney theory described above predicts that the shear-induced rate of sulfur transport into the bulk of copper to form a metastable copper sulfide film

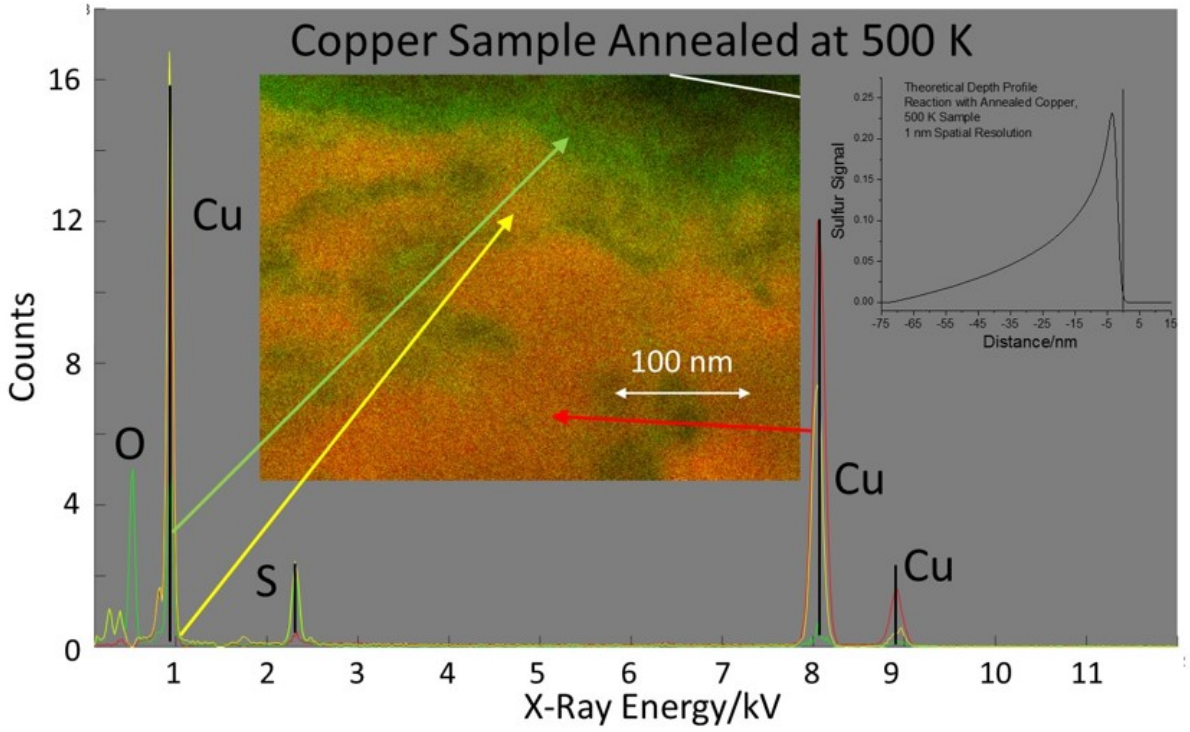

FIGURE 3.11: A 480 nm × 320 nm EDX image of a copper foil that had been cleaned and annealed in UHV at 500 K and then reacted while rubbing at an applied normal load of 0.44 N and a sliding speed of 4×10^{-3} m/s in 5×10^{-8} Torr of DMDS. The interface between the copper and the aluminum capping layer is at the top of the image and is dedicated by a white line and the X-ray spectra are displayed for various points in the image as indicated by colored arrows. The inset to the spectra shows the predicted depth profile [28] which has been broadened by 1 nm to take account of the spatial resolution of the instrument.

depends on (i) the strain-rate sensitivity of the substrate and (ii) that the distance that a sulfur overlayer penetrates the bulk is proportional to the number of times that the sample has been rubbed. The second prediction has been confirmed experimentally [66] and has been used to model the gas-phase lubrication of copper by DMDS [28]. The model correctly predicts both the sulfur depth profile and the total amount of sulfur that is accumulated in the copper bulk as a function of the number of times that the

sample has been rubbed. It should be noted that the model applies to the initial rate of reaction because the inclusion of large concentrations of sulfur in the copper subsurface will itself eventually influence the surface-to-bulk transport kinetics. However, as the experiments are carried out for rubbing in a relatively low pressure of DMDS, initial kinetics are measured.

The predicted strain-rate sensitivity dependence was tested by using samples that had been cleaned and annealed at different temperatures (500, 850, or 1020 K) to produce copper with different grain sizes (Figure 3.1, Table 3.1). Measurements of the surface-to-bulk transport kinetics of a methyl thiolate overlayer on copper by analyzing the amount of sulfur in the rubbed region as a function of the number of times that it had been rubbed yielded significantly different values of rate constant of surface-to-bulk transport, $k_2^{'}$ (Figure 3.6, Table 3.1). Since hardness of copper depends on grain size through the Hall-Petch effect [54], and the strain-rate sensitivity also depends on the size of the crystallites (Figure S1, modified from Ref, [54]) [74], this enables the dependence of the rate of surface-to-bulk transport of sulfur into copper ($k_2^{'}$) on strain-rate sensitivity m to be measured. The measured values of $k_2^{'}$ are plotted against strain-rate sensitivity m in Fig. 3.12, showing good linearity in accord with the prediction of the model.

In order to identify the origin of the strain-rate sensitivity dependence of the rate of sulfur surface-to-bulk transport, the elemental depth distribution was measured using

EDXS and the results are displayed in Figures 3.7, 3.9 and 3.11. The results of Fig. 3.7 for a sample that had been annealed at 1020 K show that the sulfur is located very close to the surface (Fig. 3.8) consistent with the measured value of $k_2^{'}$ ~0.05 per pass. Here the crystallite sizes are large (~1400 nm, Table 3.1) and the dislocation density is low (~9.5×10^{12} /m^2). The rate of surface-to-bulk transport increases to $k_2^{'}$ ~2.5 per pass as the sample preparation temperature decreases to 850 K (Figs. 3.9 and 3.10), where the crystallite size (~250 nm, Table 3.1) is sufficiently large that there are likely no dislocations in the image in shown in Fig. 3.9, while the dislocation density increases to ~2.4×10^{13} /m^2 (Table 3.1). This clearly implicates the participation of dislocations in the transport of sulfur into the subsurface region of copper.

The sample that had been prepared at a lower temperature (500 K, Fig. 3.11) contains smaller grains (~115 nm, Table 3.1) and has a higher dislocation density (~3.95×10^{13} /m^2). The sulfur penetrates still more rapidly into the bulk of the copper ($k_2^{'}$ ~4 per pass, Table 3.1), and the distance that the sulfur penetrates the copper is in agreement with predictions from measurements of the surface-to-bulk transport kinetics (Fig. 3.11, Inset). Thus, the surface-to-bulk transport rate of sulfur in crystalline regions of the copper sample scales with the dislocated density as evidenced by the plot of $k_2^{'}$ versus dislocation density in Figure 3.13, implying that strain-rate sensitivity depends on the dislocation density [75]. Note that dislocation glide has been proposed as a mechanism for plastic deformation during high-energy ball milling [12–14].

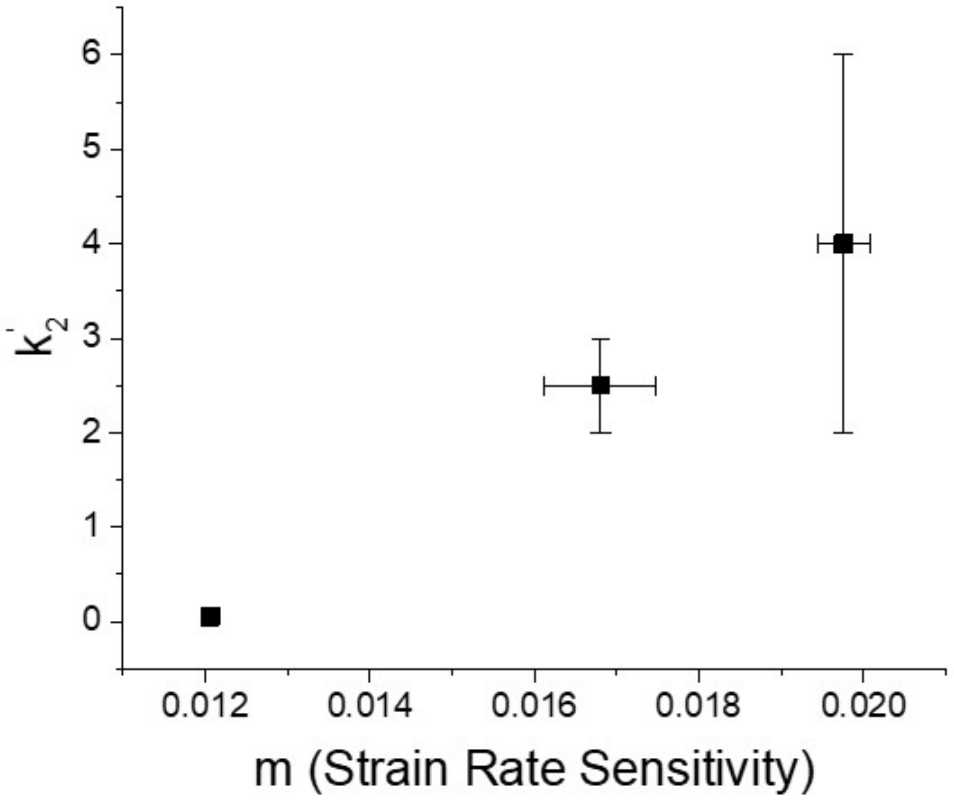

FIGURE 3.12: Plot of the rate constant for the shear-induced transport of sulfur into the sub-surface region of copper, k_2', as a function of the strain-rate sensitivity for samples modified by heating the copper sample to various temperatures.

However, in the case of a sample that had been annealed at 500 K (Fig. 3.11), some sulfur is detected even deeper into the copper in linear regions that coincide with the presence of grain boundaries that are identified by electron microscopy (Fig. 3.1(d)), suggesting that sulfur also diffuses along grain boundaries. The linear regions are ~20 nm wide, much wider than expected for grain boundaries in copper [76], and may

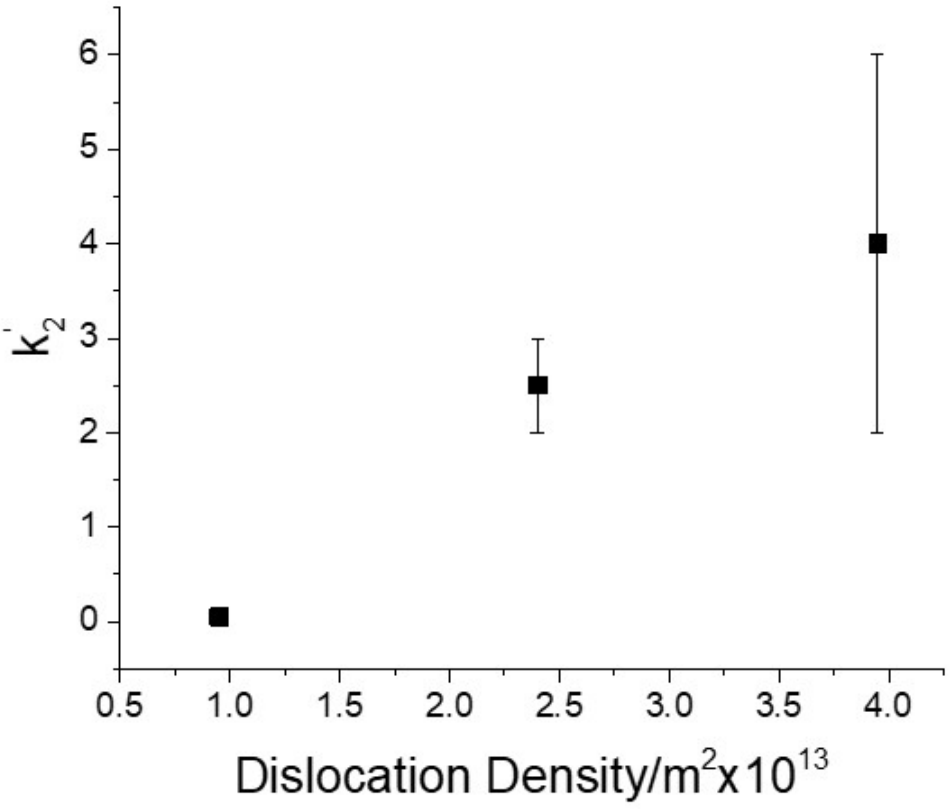

FIGURE 3.13: Plot of the rate constant for the shear-induced transport of sulfur into the subsurface region of copper, k_2', as a function of dislocation density for samples modified by heating the copper sample to various temperatures.

be due to the boundaries being tilted with respect to the incident electron beam. An alternative possibility is that, because the width of the linear regions are relatively independent of depth into the substrate, the sulfur diffuses rapidly along grain boundaries when they are present, but much more slowly via dislocations, where it moves laterally from the grain boundaries to form EDXS features that are ~20 nm wide. These results

suggest that both the presence of grain boundaries and dislocations can facilitate the shear-induced surface-to-bulk transport of sulfur.

It should be emphasized that the formation of nanostructured materials at the sliding interface by Kelvin-Helmholtz instabilities proposed by Rigney [34, 35, 77, 78] are not directly captured by the analytical Karthikeyan-Rigney model and, in principle should not mimic the experimental mixing behavior and reproduce both the kinetics and the strain-rate sensitivity dependence found experimentally, yet it does. However, finite-element simulations that have been performed using a non-linear viscosity of copper analogous to the Herschel-Bulkley model revealed deformation, material folding and the occurrence of vortices while rubbing [3].

3.6 Conclusions

The previously identified shear-induced transport of sulfur into the subsurface region of copper is investigated by modifying the material properties of the copper sample by using different annealing temperatures (500, 850, and 1020 K) during the vacuum cleaning procedure. The surface-to-bulk transport kinetics are modeled by an adaptation of a theory first proposed by Karthikeyan and Rigney that predicts that the distance that an adsorbed overlayer penetrates the bulk of the sample is proportional to the number of times that the sample is rubbed, and that the rate should be proportional

to the strain-rate sensitivity of the substrate. Previous work has verified that the linear dependence of penetration depth on the number of rubbing cycles is correct. It is found here by measuring the hardness of the copper after it has been rubbed that the temperature at which the copper sample was annealed during its preparation influences its hardness and therefore its strain-rate sensitivity, m. This enables the second prediction of the Karthikeyan-Rigney model to be tested by measuring the surface-to-bulk transport rate by monitoring the loss of sulfur from the surface as a function of the number of times that the sample had been rubbed. This demonstrated that the surface-to-bulk transport rate does vary linearly with m, in accord with the theoretical prediction.

The mechanism for this process is investigated by preparing thin samples of the bulk of copper sample that had been annealed at 500, 850, or 1020 K during the cleaning procedure using a focused-ion beam. Electron microscopy images of the samples indicated that the copper crystallites were larger for the samples that had been annealed at high temperatures, as expected. Energy-dispersive X-ray spectroscopy (EDXS) measurements as a function of depth into the sample revealed that the sulfur was highly localized on the surface for a sample that had been heated to 1020 K, penetrated a moderate distance (~10 nm) into the surface for a sample that had been annealed to 850 K, and~35 nm for a sample that had been heated to 500 K. For the samples that had been annealed to 1020 and 850 K, the crystallite size was sufficiently large that there were no grain boundaries in the analyzed region, while sulfur still penetrated

into the bulk, implying the surface-to-bulk transport if sulfur is facilitated by the presence of dislocations in the copper. This observation is in accord with previous studies of mechanical mixing (alloy formation) by ball milling, which implicates a dislocation glide mechanism in the mixing [12–14].

It was noted that the Karthikeyan and Rigney model does not specifically include Kelvin-Helmholtz-type instabilities that would lead to intermixing near the surface and the transport of adsorbates into the subsurface region. However, more detailed finite-element calculations for copper using similar shear properties as the Karthikeyan and Rigney model by Pouryazdan et al [3] identifies the presence of flow features that resemble those formed by Kelvin-Helmholtz instabilities.

Finally, it found in the case of copper samples with smaller crystallites which have been cleaned by annealing at a lower temperature (~500 K), additional subsurface copper is found deeper into the subsurface in places that electron microscopy identifies as grain boundaries. It appears that rate of surface-to-bulk transport of sulfur into copper is facilitated by the presence both of dislocations and grain boundaries.

References

[1] P. Fox, "Mechanically initiated chemical reactions in solids," *Journal of Materials Science*, vol. 10, no. 2, pp. 340–360, 1975.

[2] M. A. Meyers, A. Mishra, and D. J. Benson, "Mechanical properties of nanocrystalline materials," *Progress in Materials Science*, vol. 51, no. 4, pp. 427–556, 2006.

[3] M. Pouryazdan, B. J. Kaus, A. Rack, A. Ershov, and H. Hahn, "Mixing instabilities during shearing of metals," *Nature Communications*, vol. 8, no. 1, pp. 1–7, 2017.

[4] C. Suryanarayana, "Mechanical alloying and milling," *Progress in Materials Science*, vol. 46, no. 1-2, pp. 1–184, 2001.

[5] M. Vaidya, G. M. Muralikrishna, and B. S. Murty, "High-entropy alloys by mechanical alloying: A review," *Journal of Materials Research*, vol. 34, no. 5, pp. 664–686, 2019.

[6] H. Theophrastus, "Theophrastus's history of stones: with an english version, and critical and philosophical notes, including the modern history of the gems, &c., described by that author, and of many other of the native fossils," *London*, 1774.

[7] M. Faraday, *Chemical manipulation: being instructions to students in chemistry, on the methods of performing experiments of demonstration or of research, with accuracy and success*. Murray, 1830.

[8] G. Kaupp, "Waste-free synthesis and production all across chemistry with the benefit of self-assembled crystal packings," *Journal of Physical Organic Chemistry*, vol. 21, no. 7-8, pp. 630–643, 2008.

[9] M. K. Beyer and H. Clausen-Schaumann, "Mechanochemistry: the mechanical activation of covalent bonds," *Chemical Reviews*, vol. 105, no. 8, pp. 2921–2948, 2005.

[10] N. N. Thadhani, "Shock-induced chemical reactions and synthesis of materials," *Progress in Materials Science*, vol. 37, no. 2, pp. 117–226, 1993.

[11] S. L. James, C. J. Adams, C. Bolm, D. Braga, P. Collier, T. Friščić, F. Grepioni, K. D. Harris, G. Hyett, W. Jones, *et al.*, "Mechanochemistry: opportunities for new and cleaner synthesis," *Chemical Society Reviews*, vol. 41, no. 1, pp. 413–447, 2012.

[12] P. Bellon and R. Averback, "Nonequilibrium roughening of interfaces in crystals under shear: application to ball milling," *Physical Review Letters*, vol. 74, no. 10, p. 1819, 1995.

[13] S. Odunuga, Y. Li, P. Krasnochtchekov, P. Bellon, and R. S. Averback, "Forced chemical mixing in alloys driven by plastic deformation," *Physical Review Letters*, vol. 95, no. 4, p. 045901, 2005.

[14] Y. Ashkenazy, N. Q. Vo, D. Schwen, R. S. Averback, and P. Bellon, "Shear induced chemical mixing in heterogeneous systems," *Acta Materialia*, vol. 60, no. 3,

pp. 984–993, 2012.

[15] V. Panin, A. Kolubaev, S. Tarasov, and V. Popov, "Subsurface layer formation during sliding friction," *Wear*, vol. 249, no. 10-11, pp. 860–867, 2001.

[16] S. Tarasov, V. Rubtsov, and A. Kolubaev, "Subsurface shear instability and nanostructuring of metals in sliding," *Wear*, vol. 268, no. 1-2, pp. 59–66, 2010.

[17] A. Moshkovich, V. Perfilyev, I. Lapsker, D. Gorni, and L. Rapoport, "The effect of grain size on stribeck curve and microstructure of copper under friction in the steady friction state," *Tribology Letters*, vol. 42, no. 1, pp. 89–98, 2011.

[18] A. Moshkovich, V. Perfilyev, I. Lapsker, and L. Rapoport, "Stribeck curve under friction of copper samples in the steady friction state," *Tribology Letters*, vol. 37, no. 3, pp. 645–653, 2010.

[19] A. Mishra, B. Kad, F. Gregori, and M. Meyers, "Microstructural evolution in copper subjected to severe plastic deformation: Experiments and analysis," *Acta Materialia*, vol. 55, no. 1, pp. 13–28, 2007.

[20] J. Gubicza, N. Q. Chinh, T. Csanadi, T. Langdon, and T. Ungár, "Microstructure and strength of severely deformed fcc metals," *Materials Science and Engineering: A*, vol. 462, no. 1-2, pp. 86–90, 2007.

[21] Y. Zhang, Z. Han, K. Wang, and K. Lu, "Friction and wear behaviors of nanocrystalline surface layer of pure copper," *Wear*, vol. 260, no. 9-10, pp. 942–948, 2006.

[22] F. Gao, O. Furlong, P. V. Kotvis, and W. T. Tysoe, "Reaction of tributyl phosphite with oxidized iron: surface and tribological chemistry," *Langmuir*, vol. 20, no. 18, pp. 7557–7568, 2004.

[23] O. J. Furlong, B. P. Miller, and W. T. Tysoe, "Shear-induced surface-to-bulk transport at room temperature in a sliding metal–metal interface," *Tribology Letters*, vol. 41, no. 1, pp. 257–261, 2011.

[24] O. J. Furlong, B. P. Miller, P. Kotvis, and W. T. Tysoe, "Low-temperature, shear-induced tribofilm formation from dimethyl disulfide on copper," *ACS applied materials & interfaces*, vol. 3, no. 3, pp. 795–800, 2011.

[25] O. Furlong, B. Miller, and W. T. Tysoe, "Shear-induced boundary film formation from dialkyl sulfides on copper," *Wear*, vol. 274, pp. 183–187, 2012.

[26] B. Miller, O. Furlong, and W. T. Tysoe, "The kinetics of shear-induced boundary film formation from dimethyl disulfide on copper," *Tribology Letters*, vol. 49, no. 1, pp. 39–46, 2013.

[27] H. Adams, B. P. Miller, P. V. Kotvis, O. J. Furlong, A. Martini, and W. T. Tysoe, "In situ measurements of boundary film formation pathways and kinetics: dimethyl and diethyl disulfide on copper," *Tribology Letters*, vol. 62, no. 1, p. 12, 2016.

[28] H. Adams, B. P. Miller, O. J. Furlong, M. Fantauzzi, G. Navarra, A. Rossi, Y. Xu, P. V. Kotvis, and W. T. Tysoe, "Modeling mechanochemical reaction mechanisms," *ACS applied materials & interfaces*, vol. 9, no. 31, pp. 26531–26538, 2017.

[29] M. Varenberg, G. Ryk, A. Yakhnis, Y. Kligerman, N. Kondekar, and M. T. McDowell, "Mechano-chemical surface modification with Cu_2S: inducing superior lubricity," *Tribology Letters*, vol. 64, no. 2, p. 28, 2016.

[30] W. Thomson, "$XLVI$. hydrokinetic solutions and observations," *The London, Edinburgh, and Dublin Philosophical Magazine and Journal of Science*, vol. 42, no. 281, pp. 362–377, 1871.

[31] H. von Helmholtz, *über discontinuirliche Flüssigkeits-Bewegungen*. Akademie der Wissenschaften zu Berlin, 1868.

[32] H. J. Kim, W. K. Kim, M. L. Falk, and D. A. Rigney, "Md simulations of microstructure evolution during high-velocity sliding between crystalline materials," *Tribology Letters*, vol. 28, no. 3, pp. 299–306, 2007.

[33] A. Emge, S. Karthikeyan, H. Kim, and D. Rigney, "The effect of sliding velocity on the tribological behavior of copper," *Wear*, vol. 263, no. 1-6, pp. 614–618, 2007.

[34] H.-J. Kim, S. Karthikeyan, and D. Rigney, "A simulation study of the mixing, atomic flow and velocity profiles of crystalline materials during sliding," *Wear*, vol. 267, no. 5-8, pp. 1130–1136, 2009.

[35] S. Karthikeyan, A. Agrawal, and D. Rigney, "Molecular dynamics simulations of sliding in an $Fe - Cu$ tribopair system," *Wear*, vol. 267, no. 5-8, pp. 1166–1176, 2009.

[36] A. Emge, S. Karthikeyan, and D. Rigney, "The effects of sliding velocity and sliding time on nanocrystalline tribolayer development and properties in copper," *Wear*, vol. 267, no. 1-4, pp. 562–567, 2009.

[37] D. A. Rigney and S. Karthikeyan, "The evolution of tribomaterial during sliding: a brief introduction," *Tribology Letters*, vol. 39, no. 1, pp. 3–7, 2010.

[38] N. Argibay, M. Chandross, S. Cheng, and J. R. Michael, "Linking microstructural evolution and macro-scale friction behavior in metals," *Journal of Materials Science*, vol. 52, no. 5, pp. 2780–2799, 2017.

[39] A. Gola, R. Schwaiger, P. Gumbsch, and L. Pastewka, "Pattern formation during deformation of metallic nanolaminates," *Physical Review Materials*, vol. 4, no. 1, p. 013603, 2020.

[40] S. Karthikeyan, H. Kim, and D. Rigney, "Velocity and strain-rate profiles in materials subjected to unlubricated sliding," *Physical Review Letters*, vol. 95, no. 10, p. 106001, 2005.

[41] W. H. Herschel and R. Bulkley, "Konsistenzmessungen von gummi-benzollösungen," *Kolloid-Zeitschrift*, vol. 39, no. 4, pp. 291–300, 1926.

[42] T. Zhu, J. Li, A. Samanta, H. G. Kim, and S. Suresh, "Interfacial plasticity governs strain rate sensitivity and ductility in nanostructured metals," *Proceedings of the National Academy of Sciences*, vol. 104, no. 9, pp. 3031–3036, 2007.

[43] Y. Shen, L. Lu, M. Dao, and S. Suresh, "Strain rate sensitivity of Cu with nanoscale twins," *Scripta materialia*, vol. 55, no. 4, pp. 319–322, 2006.

[44] A. Mishra, M. Martin, N. Thadhani, B. Kad, E. A. Kenik, and M. Meyers, "High-strain-rate response of ultra-fine-grained copper," *Acta Materialia*, vol. 56, no. 12, pp. 2770–2783, 2008.

[45] R. Schwaiger, B. Moser, M. Dao, N. Chollacoop, and S. Suresh, "Some critical experiments on the strain-rate sensitivity of nanocrystalline nickel," *Acta Materialia*, vol. 51, no. 17, pp. 5159–5172, 2003.

[46] H. W. Höppel, J. May, and M. Göken, "Enhanced strength and ductility in ultrafine-grained aluminium produced by accumulative roll bonding," *Advanced engineering materials*, vol. 6, no. 9, pp. 781–784, 2004.

[47] G. Gray Iii, T. Lowe, C. Cady, R. Valiev, and I. Aleksandrov, "Influence of strain rate & temperature on the mechanical response of ultrafine-grained $Cu, Ni, and Al-4Cu-0.5Zr$," *Nanostructured Materials*, vol. 9, no. 1-8, pp. 477–480, 1997.

[48] N. Petch, "The cleavage strength of polycrystals," *Journal of the Iron and Steel Institute*, vol. 174, pp. 25–28, 1953.

[49] E. Hall, "The deformation and ageing of mild steel: III discussion of results," *Proceedings of the Physical Society. Section B*, vol. 64, no. 9, p. 747, 1951.

[50] F. Gao, O. Furlong, P. V. Kotvis, and W. Tysoe, "Pressure dependence of shear strengths of thin films on metal surfaces measured in ultrahigh vacuum," *Tribology Letters*, vol. 31, no. 2, p. 99, 2008.

[51] D. Olson, H. Gao, C. Tang, W. T. Tysoe, and A. Martini, "Pressure dependence of the interfacial structure of potassium chloride films on iron," *Thin Solid Films*, vol. 593, pp. 150–157, 2015.

[52] B. A. Sexton, "The structure of acetate species on copper (100)," *Chemical Physics Letters*, vol. 65, no. 3, pp. 469–471, 1979.

[53] L. Lu, R. Schwaiger, Z. Shan, M. Dao, K. Lu, and S. Suresh, "Nano-sized twins induce high rate sensitivity of flow stress in pure copper," *Acta materialia*, vol. 53, no. 7, pp. 2169–2179, 2005.

[54] J. Chen, L. Lu, and K. Lu, "Hardness and strain rate sensitivity of nanocrystalline Cu," *Scripta Materialia*, vol. 54, no. 11, pp. 1913–1918, 2006.

[55] W. D. Nix and H. Gao, "Indentation size effects in crystalline materials: a law

for strain gradient plasticity," *Journal of the Mechanics and Physics of Solids*, vol. 46, no. 3, pp. 411–425, 1998.

[56] G. Z. Voyiadjis and R. Peters, "Size effects in nanoindentation: an experimental and analytical study," *Acta mechanica*, vol. 211, no. 1-2, pp. 131–153, 2010.

[57] C. Suryanarayana, D. Mukhopadhyay, S. Patankar, and F. Froes, "Grain size effects in nanocrystalline materials," *Journal of Materials Research*, vol. 7, no. 8, pp. 2114–2118, 1992.

[58] C. T. Rueden, J. Schindelin, M. C. Hiner, B. E. DeZonia, A. E. Walter, E. T. Arena, and K. W. Eliceiri, "Imagej2: Image*J* for the next generation of scientific image data," *BMC Bioinformatics*, vol. 18, no. 1, p. 529, 2017.

[59] S. Graça, R. Colaço, P. Carvalho, and R. Vilar, "Determination of dislocation density from hardness measurements in metals," *Materials Letters*, vol. 62, no. 23, pp. 3812–3814, 2008.

[60] N. Simon, E. Drexler, and R. P. Reed, "Properties of copper and copper alloys at cryogenic temperatures. final report," tech. rep., National Inst. of Standards and Technology (MSEL), Boulder, CO (United States, 1992.

[61] Y. Miyajima, S. Okubo, H. Abe, H. Okumura, T. Fujii, S. Onaka, and M. Kato, "Dislocation density of pure copper processed by accumulative roll bonding and

equal-channel angular pressing," *Materials Characterization*, vol. 104, pp. 101–106, 2015.

[62] D. Rigney, "Dislocation content at large plastic strains," 1979.

[63] D. Rigney, M. Naylor, R. Divakar, and L. Ives, "Low energy dislocation structures caused by sliding and by particle impact," *Materials Science and Engineering*, vol. 81, pp. 409–425, 1986.

[64] T. Smetyukhova, A. Druzhinin, and D. Podgorny, "Features of the auger spectra of $Ti_2C, SiC, and WC$," *Journal of surface investigation: X-ray, Synchrotron and Neutron Techniques*, vol. 11, no. 2, pp. 414–419, 2017.

[65] B. D. S. MP, "Practical surface analysis, *A*uger and *X*-ray photoelectron spectroscopy, vol. 1," 1990.

[66] B. Miller, O. Furlong, and W. T. Tysoe, "The kinetics of shear-induced boundary film formation from dimethyl disulfide on copper," *Tribology Letters*, vol. 49, no. 1, pp. 39–46, 2013.

[67] O. J. Furlong, B. P. Miller, Z. Li, J. Walker, L. Burkholder, and W. T. Tysoe, "The surface chemistry of dimethyl disulfide on copper," *Langmuir*, vol. 26, no. 21, pp. 16375–16380, 2010.

[68] H. L. Adams, M. T. Garvey, U. S. Ramasamy, Z. Ye, A. Martini, and W. T. Tysoe,

"Shear-induced mechanochemistry: pushing molecules around," *The Journal of Physical Chemistry C*, vol. 119, no. 13, pp. 7115–7123, 2015.

[69] P. G. Kotula, M. R. Keenan, and J. R. Michael, "Automated analysis of sem *X*-ray spectral images: A powerful new microanalysis tool," *Microscopy and Microanalysis*, vol. 9, no. 1, p. 1, 2003.

[70] P. G. Kotula and M. R. Keenan, "Application of multivariate statistical analysis to stem *X*-ray spectral images: Interfacial analysis in microelectronics," *Microscopy and Microanalysis*, vol. 12, no. 6, pp. 538–544, 2006.

[71] Y. Mishin, C. Herzig, J. Bernardini, and W. Gust, "Grain boundary diffusion: fundamentals to recent developments," *International Materials Reviews*, vol. 42, no. 4, pp. 155–178, 1997.

[72] F. Moya, G. Moya-Gontier, and F. Cabane-Brouty, "Sulphur diffusion in copper: departure from the arrhenius plot," *physica status solidi (b)*, vol. 35, no. 2, pp. 893–901, 1969.

[73] J. Ladet, B. Aufray, and F. Maya, "Sulphur diffusion in silver and copper single crystals," *Metal Science*, vol. 12, no. 4, pp. 195–197, 1978.

[74] G. Malygin, "Analysis of the strain-rate sensitivity of flow stresses in nanocrystalline fcc and bcc metals," *Physics of the Solid State*, vol. 49, no. 12, pp. 2266–2273, 2007.

[75] J. A. Rodríguez-Martínez, M. Rodríguez-Millán, A. Rusinek, and A. Arias, "A dislocation-based constitutive description for modeling the behavior of fcc metals within wide ranges of strain rate and temperature," *Mechanics of materials*, vol. 43, no. 12, pp. 901–912, 2011.

[76] R. Islamgaliev, K. Pekala, M. Pekala, and R. Valiev, "The determination of the grain boundary width of ultrafine grained copper and nickel from electrical resistivity measurements," *physica status solidi (a)*, vol. 162, no. 2, pp. 559–566, 1997.

[77] H. J. Kim, W. K. Kim, M. L. Falk, and D. A. Rigney, "Md simulations of microstructure evolution during high-velocity sliding between crystalline materials," *Tribology Letters*, vol. 28, no. 3, pp. 299–306, 2007.

[78] D. A. Rigney and S. Karthikeyan, "The evolution of tribomaterial during sliding: a brief introduction," *Tribology Letters*, vol. 39, no. 1, pp. 3–7, 2010.

Chapter 4

Reaction between Dimethyl Disulfide and Copper by Sliding Graphitic Carbon Covered Tungsten Carbide Tribopin: Influence of the Counterface on Mechanochemistry

4.1 Introduction

Chemical changes can occur at the interface between a sliding pair of materials caused by interfacial shear. The mechanical force destabilizes the electronic structure of pre-existing bonds to facilitate a chemical reaction. Processes such as mechanical alloying, tribochemistry and wear are dominated by mechanical phenomena [1] and it is observed that antiwear films are formed from the surface reaction of additives that are included in the lubricant during the rubbing process [2, 3]. This was illustrated

in the previous chapter for the gas-phase lubrication of copper by dimethyl disulfide where the sulfur formed by methyl thiolate decomposition reacts with copper to form a metastable CuS_x film. This reaction is initiated by surface-to-bulk transport of sulfur under the influence of mechanical shear [4], where a tungsten carbide tribopin is used for shearing. The sulfur transport kinetics on copper samples annealed at different temperature (500, 850, or 1020 K) were observed to be influenced by the grain sizes in the copper substrate during rubbing experiments conducted by a tungsten carbide tribopin cleaned by e-beam heating to remove any carbonaceous deposits from the surface (Chapter 3).

The different grain sizes for copper samples annealed at different temperatures as reported in Chapter 3 are expected to be correspondingly similar for different samples used in the work described in this Chapter, where copper samples are rubbed with an untreated tungsten carbide tribopin. Since the tribopin was used multiple times for rubbing the DMDS dosed copper surface, the untreated tungsten carbide tribopin will have a carbonaceous carbon layer deposited on its surface. Previous studies have shown that a graphitization of amorphous carbon occurs during the shearing at a sliding interface [5], so that it is expected that the untreated tribopin is covered by a graphitic layer if it is not cleaned periodically. The presence of graphitic carbon on surface of the tribopin can play significant role in reducing the friction coefficient (CoF) [6–8] so that it is anticipated that the nature of the tribopin surface can influence the

rate of mechanochemical reactions caused by shearing.

To investigate the possible effect of the nature of tribopin on the surface-to-bulk transport of sulfur on DMDS-covered copper, experiments to measure the sulfur transport rate, methyl thiolate decomposition rate and friction were performed and discussed further in this chapter.

4.2 Experimental

Tribological measurements were carried out in a stainless-steel, ultrahigh vacuum (UHV) chamber operating at a base pressure of ~ 2×10^{-10} Torr following bakeout, which has been described in detail elsewhere [9]. Briefly, the chamber was equipped with a UHV-compatible tribometer, which simultaneously measures normal load, lateral force and the contact resistance between the tip and substrate. All tribological measurements were made with sliding speed of ~ 4×10^{-3} m/s at a normal load of 0.44 N. Previous work has shown that the maximum interfacial temperature rise for a copper sample under these conditions is much less than 1 K [4]. The spherical tribopin (~ 1.27×10^{-2} m diameter) was made from tungsten carbide containing some cobalt binder. Although the pin could be heated by electron bombardment in vacuo or by Argon ion bombardment in order to clean the surface, the experiments described here were performed without cleaning the pin to allow a carbonaceous layer to be deposited on the surface

of the pin. The pin was attached to a tribo-arm that contained strain gauges to enable the normal and lateral forces to be measured. The tribo-arm was mounted to a rotatable 2¾" Conflat® flange to allow the pin to be rotated to face the cylindrical mirror analyzer (CMA) to enable Auger spectra of the pin surface to be obtained.

The chamber contained a single-pass CMA for Auger analysis, and an Argon ion bombardment source for sample cleaning and depth profiling. Auger spectra were collected using an electron beam energy of 5 kV. A high-resolution electron gun and a channeltron secondary electron detector were also incorporated into the vacuum chamber to allow scanning electron microscopy (SEM) images of the sample, and in particular of the wear track, to be collected. It also enabled Auger elemental profiles to be obtained across the rubbed regions to measure the loss of sulfur from the surface as a function of the number of times that the sample had been rubbed. To ensure that the sulfur signal was being measured only in the rubbed region and to exclude any influence from the signals from the unrubbed region, calibration experiments were carried out to test the spatial resolution by attaching a 100-μm diameter silver wire to the copper sample and by detecting Auger signals due to silver. Since the wear tracks formed during rubbing the copper sample are ~100 μm across, this experiment provides information on the spatial resolution of electron beam [4]. Auger concentration profiles across the rubbed region were measured either by moving the sample laterally by translating the precision manipulator to which the copper sample was mounted,

or by deflecting the electron beam by using capacitor plates incorporated in the high-resolution electron gun. Both methods yielded identical results for the variation in Auger signal as a function of the number of times that it had been rubbed. Finally, the chamber also included a quadrupole mass spectrometer for leak checking, for gauging reactant purity and to collect the gas-phase products produced during the unidirectional sliding of pin away from the mass spectrometer.

Experiments were performed by initially rubbing the tribopin against the clean copper sample (~ 1.7×1.7 cm^2 by ~ 1 mm thick) until a constant friction coefficient was obtained. This resulted in the formation of a wear track. The DMDS was dosed through a leak valve connected to a dosing tube (with an internal diameter of 4×10^{-3} m) directed towards the sample so that the pressure at the sample is enhanced compared to the measured background pressure, which was set at 1×10^{-8} Torr during DMDS dosing (where pressures are not corrected for ionization gauge sensitivity). During the unidirectional sliding of the pin over the DMDS-dosed wear track, the 16 amu mass spectrometer fragment of the evolving gas-phase products was monitored by using a UTi quadrupole mass spectrometer located inside the vacuum chamber and placed close to and in-line-of-sight of the rubbing interface.

The copper samples (Fisher Scientific, 99.99% pure, 1 mm thick) were polished to a mirror finish using 1 μm diamond paste and then rinsed with deionized water and degreased ultrasonically in acetone. The copper samples were cleaned using a standard

procedure which consisted of Argon ion bombardment (~ 1 kV, ~ 2 μ A/cm^2) and annealing cycles up to various temperatures of ~ 500, 850 or 1020 K. As discussed in chapter 3, this resulted in different grain sizes and thus in different mechanical properties of the sample. The cleanliness of the samples was monitored using Auger spectroscopy.

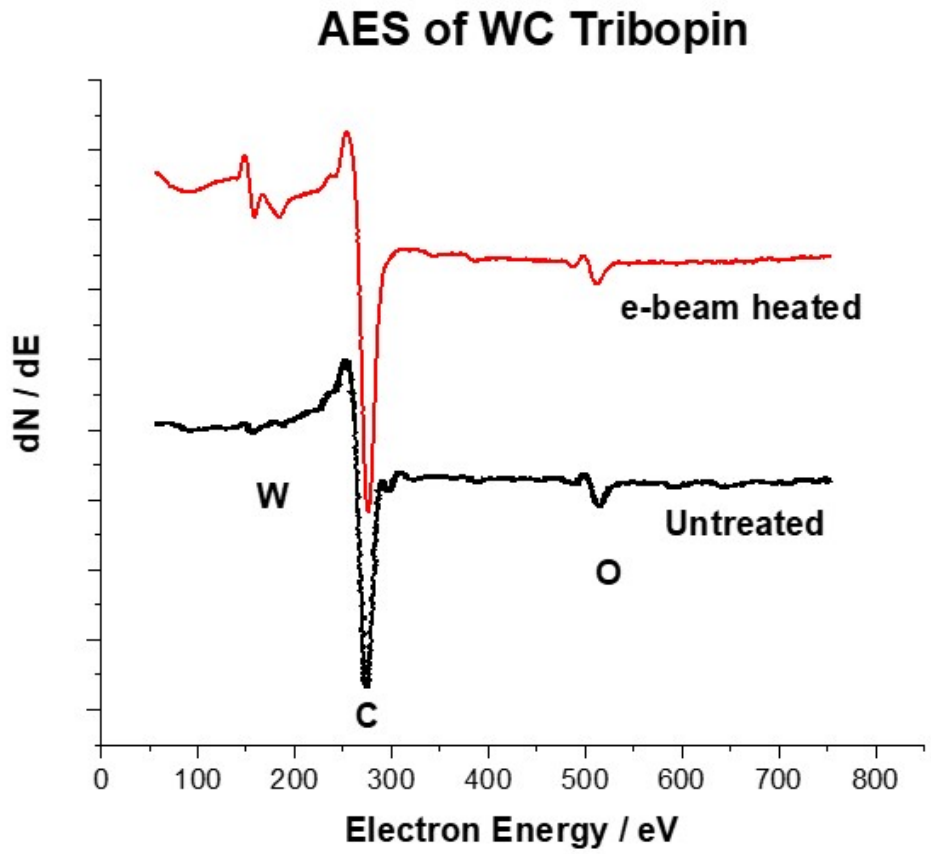

FIGURE 4.1: Comparison of the Auger spectra of the tribopin; the red (top) spectrum is collected after e-beam heating and the black (lower spectrum) is for the untreated tibopin. Less W is detected in untreated tribopin and graphitic carbon is profoundly dominant in the untreated tribopin.

4.3 Results

4.3.1 Analysis of the surface of the tribopin

Irradiating a surface with an electron beam excite surface atoms to produces energetic electrons and the kinetic energy (eV) of these electrons is measured to produce an Auger spectrum [10]. Auger spectra of a treated and untreated tribopin are shown in Figure 4.1, where it is clear that the cleanliness of the untreated tribopin is different from the e-beam-heated tribopin. The Auger spectrum of the untreated tribopin shows a very small W (NNN) peak at ~163 eV [11–13] kinetic energy (KE) compared with the cleaned tribopin. The C (KLL): W_{163} (NNN) ratio of an untreated tribopin is ~33.3, but for e-beam heated tribopin it is reduced to ~6.2. This indicates that the untreated tribopin is abundantly covered with graphitic carbon, where the graphitic carbon is formed on shearing the tungsten carbide tribopin on a DMDS-dosed copper surface [5].

4.3.2 Methyl thiolate decomposition rate on copper samples annealed at 500, 850, and 1020 K with graphitic carbon-covered tribopin

To understand the surface-to-bulk sulfur transport mechanism, the rate of shear-induced methyl thiolate decomposition was measured from the rate of methane evolution during sliding (Figure 4.2). The tribopin was slid away from the mass spectrometer, while the 16 amu mass spectrometer fragment signal was monitored until the 7^{th} pass of the pin over the sample. Rates of methyl thiolate decomposition were calculated by plotting $n-1$ against ln(Methane Yield), where the methane yield was measured from the 16 amu mass spectrometer intensity and n is the number of passes [14]. The inset in Figure 4.2 shows that the rate of methyl thiolate decomposition obeys first-order kinetics. The first-order rate constants are summarized in Table 4.1 as a function of dimethyl disulfide doses and copper sample annealing temperatures, where the rates vary slightly. A slightly decreased rate was observed for an increased dose within the same copper sample, and the methyl thiolate decomposition rate slightly increased in the order of sample annealing temperatures: 500<850<1020 K, for the annealed copper samples.

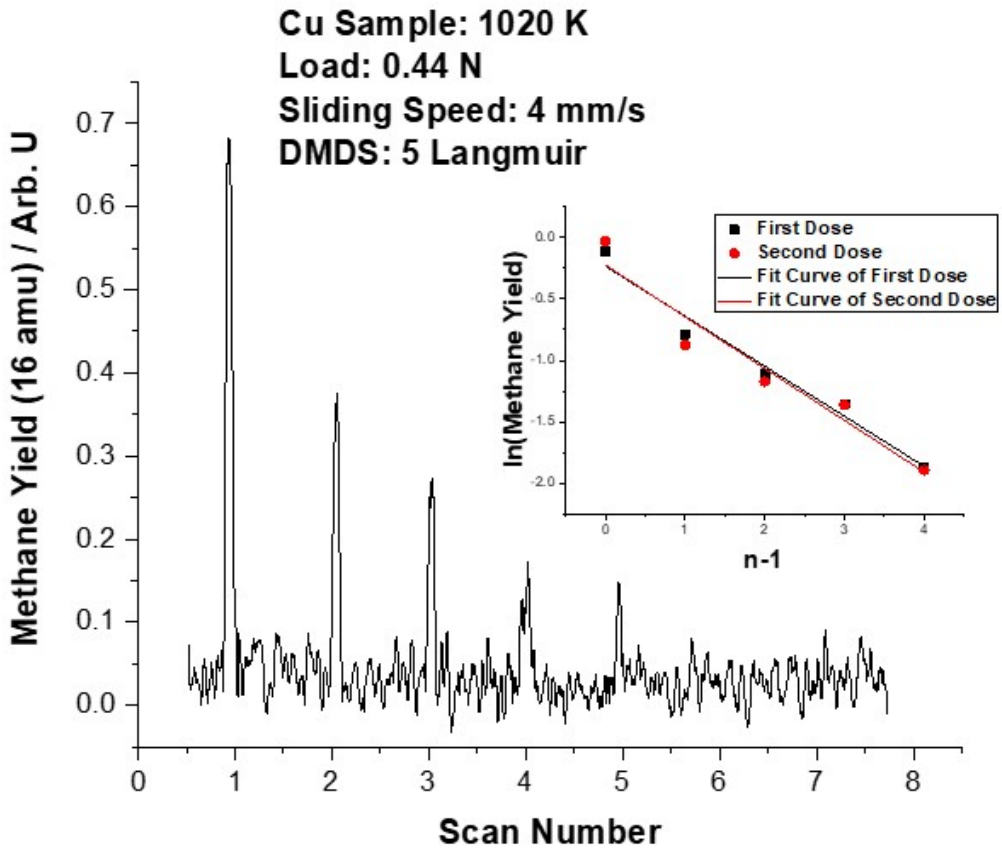

FIGURE 4.2: The desorption of methane from a methyl thiolate overlayer (formed from 5 L exposure to DMDS) on copper that had been annealed to 1020 K. The inset shows a plot of ln(Methane Yield) versus $n-1$, where n is the number of passes, indicative of a first-order reaction.

Annealing Temperature/K	**500**	**850**	**1020**
Dose/L	Rate/pass	Rate/pass	Rate/pass
1	0.52±0.04	0.58±0.07	-
2	0.42±0.03	0.51±0.05	0.45±0.03
5	0.35±0.06	0.41±0.04	0.41±0.05
10	0.36±0.03	0.40±0.03	0.41±0.03

TABLE 4.1: Rate constants for shear-induced methyl thiolate decomposition on copper.

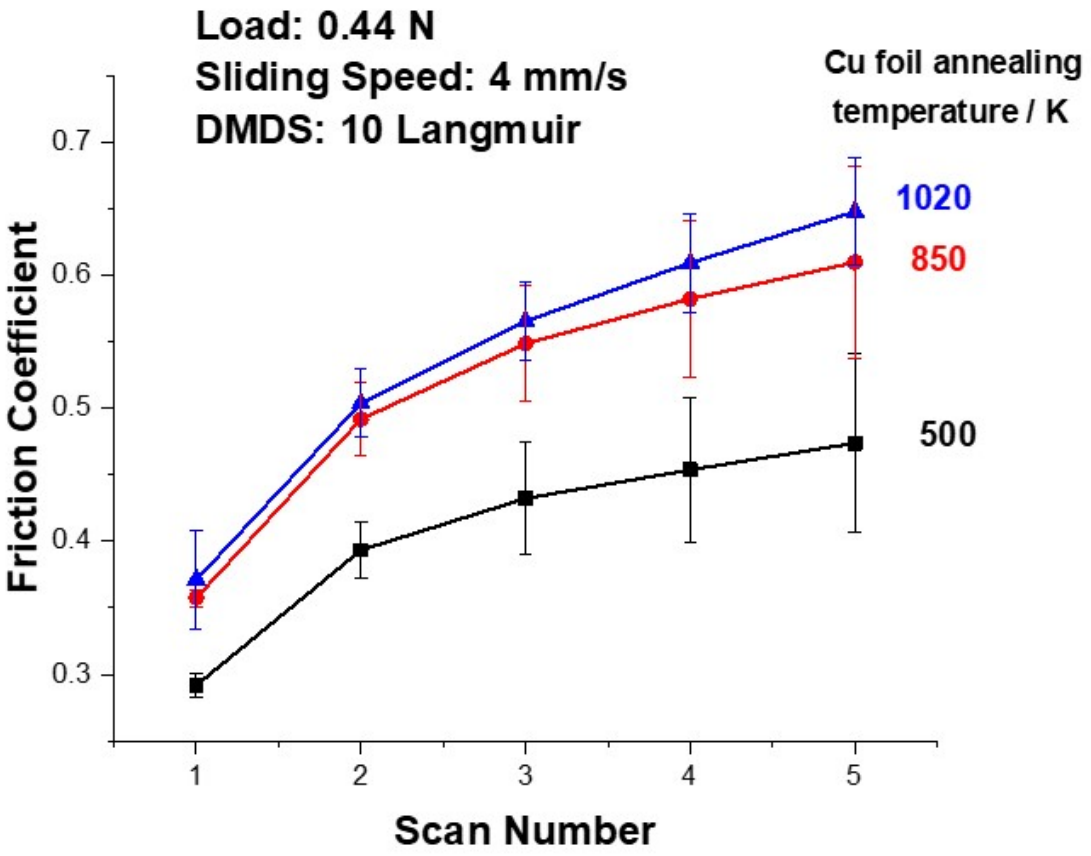

FIGURE 4.3: Plot of the relative friction coefficient measured with 10 Langmuir of DMDS on the copper samples that had been rubbed at an applied normal load of 0.44 N and a sliding speed of 4×10^{-3} m/s after being cleaned and annealed at 500 (■), 850 (●), or 1020 (▲) K.

4.3.3 Friction coefficient and average roughness of copper samples

The friction coefficients (CoF) of copper samples annealed at different temperatures during cleaning were measured by sliding the tribopin against the DMDS-covered copper samples. For a sample dosed with 10 L of DMDS, the measured CoF increases monotonically with the number of times that the sample was rubbed until the 5^{th} pass

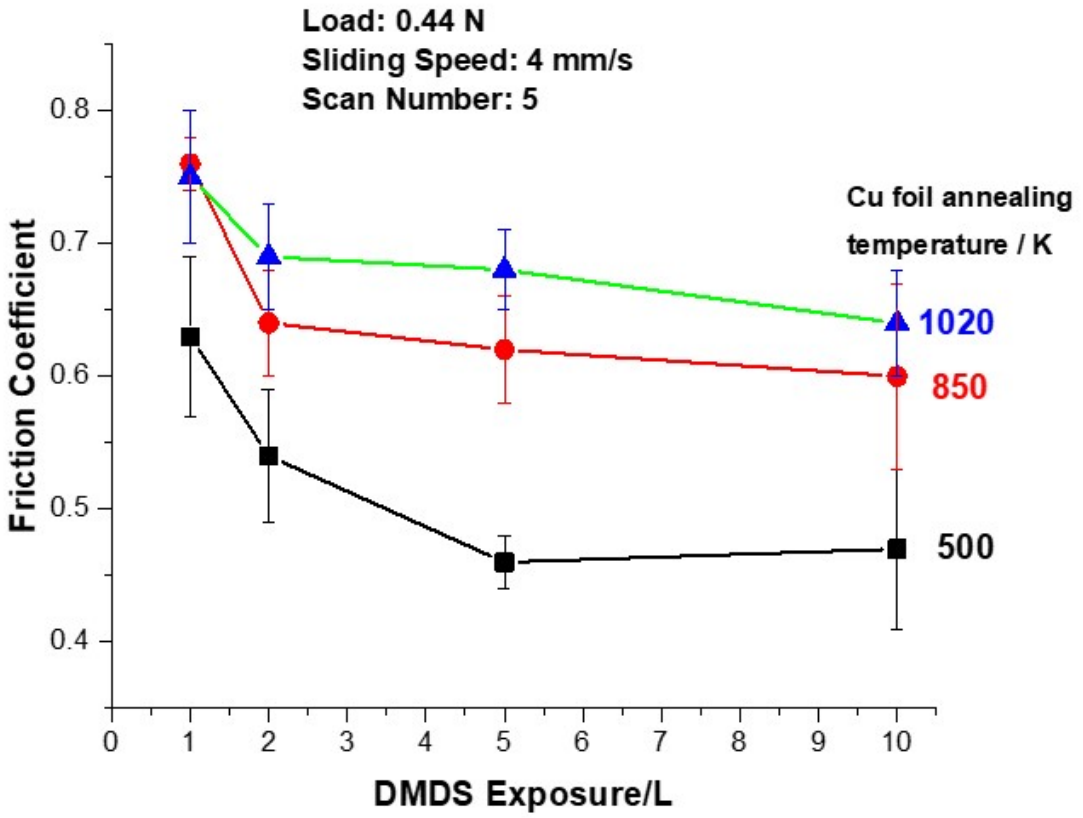

FIGURE 4.4: Plot of the relative friction coefficient measured at 5^{th} scan with 1, 2, 5, and 10 Langmuir of DMDS exposure on the copper samples that had been rubbed at an applied normal load of 0.44 N and a sliding speed of 4×10^{-3} m/s after being cleaned and annealed at 500 (■), 850 (●), or 1020 (▲) K.

as illustrated in Figure 4.3. The trend in CoF as a function of the number of scans as illustrated in Figure 4.3 is maintained for all copper samples for that have been dosed with 1, 2, or 5 L of DMDS (Table 4.2). Similarly, for 500, 850, or 1020 K annealed copper samples exposed to 1, 2, 5, or 10 L of DMDS, the measured friction coefficients after the 5^{th} pass (Figure 4.4) show that the CoF decreases with increased DMDS exposure, and

the lowest CoF was observed in the 500-K annealed copper samples. Also, the average roughness (Ra) measured for copper samples after being cleaned and annealed at 500, 850, or 1020 K shows that roughness increases with sample annealing temperature as depicted in Figure 4.5.

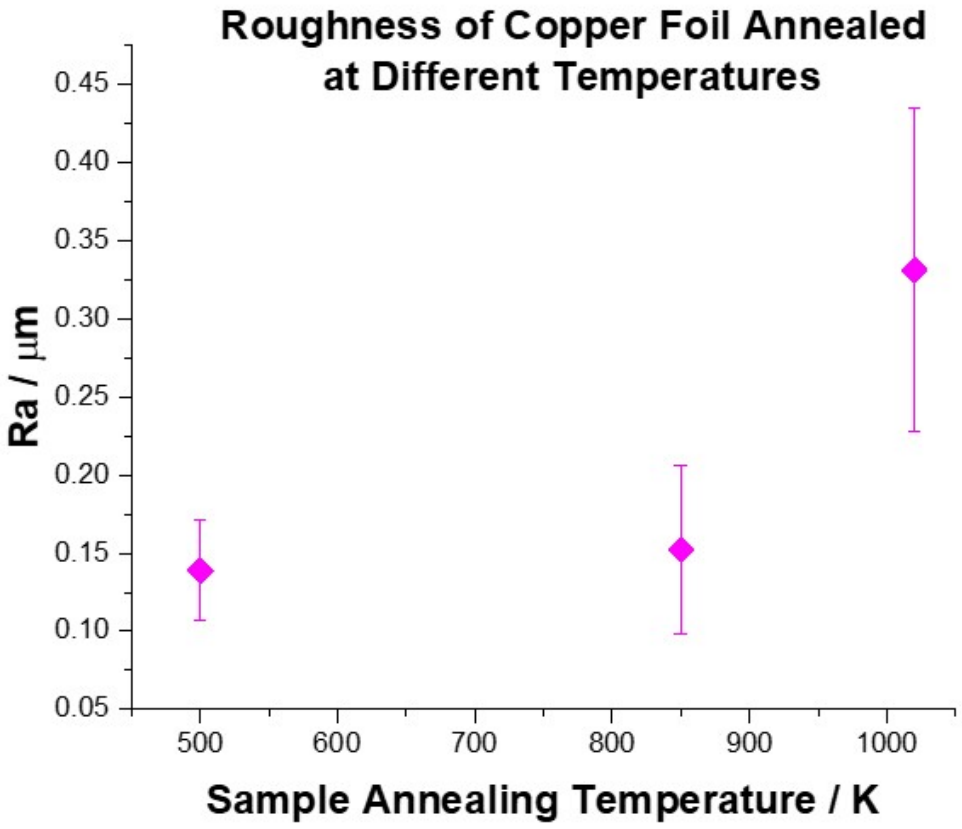

FIGURE 4.5: Plot of average roughness (Ra) measured on copper samples after being cleaned and annealed at 500, 850, or 1020 K measured using a confocal laser microscope (♦).

500 K				
Scan Number	**CoF (1 L)**	**CoF (2 L)**	**CoF (5 L)**	**CoF (10 L)**
1	0.43±0.01	0.38±0.01	0.30±0.01	0.29±0.01
2	0.53±0.04	0.43±0.04	0.39±0.01	0.39±0.02
3	0.56±0.05	0.47±0.05	0.42±0.01	0.43±0.04
4	0.60±0.05	0.50±0.05	0.44±0.01	0.45±0.04
5	0.63±0.05	0.54±0.05	0.48±0.02	0.47±0.05
850 K				
Scan Number	**CoF (1 L)**	**CoF (2 L)**	**CoF (5 L)**	**CoF (10 L)**
1	0.55±0.01	0.40±0.01	0.41±0.01	0.35±0.01
2	0.69±0.01	0.53±0.01	0.55±0.01	0.49±0.02
3	0.73±0.01	0.58±0.02	0.60±0.01	0.54±0.04
4	0.76±0.02	0.61±0.03	0.64±0.03	0.58±0.05
5	0.78±0.02	0.64±0.04	0.62±0.04	0.60±0.04
1020 K				
Scan Number	**CoF (1 L)**	**CoF (2 L)**	**CoF (5 L)**	**CoF (10 L)**
1	0.39±0.03	0.36±0.03	0.38±0.01	0.37±0.03
2	0.51±0.05	0.49±0.03	0.54±0.02	0.50±0.02
3	0.64±0.05	0.60±0.03	0.63±0.02	0.56±0.02
4	0.66±0.05	0.65±0.03	0.67±0.03	0.60±0.03
5	0.70±0.05	0.69±0.04	0.71±0.03	0.64±0.04

TABLE 4.2: Friction coefficients measured for first 5 scans after dosing with 1, 2, 5, or 10 Langmuir of DMDS on the copper samples that had been rubbed at an applied normal load of 0.44 N and a sliding speed of 4×10^{-3} m/s after being cleaned and annealed at 500, 850, or 1020 K.

4.3.4 Measurement of the kinetics of surface-to-bulk sulfur transport with graphitic carbon-covered tribopin

The sulfur transport experiments were conducted by rubbing a carbonaceous- (graphitic) film-covered tungsten carbide tribopin on a copper sample dosed with a low coverage (2 Langmuir(L) exposure) of DMDS (Figure 4.6) and revealed that the rates of surface-to-bulk sulfur transport are essentially identical for all copper samples annealed to 500,

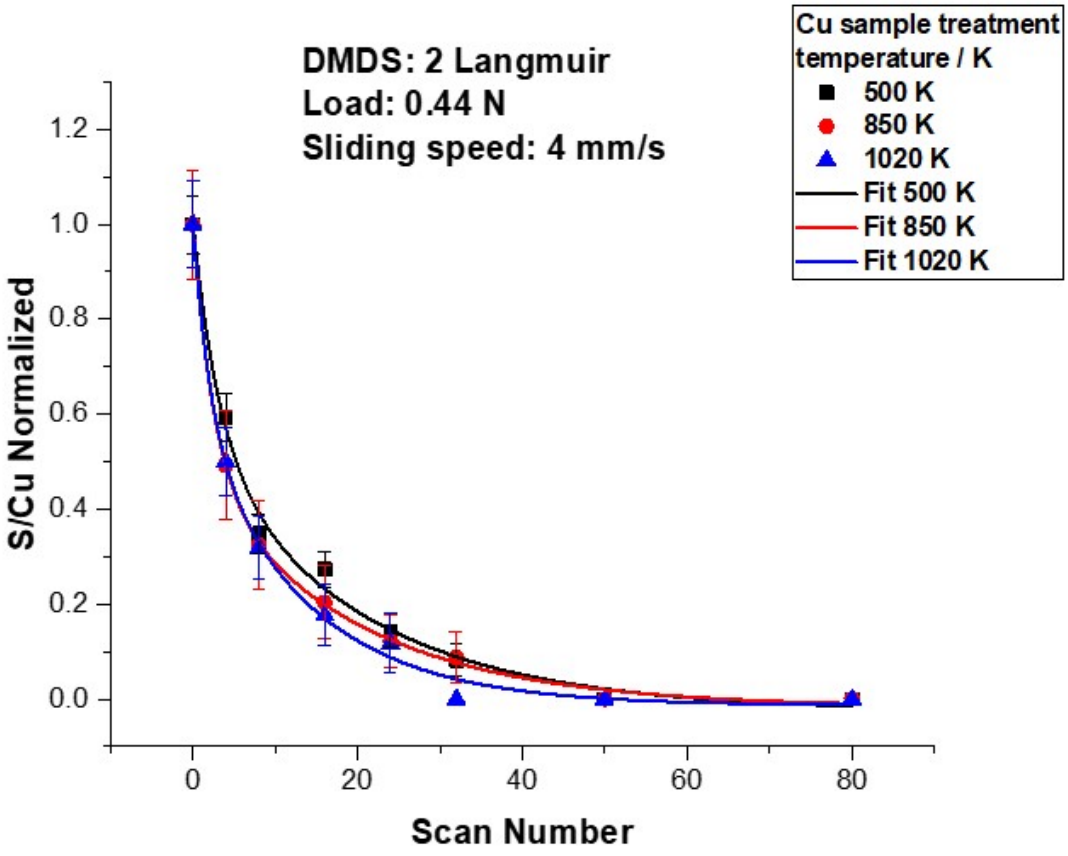

FIGURE 4.6: Plot of the relative sulfur to copper (S/Cu) Auger ratio measured inside the wear track as a function of the number of times that the copper samples had been rubbed at an applied normal load of 0.44 N and a sliding speed of 4×10^{-3} m/s after being cleaned and annealed at 500 (■), 850 (●), and 1020 (▲) K.

850 and 1020 K. Note that this result is different from that obtained with a cleaned tribopin (Chapter 3). Similar experiments were conducted with a copper sample dosed with a higher exposure (10 L) of DMDS and now different surface-to-bulk sulfur transport rates were measured on copper samples annealed at different temperatures. The results are displayed in Figure 4.7 and the transport rates vary in the order of sample

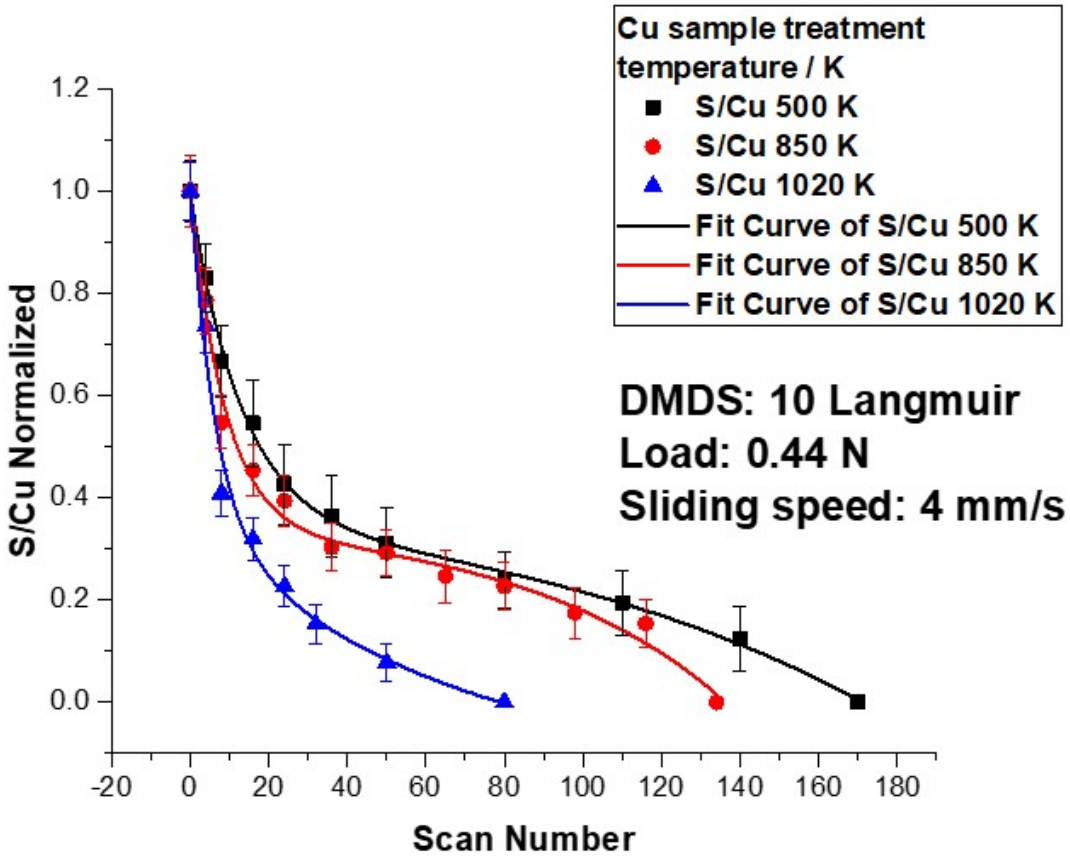

FIGURE 4.7: Plot of the relative sulfur to copper (S/Cu) Auger ratio measured inside the wear track as a function of the number of times that the copper samples had been rubbed at an applied normal load of 0.44 N and a sliding speed of 4×10^{-3} m/s after being cleaned and annealed at 500 (■), 850 (●), and 1020 (▲) K.

annealing temperature as 500<850<1020 K. The observed variation in sulfur signal as a function of the number of scans depends not only on the surface-to-bulk diffusion rate but also on the methyl thiolate decomposition rates, which were also measured using the graphitic carbon-covered tribopin. Since the transport rate may also depend on the adsorbate, the friction coefficients were also measured, and the results are described in

section 4.3.3.

4.4 Discussion

The experiments performed with a tribopin cleaned by e-beam heating leaves very little or no graphitic-carbon on the counter surface of the tribopin as evidenced by the measured C (KLL): W_{163} (NNN) Auger ratio (Fig 4.1). Here experiments were carried out using graphite-covered tribopin.

The measured kinetics of sheared-induced formation of a metastable copper sulfide phase on copper annealed at 500, 850, or 1020 K did not follow the trend that was observed previously with a cleaned tribopin as discussed in Chapter 3. The mechanical properties of the copper sample substrates used in this experiment are identical to those reported in Chapter 3 because the copper samples were treated to 500, 850, or 1020 K during the sample cleaning procedure in both sets of experiments. Therefore, it is believed that the nature of the pin plays a significant role in influencing the surface-to-bulk sulfur transport rates.

Graphitic carbon present on the tribopin plays a significantly different role from an electron-beam heated tungsten carbide tribopin on the surface-to-bulk transport of sulfur into the copper. This graphitic layer is developed from the repeated rubbing of the tribopin on DMDS-dosed copper samples and the graphitic carbonaceous

layer remains if not cleaned by heating or ion bombardment. The graphitic carbon plays a significant role in the reduction of the friction coefficient [6–8]. The measured friction coefficients for the three different copper samples with the same methyl thiolate coverages on the copper surface revealed that highest CoF was observed in a 1020-K annealed copper sample, where the trend of CoF was observed to be in the order: CoF_{1020}>CoF_{850}>CoF_{500} K, (Figures 4.3 and 4.4). The methyl thiolate decomposition rates and surface-to-bulk sulfur transport rates are the most rapid on the high-temperature annealed copper samples because of the severe contact between the graphitic carbon-covered tungsten carbide tribopin and copper sample. Further, it is evident that, from Figure 4.5, the average roughness of the copper substrate increases with increasing annealing temperature. The increased roughness on the copper samples contributes to induce higher friction coefficients. It is reported that the CoF increases as roughness increases, where asperity interlocking occurs [17, 18]. The increased CoF on high-temperature-annealed copper samples indicates that the contact conditions are more severe at the interface of copper samples that had been annealed to higher temperature annealed samples, so that for high DMDS-dose (10 L DMDS dose) the methyl thiolate decomposition and surface-to-bulk sulfur transport rates vary in the order of copper annealing temperatures as: 1020>850>500 K.

For a 2 L DMDS dose, the sulfur transport rates are similar for all sample as shown in Figure 4.6. Differences in sulfur transport rates are observed for a 10-L DMDS dosed

sample where the surface-to-bulk sulfur transport experiments show that the rates vary with sample annealing temperature as in the order of annealing temperature as 1020>850>500 K. This indicates that the methyl thiolate coverage plays a significant role in the sulfur transport rates. After the 5^{th} pass over the surface, a higher friction coefficient was observed for a 2-L-DMDS dosed sample (as shown in Fig. 4.4), where the methyl thiolate coverage is low. On the other hand, the sulfur transport rates observed for a higher methyl thiolate coverage (for a 10 L DMDS dose), are influenced by the methyl thiolate coverage in the wear track, which helps to decrease the friction and leads to differences in the sulfur transport rates for the different copper samples (Table 4.1), where the methyl thiolate decomposition rates are faster with a low methyl thiolate coverage, where faster surface-to-bulk sulfur transport rates are observed in 2 L DMDS-dosed copper samples compared to 10 L DMDS-dosed copper samples. For a high methyl thiolate coverage (10 L DMDS-dose), the methyl thiolate decomposition rates are slower in low-temperature-annealed copper samples compared to high-temperature-annealed copper samples. This suggests that, in high-temperature-annealed copper samples, sulfur becomes readily available to be transported as soon as the methyl thiolate decomposition reaction is complete, and sulfur is transported into the bulk [14–16].

4.5 Conclusions

Measurements of the rates of the surface-to-bulk transport of sulfur and methyl thiolate decomposition were carried out by rubbing a graphitic carbon-covered tribopin on different-temperature-annealed-copper samples. It is found that the roughness of the samples increases with annealing temperature, where methyl thiolate decomposition rates increase with higher roughness on the surface of the samples. Faster surface-to-bulk sulfur transport rates are accompanied by higher methyl-thiolate decomposition rates. Thus, the overall order of sulfur transport rates, methyl thiolate decomposition rates and the roughness of the copper samples are observed to be in the order of annealing temperature as: 500<850<1020 K. The results show that the surface-to-bulk sulfur transport rates are influenced by the nature of the tribopin since the rates measured using a graphitic-carbon-covered tribopin are different from the sulfur-transport rates measured by using the tungsten carbide tribopin, where the results are discussed in Chapter 3.

References

[1] M. A. Meyers, A. Mishra, and D. J. Benson, "Mechanical properties of nanocrystalline materials," *Progress in Materials Science*, vol. 51, no. 4, pp. 427–556, 2006.

[2] M. Pouryazdan, B. J. Kaus, A. Rack, A. Ershov, and H. Hahn, "Mixing instabilities during shearing of metals," *Nature Communications*, vol. 8, no. 1, pp. 1–7, 2017.

[3] C. Suryanarayana, "Mechanical alloying and milling," *Progress in Materials Science*, vol. 46, no. 1-2, pp. 1–184, 2001.

[4] O. J. Furlong, B. P. Miller, and W. T. Tysoe, "Shear-induced surface-to-bulk transport at room temperature in a sliding metal-metal interface," *Tribology Letters*, vol. 41, no. 1, pp. 257–261, 2011.

[5] K. Oohashi, T. Hirose, and T. Shimamoto, "Shear-induced graphitization of carbonaceous materials during seismic fault motion: Experiments and possible implications for fault mechanics," *Journal of Structural Geology*, vol. 33, no. 6, pp. 1122–1134, 2011.

[6] H. Sarmadi, A. Kokabi, and S. S. Reihani, "Friction and wear performance of copper–graphite surface composites fabricated by friction stir processing (FSP)," *Wear*, vol. 304, no. 1-2, pp. 1–12, 2013.

[7] L. Su, F. Gao, X. Han, R. Fu, and E. Zhang, "Tribological behavior of copper–graphite powder third body on copper-based friction materials," *Tribology Letters*, vol. 60, no. 2, p. 30, 2015.

[8] A. Senouci, J. Frene, and H. Zaidi, "Wear mechanism in graphite–copper electrical sliding contact," *Wear*, vol. 225, pp. 949–953, 1999.

[9] F. Gao, O. Furlong, P. V. Kotvis, and W. Tysoe, "Pressure dependence of shear strengths of thin films on metal surfaces measured in ultrahigh vacuum," *Tribology Letters*, vol. 31, no. 2, p. 99, 2008.

[10] P. Auger, "Sur l'effet photoélectrique composé," *Journal de Physique et le Radium*, vol. 6, no. 6, pp. 205–208, 1925.

[11] T. Haas, J. Grant, and G. Dooley, "Auger-electron spectroscopy of transition metals," *Physical Review B*, vol. 1, no. 4, p. 1449, 1970.

[12] A. Hoffman, P. Evans, D. Cohen, and P. Paterson, "Compaction, distribution, and chemical bonding of tungsten-implanted glassy carbon," *Journal of applied physics*, vol. 72, no. 12, pp. 5687–5694, 1992.

[13] C. Powell, "Recommended auger-electron kinetic energies for 42 elemental solids," *Journal of Electron Spectroscopy and Related Phenomena*, vol. 182, no. 1-2, pp. 11–18, 2010.

[14] H. L. Adams, M. T. Garvey, U. S. Ramasamy, Z. Ye, A. Martini, and W. T. Tysoe, "Shear-induced mechanochemistry: pushing molecules around," *The Journal of Physical Chemistry C*, vol. 119, no. 13, pp. 7115–7123, 2015.

[15] H. Adams, B. P. Miller, P. V. Kotvis, O. J. Furlong, A. Martini, and W. T. Tysoe, "In situ measurements of boundary film formation pathways and kinetics: dimethyl and diethyl disulfide on copper," *Tribology Letters*, vol. 62, no. 1, p. 12, 2016.

[16] H. Adams, B. P. Miller, O. J. Furlong, M. Fantauzzi, G. Navarra, A. Rossi, Y. Xu, P. V. Kotvis, and W. T. Tysoe, "Modeling mechanochemical reaction mechanisms," *ACS applied materials & interfaces*, vol. 9, no. 31, pp. 26531–26538, 2017.

[17] H. Song, R. Dikken, L. Nicola, and E. Van der Giessen, "Plastic ploughing of a sinusoidal asperity on a rough surface," *Journal of Applied Mechanics*, vol. 82, no. 7, 2015.

[18] I. Ford, "Roughness effect on friction for multi-asperity contact between surfaces," *Journal of Physics D: Applied Physics*, vol. 26, no. 12, p. 2219, 1993.

Chapter 5

Tribochemical Reaction Pathways of Carboxylic Acid Monolayers on Copper in Ultrahigh Vacuum

5.1 Introduction

Fatty acids are often used as so-called friction modifiers to lubricants to reduce friction by forming an adsorbed overlayer on the surface [1–4] and often consist of long-chain carboxylic acids (fatty acids) in which the carboxylate group binds to the substrate, thereby exposing a weakly interacting carbonaceous outer surface. This overlayer can be removed during the sliding process but is then replenished from the lubricant and thus has the advantage of providing a self-healing film.

In some cases, tribochemical reactions of the adsorbed layer can form low-friction carbonaceous surfaces [1, 3, 5–7] and thus, in this case, act as chemically reactive additives. The mechanism of operation of such fatty acid lubricant additives on tetrahedral

amorphous carbon (ta-C) and the role of carbon-carbon double bonds on the reaction pathway have been investigated theoretically using a combination of molecular dynamics (MD) simulations with a reactive potential, combined with first-principles density functional theory (DFT) calculations [2]. These simulations reveal that carboxylic acid binds via the -COOH functionality, but the presence of a vinyl group in the carbonaceous chain can influence the tribochemical reactivity by binding to the moving counterface. Interestingly, the conformation of the chain and the resulting steric ability of the vinyl group to interact with the counter-surface is found to influence the rate of tribofilm formation. Thus, the adsorbed reactant (the fatty acid) can bind both to the substrate via an attachment point (AP) and to the moving counterface at a pulling point (PP) where the strengths of AP and PP binding relative to the activation energy of tribochemical reaction is likely to control the reactivity [8]; for example, interactions with the counterface have recently been suggested to play a role in the mechanochemical etching of silicon [9]. These ideas are tested in the following by selecting molecules that tune the PP functionality while keeping the AP interaction constant using carboxylic acids adsorbed on a copper substrate, which bind strongly to the surface a bidentate η^2 configuration as a carboxylate [10, 11], while sliding against a tungsten carbide counterface that can bind to a terminal vinyl group.

This mechanochemistry is investigated by adsorbing various carboxylic acids onto copper; 7-octenoic acid (a C_8 hydrocarbon with a terminal C=C group), octanoic acid

(with a C_8 alkyl chain), heptanoic acid (with a C_7 alkyl chain), and 6-heptenoic acid (with a C_7 terminal vinyl group). As will be shown below, the carbon chain length influences the orientation of the terminal vinyl group relative to the surface and thereby its potential ability to interact with the (tungsten carbide) counterface. In addition to the hardness of tungsten carbides that will not wear when rubbed against copper, tungsten and molybdenum carbides have been suggested to have catalytic properties akin to those found for noble metals (platinum and palladium) [12–14], and this concept has been borne out by UHV surface studies [15, 16], implying that the vinyl groups will bind to the surface of the tribopin.

Carboxylic acids bind to copper via the formation of acetate species [10] and decompose via the evolution of carbon dioxide with the simultaneous formation of hydrocarbon fragments at temperature between 570 and 580 K in temperature-programmed desorption [17–20]. The MD simulations referred to above indicate that fatty acids react during sliding by the acid group interacting with the surface and subsequently undergoing cross-linking reactions with the counterface to enable high forces to be exerted on the molecule, leading to its rapid decomposition. Note that this process differs from the copper-tungsten carbide interface investigated here because, in this case the carboxylic acid is pre-adsorbed on copper rather than being allowed to react at the sliding interface. The simulations indicate that the reaction is initiated by the decomposition of the carboxylate group to form carbon monoxide and adsorbed atomic oxygen,

in contrast to the thermal chemistry found on copper. The repeated rupture and cross-linking of the resulting carbonaceous fragments lead to the formation of shorter-chains hydrocarbons and the eventual passivation of the surface.

5.2 Experimental

Experiments were carried out in two stainless-steel, ultrahigh vacuum (UHV) chambers operating at a base pressure of $\sim 2 \times 10^{-10}$ Torr following bakeout, one for surface analyses of the carboxylic acids [21] and the second for tribological measurements [22]. Briefly, the tribology chamber was equipped with a UHV-compatible tribometer, which simultaneously measures normal load, lateral force and the contact resistance between the tip and substrate. All tribological measurements were made using a sliding speed of $\sim 4 \times 10^{-3}$ m/s at a normal load of 0.44 N. Previous work has shown that the maximum interfacial temperature rise for a copper sample under these conditions is much less than 1 K [23]. The spherical tribopin ($\sim 1.27 \times 10^{-2}$ m diameter) was made from tungsten carbide containing some cobalt binder and could be heated by electron bombardment in *vacuo* or by Argon ion bombardment in order to clean it. The pin was attached to an arm that contained strain gauges to enable the normal and lateral forces to be measured. The arm was mounted to a rotatable 2¾″ Conflat® flange to allow the pin to be rotated to face the cylindrical mirror analyzer (CMA) to enable Auger spectra of the pin surface to be obtained. Additional experiments were carried out by

analyzing the tungsten carbide pin by X-ray photoelectron spectroscopy after Argon ion bombardment using a spectrometer containing a hemispherical analyzer built by ThermoFisher (220i) with a focused monochromatic X-Ray source.

The copper samples (Alfa Aesar, 99.99% pure, 1 mm thick) were polished to a mirror finish using 1 μm diamond paste and then rinsed with deionized water and degreased ultrasonically in acetone before mounting in the UHV chamber. The copper was cleaned using a standard procedure which consisted of Argon ion bombardment (~1 kV, ~2 $\mu A/cm^2$) and annealing cycles and the cleanliness of the samples was monitored using Auger spectroscopy.

The tribometer chamber contained a single-pass CMA for Auger analysis, and an Argon ion bombardment source for sample cleaning and depth profiling. Auger spectra were either collected using the coaxial electron gun in the CMA with an electron beam energy of 3 kV or with a Staib model EK050M2 Microfocus electron gun. The chamber is also equipped with a channeltron secondary electron detector which allowed scanning electron microscopy (SEM) images of the wear scar to be collected using the high-resolution electron gun, which also enabled Auger elemental profiles to be obtained across the rubbed regions.

Experiments were performed by initially rubbing the tribopin against the clean copper sample (~1.7 × 1.7 cm^2 by ~1 mm thick) until a constant friction coefficient was

obtained. This resulted in the formation of a wear track. The carboxylic acids were dosed through a Knudsen source connected to a dosing tube (with an internal diameter of 4.0×10^{-3} m) directed towards the sample so that the pressure at the sample is enhanced compared to the measured background pressure, where pressures are not corrected for ionization gauge sensitivity.

Infrared spectra and temperature-programmed desorption (TPD) data were collected in a chamber operating at base pressures of $\sim 1 \times 10^{-10}$ Torr following bakeout and has been described in detail elsewhere [21]. RAIRS data were collected with a Bruker Equinox spectrometer, typically for 1000 scans at a resolution of 4 cm^{-1}. TPD experiments were carried out in another chamber that was equipped with a Dycor quadrupole mass spectrometer interfaced to a computer that allowed up to six masses to be sequentially monitored in a single experiment. The sample could be cooled to 80 K in both chambers by thermal contact to a liquid-nitrogen-filled reservoir and resistively heated to ~1200 K.

The 7-octenoic acid (Aldrich, ≥97.0% purity), octanoic acid (Aldrich, ≥98.0% purity), 6-heptenoic acid (Aldrich, ≥99.0% purity), and heptanoic acid (Aldrich, ≥99.0% purity) were transferred to glass bottles and attached to the gas-handling system of the vacuum chamber, where it was subjected to several freeze-pump-thaw cycles.

Density functional theory (DFT) calculations were performed with the projector

augmented wave (PAW) method [24, 25] as implemented in the Vienna ab initio simulation package, VASP [26–28]. The exchange-correlation potential was described using the generalized gradient approximation (GGA) of Perdew, Burke and Ernzerhof [29]. A cutoff of 400 eV was used for the plane wave basis set, and the wavefunctions and electron density were converged to within ~ 1×10^{-5} eV. The first Brillouin zone was sampled with a 4×4×1 Γ-centered k-point mesh. Geometric relaxations were considered to be converged when the force was less than 0.02 eV/Å on all unrestricted atoms.

5.3 Results

5.3.1 Surface Structure Determination

Reflection-absorption infrared spectra (RAIRS) were collected for the various carboxylic acids adsorbed on a Cu(100) substrate (Fig. 5.1). The acid group can bind strongly in a bidentate η^2 configuration to metal surfaces as a carboxylates [10, 11], and the presence of an intense feature at ~1440 cm^{-1} for all carboxylic acids following adsorption at room temperature indicates that they all form strongly bound carboxylates and thus these model systems provide a strong attachment points.

The organic acids are identical in their surface bonding but differ only in the length of the carbon chain and the nature of the terminal groups. The most stable structures for each of the carboxylic acids, predicted by DFT, are shown in Fig. 5.2 for bidentate η^2

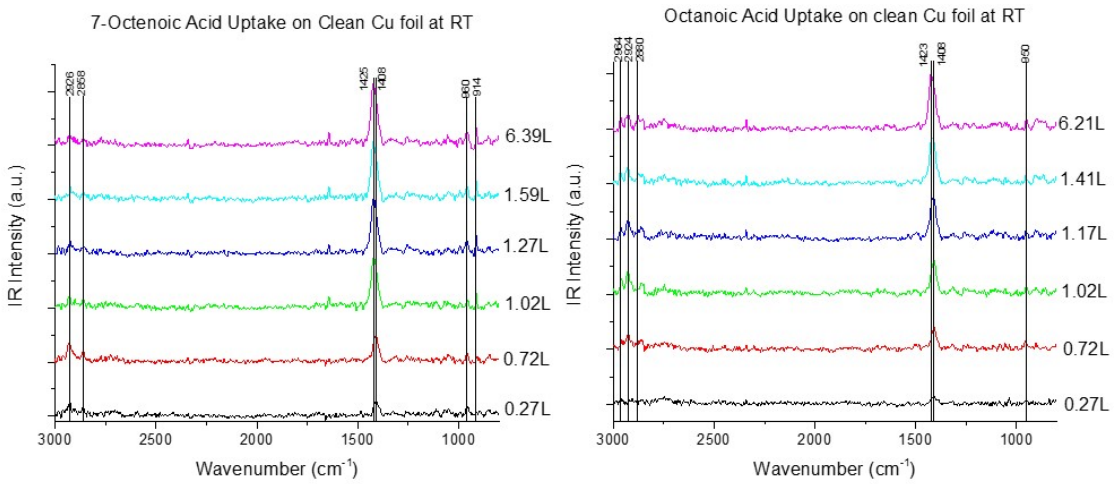

FIGURE 5.1: Reflection-absorption infrared spectra of (a) 7-octenoic acid and (b) octanoic acid adsorbed on a Cu(100) single crystal surface at room temperature. Courtesy of Robert Vincent Bavisotto, UW-Milwaukee, USA.

structures on a Cu(100) surface. The carbon chain length and the presence of a terminal vinyl group strongly influences the terminal group orientation and thus potentially the strength of the pulling-point interaction. In the case of the saturated hydrocarbons, both octanoic and heptanoic acids have hydrocarbon groups that are terminated by an ethyl group which, in the case of octanoic acid has a C–C bond that is oriented close to perpendicular to the Cu(100) surface plane, while in heptanoic acid, it is tiled with respect to the plane. The number of carbon atoms in the chain also influence the orientation of the terminal vinyl group. In the case of 6-heptenoic acid, the lobes of the π-electron density of the terminal $CH{=}CH_2$ group are oriented parallel to the surface, and therefore not easily accessible to the counterface, while in 7-octenoic acid, the lobes protrude from the surface and should therefore be more easily accessible.

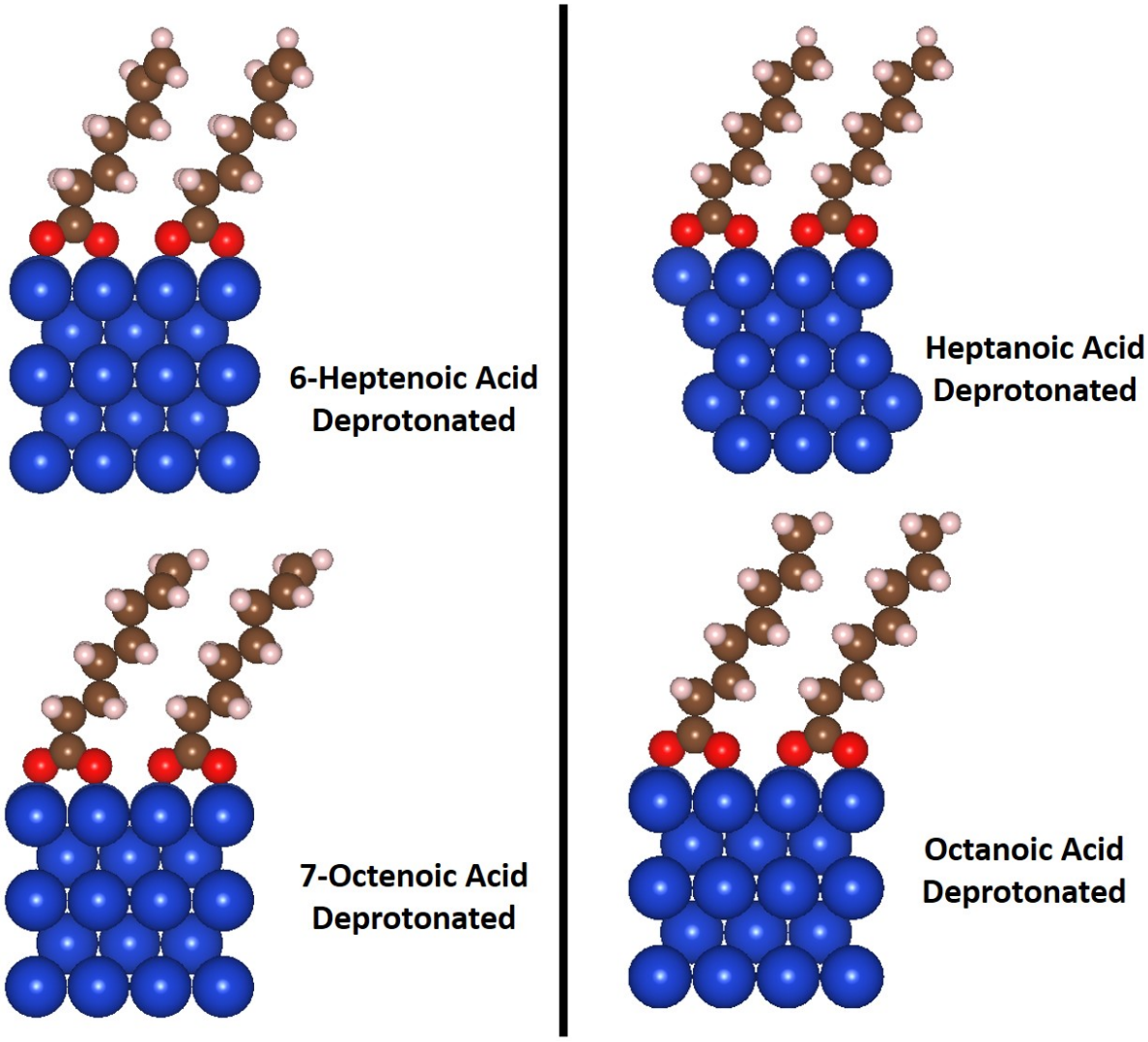

FIGURE 5.2: Structures of various carboxylic acids adsorbed on a Cu(100) surface in a (2×2) units cell, assuming that the carboxylic acids adsorb on the surface via the carboxylate group as suggested by infrared spectroscopy (Figure 5.1). Courtesy of Robert Vincent Bavisotto, UW-Milwaukee, USA.

Auger and X-ray photoelectric spectroscopic analyses of the tungsten carbide pin are shown in Figure 5.3. The tungsten carbide pin is routinely cleaned by electron-beam heating from a filament located inside the UHV chamber. It can also be cleaned

by Argon ion bombardment, although the latter strategy may also change the surface microstructure so that e-beam heating was used. The effect of e-beam heating on the pin is illustrated in Fig. 5.3A, which shows that that the untreated pin immediately after inserting into the UHV chamber is covered by carbon. Heating briefly until the sample glows red causes a change in the spectrum and the appearance of features due to tungsten, and consistent with the presence of tungsten carbide in the pin [30]. The presence of tungsten carbide was confirmed from the XPS spectrum in Fig. 5.3B, obtained after ion bombarding, which shows peaks characteristic of tungsten carbide. Cobalt has a characteristic feature at ~800 eV binding energy [31] and no features are detected at this energy is the spectrum indicating that there is little cobalt binder on the surface of the pin.

Tungsten and molybdenum carbides have been suggested to have catalytic properties akin to those found for noble metals (platinum and palladium) [12–14] and this has been borne out by UHV surface studies [15, 16], indicating that vinyl groups could bind to the surface of the tribopin. If binding to the counterface is important to the tribochemical reaction kinetics [2], 7-octenoic acid should react the most rapidly.

5.3.2 Thermal Decomposition of Carboxylic Acids on Copper

As indicated above, both the thermal and tribochemical reactions on Cu(100) are expected to occur in a two-step process initiated by scission of the bond between the

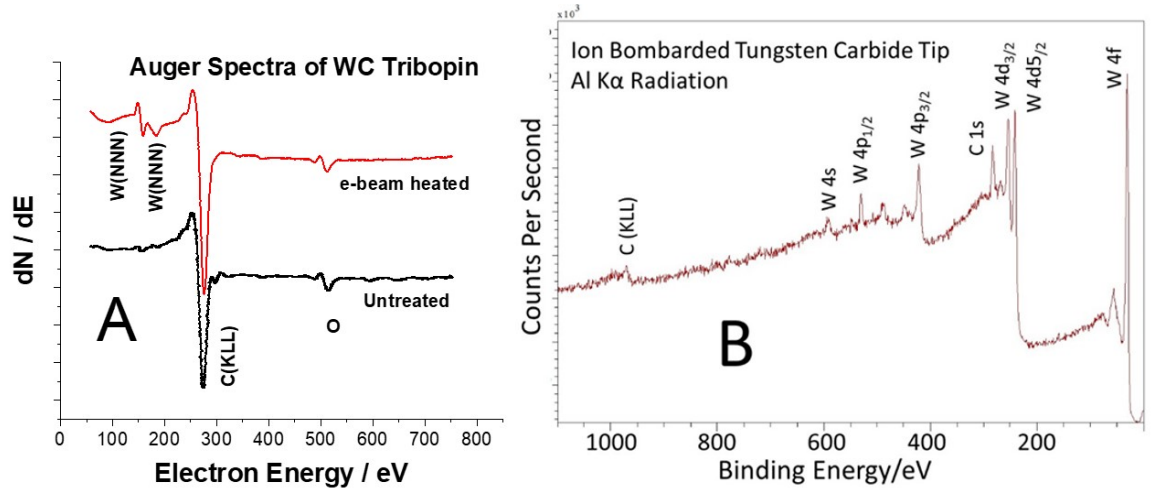

FIGURE 5.3: Analyses of the surface of the tungsten carbide tribopin. Figure A shows the initially contaminated pin showing predominantly carbon on the surface and the upper trace shows the effect of e-beam heating now revealing the presence of tungsten. Figure B shows an Al K_α X-ray photoelectron spectrum of the tungsten carbide pin that has been Argon ion bombarded. Figure B courtesy of Jules Galipaud and Thierry LeMogne, Ecole Centrale de Lyon, France.

carboxylate group and the hydrocarbon moiety to form CO and/or CO_2, with the subsequent decomposition of the alkyl group to form gas-phase products and deposit carbonaceous species on the surface. In order to clarify the thermal chemistry, TPD data were collected for 7-octenoic, octanoic, 6-heptenoic and heptanoic acids adsorbed on a clean copper foil at room temperature. The carbon dioxide (44 amu) signal was monitored to monitor the onset of molecular decomposition. The most intense molecular fragment of the adsorbed carboxylic acid was monitored as well as 18 amu (water), 28 amu (carbon monoxide and ethylene), 27 amu (ethylene) and 16 amu (methane). We note that the product distribution for fragments that are formed tribochemically at 300 K and likely to be different from those formed thermally at higher temperatures.

However, the reaction data will provide mechanistic information on the decomposition pathway of these carboxylic acids on copper. All experiments were carried out for a saturated overlayer formed at 300 K.

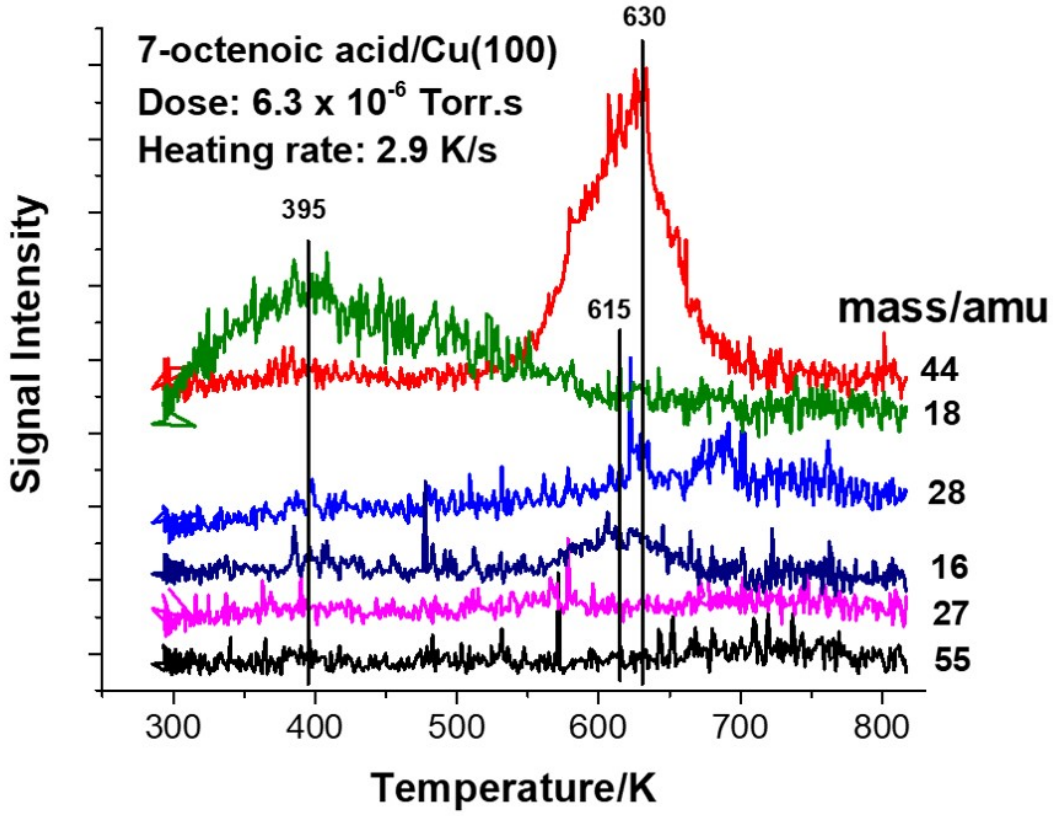

FIGURE 5.4: Temperature-programmed desorption profiles of 6.3×10^{-6} Torr.s of 7-octenoic acid adsorbed on a copper foil at 300 K monitored at various masses using a heating rate of 2.9 K/s, where the monitored masses are displayed adjacent to the corresponding spectrum.

The results are displayed in Figs. 5.4 to 5.7 where all desorption profiles show an intense 44 amu (carbon dioxide) signal just above 600 K, higher temperatures than those

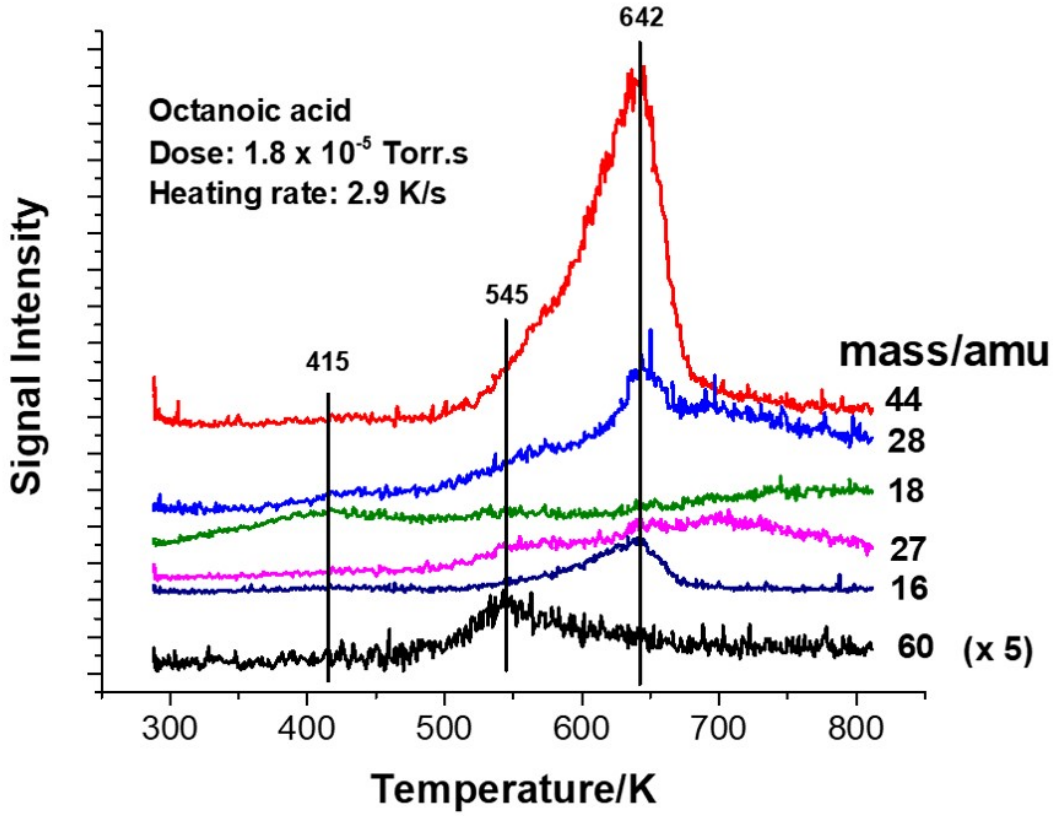

FIGURE 5.5: Temperature-programmed desorption profiles of 1.8×10^{-5} Torr.s of octanoic acid adsorbed on a copper foil at 300 K monitored at various masses using a heating rate of 2.9 K/s, where the monitored masses are displayed adjacent to the corresponding spectrum.

found for the desorption of shorter-chain carboxylic acids on copper [17–20]. The CO_2 desorbs at slightly lower temperatures for carboxylic acids containing a terminal vinyl group (~625 K) than saturated carboxylic acids (~640 K). The difference in reactivity is also evidenced by the desorption of molecular species, where octanoic and heptanoic acids (60 amu) desorb at 545 (Fig. 5.5) and 555 K (Fig. 5.7), while no desorption is found for the carboxylic acids with carbon-carbon double bonds in Fig. 5.4 for 7-octenoic acid

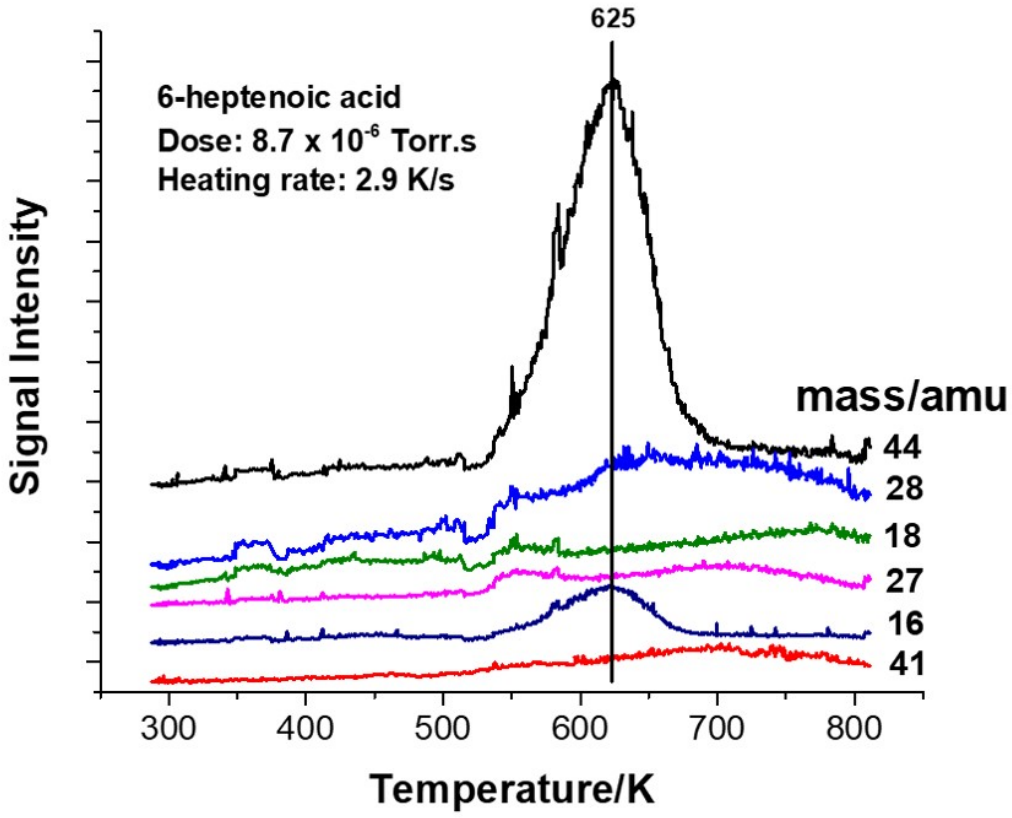

FIGURE 5.6: Temperature-programmed desorption profiles of 8.7×10^{-6} Torr.s of 6-heptenoic acid adsorbed on a copper foil at 300 K monitored at various masses using a heating rate of 2.9 K/s, where the monitored masses are displayed adjacent to the corresponding spectrum.

at 55 amu, and Fig. 5.6 for 6-heptenoic acid at 41 amu. Finally, while no attempt was made to fully characterize the nature of the resulting hydrocarbon fragments, small hydrocarbons form coincidentally with or at slightly higher temperatures than the formation of CO_2. Methane seems to be formed at the same temperature as CO_2, while C_2 hydrocarbons desorb at ~700 K. However, the results collectively indicate that molecular decomposition is initiated by the formation of a CO_2 fragment from the anchoring

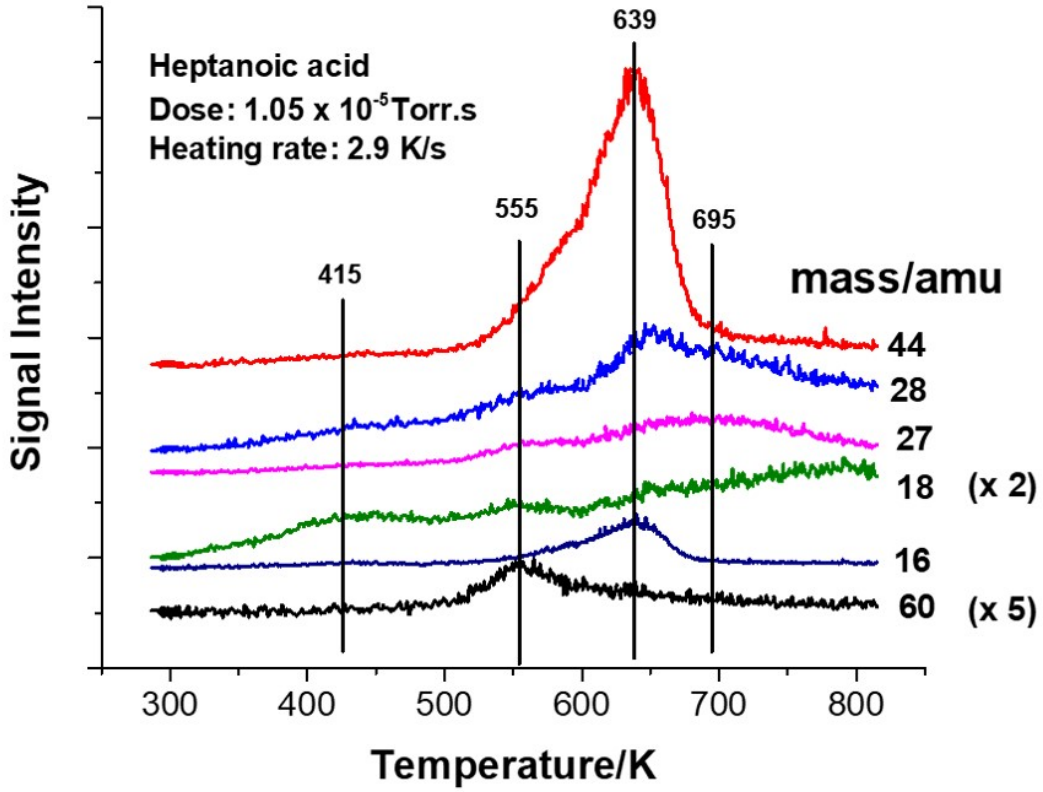

FIGURE 5.7: Temperature-programmed desorption profiles of 1.05×10^{-5} Torr.s of heptanoic acid adsorbed on a copper foil at 300 K monitored at various masses using a heating rate of 2.9 K/s, where the monitored masses are displayed adjacent to the corresponding spectrum.

carboxylate group, followed by the decomposition of the hydrocarbon fragments. The reactivity of the fragments is also influenced by the presence of a terminal vinyl group in the chain.

5.3.3 Tribochemical Reactions of Carboxylic Acids on Copper

Tribochemical experiments were carried out by rubbing a carboxylate-covered surface with a cleaned tungsten carbon ball at a sliding speed of 4×10^{-3} m/s at a normal load of 0.44 N. The rubbed region was then analyzed using Auger spectroscopy. Attempts were made to monitor the gas-phase products formed during sliding as done previously [32–34] but the residual background signal after sample dosing precluded such experiments from being carried out. Figure 5.8 shows the results of experiments carried out for a saturated overlayer of 7-octenoic acid on copper. Here the surface was first rubbed to create a wear track and then dosed with 7-octenoic acid, where the saturation dose was gauged by measuring the C KLL Auger spectral intensity as a function of exposure. This yields a C/Cu peak-to-peak intensity ratio of ~0.65. The decrease in the amount of carbon on the surface as the surface is rubbed (■) indicates that the adsorbed 7-octenoate undergoes a tribochemical reaction. The signal decreases to a final C/Cu Auger ratio of ~0.12 after ~35 passes and a fit to an exponential decrease yields a number of passes to reduce the signal by 1/e of 7.9 ± 1.1 scans. The exponential decay in carbon Auger signal suggests a first-order decomposition rate, but the surface signal does not account for any products lost into the gas-phase so that caution must be used in assuming a reaction order from these data.

The experiment was repeated without cleaning the substrate or the pin (Fig. 5.8, ●)

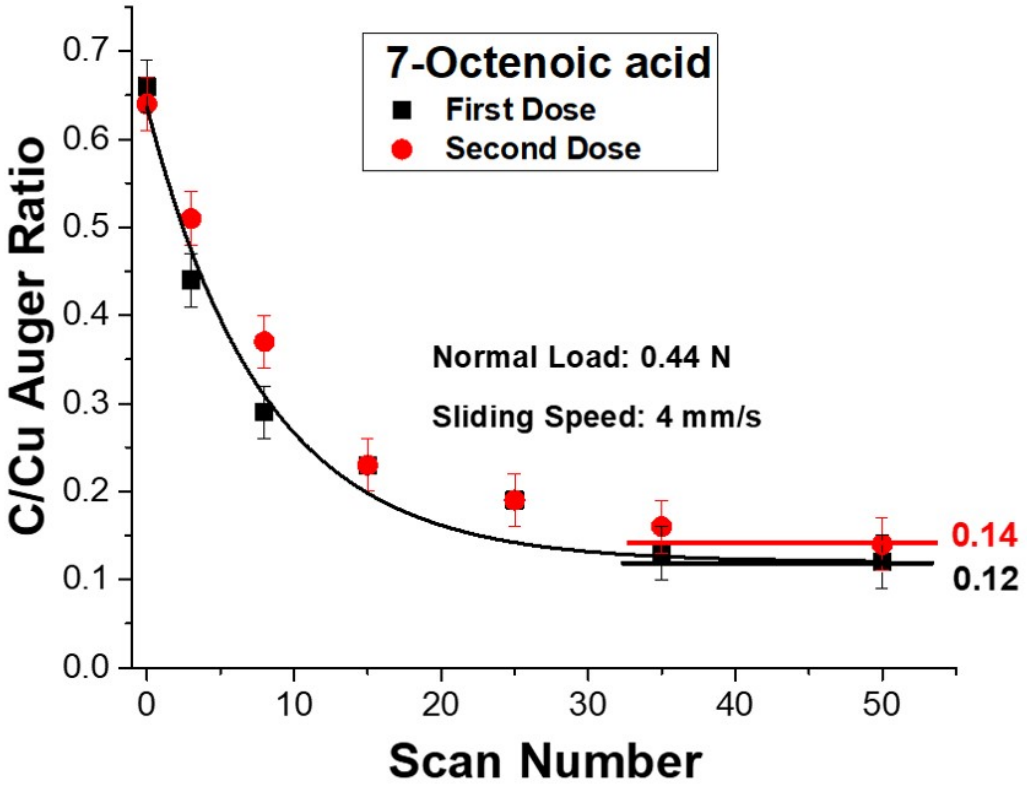

FIGURE 5.8: Plot of the C/Cu Auger ratio in the wear track of a saturated overlayer of 7-octenoic acid on a copper foil as a function of the number of passes at a normal load of 0.44 N and a sliding speed of 4×10^{-3} m/s, for 7-octenoic acid on a clean surface (■) and after a second dose of 7-octanoic acid on the previously rubbed surface.

to assess how the presence of carbonaceous product influenced the reaction kinetics. The results are also plotted on the figure, where the signal decay rate is approximately identical to the first experiment, but there is a slight increase in the amount of carbon on the surface (to a C/Cu ratio of 0.14 after the second scan). In order to investigate

this further, the surface was repeatedly dosed and rubbed until the carbon Auger signal intensity remained constant. The results are displayed in Figure 5.9 for 7-octenoic acid adsorption. Here, the amount of carbon on the surface increases significantly after that surface has been dosed and rubbed 4 times to yield a S/Cu ratio of 0.26 at a rate of 0.047 ± 0.008 C/Cu per scan, and then does not change. The amount of carbon initially on the surface after dosing the sample with 7-octenoic acid decreases (note that this is the sum of the carbon deposited during the previous cycles plus the 7-octenoic acid then adsorbed on the surface) as the surface becomes covered by carbon. However, the blocking is not complete, implying that some of the carbon has penetrated the bulk (see below). The results also imply that the tribochemical reaction for a surface that accumulates sufficient carbon to yield a S/Cu ratio of 0.26 results in the deposition of no more additional carbon on the surface, suggesting that 7-octenoate decomposition on this surface yields only gas-phase products or that the loss of carbon by diffusion into the bulk equals that formed on the surface by the decomposition of 7-octenoic acid. Since a saturated overlayer of 7-octenoic acid has a C/Cu Auger ratio of 0.66, the additional carbon after ≥5 doses (the difference between the signal for the saturated overlayer with a C/Cu Auger ratio of 0.59 and the surface after rubbing with a C/Cu Auger ratio of 0.26) corresponds to a relative coverage of ~0.56 monolayer of 7-octenoate species. The Auger spectrum of the pin (data not shown) indicates that carbon is also deposited on the counterface as evidence by the relatively weaker tungsten

signal.

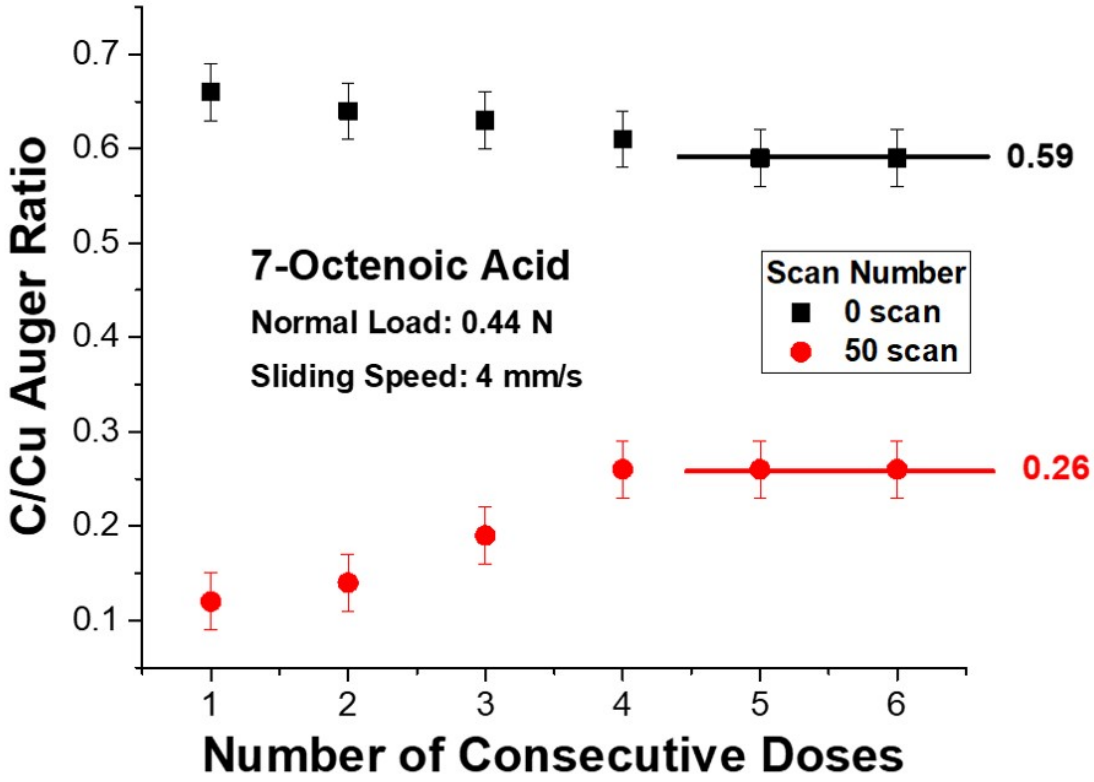

FIGURE 5.9: Plot of the initial (indicated as 0 scan) and final (indicated as 50 scans) carbon to copper Auger ratio measured in the wear track after rubbing a copper surface saturated with 7-octenoic acid at a normal load of 0.44 N at a sliding speed of 4×10^{-3} m/s. Neither the copper surface nor the tungsten carbide pin was cleaned between scans so that each consecutive scan is for an interface that includes the accumulated carbon from previous scans.

A similar sequence of experiments was carried out on a copper surface dosed with octanoic acid. Because of the lack of any unsaturation in the chain to bind strongly to the tungsten carbide pin, this is anticipated to be the least tribochemically reactive surface species. The variation in C/Cu Auger ratio with the number of rubbing cycles

is shown in Figure 5.10. Some carbon is deposited onto the surface at the end of 50 rubbing cycles with a C/Cu Auger ratio of ~0.11, and the curve yields a number of passes to 1/e of the original intensity of 1.8 ± 0.2 scans; much faster than for 7-octenoic acid (Fig. 5.8). The effect of repeated dosing is shown in Fig. 5.11, where there is a significant blocking of the surface by the reaction products, although the final amount of carbon 1.8 (corresponding to a C/Cu ratio of 0.27) is the same as for 7-octenoic acid. The amount of carbon on the surface increases at a rate of 0.042 ± 0.004 C/Cu per dose, similar to that found for 7-octenoic acid (Fig. 5.9).

A similar series of experiments was carried out for C_7 hydrocarbons. The results for 6-heptenoic acid are displayed in Figure 5.12 where the amount of carbon remaining after 50 scans is slightly less that for the C_8 hydrocarbons and the number of scans to decrease the signal to 1/e of its original value is 11.3 ± 1.8 scans and is therefore the least reactive of all carboxylic acids tested. The results of experiments in which the sample is repeatedly dosed and rubbed is shown in Fig. 5.13, where the carbon accumulation rate is 0.048 ± 0.01 C/Cu per dose. Finally the relative coverage that can be accommodated after ≥5 scans is ~0.25 ML. Similar results are displayed for the corresponding saturated C_7 hydrocarbon, heptanoic acid (Figure 5.14), where the remaining carbon has a C/Cu Auger ratio of ~0.08 and the carbon removal rate is 4.1 ± 0.4 scans to reduce the carbon signal to 1/e of its original value. The effect of repeated dosing and rubbing in shown in Figure 5.15, where the rate of carbon accumulation

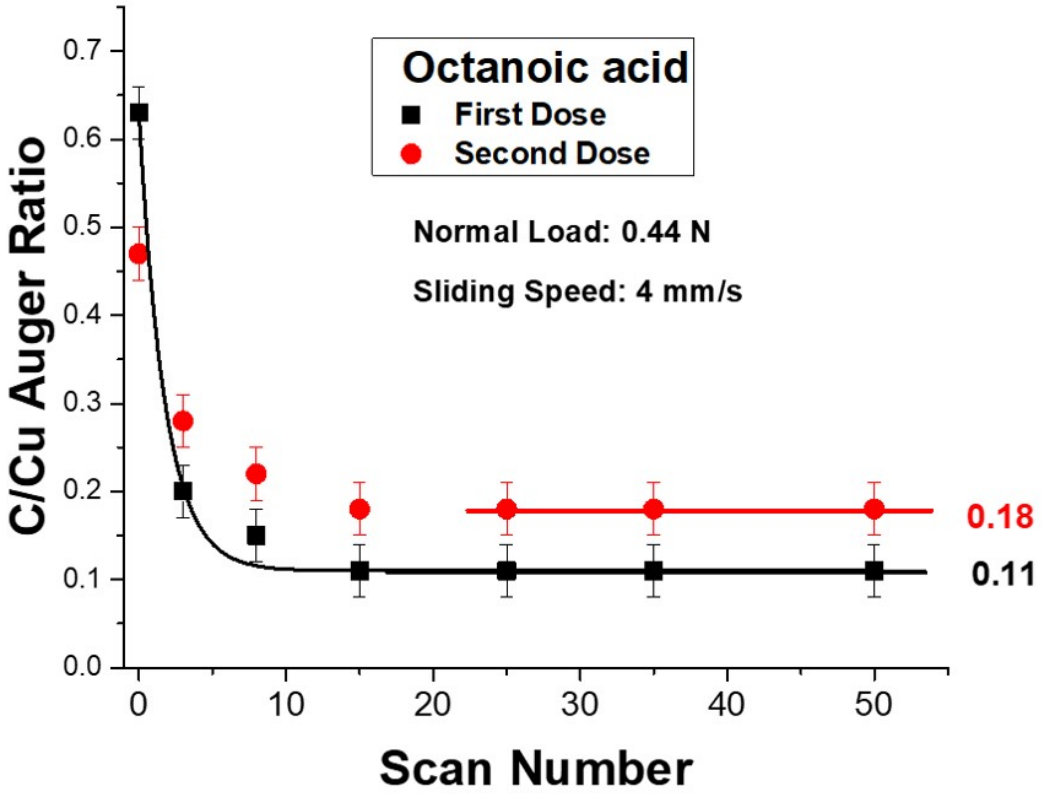

FIGURE 5.10: Plot of the C/Cu Auger ratio in the wear track of a saturated overlayer of octanoic acid on a copper foil as a function of the number of passes at a normal load of 0.44 N and a sliding speed of 4×10^{-3} m/s, for octanoic acid on a clean surface (■) and after a second dose of octanoic acid on the previously rubbed surface.

is 0.036 ± 0.001 C/Cu per scans and the coverage of the heptanoic acid that can be accommodated onto the surface after ≥4 scans is ~0.38 ML.

The rates of the removal of carbon are summarized in Table 5.1 for the various carboxylic acids. It is evident that the carbon signal decreases much more rapidly as a

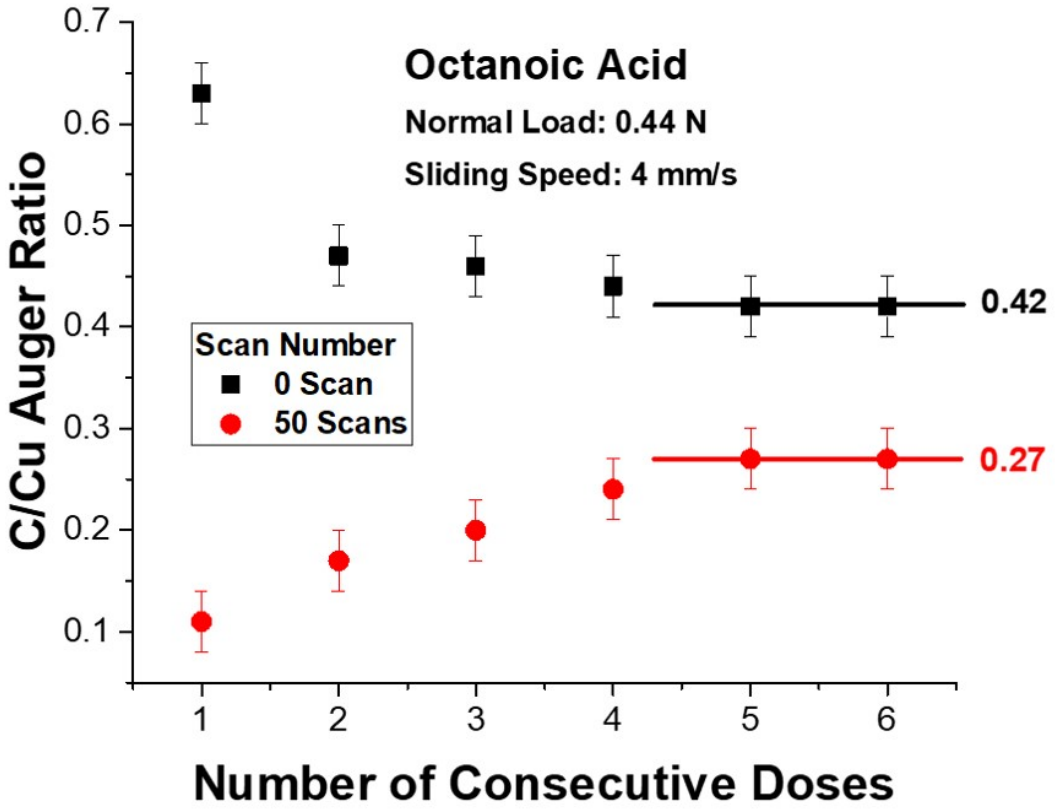

FIGURE 5.11: Plot of the initial (indicated as 0 scan) and final (indicated as 50 scans) carbon to copper Auger ratio measured in the wear track after rubbing a copper surface saturated with octanoic acid at a normal load of 0.44 N at a sliding speed of 4×10^{-3}. Neither the copper surface nor the tungsten carbide pin was cleaned between scans so that each consecutive scan is for an interface that includes the accumulated carbon from previous scans.

function of the number of times that the sample had been rubbed for alkyl-group containing carboxylic acids (octanoic and heptanoic acids) compared to those containing a terminal vinyl group (7-octenoic and 6-heptenoic acids). However, the surface chemistry experiments indicate that the thermal reaction involves the formation of carbon

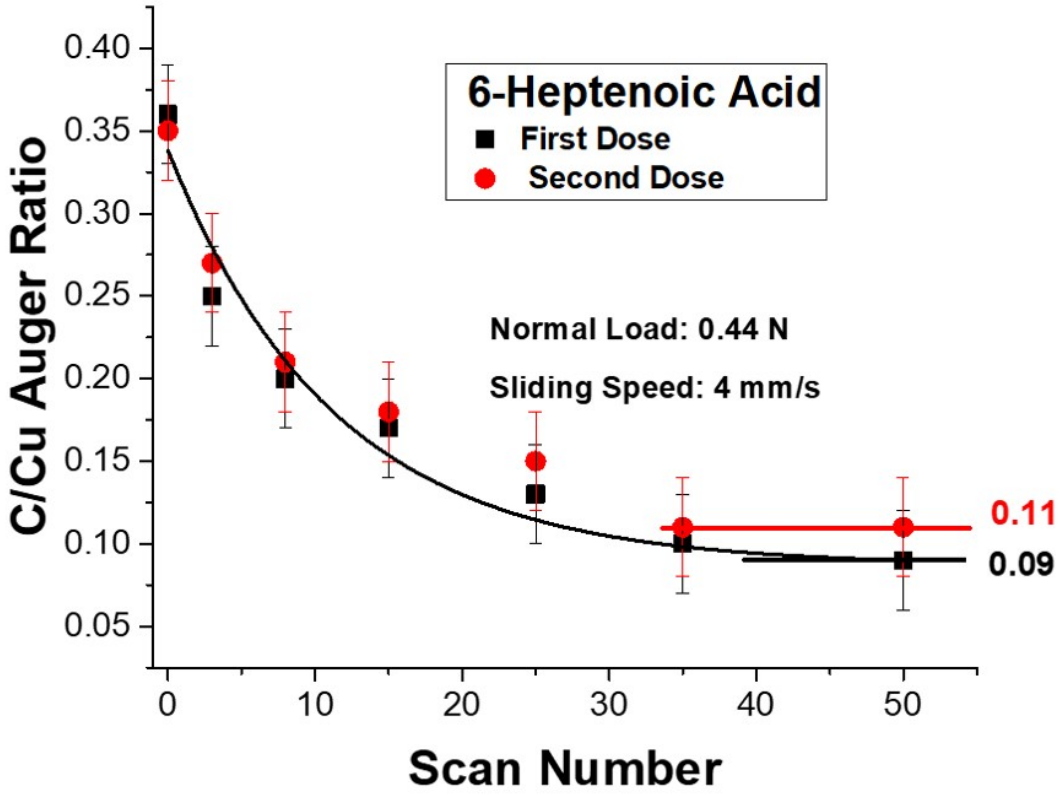

FIGURE 5.12: Plot of the C/Cu Auger ratio in the wear track of a saturated overlayer of 6-heptenoic acid on a copper foil as a function of the number of passes at a normal load of 0.44 N and a sliding speed of 4×10^{-3} m/s, for 6-heptenoic on a clean surface (■) and after a second dose of 6-heptenoic on the previously rubbed surface.

dioxide from the carboxylate group followed by the reaction of the resulting hydrocarbon fragment so that the removal of carbon is the result of several reaction steps. To disentangle these effects, the loss of oxygen from the surface as a function of the number of passes was also monitored and the results are displayed in Figure 5.16. Note that the oxygen Auger signal is much small than the carbon signal because there is much

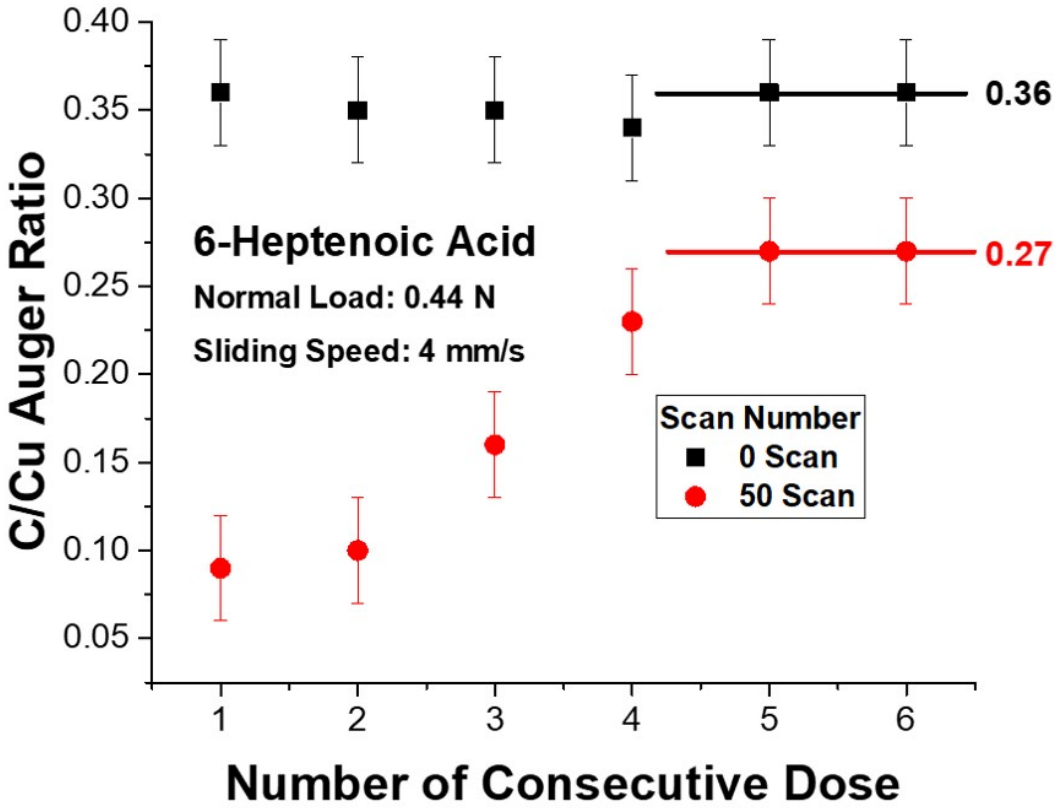

FIGURE 5.13: Plot of the initial (indicated as 0 scan) and final (indicated as 50 scans) carbon to copper Auger ratio measured in the wear track after rubbing a copper surface saturated with 6-heptenoic acid at a normal load of 0.44 N at a sliding speed of 4×10^{-3} m/s. Neither the copper surface nor the tungsten carbide pin was cleaned between scans so that each consecutive scan is for an interface that includes the accumulated carbon from previous scans.

more carbon than oxygen in the adsorbed layer and the oxygen is buried at the surface, while the carbon is in the outermost layer. The amount of oxygen decreases identically for all carboxylate overlayers at a rate of 2.0 ± 0.1 O/Cu per scan, similar to the rate of carbon removal from octanoic acid (Table 5.1). This implies that there is little effect of varying the nature of the outermost functionality and thus the nature of the pulling

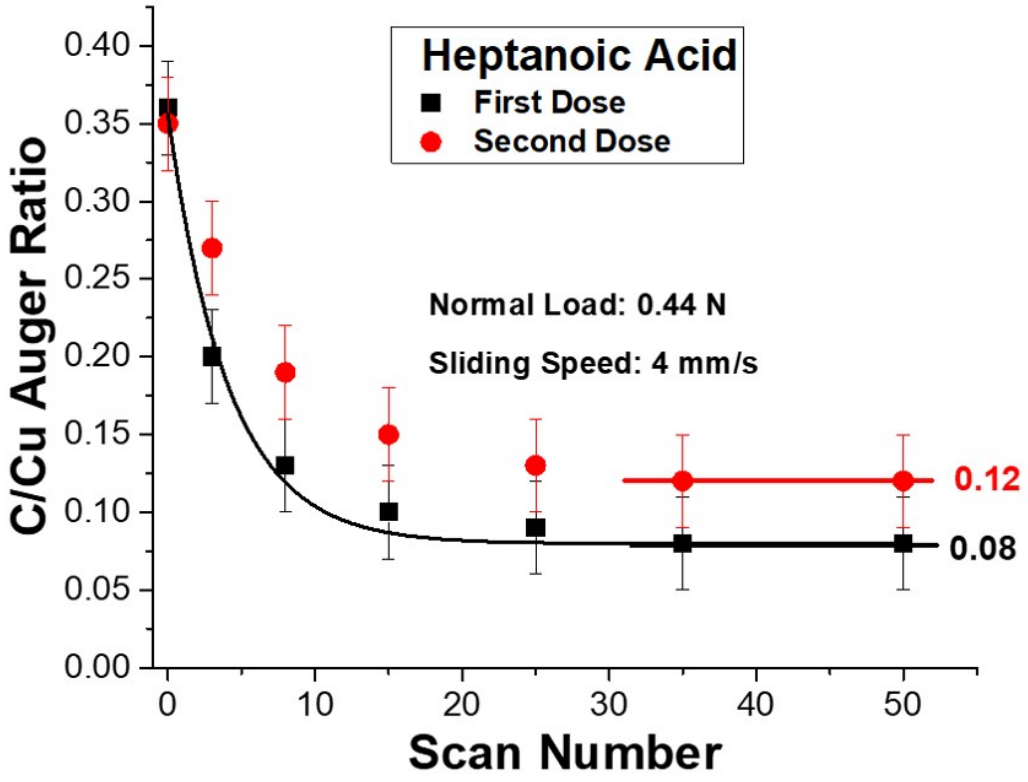

FIGURE 5.14: Plot of the C/Cu Auger ratio in the wear track of a saturated overlayer of heptanoic acid on a copper foil as a function of the number of passes at a normal load of 0.44 N and a sliding speed of 4×10^{-3} m/s, for heptanoic on a clean surface (■) and after a second dose of heptanoic on the previously rubbed surface.

point on the overall shear-induced rate of decomposition of the carboxylic acids. As a result, this implies that differences in the rates of carbon removal are caused by the rates at which the resulting hydrocarbon fragments react. Furthermore, if differences in the terminal functionality do not influence the shear-induced reactivity, this should

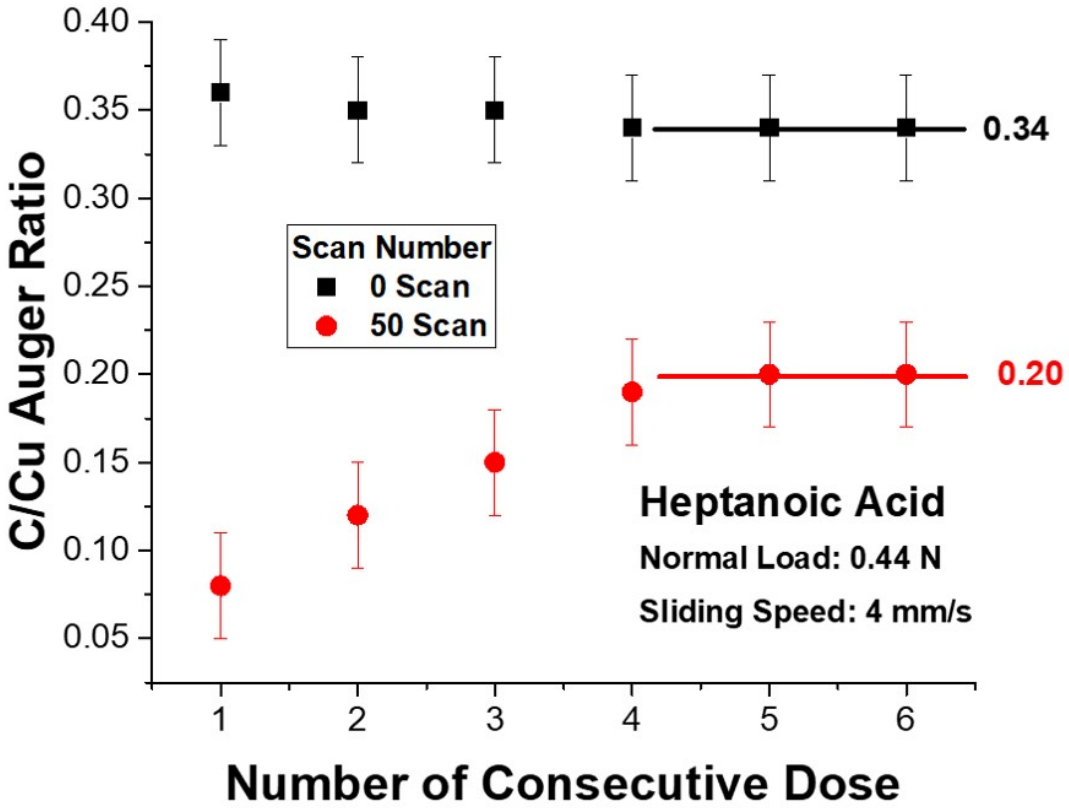

FIGURE 5.15: Plot of the initial (indicated as 0 scan) and final (indicated as 50 scans) carbon to copper Auger ratio measured in the wear track after rubbing a copper surface saturated with heptanoic acid at a normal load of 0.44 N at a sliding speed of 4×10^{-3} m/s. Neither the copper surface nor the tungsten carbide pin was cleaned between scans so that each consecutive scan is for an interface that includes the accumulated carbon from previous scans.

also be evident from the friction coefficient of the various carboxylic acid covered surfaces. Such measurements will also provide information on the frictional properties of the various tribochemically formed surfaces and are discussed in the next section.

Compound	Carbon Removal Sliding Number/Scan	Friction Coefficient
7-Octenoic Acid	7.9 ± 1.1	0.23 ± 0.08
Octanoic Acid	1.8 ± 0.2	0.22 ± 0.06
6-Heptenoic Acid	11.3 ± 1.8	0.18 ± 0.08
Heptanoic Acid	4.1 ± 0.4	0.21 ± 0.08

TABLE 5.1: The number of scans at a load on 0.44 N at a sliding speed of 4×10^{-3} m/s to decrease the C KLL Auger intensity to 1/e of its original value for the adsorption of each of the carboxylic acids on copper, compared with the initial friction coefficient of the saturated overlayer of each compound.

5.3.4 Frictional Behavior of Carboxylic Acids on Copper

The evolution of the friction coefficient as a function of the number of passes for a 7-octenoic acid overlayer on clean copper is shown in Figure 5.17. The presence of the 7-octenoic acid on the surface significantly reduces the initial friction coefficient to ~0.23 ± 0.08 (■, Table 5.1), but this rises as the surface is rubbed in accord with the loss of carbon from the surface (Fig. 5.8). The corresponding scan after the surface has been dosed and rubbed for 50 scans with 7-octenoic acid six times is also shown (●). Here the initial friction coefficient is identical to that on clean Cu saturated with 7-octenoic acid but the friction coefficient increases but then forms a plateau due to the carbonaceous species previously formed on the surface.

Similar behavior is seen for an octanoic acid overlayer on copper (Figure 5.18) where the initial friction coefficient it 0.22 ± 0.06 (■), and increases as the overlayer is removed from the surface. The overlayer on a substrate that has been dosed with

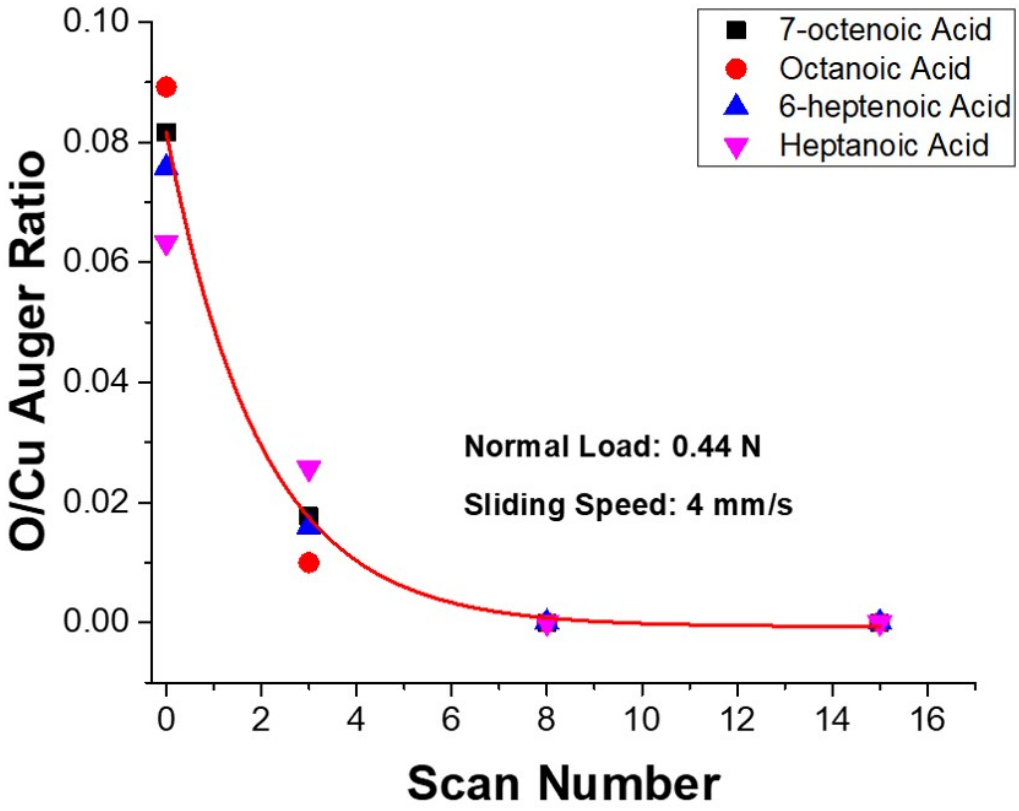

FIGURE 5.16: Plot of the O/Cu Auger ratio in the wear track of a saturated overlayer of 7-octenoic acid (■), octanoic acid (●), 6-heptenoic acid (▲), and heptanoic acid (▼) as a function of the number of passes at a normal load of 0.44 N and a sliding speed of 4×10^{-3} m/s.

octanoic acid and rubbed six times again has a similar initial friction coefficient and reaches a lower plateau after rubbing due to the presence of carbon on the surface.

Identical behavior is seen for 6-heptenoic acid (Fig. 5.19), where the friction coefficients for the initial overlayer on both surfaces is 0.17 ± 0.08 and for heptanoic acid

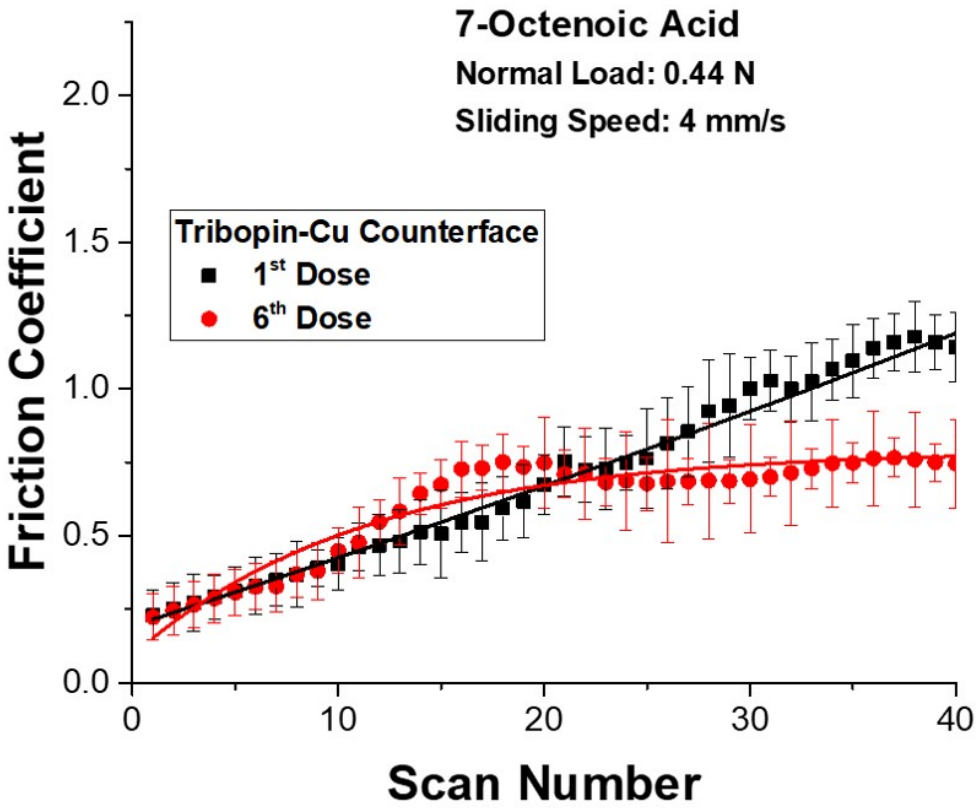

FIGURE 5.17: Plot of the evolution in the friction coefficient of a 7-octenoic acid overlayer on copper rubbed at a normal load of 0.44 N and a sliding speed of 4×10^{-3} m/s for an overlayer formed on a clean surface (■) and on a surface that has been dosed and rubbed six times (●).

(Fig. 5.20), where the initial friction coefficient it 0.21 ± 0.08. Thus the friction behavior mimics the surface analyses, where the friction is initially low due to the presence of the organic overlayer. The initial friction coefficient are essentially identical for both the carboxylic acids on the clean and carbon-covered surfaces. This indicates that some blocking of the copper by carbon, which reduces the coverage of the carboxylate, but does not significantly influence the friction. More significant is the similarity between

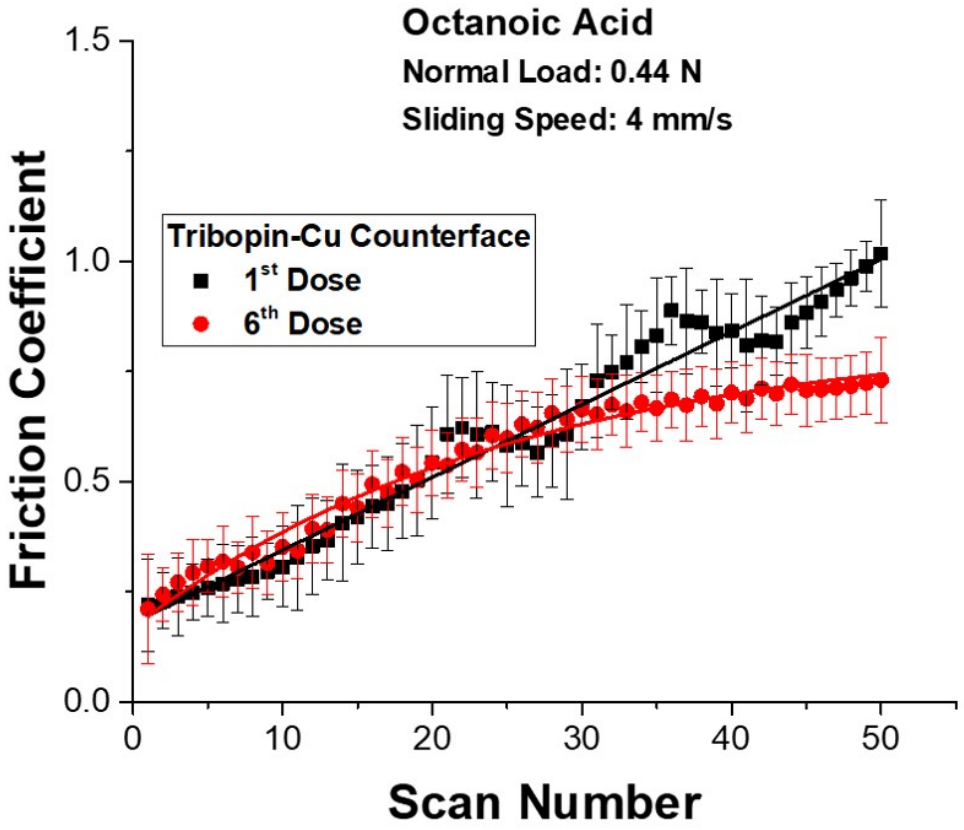

FIGURE 5.18: Plot of the evolution in the friction coefficient of a octanoic acid overlayer on copper rubbed at a normal load of 0.44 N and a sliding speed of 4×10^{-3} m/s for an overlayer formed on a clean surface (■) and on a surface that has been dosed and rubbed six times (●).

the friction coefficients of all carboxylic acids irrespective of the nature of the terminal group, indicating that this does not lead to larger forces acting on the adsorbate. This is consistent with the observed similarity in initial tribochemical reaction rates.

These experiments involve the accumulated adsorption of a significant amount of carbon on the surface, which then undergoes shear-induced reactions, yet the surface

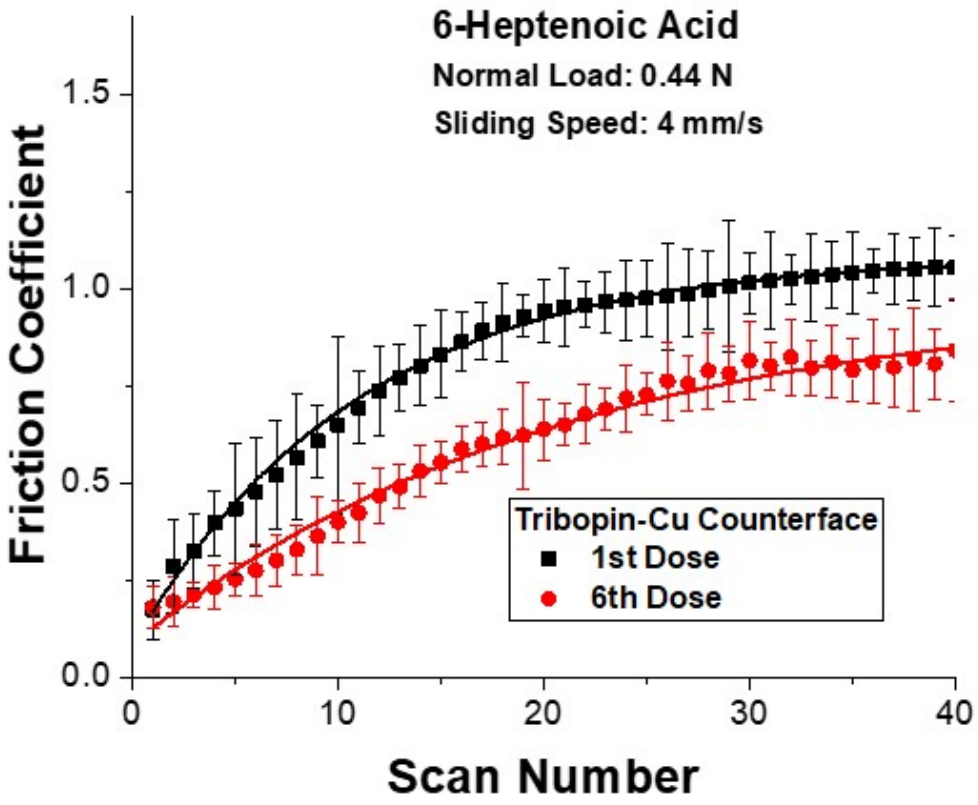

FIGURE 5.19: Plot of the evolution in the friction coefficient of a 6-heptenoic acid overlayer on copper rubbed at a normal load of 0.44 N and a sliding speed of 4×10^{-3} m/s for an overlayer formed on a clean surface (■) and on a surface that has been dosed and rubbed six times (●).

can still adsorb a significant amount of carboxylic acid. This implies that the sliding interface has induced the transport of carbon from the surface into the subsurface region in a similar way to the shear-induced surface-to-bulk transport of sulfur on copper [23, 32–34]. This is explored in the next section for the tribochemical reaction of 6-heptenoic acid on copper.

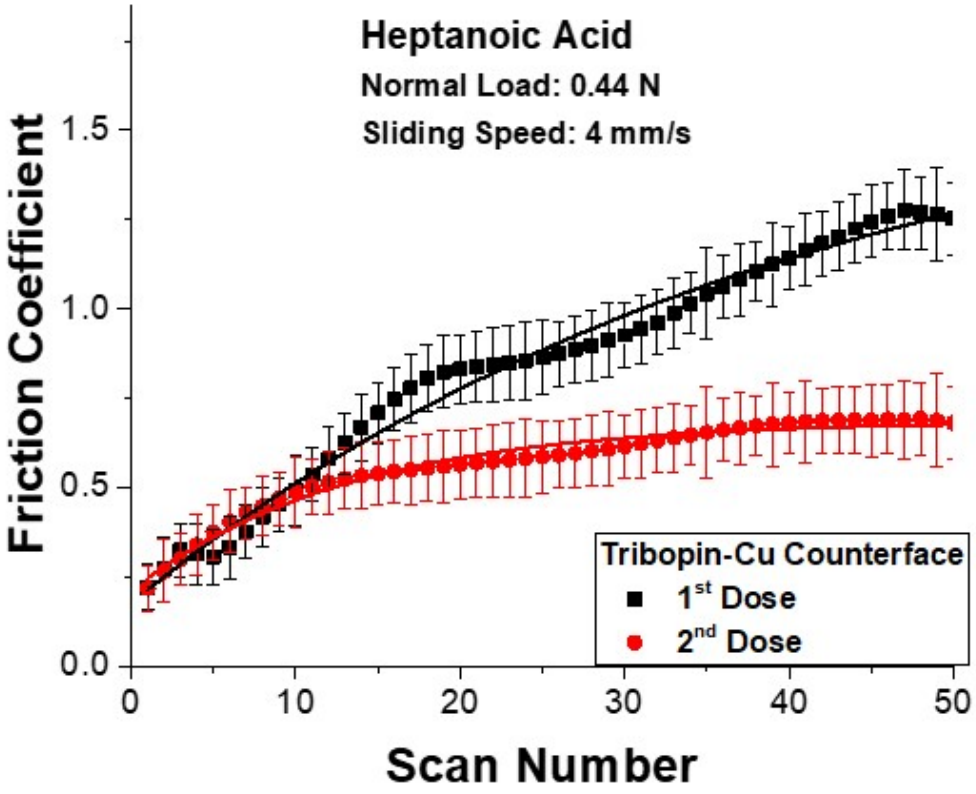

FIGURE 5.20: Plot of the evolution in the friction coefficient of a heptanoic acid overlayer on copper rubbed at a normal load of 0.44 N and a sliding speed of 4×10^{-3} m/s for an overlayer formed on a clean surface (■) and on a surface that has been dosed and rubbed six times (●).

5.3.5 Surface-to-Bulk Transport of Carbon into the Copper Subsurface Region

The possibility of carbon having diffused into the bulk of the sample to form a metastable carbide is investigated by heating the sample to ~780 K to cause the subsurface carbon

to diffuse to the surface on heating [32]. This however requires that all carbon be selectively removed from the surface by ion bombardment. This experiment was carried out for a copper sample that had been saturated with 6-heptenoic acid and rubbed 50 times and was then redosed without cleaning for a total of six times. The results of the experiment are shown on Fig. 5.21, where the rubbed region is indicated. The top trace (black line) shows the initial carbon KLL Auger signal intensity as a function of position across the wear track. The region outside the wear track is due to adsorbed 6-heptenoic acid and the slightly lower signal is due to the removal of the adsorbed layer to reveal the carbonaceous film formed by the tribochemical reaction as shown in Fig 5.13. The sample was then bombarded with Argon ions to remove the majority of the molecular overlayer to produce the bottom trace shown (blue line). Note that not all the carbon outside the wear track has been removed by this process, but was stopped at this point to avoid removing subsurface carbon. The sample was then heated to 780 K, resulting on the red profile (red line), where there is an enhanced carbon Auger signal in the region that was rubbed thereby confirming that carbon has penetrated the bulk of the carbon. There is also a significant increase in the C CLL Auger intensity well outside the wear track. Note that this experiment involved the deposition of equivalent of up to ~40 monolayers of carbon (six repeated doses of 6-heptenoic acid overlayers). Some of the carbon may have been removed by the tribochemical formation of small

hydrocarbons, but a significant proportion must have penetrated the bulk after a total of 300 rubbing cycles to still leave vacant sites for 6-heptenoic acid to adsorb. The subsurface carbon will diffuse isotropically until it reaches the surface to form a stable carbonaceous overlayer. The fact that it moves several hundred microns laterally as it diffuses toward the surface implies that it must have penetrated a similar distance into the bulk of the copper.

5.4 Discussion

These results indicate that relatively long-chain carboxylic acids adsorbed on copper undergo tribochemical reactions to deposit carbonaceous species on the surface and in the subsurface region. In addition to carboxylic acids functioning as friction modifiers by forming protective adsorbed molecular overlayers [4], they can react at the interface to form lubricious carbonaceous films [1, 5, 6] and thus also function as friction-reducing additives. An important conclusion from this work is that this reaction is mechanochemically induced rather that the rate being accelerated by some other process such as interfacial heating since the temperature rise during sliding on copper under the conditions used here is negligible. This is in accord with the predictions from simulations [2] and appears to be a common feature that the chemistry of lubricant additives is mechanochemically driven as, for example, for zinc dialkyl dithiophosphate (ZDDP) and phosphate esters [35–37].

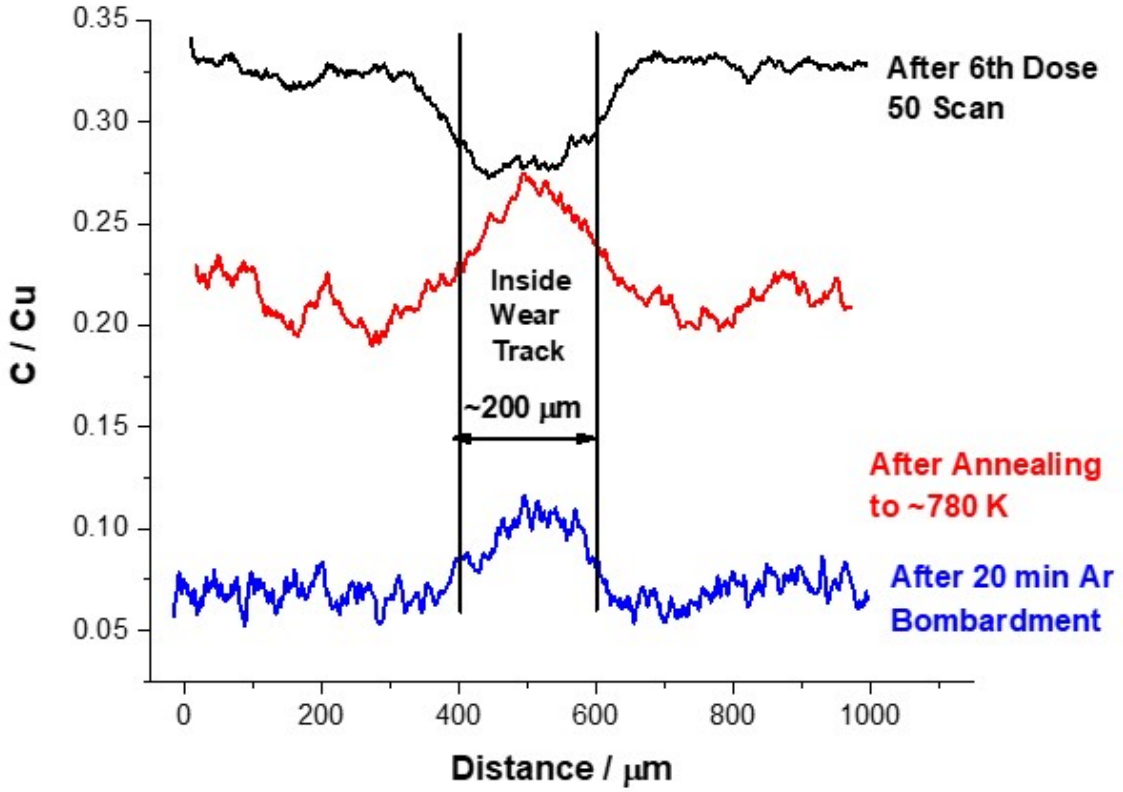

FIGURE 5.21: C CKK Auger profiles across a wear track for a tribochemical reaction of 6-heptenoic acid on copper following 50 scans over the surface for six doses of 6-heptenoic acid (black line) showing the Auger signal of the 6-heptenoate overlayer outside the rubbed region and the reduction in Auger signal in the rubbed region due to the tribochemical reaction. The sample was then Argon ion bombarded to remove the majority of the surface carbon (blue line) and the sample was then heated to 790 K to cause any subsurface carbon to diffuse to the surface once again (red line).

This work shows that the tribochemical reaction is initiated by the cleavage of the bond between the carboxylate anchoring group and the hydrocarbon chain likely forming carbon dioxide that will rapidly desorb from the surface, along with a hydrocarbon radical, which then undergoes subsequent reactions on the surface. This pathway is

similar to the thermal reaction as identified by TPD (Figs. 5.4-5.7), where the reaction is initiated above 600 K, while the tribochemical reaction takes place at room temperature. In this case, the subsequent reaction of the side chain are likely to differ in some details between the thermal reaction (where they occur at ~600 K) and for tribochemical reactions (when they occur at 300 K).

It was postulated that the interaction between the terminus of the hydrocarbon chain and the moving counterface (the pulling point) might influence the tribochemical reaction rate where the stronger binding of a vinyl than an alkyl group to the tungsten carbide surface (Fig. 5.3) should result in higher forces being exerted for vinyl-terminated surfaces, resulting in higher reactivity. The stereochemistry of this interaction was also investigated by using C_7 and C_8 chains. However, no dependence was found on the rate of oxygen removal from the surface while rubbing (Fig. 5.16) for carboxylic acids on changes in the nature of the terminus of the chain. In addition, the initial friction coefficients of the overlayers were independent of the nature of the hydrocarbon (Table 5.1).

There are various possibilities for this effect. First, it may be that a reaction does occur with different rates on the initially clean tungsten carbide surface, thereby rapidly forming a carbon-covered surface which forms van der Waals bonds with the adsorbed molecule that masks the difference between the alkyl and vinyl terminations. It may also be that the interface is sufficiently rough that such steric effects are obscured. In

any case, this result implies that any differences in the reaction kinetics is not controlled by the initial decomposition step, but is instead controlled by the tribochemical decomposition of the hydrocarbon fragment that is formed. This results in the rate of the removal of carbon from alkyl chains being much more rapid than for chains with terminal carbon-carbon double bonds (Table 5.2). Alkyl species adsorbed on copper either undergo a β-hydride elimination reaction to form an alkene or hydrogenates to form an alkane, both of which occur below room temperature [38, 39]. This accounts for the rapid rate of carbon removal for alkyl functionalized carboxylic acids, where the rate of carbon removal is similar to the rate that oxygen in removed. This conclusion is in accord with the observation that hydrocarbon are formed at the same temperature as carbon dioxide in TPD; the rate-limiting step is the formation of carbon dioxide and the rates of the subsequent reactions are fast.

Compound	Carbon Ratio after Rubbing(1^{st} dose)/%	Carbon Ratio after TPD/%
7-Octenoic Acid	18%	67%
Octanoic Acid	17%	81%
6-Heptenoic Acid	25%	76%
Heptanoic Acid	22%	60%

TABLE 5.2: The proportion of carbon on the surface after Rubbing and TPD experiments.

It is likely that the carboxylic acids with terminal C=C groups react more slowly because the terminal vinyl group can also interact with the surface to lower the rate that it is removed (Table 5.1). The effectiveness of this process will depend on the

length of the carbon chain and the location of the carbon-carbon double bond within it.

5.5 Conclusions

The tribochemical reaction of the carboxylic acid is initiated by the cleavage of the bonds between the carboxylate anchoring group and the hydrocarbon chain likely to form carbon dioxide that will rapidly desorb from the surface, and a hydrocarbon radical, which then undergoes subsequent reaction. The reaction kinetics is not controlled by the initial decomposition step but is instead controlled by the tribochemical decomposition of the hydrocarbon fragment that is formed. The carboxylic acids with terminal C=C groups react more slowly because the terminal vinyl group can also interact with the surface to lower the rate that it is removed. The effectiveness of reaction depends on the length of the carbon chain and the location of the carbon-carbon double bond within a carboxylic acid.

References

[1] M. I. D. B. Bouchet, J. M. Martin, C. Forest, T. Le Mogne, M. Mazarin, J. Avila, M. C. Asensio, and G. L. Fisher, "Tribochemistry of unsaturated fatty acids as friction modifiers in (bio) diesel fuel," *RSC advances*, vol. 7, no. 53, pp. 33120–33131, 2017.

[2] T. Kuwahara, P. A. Romero, S. Makowski, V. Weihnacht, G. Moras, and M. Moseler, "Mechano-chemical decomposition of organic friction modifiers with multiple reactive centres induces superlubricity of ta-C," *Nature Communications*, vol. 10, no. 1, pp. 1–11, 2019.

[3] S. Campen, J. Green, G. Lamb, and H. Spikes, "In situ study of model organic friction modifiers using liquid cell afm; saturated and mono-unsaturated carboxylic acids," *Tribology Letters*, vol. 57, no. 2, p. 18, 2015.

[4] H. Spikes, "Friction modifier additives," *Tribology Letters*, vol. 60, no. 1, p. 5, 2015.

[5] M. I. D. B. Bouchet, J. M. Martin, J. Avila, M. Kano, K. Yoshida, T. Tsuruda, S. Bai, Y. Higuchi, N. Ozawa, M. Kubo, *et al.*, "Diamond-like carbon coating under oleic acid lubrication: Evidence for graphene oxide formation in superlow friction," *Scientific Reports*, vol. 7, no. 1, pp. 1–13, 2017.

[6] M. Kano, J. M. Martin, K. Yoshida, and M. I. D. B. Bouchet, "Super-low friction of ta-c coating in presence of oleic acid," *Friction*, vol. 2, no. 2, pp. 156–163, 2014.

[7] S. M. Lundgren, M. Ruths, K. Danerlöv, and K. Persson, "Effects of unsaturation on film structure and friction of fatty acids in a model base oil," *Journal of colloid and interface science*, vol. 326, no. 2, pp. 530–536, 2008.

[8] A. M. Khan, H. Wu, Q. Ma, Y.-W. Chung, and Q. J. Wang, "Relating tribological performance and tribofilm formation to the adsorption strength of surface-active precursors," *Tribology Letters*, vol. 68, no. 1, p. 6, 2020.

[9] L. Chen, J. Wen, P. Zhang, B. Yu, C. Chen, T. Ma, X. Lu, S. H. Kim, and L. Qian, "Nanomanufacturing of silicon surface with a single atomic layer precision via mechanochemical reactions," *Nature communications*, vol. 9, no. 1, pp. 1–7, 2018.

[10] B. A. Sexton, "The structure of acetate species on copper (100)," *Chemical Physics Letters*, vol. 65, no. 3, pp. 469–471, 1979.

[11] J. James, D. K. Saldin, T. Zheng, W. Tysoe, and D. S. Sholl, "Structure and binding site of acetate on *Pd* (1 1 1) determined using density functional theory and low energy electron diffraction," *Catalysis Today*, vol. 105, no. 1, pp. 74–77, 2005.

[12] R. Levy and M. Boudart, "Platinum-like behavior of tungsten carbide in surface catalysis," *science*, vol. 181, no. 4099, pp. 547–549, 1973.

[13] L. Bennett, J. Cuthill, A. McAlister, N. Erickson, and R. Watson, "Electronic structure and catalytic behavior of tungsten carbide," *Science*, vol. 184, no. 4136, pp. 563–565, 1974.

[14] S. Oyama, "Preparation and catalytic properties of transition metal carbides and nitrides," *Catalysis Today*, vol. 15, no. 2, pp. 179–200, 1992.

[15] H. H. Hwu and J. G. Chen, "Surface chemistry of transition metal carbides," *Chemical Reviews*, vol. 105, no. 1, pp. 185–212, 2005.

[16] J. B. Benziger, E. Ko, and R. J. Madix, "The characterization of surface carbides of tungsten," *Journal of Catalysis*, vol. 54, no. 3, pp. 414–425, 1978.

[17] H.-P. Lin, Z.-X. Yang, S.-H. Lee, T.-Y. Chen, Y.-J. Chen, Y.-H. Chen, G.-J. Chen, S.-X. Zhan, and J.-L. Lin, "Adsorption and reactions of propenoic acid and 2-fluoropropanoic acid on Cu (100) and O/Cu (100)," *The Journal of chemical physics*, vol. 150, no. 16, p. 164703, 2019.

[18] O. Karis, J. Hasselström, N. Wassdahl, M. Weinelt, A. Nilsson, M. Nyberg, L. G. Pettersson, J. Stöhr, and M. G. Samant, "The bonding of simple carboxylic acids on Cu (110)," *The Journal of Chemical Physics*, vol. 112, no. 18, pp. 8146–8155, 2000.

[19] M. Bowker and R. Madix, "The adsorption and oxidation of acetic acid and acetaldehyde on Cu (110)," *Applications of Surface Science*, vol. 8, no. 3, pp. 299–317, 1981.

[20] N. Canning and R. Madix, "Towards an organometallic chemistry of surfaces," *The Journal of Physical Chemistry*, vol. 88, no. 12, pp. 2437–2446, 1984.

[21] M. Kaltchev, A. Thompson, and W. Tysoe, "Reflection-absorption infrared spectroscopy of ethylene on palladium (111) at high pressure," *Surface science*, vol. 391, no. 1-3, pp. 145–149, 1997.

[22] F. Gao, O. Furlong, P. V. Kotvis, and W. Tysoe, "Pressure dependence of shear strengths of thin films on metal surfaces measured in ultrahigh vacuum," *Tribology Letters*, vol. 31, no. 2, p. 99, 2008.

[23] O. J. Furlong, B. P. Miller, and W. T. Tysoe, "Shear-induced surface-to-bulk transport at room temperature in a sliding metal–metal interface," *Tribology Letters*, vol. 41, no. 1, pp. 257–261, 2011.

[24] G. Kresse and D. Joubert, "From ultrasoft pseudopotentials to the projector augmented-wave method," *Physical Review b*, vol. 59, no. 3, p. 1758, 1999.

[25] P. E. Blöchl, "Projector augmented-wave method," *Physical Review B*, vol. 50, no. 24, p. 17953, 1994.

[26] G. Kresse and J. Hafner, "Ab initio molecular dynamics for liquid metals," *Physical Review B*, vol. 47, no. 1, p. 558, 1993.

[27] G. Kresse and J. Furthmüller, "Efficient iterative schemes for ab initio total-energy calculations using a plane-wave basis set," *Physical Review B*, vol. 54, no. 16, p. 11169, 1996.

[28] G. Kresse and J. Furthmüller, "Efficiency of ab-initio total energy calculations for metals and semiconductors using a plane-wave basis set," *Computational Materials Science*, vol. 6, no. 1, pp. 15–50, 1996.

[29] J. P. Perdew, K. Burke, and M. Ernzerhof, "Generalized gradient approximation made simple," *Physical Review Letters*, vol. 77, no. 18, p. 3865, 1996.

[30] T. Smetyukhova, A. Druzhinin, and D. Podgorny, "Features of the auger spectra of $Ti_2C, SiC, and WC$," *Journal of surface investigation: X-ray, Synchrotron and Neutron Techniques*, vol. 11, no. 2, pp. 414–419, 2017.

[31] B. D. S. MP, "Practical surface analysis, auger and x-ray photoelectron spectroscopy, vol. 1," 1990.

[32] O. J. Furlong, B. P. Miller, P. Kotvis, and W. T. Tysoe, "Low-temperature, shear-induced tribofilm formation from dimethyl disulfide on copper," *ACS applied materials & interfaces*, vol. 3, no. 3, pp. 795–800, 2011.

[33] B. Miller, O. Furlong, and W. T. Tysoe, "The kinetics of shear-induced boundary film formation from dimethyl disulfide on copper," *Tribology Letters*, vol. 49, no. 1, pp. 39–46, 2013.

[34] H. Adams, B. P. Miller, P. V. Kotvis, O. J. Furlong, A. Martini, and W. T. Tysoe, "In situ measurements of boundary film formation pathways and kinetics: dimethyl and diethyl disulfide on copper," *Tribology Letters*, vol. 62, no. 1, p. 12, 2016.

[35] N. Gosvami, J. Bares, F. Mangolini, A. Konicek, D. Yablon, and R. Carpick, "Mechanisms of antiwear tribofilm growth revealed in situ by single-asperity sliding contacts," *Science*, vol. 348, no. 6230, pp. 102–106, 2015.

[36] J. Zhang and H. Spikes, "On the mechanism of $ZDDP$ antiwear film formation," *Tribology Letters*, vol. 63, no. 2, p. 24, 2016.

[37] F. Gao, O. Furlong, P. V. Kotvis, and W. T. Tysoe, "Reaction of tributyl phosphite with oxidized iron: surface and tribological chemistry," *Langmuir*, vol. 20, no. 18, pp. 7557–7568, 2004.

[38] C. J. Jenks, C. M. Chiang, and B. E. Bent, "Alkyl iodide decomposition on copper surfaces:. alpha.-elimination and. beta.-hydride elimination from adsorbed alkyls," *Journal of the American Chemical Society*, vol. 113, no. 16, pp. 6308–6309, 1991.

[39] C. J. Jenks, B. E. Bent, and F. Zaera, "The chemistry of alkyl iodides on copper surfaces. 2. influence of surface structure on reactivity," *The Journal of Physical Chemistry B*, vol. 104, no. 14, pp. 3017–3027, 2000.

Chapter 6

Tribochemical Mechanisms of Trimethyl and Triethyl Phosphite on Oxidized Iron in Ultrahigh Vacuum

6.1 Introduction

Commercial lubricants comprise a base oil whose properties are tailored by adding a wide range of compounds including, for example, antioxidants, detergents, corrosion inhibitors, anti-foaming agents and viscosity index improvers, as well as those that react at the sliding interface to form friction- or wear-reducing films [1], and often contain elements such as sulfur, phosphorus or halogens [2]. In particular, phosphate and phosphite esters are extensively used as lubricant additives where Fe(III) surfaces were found to be the most reactive for film formation [3, 4]. It is generally accepted that phosphate esters react to form a phosphate film in the oxide surface layer [5–9].

The chemistry of tributyl phosphate has been investigated previously on clean iron

surfaces in ultrahigh vacuum (UHV) [10]. It has been suggested that the surface reaction could be initiated either by cleavage of the P–O bond to yield a surface alkoxy species or alternatively by the cleavage of the C–O bond to yield surface alkyl groups. It was found on clean iron that the formation of alkyl species dominated the surface reaction [11–14]. In contrast, the surface chemistry of tributyl phosphite (TBPi) and phosphate on oxidized iron were found to occur by P–O scission to predominantly form butoxide species on the surface [15, 16]. In this case, a depth profile of the oxide surface heated to high temperatures after reaction with the phosphite ester revealed the presence of subsurface phosphorus in the film.

A number of investigations have been carried out to measure the friction coefficient of surfaces lubricated by phosphate and phosphite esters. A relatively low friction coefficient of ~0.2 was obtained for gas-phase lubrication of trimethyl phosphite (TMPi) with a gas-phase pressure of $>10^{-2}$ hPa (1 hPa = 0.75 Torr) at a sample temperature of ~300 K, or with 5 hPa at 373 K [17, 18]. Work has also compared the gas-phase lubrication behavior of TMPi, dimethyl phosphite and trimethyl phosphate and found limiting values of the friction coefficients that depended on the nature of the gas-phase lubricant, reaching a steady-state value of ~0.23 for TMPi, ~0.34 for dimethyl phosphite and ~0.46 for trimethyl phosphate, close to the value for these lubricant additives in the liquid phase [17, 19]. The observed friction found using phosphites compared to phosphates was correlated to the type of the tribofilm formed [19]. Low-friction films

were found for tricresyl phosphate (TCP) and trioctyl phosphate (TOP) in a four-ball machine, where the friction of TOP stabilized ~0.126, while using TCP showed a final friction value of ~0.14 [6, 20]. These results indicate that, while the alkyl groups in phosphate and phosphite esters allows them to dissolve in the base oil, the nature of the side groups can influence the resulting tribological behavior.

Since the oxidation state of the substrates influences the friction of the tribofilm, the following compares the surface chemistry of TMPi and triethyl phosphite (TEPi) on oxidized iron measured in UHV and the results are compared with the gas-phase lubrication behavior of TEPi measured using a UHV tribometer.

6.2 Experimental Section

Surface chemistry experiments were carried out in a UHV chamber where the base pressure after the bakeout is ~ 2×10^{-10}. An iron foil (0.1 mm thick, Alfa-Aesar, 99.99% pure) was mounted onto a UHV-compatible sample manipulator via a ~0.45 mm thick steel plate to ensure that the sample was rigid, in particular for subsequent tribological experiments, and a K-type thermocouple was attached to the back of the steel base to monitor the temperature of the sample. The sample was in contact with a liquid-nitrogen filled reservoir that allowed it to be cooled to ~180 K and it could also be resistively heated to ~950 K. The analysis chamber was equipped with an X-ray source

with both Al and Mg anodes and a double-pass cylindrical mirror analyzer (CMA) for electron energy analysis. Experiments were carried out using an X-ray source energy of 250 W and collected with an analyzer pass energy of 100 eV. After a Shirley background subtraction [21], the energy profiles were fit using XPSPEAK with a fixed Gaussian-to-Lorentzian ratio. The analysis chamber also contained a Dycor quadrupole mass spectrometer for temperature programmed desorption (TPD) measurements, leak checking and for monitoring the purity of chemicals that were used in the experiments.

The tribological studies of TEPi on an oxidized surface were carried out in an UHV-compatible tribometer with a tungsten carbide pin (diameter of 1.27×10^{-2}m), which reciprocates with the sliding speed of 4×10^{-3}m/s [22]. The friction coefficient (μ) and contact resistance (Ω) were continually monitored while sliding. The tribometer is controlled by micro stepper motors, which can move linearly for locating the pin at the desired rubbing position on the flat, and reciprocates during the friction test. The tribo-arm can be rotated towards the ion gun for cleaning the tungsten carbide pin by Ar ion bombardment, or towards the CMA for monitoring the cleanliness of the tungsten carbide tip surface by Auger electron spectroscopy (AES).

The iron foil was cleaned in UHV by Ar ion bombardment with a 3.5 $\mu A/cm^2$ sample current using a 2 keV beam energy and then annealed at ~1000 K to remove any remaining surface contaminants predominantly consisting of sulfur. This cycle was

repeated until the sample was clean by AES except for a small amount of oxygen remaining on the surface that was not completely removed as the surface would later be oxidized. The clean iron foil was oxidized using a procedure describe previously [15] by heating in a background pressure of 5×10^{-7} Torr of O_2 (99.998% pure) for 30 minutes at 800 K. TPD experiments were carried out using a sample heating rate of 4.2 K/s with the front of the sample placed close to and in-line-of-sight of the quadrupole mass spectrometer ionizer.

The trimethyl phosphite (TMPi, Sigma Aldrich, ≥99.0% purity) and triethyl phosphite (TEPi, Sigma Aldrich, 98.0% purity) were transferred to glass bottles and were purified by several freeze-pump-thaw cycles. The purity of the phosphite esters was checked by GCMS and by using a quadrupole mass spectrometer after introduction into the UHV chamber.

6.3 Results

6.3.1 Formation, Characterization and Friction of Iron Oxide Films on Clean Iron

The iron oxide film was grown on a clean iron substrate by heating in a background pressure of 5.0×10^{-7} Torr of oxygen at a sample temperature of 800 K for 30 minutes

(corresponding to a 900 L oxygen exposure, 1L (Langmuir) = 1.0×10^{-6} Torr.s). Previous work has shown that these oxidation conditions produce an Auger spectrum that is consistent with the formation of an Fe_3O_4 film on the iron substrate [15, 16]. It has also been shown that Fe_3O_4 films are found on iron after oxygen exposures above ~400 L for reaction at 800 K [23]. The oxide film was monitored here using X-ray photoelec-

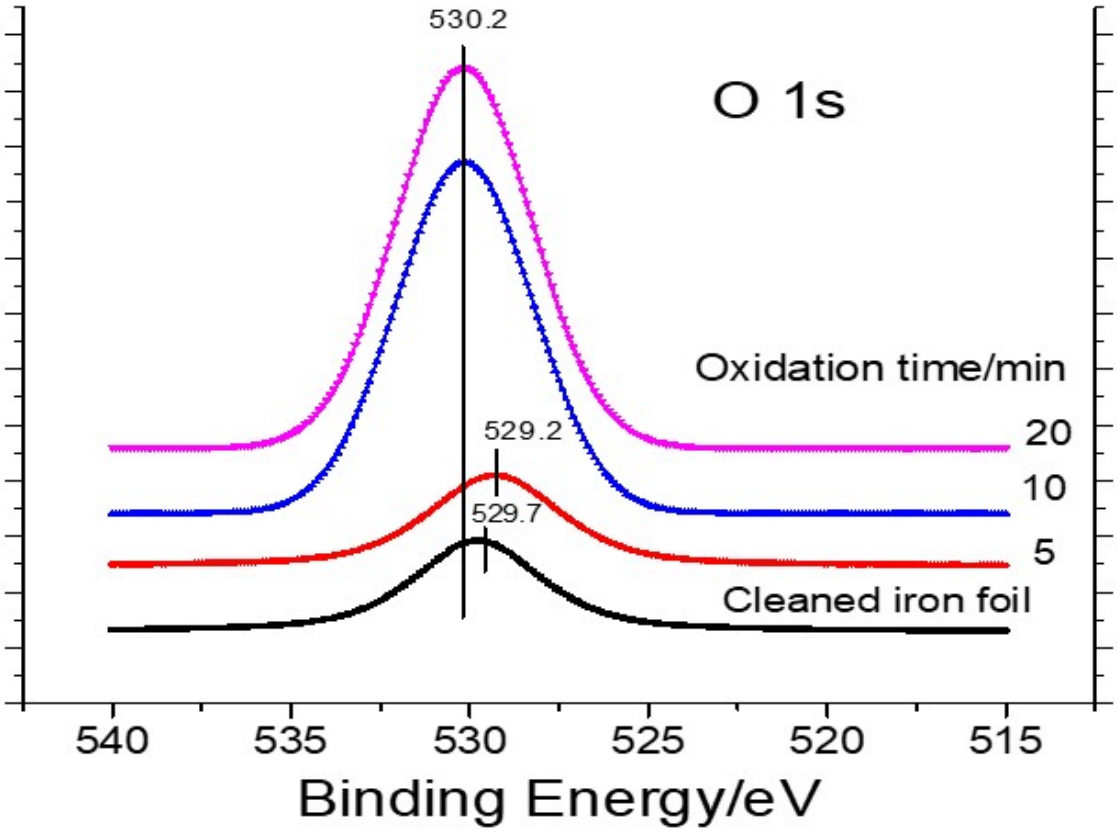

FIGURE 6.1: O 1s X-ray photoelectron spectrum of an iron foil oxidized in a background pressure of 5×10^{-7} Torr of oxygen at 800 K for various times. The reaction times are indicated adjacent to the corresponding spectrum.

tron spectroscopy (XPS) where Figure 6.1 displays the evolution in intensity of the O

1s feature on the iron foil as a function of oxidation time at 800 K in a background pressure of 5.0×10^{-7} Torr of oxygen. This shows the presence of a small O 1s signal after initially cleaning the sample in oxygen and then heating the iron foil. Heating in oxygen causes the O 1s intensity to increase with reaction time and then saturate after 600 s, consistent with the kinetics of oxide formation on an iron single crystal [23]. The final O 1s binding energy of 530.2 ± 0.1 eV is also consistent with the formation of an Fe_3O_4 surface film [24, 25].

Since experiments are carried out to study the friction of the oxide film on iron in the presence of background pressures of phosphite esters, it is necessary to ensure that the oxide film is not removed during rubbing. Accordingly, a freshly oxidized film, formed using the procedure described above, was rubbed in vacuo at a load of 0.29 N at a sliding speed of 4.0×10^{-3} m/s and the resulting values of contact resistance (■) and friction coefficient (●) are displayed as a function of the number of passes in Figure 6.2. Note that the initial contact resistance of ~1.2 Ω is consistent with the presence of an oxide film as the contact resistance of a clean iron substrate is ~0.5 Ω. In addition, the initial friction coefficient of ~1.6 reduces over the first ~20 passes to a stable value of 1.0 ± 0.2 (●), which is within the range found for oxidized steel surfaces in vacuum [18, 19, 26, 27]. The friction data are noisy due to the large stick-slip amplitude during sliding. The contact resistance (■) also decreases slightly during the initial run-in period to stabilize at 1.17 ± 0.01 Ω after approximately 20 cycles,

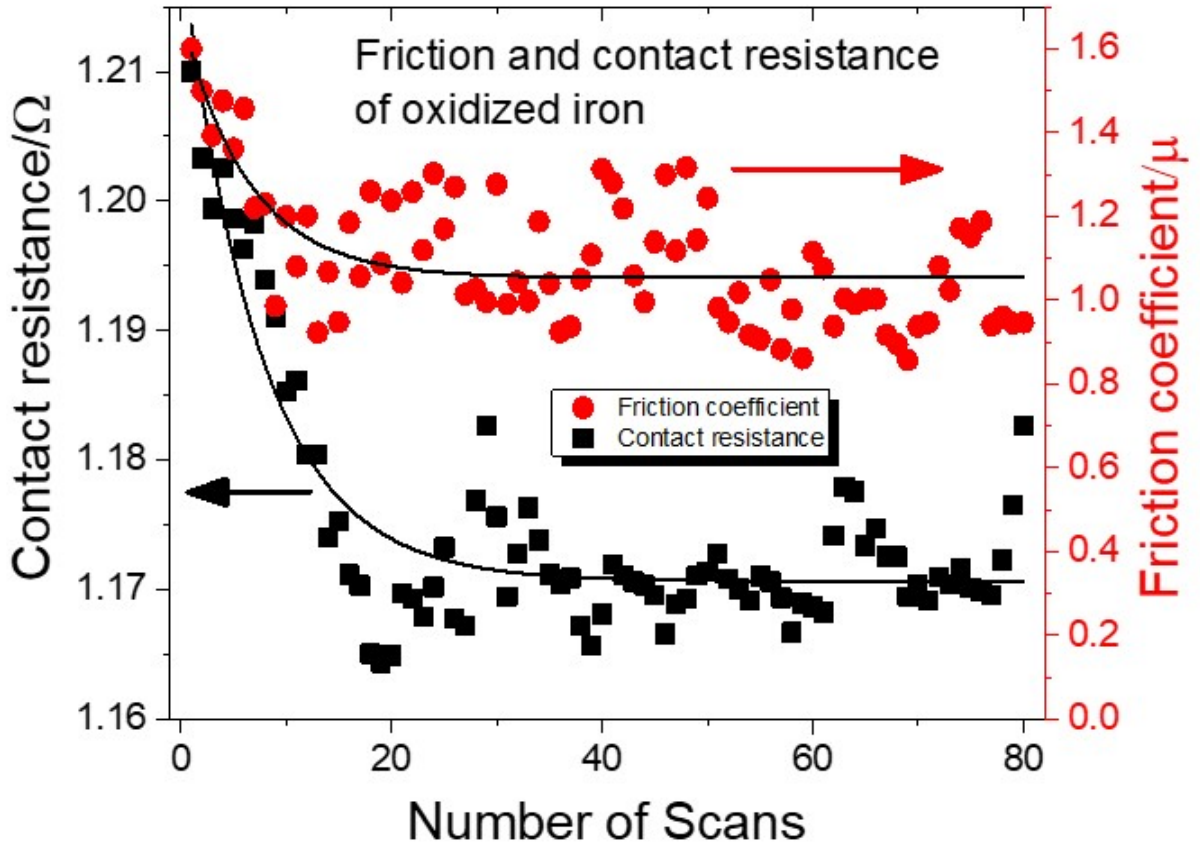

FIGURE 6.2: Friction coefficient (●) and contact resistance (■) of an oxide film grown on iron as a function of the number of passes at a sliding speed of 4×10^{-3} m/s at a normal load of 0.29 N.

consistent with the variation in friction coefficient. This suggests the formation of a wear track in the oxide layer. However, this does not remove the film to expose the metal beneath because the steady-state contact resistance remains much higher than that found for the clean metal. This indicates that tribochemical reactions carried out on thin Fe_3O_4 films will reflect the chemistry occurring on the oxide film.

6.3.2 Surface Chemistry of Trimethyl Phosphite on Fe_3O_4 Films on Iron

The surface chemistry of TMPi is followed using TPD and XPS on a thin Fe_3O_4 film grown on a polycrystalline iron as described above [15] by oxidizing the iron at 800 K for 30 minutes in a background of oxygen at 5×10^{-7} Torr. The surface chemistry was followed by monitoring the desorption products after exposure to the phosphite ester at a sample temperature of 180 K, and heating at 4.2 K/s while monitoring the desorption products at various masses. Figure 6.3 shows the 63 amu desorption profile, due to molecular TMPi, as a function of TMPi exposure in Langmuirs. Note that the exposures are not corrected for the ionization gauge sensitivity. This reveals a broad feature centered at ~280 K with a tail extending to ~500 K. Spectra collected at other masses confirms that this feature is due to the desorption of molecular TMPi. A Redhead analysis [28] using a pre-exponential factor of 1×10^{13} s^{-1} yields an estimated desorption activation energy of ~71 kJ/mol, which is a measure of the heat of adsorption of TMPi on the oxide surface. No TMPi desorbs for an exposure of 0.5 L, and little desorption is found for a 1 L exposure, suggesting that all the TMPi reacts for exposures below ~1L. Significant TMPi molecular desorption is observed for exposures greater than 2 L.

TPD (Figs. 6.4 and 6.5) reveals that the major desorption products are consistent with TMPi reacting by P–O bond scission as found for tributyl phosphite [15] where,

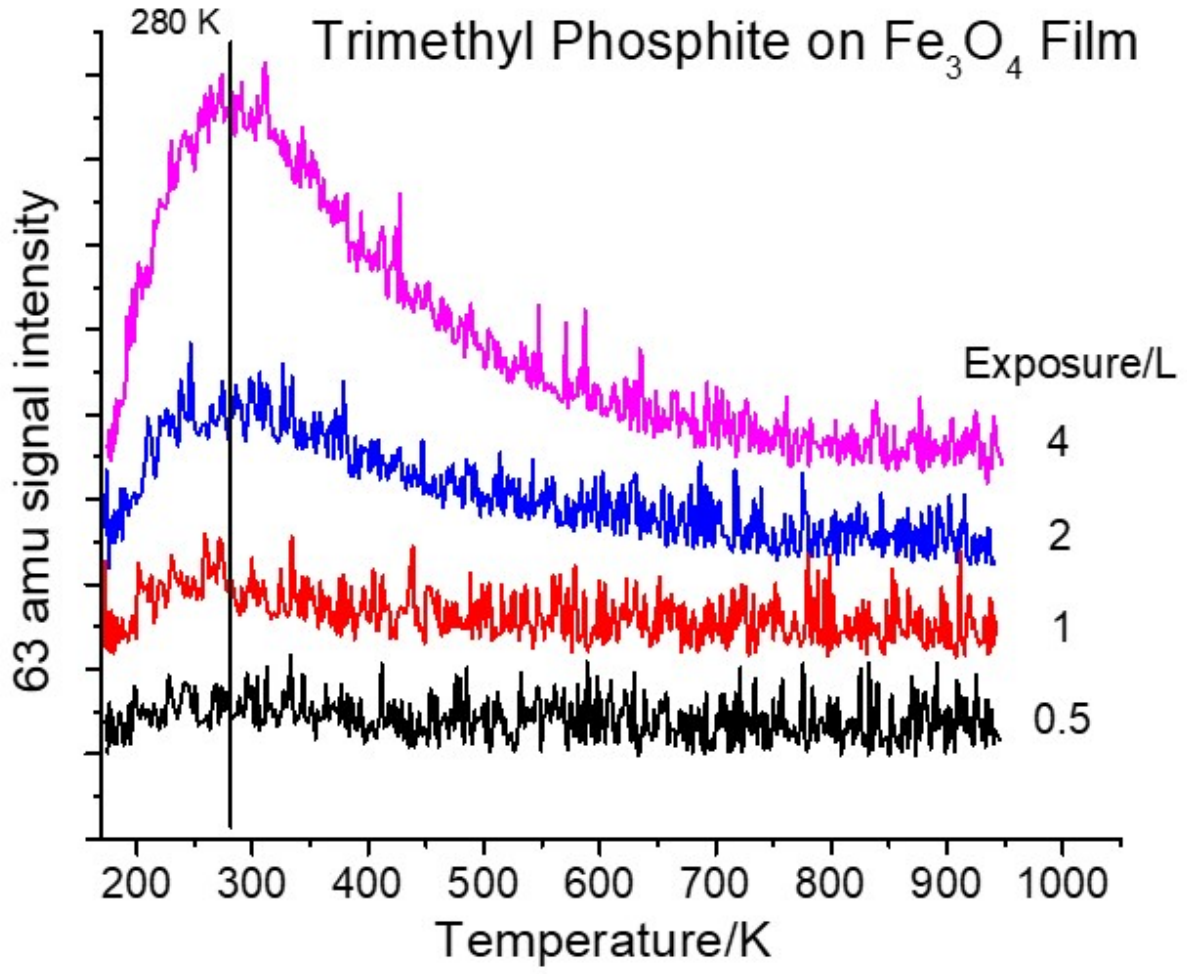

FIGURE 6.3: 63 amu TPD profiles as a function of exposure, in Langmuirs, of trimethyl phosphite on a Fe_3O_4 film on iron collected using a heating rate of 4.2 K/s. The trimethyl phosphate exposures are indicated adjacent to the corresponding spectrum.

in the case of TMPi, the resulting methoxy group can hydrogenate to form methanol or dehydrogenate to produce formaldehyde. This is illustrated by the 31 amu signal (Fig. 6.4), which is the most intense in the mass spectrum of methanol, while formaldehyde contains no 31 intensity, as a function of TMPi exposure. The intensity increases rapidly up to an exposure of ~1 L, and more slowly thereafter, coincident with the

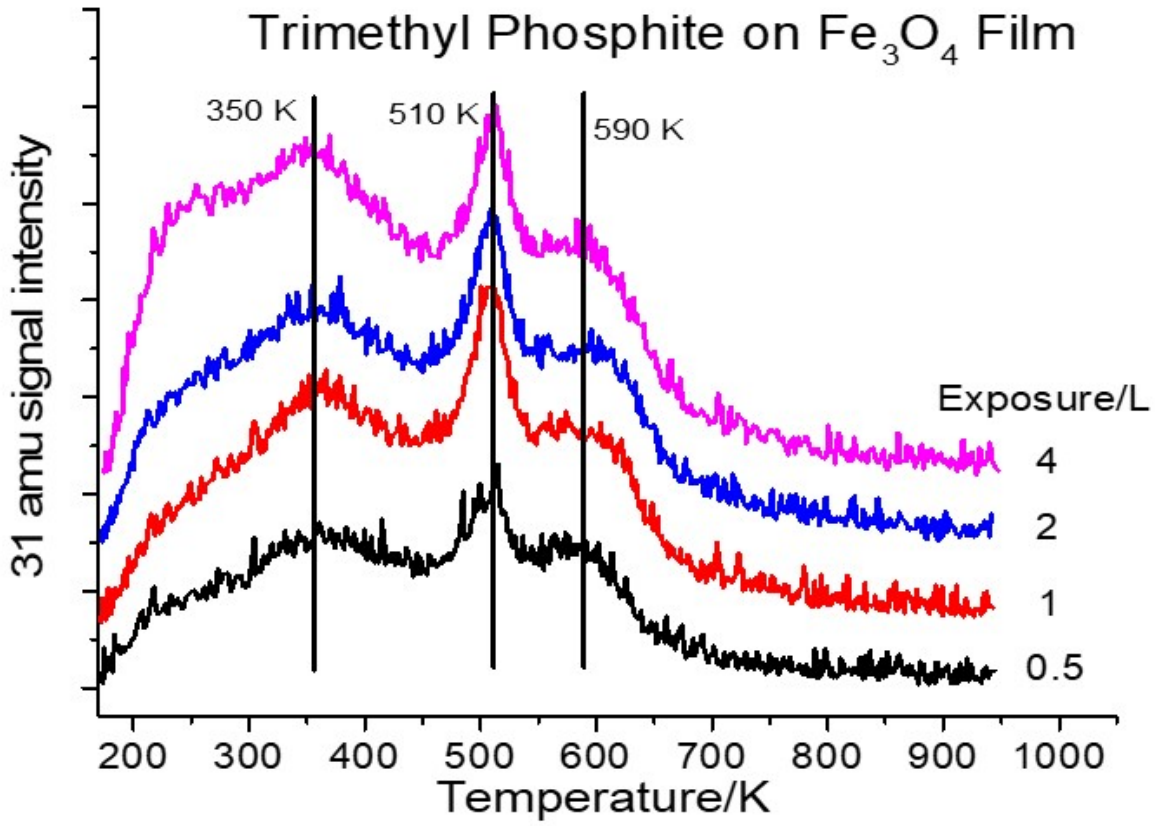

FIGURE 6.4: TPD data collected at 31 amu as a function of exposure, in Langmuirs, of trimethyl phosphite on a Fe_3O_4 film on iron collected using a heating rate of 4.2 K/s. The trimethyl phosphite exposures are indicated adjacent to the corresponding spectrum.

desorption of molecular TMPi (Figure 6.3). The profile consists of three distinct desorption states centered at ~350, ~510 and ~590 K, which grow equally as the TMPi coverage increases. This implies that methanol is formed in sequential steps from the decomposition of TMPi on the surface, presumably arising from each of the methoxy species in TMPi (see below). In order to explore whether TMPi decomposes to form exclusively methanol, the desorption spectra obtained by simultaneously monitoring

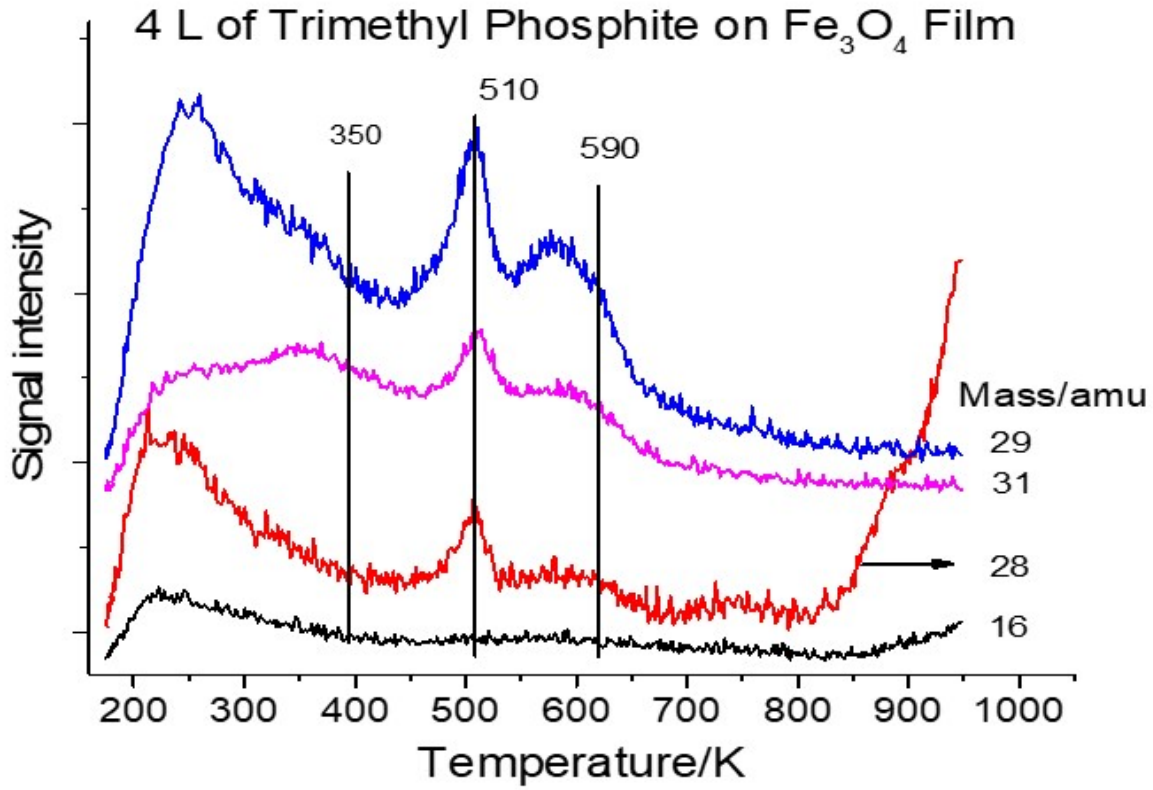

FIGURE 6.5: TPD data collected at various masses (indicated adjacent to the corresponding spectrum) following the exposure of 4 L of trimethyl phosphite on oxidized iron at 180 K.

signals at 29, 31, 28 and 16 amu are displayed in Fig. 6.5 for a 4 L TMPi exposure. These spectra show the same desorption states as in Fig. 6.4, but now with different relative intensities. Here, the 28 amu signal also corresponds to carbon monoxide desorption producing a rising background above ~800 K due to the reaction of some adsorbed carbonaceous species with the oxide film. This implies that a portion of the phosphite ester completely decomposes on the Fe_3O_4 surface. In addition, no methane (16 amu) is formed and thus confirms that TMPi decomposes by P–O bond scission.

The mass spectrum for methanol has a low 28 amu intensity so that the absence of any significant intensity at 28 amu for the ~350 K desorption states suggests that it is primarily due to the formation of methanol. However the ~510 and 590 K desorption states contain a significant 29 and 28 amu intensity showing that they arise from a combination of methanol and formaldehyde desorption and the relative intensities of the two states at various masses can be reproduced by a linear combination of the fragmentation patterns of methanol and formaldehyde, although their stoichiometric ratios cannot be obtained in this way because their absolute mass spectrometer sensitivities are not known. However, it is plausible that they desorb in equimolar amounts where the hydrogen required to form methanol from methoxy species is supplied by methoxy dehydrogenation to produce formaldehyde. This conjecture is corroborated from measurement of the integrated areas of the ~510 and 590 K desorption profiles where the ~510 K state comprises 0.49 ± 0.02 of the total yield for all exposures (from the data in Fig. 6.4).

Thus, TMPi decomposes on Fe_3O_4 in a sequential demethoxylation reaction to deposit phosphorus on the surface. Assuming that the product formation rates are controlled by P–O scission yields activation energies of ~90, ~132 and ~153 kJ/mol for the three steps. That is, as each methoxy group is removed, the subsequent reaction step becomes less energetically favored. The evolution in the nature of a Fe_3O_4 surface exposed to 30 L of TMPi is followed using XPS collected as a function of temperature.

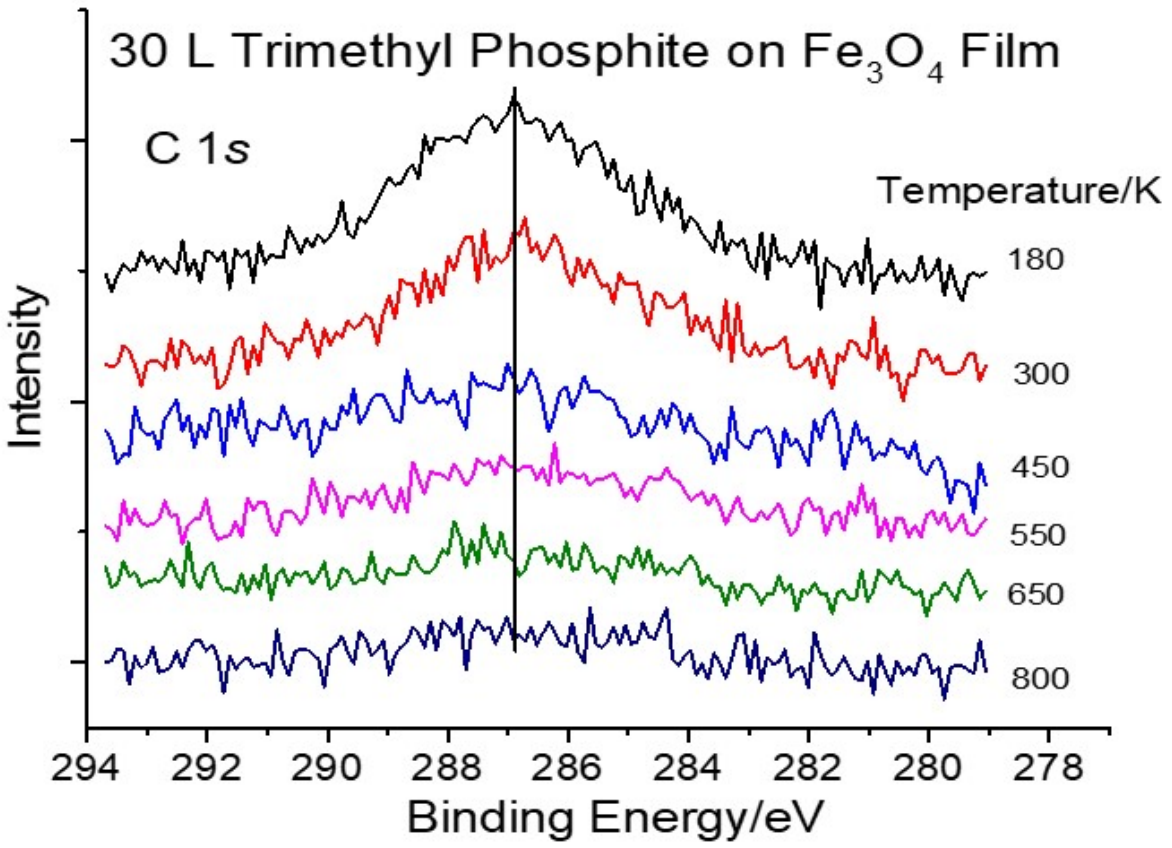

FIGURE 6.6: C 1s XPS spectra collected at various temperatures (indicated adjacent to the corresponding spectrum) following the exposure of 30 L of trimethyl phosphite on Fe_3O_4 at 180 K.

The resulting C 1s spectra are displayed in Fig. 6.6, showing a broad feature centered at ~286.9 eV binding energy (BE). The amount of carbon on the surface decreases as the sample is heated, where the C 1s signal has almost disappeared on heating to ~650 K in accord with the TPD data shown in Figs. 6.4 and 6.5. Very little carbon remains on heating to ~800 K and the small amount of remaining carbon reacts with the oxide

substrate to desorb CO at high temperatures (Fig. 6.5). The corresponding P 2p photoelectron spectra are displayed in Fig. 6.7, where the resolution is not sufficient to resolve the spin-orbit splitting so that the spectrum appears as a single feature. However,

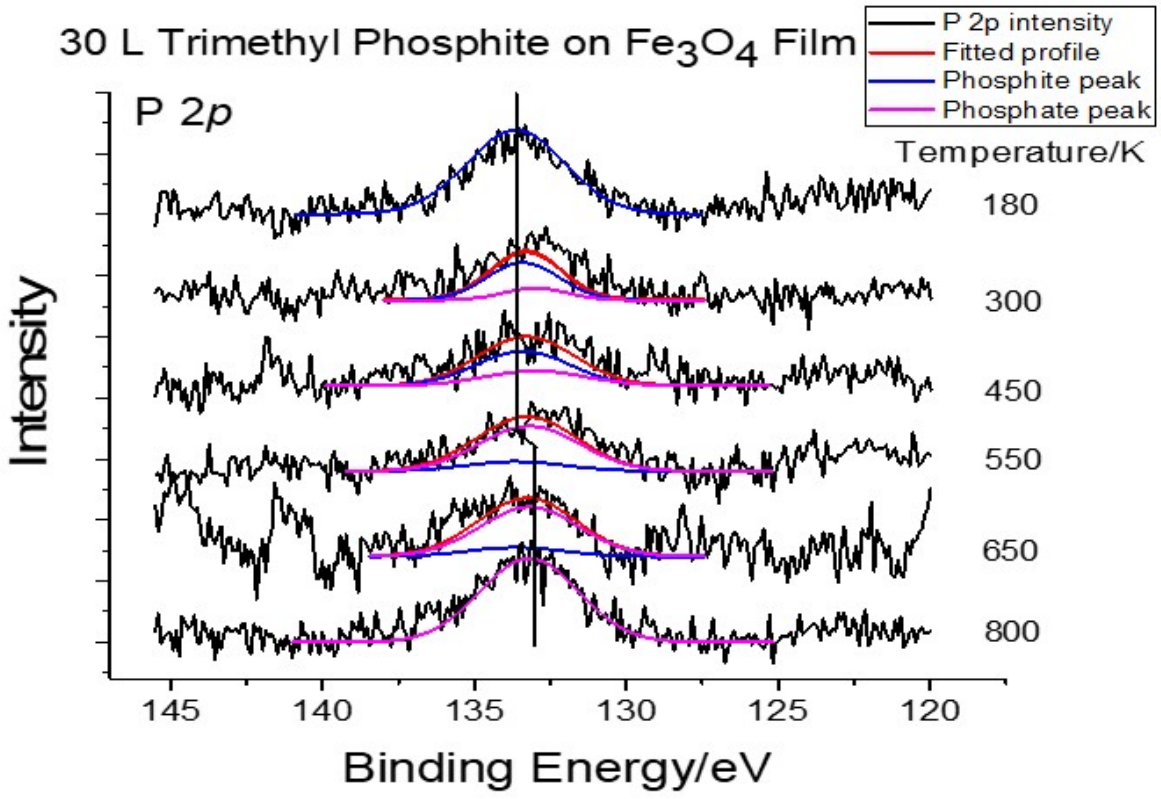

FIGURE 6.7: P 2p XPS spectra collected at various temperatures (indicated adjacent to the corresponding spectrum) following the exposure of 30 L of trimethyl phosphite on Fe_3O_4 at 180 K.

unlike the C 1s results, the phosphorus signal intensity remains essentially constant in accord with the demethoxylation chemistry described above. The spectrum for TMPi adsorbed at 180 K shows a P 2p peak with a binding energy (BE) of 133.6 eV. Since this temperature is below that at which any reaction takes place, it is assigned to adsorbed

molecular TMPi on the Fe_3O_4 surface [19]. However, TMPi condensed on a Fe(110) single crystal at 100 K shows a C 1s feature at 286.9 eV BE, identical to that found for TMPi on Fe_3O_4 (Fig. 6.6), but a P 2p peak at 133.9 eV BE [10]. The binding energy of TMPi adsorbed directly onto the metal decreases to 132.5 eV, having a greater chemical shift (to 133.6 eV BE) than for TMPi adsorbed on Fe_3O_4 (Fig. 6.7). The C 1s intensity deceases as the sample is heated and the carbon is essentially completely removed after heating to ~650 K, coincident with the completion of the reaction (Figs. 6.4 and 6.5). In the case of TMPi on Fe(110), the C 1s peak shifts to ~286.2 eV BE on heating and is assigned to methoxy species [29] formed during TMPi decomposition. However, no significant intensity is detected at this binding energy for TMPi on Fe_3O_4, suggesting that the methoxy species react as soon as they are formed in accord with the previous discussions. As the sample is heated, the P 2p intensity remains essentially constant, while there is a slight increase in binding energy to ~133.3 eV (Fig. 6.7), where the shift is highlighted by the solid line in the P 2p spectra. This is consistent with previous work that showed the presence of surface phosphorus after TBPi adsorption and heating, where a depth profile measured after reaction with an Fe_3O_4 film at ~800 K revealed that the phosphorus had diffused into the oxide film [15]. The 133.3 eV-BE feature is not due to remaining TMPi as it has all decomposed at this temperature, and a phosphide would appear at a binding energy of ~129 eV [17, 19, 30] clearly indicating

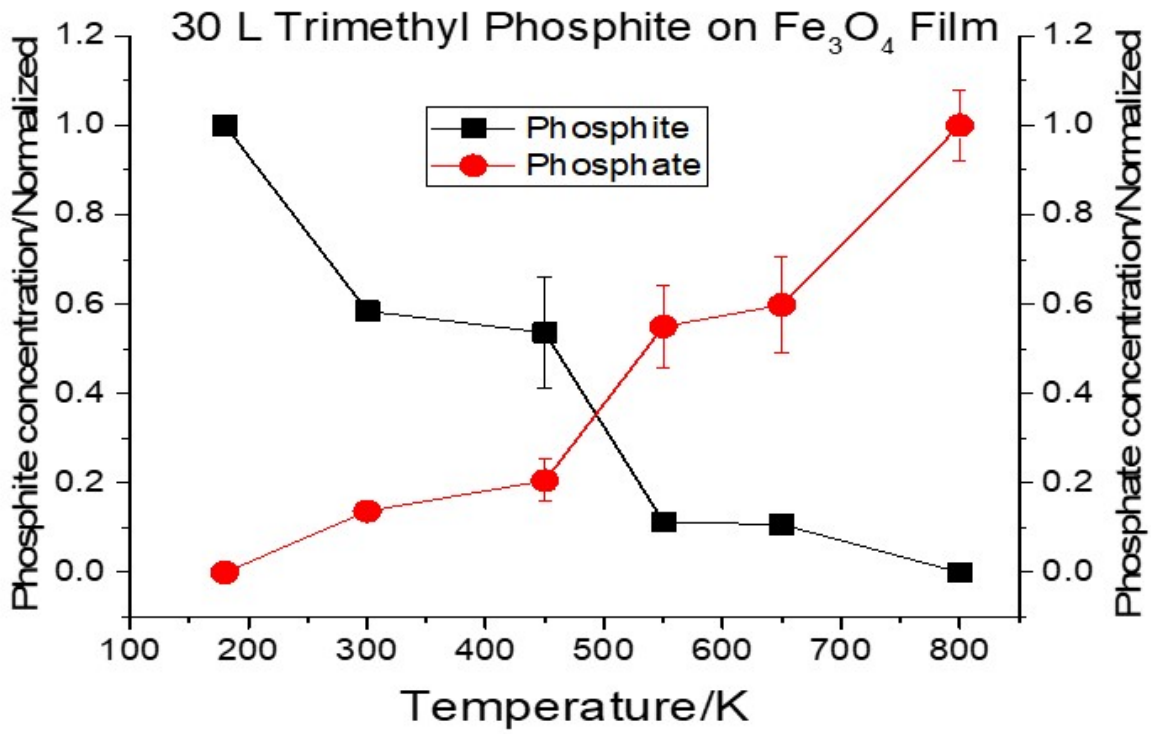

FIGURE 6.8: Proportion of phosphate and phosphite species on oxidized iron as a function of temperature following the exposure of 30 L of trimethyl phosphite at 180 K.

that the phosphorus in the film is oxidized. Polyphosphate films have a binding energy of ~133.6 eV [19, 31–33], slightly higher than that shown in Figure 6.7. However, since the films are formed in UHV, the phosphorus content is relatively low and this has been suggested to lead to a decrease in P 2p binding energy [34]. Consequently, the XPS feature at ~133.3 eV BE energy is assigned to the formation of a phosphate-containing film. Fits to the XPS profile in Fig. 6.7 enable the relative proportion of trimethyl phosphite (at ~133.6 eV BE) and the phosphate film (at ~133.3 eV BE) to be measured. The fits to the two features were constrained by fixing the positions and

widths of the combined Gaussian/Lorenztian profiles of the components and by only allowing the relative intensities to vary. The results are displayed in Figure 6.8.

6.3.3 Surface Chemistry of Triethyl Phosphite on Fe_3O_4 Films on Iron

Based on the results described above on the surface chemistry of TMPi on Fe_3O_4, analogous chemistry is expected for TEPi on oxidized iron in which the phosphite ester reacts by P–O bond scission to form ethoxy species that can either react to produce ethanol or dehydrogenate to yield acetaldehyde. In contrast to TMPi, TEPi can also undergo a β-hydride elimination reaction to form ethylene. The mass spectrum of ethanol has a parent peak at 31 amu, while acetaldehyde also has measurable intensity at this mass. The 31 amu desorption profiles of TEPi adsorbed on the Fe_3O_4 film as a function of exposure are displayed in Fig. 6.9. TEPi shows similar behavior as TMPi on the oxide film (shown in Figs. 6.4 and 6.5), exhibiting peaks at 350, 470 and 550 K. Note that the peak temperatures are lower than those found after TMPi adsorption which appear at 350, 510 and 590 K, suggesting that P–O bond scission is more facile as the alkyl chain length increases. The corresponding reaction activation energies, estimated from the Redhead equation [28], are ~90, 120 and 143 kJ/mol. Again, the yields measured from the integrated intensities of each desorption state are essentially the same.

The corresponding desorption profiles obtained while simultaneously monitoring

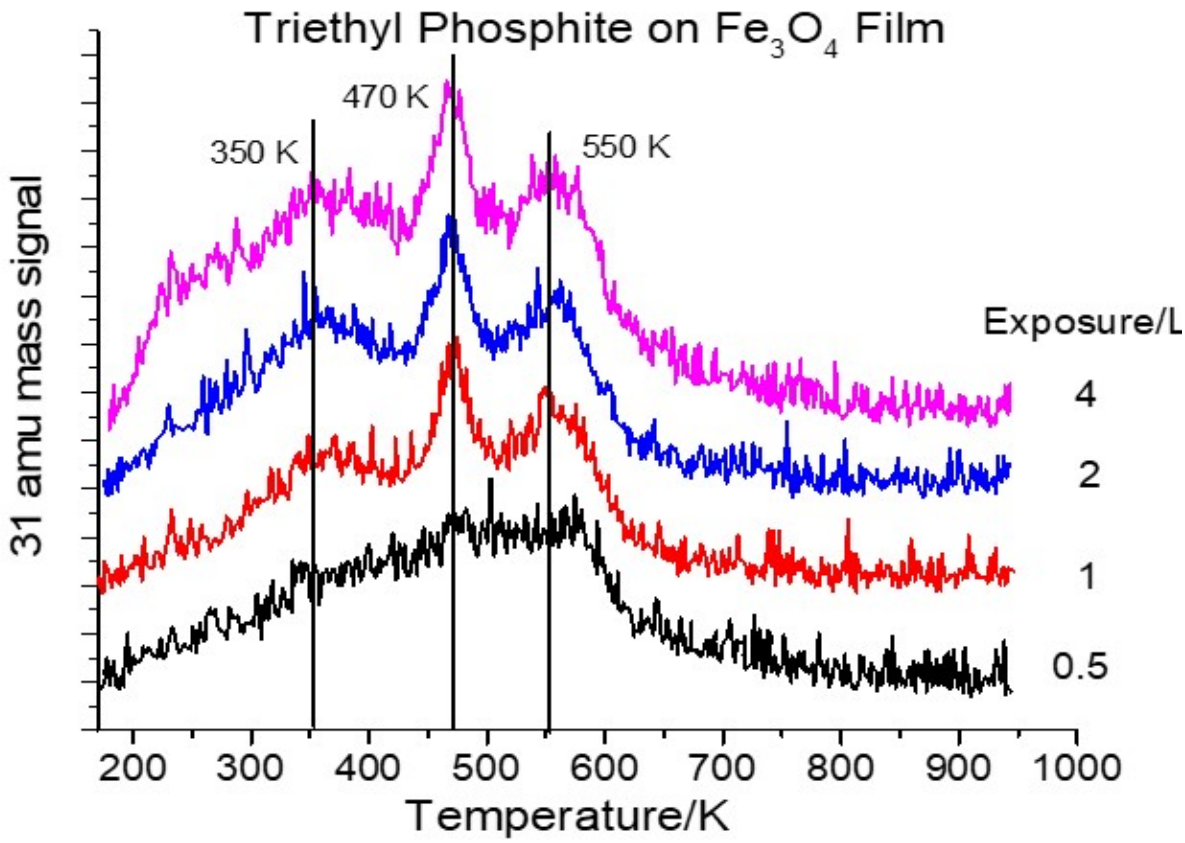

FIGURE 6.9: TPD data collected at 31 amu function of exposure, in Langmuirs, of triethyl phosphite on a Fe_3O_4 film on iron collected using a heating rate of 4.2 K/s. The triethyl phosphate exposures are indicated adjacent to the corresponding spectrum.

several masses are displayed in Fig. 6.10 for 4 L of TEPi on a Fe_3O_4 film. The profiles show intense features at 29 amu, indicating the formation of substantial amounts of acetaldehyde and the ratio of the 31 to 27 amu fragments is in accord with the 31 amu signal being due to ethanol. The 28-amu profile again shows the onset of carbon monoxide desorption above ~800 K due to oxidation of some adsorbed carbon by the oxide film. Note that there is a slight difference between the positions of the 31 and

29 amu features with the 29 amu (acetaldehyde) peak appearing at a slightly lower temperature than the 31 (ethanol) feature, in accord with the idea that ethoxy dehydrogenation to form acetaldehyde produces the hydrogen required to form ethanol.

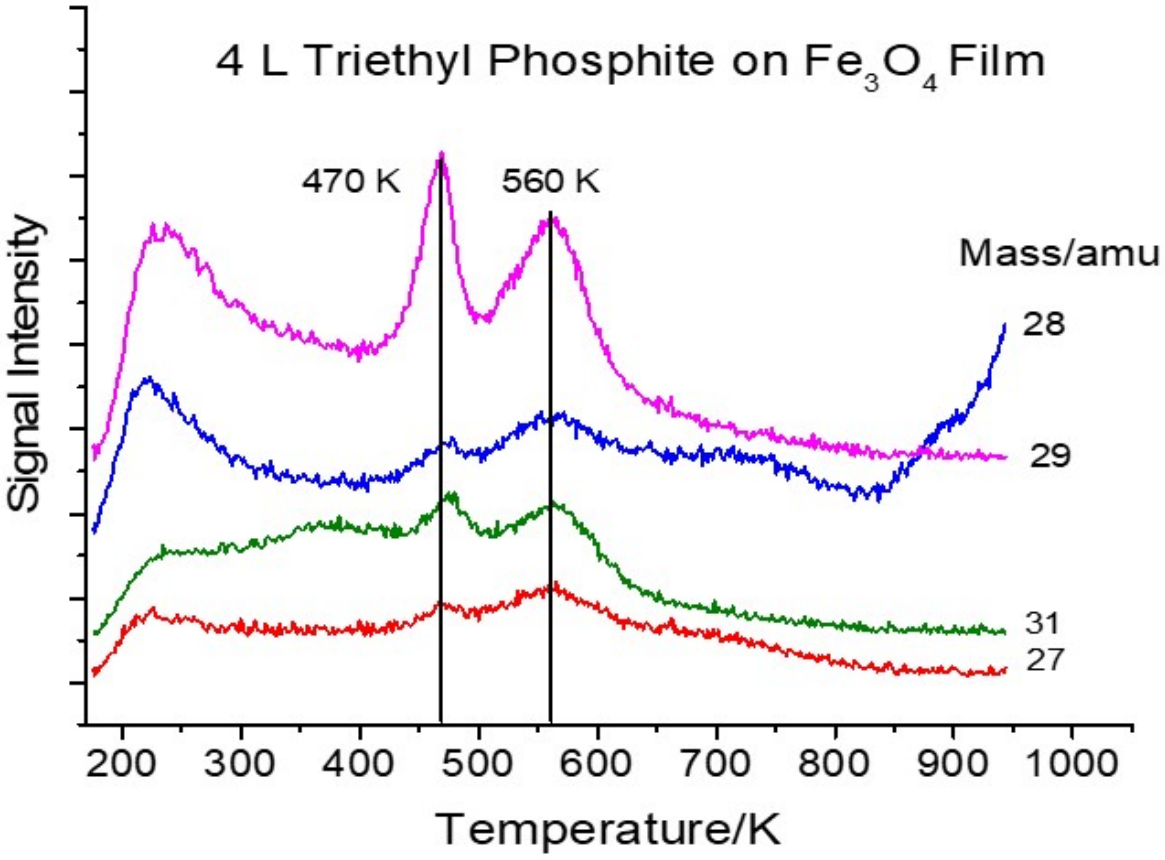

FIGURE 6.10: TPD data collected at various masses (indicated adjacent to the corresponding spectrum) following the exposure of 4 L of triethyl phosphite on oxidized iron at 180 K.

The C 1s spectra collected following the adsorption of 30 L of TEPi on the oxide film are displayed in Figure 6.11, which shows the removal of the ethoxy species in

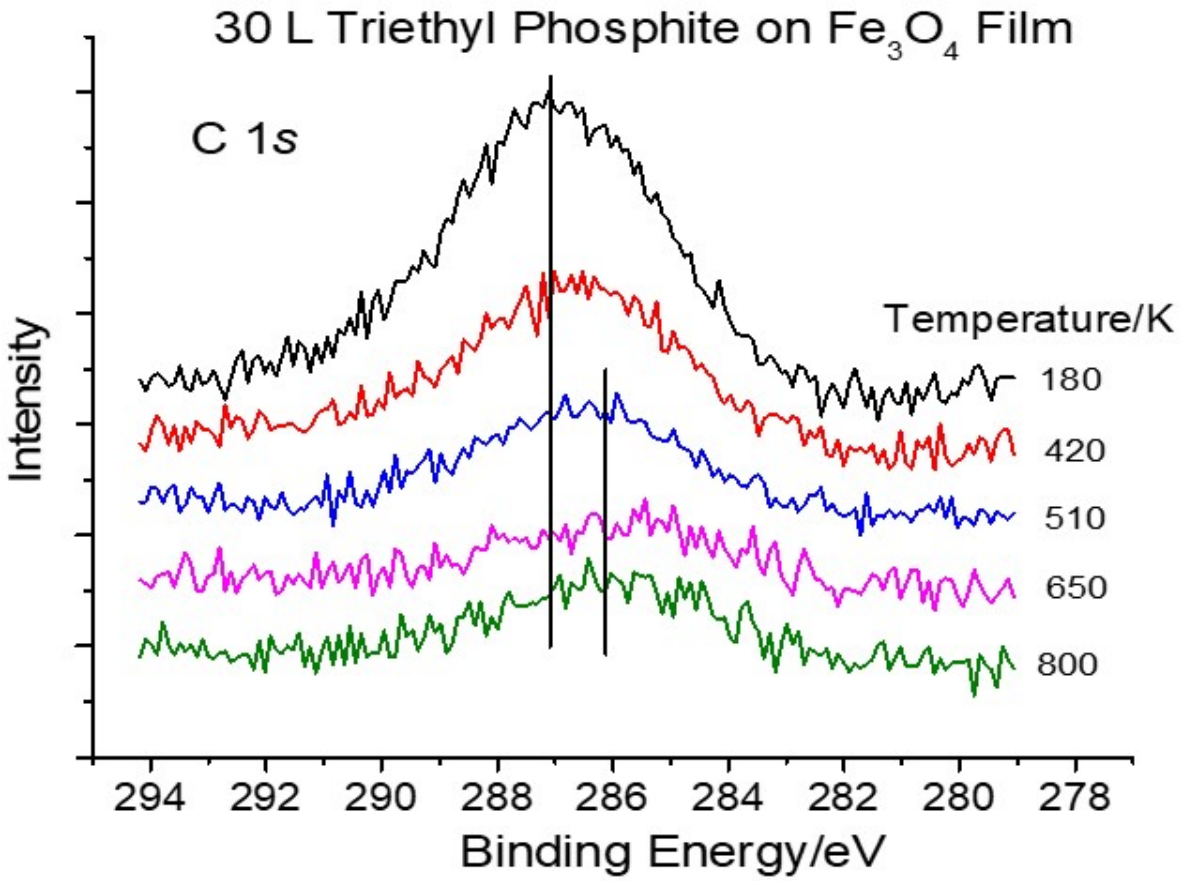

FIGURE 6.11: C 1s XPS spectra collected at various temperatures (indicated adjacent to the corresponding spectrum) following the exposure of 30 L of triethyl phosphite on oxidized iron at 180 K.

TEPi, which has a C 1s BE of 287.0 eV, similar to that found for TMPi. However, in this case, additional carbonaceous species remain on the surface (with a C 1s BE of 286.0 eV) after TEPi has reacted implying that, while P–O bond scission is more facile for TEPi than TMPi, the removal of the resulting alkoxy species is less efficient as the chain lengths increase, presumably because of the possibility of β-hydride elimination pathways. Note that the C 1s binding energy is not due to the formation of elemental

carbonaceous species on the surface, which should appear at ~285.5 eV BE [35] and implies that the carbon is oxidized, presumably due to interaction with the iron oxide substrate. Finally, there is some evidence of ethylene desorption in a broad state centered at ~750 K in the 28 and 27 amu profiles. The corresponding P 2p XPS spectra

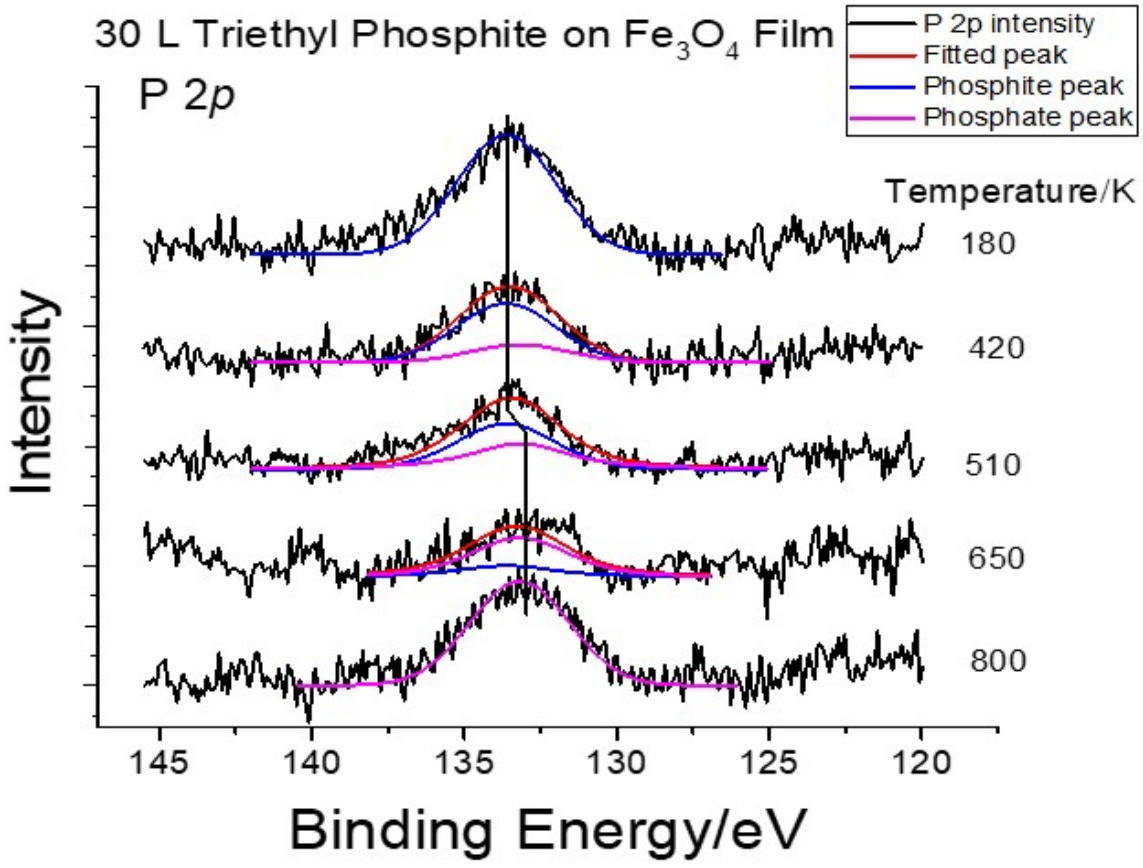

FIGURE 6.12: P 2p XPS spectra collected at various temperatures (indicated adjacent to the corresponding spectrum) following the exposure of 30 L of triethyl phosphite on oxidized iron at 180 K.

collected as a function of sample temperature are displayed in Figure 6.12 and show the same evolution as found for trimethyl phosphite, with a P 2p feature found at low

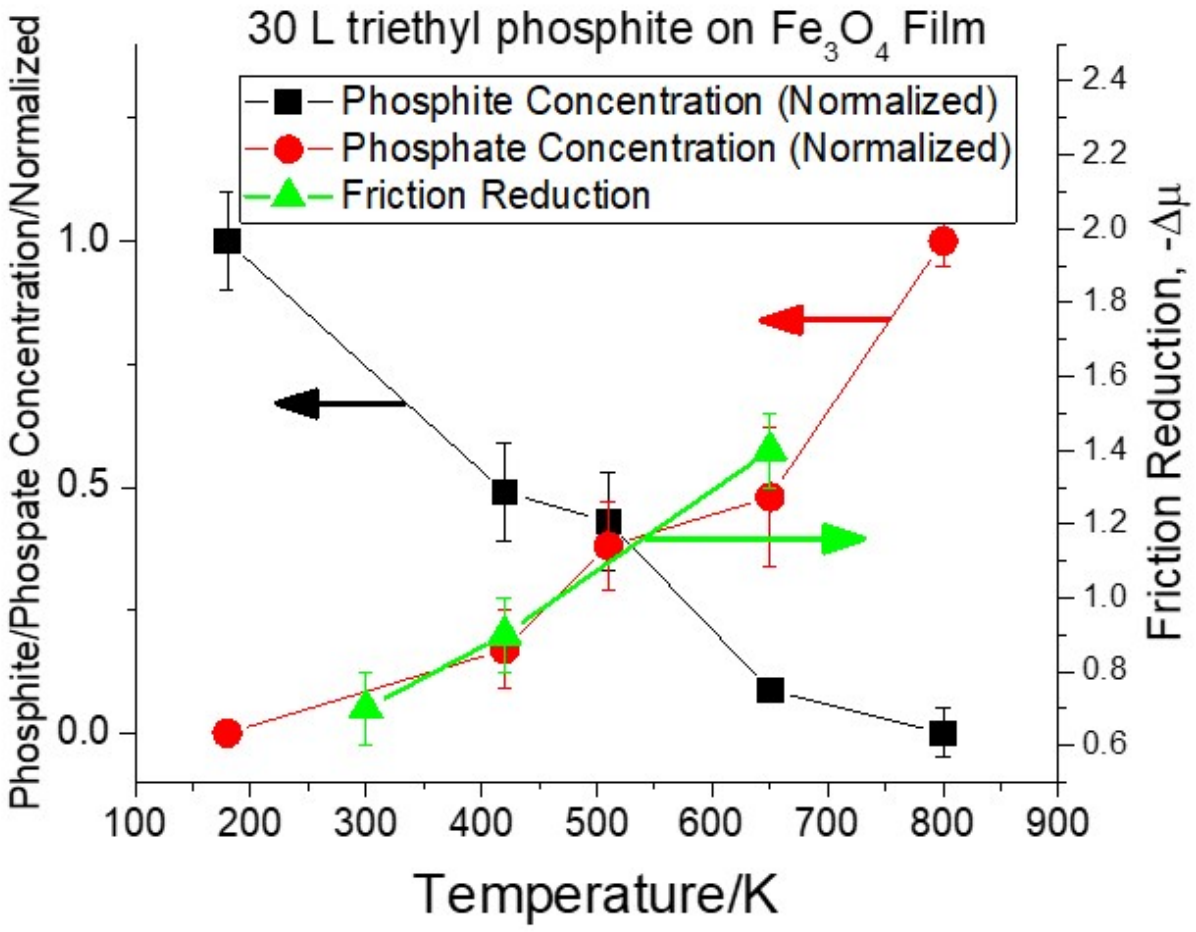

FIGURE 6.13: Proportion of phosphate (●) and phosphite (■) species on oxidized iron as a function of temperature following the exposure of 30 L of triethyl phosphite at 180 K. Reduction in friction during gas-phase lubrication of oxidized iron at various temperatures (▲, see text).

temperatures due to the phosphite ester shifting with increasing annealing temperature to indicate the formation of a phosphate. This is emphasized in the data plotted in Figure 6.13, which shows the proportion of phosphate and phosphite species on the surface as a function of annealing temperature again showing the formation of iron phosphate over the temperature at which ethanol and acetaldehyde desorb.

6.3.4 Gas-Phase lubrication of Fe_3O_4 Films on Iron by Triethyl Phosphite

In order to correlate the surface chemistry of TEPi with its tribological properties, the evolution in friction of a Fe_3O_4 film was measured in the presence of 1×10^{-7} Torr of TEPi with the sample held at 300, 420 and 650 K while rubbing under a load of 0.29 N at a sliding speed of 4×10^{-3} m/s. The decrease in friction relative to that of the initial oxide film is shown in Figure 6.14 (a) for reaction at 300 K, (b) for reaction at 420 K and (c) for reaction at 650 K, as a function of the number of times that the sample was rubbed, which decreases to a steady-state value between 20 and 40 scans. Since each cycle takes approximately 20 s, this corresponds to a total TEPi exposure of 40 to 80 L. The friction reduction increases with increasing reaction temperature from $\Delta\mu$ ~0.7 at 300 K, ~0.9 at 420 K and ~1.4 at 650 K and arises from a combination of the initial run-in period (Fig. 6.2) and the formation of a friction-reducing film. In addition, the number of passes required for the friction coefficient to attain its minimum value increases as the reaction temperature increases, likely due to a decrease in the TEPi coverage at higher temperatures. These results correlate with the increase in phosphate coverage with increasing reaction temperature (Figure 6.13), where the friction reduction is plotted along with the XPS results for the film composition (▲) indicating that the formation of a phosphate-containing film is responsible for the significant reduction in friction.

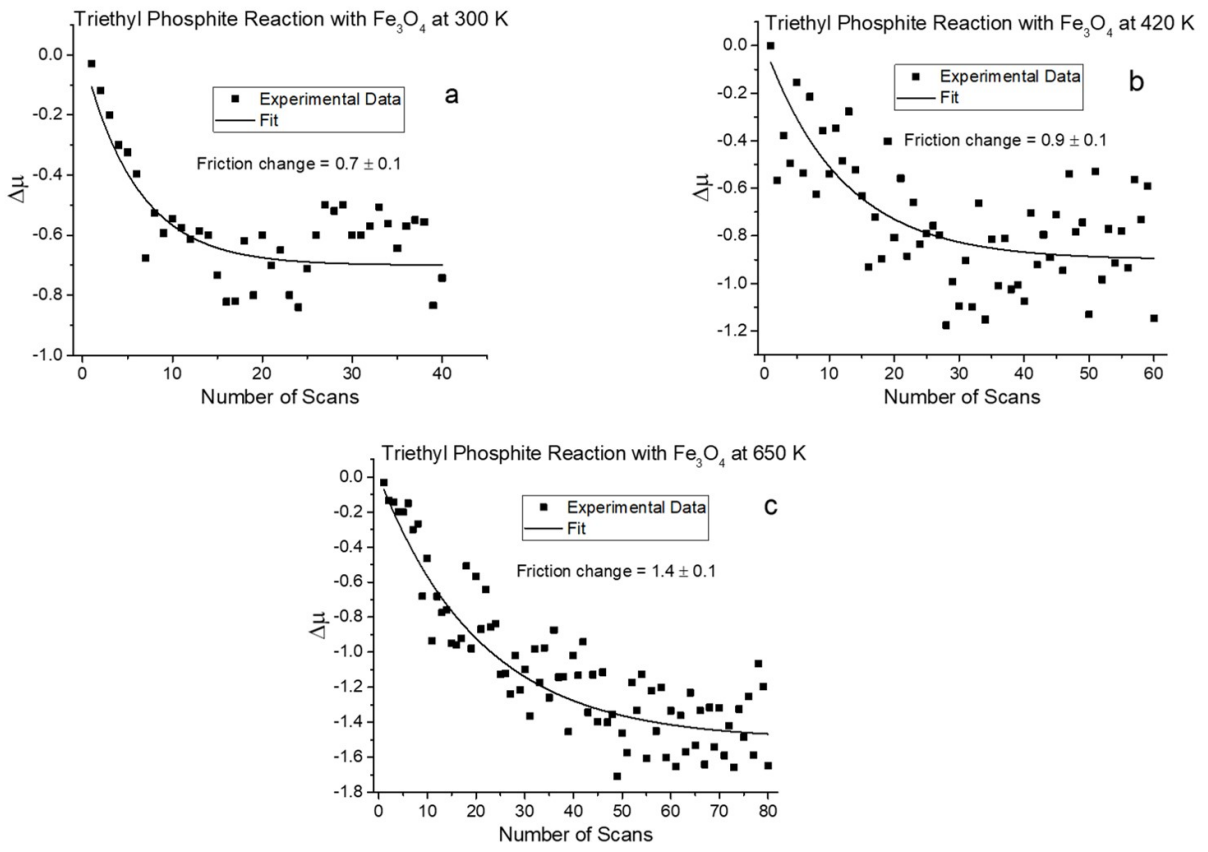

FIGURE 6.14: Friction reduction of a Fe_3O_4 film formed by heating an iron foil at 800 K for 90 mins in 5×10^{-7} Torr of oxygen at a normal load of 0.29 N at a sliding speed of 4×10^{-3} m/s in the presence of 1×10^{-7} Torr of triethyl phosphite at sample temperatures of (a) 300, (b) 420 and (c) 650 K.

6.4 Discussion

Tribochemical processes consist of a series of elementary-step reactions that involve the initial adsorption of an active component from the lubricant, followed by a thermal reaction to form precursor adsorbates on the surface. These can then further decompose under the influence of shear at the sliding interface to form a friction- and/or

wear-reducing tribofilm [36, 37]. Thus, understanding of the initial thermal chemistry of model lubricant additives on surfaces is central to fully understanding tribochemical reaction pathways since changes in the structure of the precursor molecule can have a profound influence on the friction and the nature of the film [38].

Molecular TMPi desorbs at ~280 K (Fig. 6.3, where a Redhead analysis yields a desorption activation energy of ~71 kJ/mol), while TEPi desorbs molecularly at ~267 K (data not shown), with an activation energy of ~67 kJ/mol. A decrease in P 2p binding energy of ~1.4 eV following TMPi adsorption on Fe(110) [10] suggests that electrons are donated to the phosphorus atom during adsorption, with a lower extent of donation for TMPi on Fe_3O_4 than on Fe as evidenced by the smaller chemical shift (of ~0.3 eV). This result differs from predictions from density functional theory (DFT) calculations of TMPi on Fe(110) [39], which suggests that it binds by electron donation to the metal. Electron donation to phosphite ester ligands has also been found in organometallic compounds where the extent of electron donation has been gauged from the CO frequency shift in metal carbonyls with various phosphorus-containing ligands [40]. The higher CO stretching frequency for metal carbonyls with a TMPi ligand (2079.5 cm^{-1}) compared to TEPi (2076.3 cm^{-1}) indicates that TMPi is a slightly better electron acceptor than TEPi, thus accounting for its slightly stronger adsorption on Fe_3O_4. Furthermore, the calculated lowest-occupied molecular orbital (LUMO) energies for a number of phosphite esters [41] show that the TEPi LUMO energy (~0.73

eV) is higher than that for TMPi (~0.65 eV) and will lead to less electron donation and weaker binding, consistent with the above discussion. The LUMO for TBPi is located at ~0.44 eV, thus accounting for its stronger binding on Fe_3O_4 compared to TMPi and TEPi [15].

The phosphate esters show similar chemistry, showing three distinct features initiated by sequential P–O bond scission to form adsorbed alkoxy species, which primarily react to form mixtures of the corresponding alcohol or aldehyde, suggesting that the hydrogen required to form the alcohol derives from alkoxide dehydrogenation. A similar behavior is found for tributyl phosphite on Fe_3O_4, where 1-butanol and butanal are formed [15]. This behavior was also found for 1-butanol adsorbed directly on the Fe_3O_4 surface where a mixture of 1-butanol and butanal were produced predominantly in a feature centered at ~250 K [15] and indicates that the higher-temperature features from the decomposition of the trialkyl esters reflects the rates at which the sequential P–O bond scission processes occur. The activation energies for the two highest alcohol+aldehyde desorption states for TMPi, TEPi and tributyl phosphite are plotted as a function of the number of carbon atoms in the n-alkyl chain in Figure 6.15. This indicates that the energy required to remove the final alkoxy group is the highest, and that TEPi has the lowest activation energy of the studied phosphite esters. In the case of TBPi, the higher activation energy for P–O bond scission leads to some C–O bond scission, which results in the deposition of carbon on the surface as indicated by Auger

spectroscopy. The XPS data in Figure 6.11 also indicate that some carbon forms on the surface after decomposing TMPi. In the case of the surface formed after dosing and heating tributyl phosphite, a depth profile indicated that the carbon was located primarily on the surface. Interestingly, TMPi deposits very little carbon on the surface (Fig. 6.6), likely because of the lack of a β-hydrogen in the alkyl group that would allow an alkene to form.

In summary, phosphite esters adsorb relatively weakly on Fe_3O_4 to bind via electron donation to the phosphorus and then decompose on heating to deposit phosphorus and carbon on the surface. The phosphorus XPS data indicate that the original phosphite converts into a phosphate (Figs. 6.7 and 6.12) over the range of temperatures that the phosphite ester decomposes (Figs.6.8 and 6.13). This is in accord with the observation that the phosphorus penetrates a significant distance into the oxide film after reaction with TBPi, where (poly)phosphates have been identified by NEXAFS [9] and ToF-SIMS and infrared spectroscopy [42].

Gas-phase lubrication was measured in the presence 1×10^{-7} Torr of TEPi at a normal load of 0.29 N at a sliding speed of 4×10^{-3} m/s (Fig. 6.14). This shows that TEPi does indeed act as a gas-phase lubricant where the friction coefficient reduces by ~0.7 at sample temperature of 300 K, by ~0.9 at a sample temperature of 420 K, and by ~1.4 at a sample temperature of ~650 K, indicating that the (poly)phosphate has relatively low friction and is in the range found following gas-phase lubrication of oxidized steel

in vacuum [18, 19, 26, 27]. The number of scans required to reach steady-state friction decreases with increasing temperature from ~20 scans at 300 K, ~30 scans at 420 K and ~50 scans at 650 K, likely due to the lower coverage of the phosphite ester at higher reaction temperatures. The friction reduction for each reaction temperature is plotted with the proportion of phosphite and phosphate on the surface for a reaction with TEPi (▲, Fig. 6.13), where the friction reduction correlates with the proportion of (poly)phosphate on the surface, confirming that the presence of a phosphate film is responsible for lubrication.

The tribochemical reactions of alkyl phosphite esters can be summarized by the following steps: First is the adsorption of the phosphite ester on the surface, where the bonding shows a weak dependence on the nature of the alkyl group. The second step is the removal of alkoxy groups that produce the corresponding alcohols and aldehydes, and results in phosphorus transport into the subsurface region to form phosphates. These processes occur thermally at relatively high temperatures and are not complete until the sample has been heated to ~650 K (Figs. 6.4, 6.5, 6.9 and 6.10), while significant friction reduction is observed even at 300 K (Fig. 6.14 a). This may imply that the rates of these reactions are accelerated by the shearing interface [43, 44], in a tribochemical reaction cycle that follows the general elementary reaction steps found for the gas-phase lubrication of copper by dimethyl disulfide [37]. It has also been suggested that shorter-chain alkyl groups provide the best anti-wear behavior [45], which may

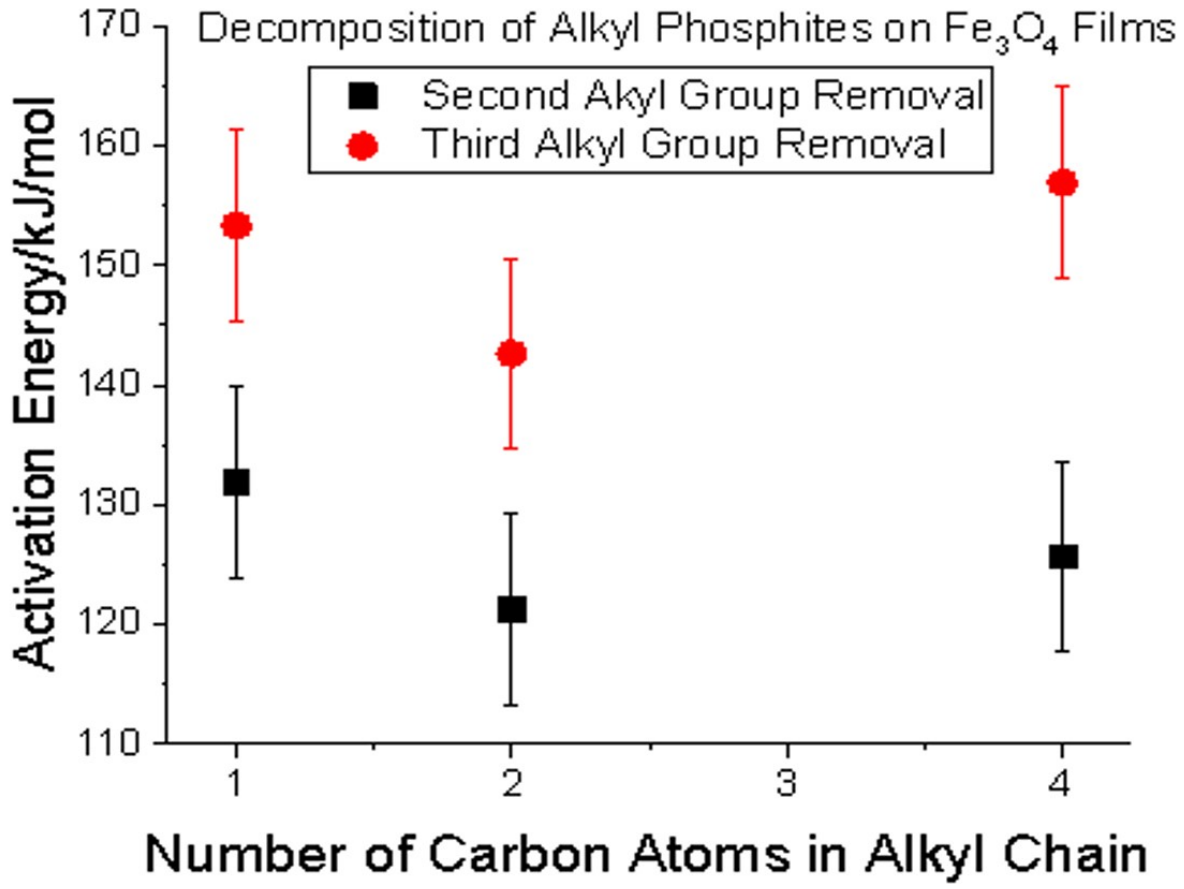

FIGURE 6.15: Plot of the formation activation energies for the removal of the second and third alkyl groups for trialkyl phosphites on Fe_3O_4 for trimethyl, triethyl and tributyl phosphite [15] as a function of the number of carbon atoms in the alkyl chain. Activation energies are obtained using the Redhead equation [28] by assuming a pre-exponential factor of $1{\times}10^{13}s^{-1}$, and using the experimental heating rate of 4.2 K/s for this work and a value of 10 K/s for tributyl phosphite.

be related to the increased stability of longer alkyl chains (Fig. 6.15). However, phosphite esters with longer alkyl chains also produce more carbon, which could inhibit the surface-to-bulk transport of phosphorus into the bulk. A carbon film may also be lubricious so could influence the friction and this issue warrants further investigation.

Aryl side chains can also influence the surface reaction and thus the resulting tribological properties. For example, diphenyl phosphate forms an iron(II) polyphosphate on oxidized steel during heating, while triphenyl phosphate forms no film at 423 K [46]. However, both phosphate esters formed polyphosphates while rubbing at 363 K [9], suggesting that the reaction is indeed mechanically assisted.

Since the surface chemistry is strongly influenced by the nature of the substrate, and because wear of the oxide film can expose the clean metal, the surface chemistry of phosphate and phosphite esters has been studied on clean iron where the chemistry is now dominated by C–O rather than P–O scission [10–14]. However, in the case of tricresyl phosphate, which includes a methyl side group on the aryl ring [4, 5, 20], the reaction on metallic iron is dominated by P–O bond scission to produce of aryloxy species [14, 47] and this chemistry has recently be confirmed by DFT calculations [48].

6.5 Conclusions

Phosphite esters adsorb onto a thin Fe_3O_4 film grown on an iron substrate by electron donation into the phosphorus atom, leading to a binding energy that increases in the order TBPi>TMPi>TEPi, and correlates well with the location of the vacant LUMO energy. The phosphite esters decompose via sequential P–O bond scission to form adsorbed alkoxy species, which then react on the surface either by hydrogen addition

to form the corresponding alcohol or by hydrogen abstraction to yield an aldehyde. Because the alcohol and aldehyde form simultaneously, this suggests that the hydrogen required to form the alcohol derives from the alkoxy dehydrogenation to form the aldehyde. The stronger binding of TEPi compared to TMPi results in the formation of a larger coverage of carbonaceous species after the adsorbates have completely thermally decomposed. The surface carbon is oxidized, presumably due to an interaction with the iron oxide substrate, and the reaction also results in the formation of a stable phosphorus-containing film.

The friction coefficient during gas-phase lubrication with TEPi using a 0.29 N load was significantly reduced for reaction at 300 ($\Delta\mu$ ~ 0.7), 420 ($\Delta\mu$ ~ 0.9) and 650 ($\Delta\mu$ ~ 1.4) K. The friction reduction correlates with the relative concentration of phosphorus in the phosphate-containing tribofilm confirming that the formation of the film is responsible for the considerable reduction in friction. It seems that phosphorus can penetrate the oxide film, even at ~300 K, well below the temperature at which the alkoxide species are thermally removed. This implies that interfacial shear can facilitate the removal of alkoxy species in a tribochemical process as found for the formation of tribofilms from dimethyl disulfide [36, 37, 49] and zinc dialkyl dithiophosphate (ZDDP) [43, 44].

References

[1] T. Mang and W. Dresel, *Lubricants and lubrication*. Wiley-VCH, Weinheim; New York; Chichester, 2001.

[2] L. O. Farng and L. Rudnick, "Ashless antiwear and extreme-pressure additives," *Lubricant Additives: Chemistry and Application*, pp. 223–257, 2003.

[3] D. Johnson and J. Hils, "Phosphate esters, thiophosphate esters and metal thiophosphates as lubricant additives," *Lubricants*, vol. 1, no. 4, pp. 132–148, 2013.

[4] C. Saba and N. Forster, "Reactions of aromatic phosphate esters with metals and their oxides," *Tribology Letters*, vol. 12, no. 2, pp. 135–146, 2002.

[5] A. Gauthier, H. Montes, and J. Georges, "Boundary lubrication with tricresylphosphate (TCP). importance of corrosive wear," *ASLE TRANSACTIONS*, vol. 25, no. 4, pp. 445–455, 1982.

[6] Y. Yamamoto and F. Hirano, "The effect of the addition of phosphate esters to paraffinic base oils on their lubricating performance under sliding conditions," *Wear*, vol. 78, no. 3, pp. 285–296, 1982.

[7] D. G. Placek and S. G. Shankwalkar, "Phosphate ester surface treatment for reduced wear and corrosion protection," *Wear*, vol. 173, no. 1-2, pp. 207–217, 1994.

[8] E. Forbes, "The load-carrying action of organo-sulphur compounds—a review," *Wear*, vol. 15, no. 2, pp. 87–96, 1970.

[9] M. Najman, M. Kasrai, G. Bancroft, and A. Miller, "Study of the chemistry of films generated from phosphate ester additives on 52100 steel using x-ray absorption spectroscopy," *Tribology Letters*, vol. 13, no. 3, pp. 209–218, 2002.

[10] A. Holbert, J. Batteas, A. Wong-Foy, T. Rufael, and C. Friend, "Passivation of *Fe* (110) via phosphorus deposition: the reactions of trimethylphosphite," *Surface science*, vol. 401, no. 3, pp. L437–L443, 1998.

[11] D. Ren and A. J. Gellman, "Initial steps in the surface chemistry of vapor phase lubrication by organophosphorus compounds," *Tribology Letters*, vol. 6, no. 3-4, pp. 191–194, 1999.

[12] D. Ren and A. J. Gellman, "The carbon deposition mechanism in vapor phase lubrication," *Tribology Transactions*, vol. 43, no. 3, pp. 480–488, 2000.

[13] D. Ren and A. J. Gellman, "Reaction mechanisms in organophosphate vapor phase lubrication of metal surfaces," *Tribology International*, vol. 34, no. 5, pp. 353–365, 2001.

[14] D. Sung and A. Gellman, "The surface chemistry of alkyl and arylphosphate vapor phase lubricants on fe foil," *Tribology international*, vol. 35, no. 9, pp. 579–590, 2002.

[15] F. Gao, O. Furlong, P. V. Kotvis, and W. T. Tysoe, "Reaction of tributyl phosphite with oxidized iron: surface and tribological chemistry," *Langmuir*, vol. 20, no. 18, pp. 7557–7568, 2004.

[16] F. Gao, P. Kotvis, D. Stacchiola, and W. Tysoe, "Reaction of tributyl phosphate with oxidized iron: surface chemistry and tribological significance," *Tribology Letters*, vol. 18, no. 3, pp. 377–384, 2005.

[17] D. Philippon, M.-I. de Barros-Bouchet, T. Mogne, E. Gresser, and J.-M. Martin, "Experimental simulation of phosphites additives tribochemical reactions by gas phase lubrication," *Tribology-Materials, Surfaces & Interfaces*, vol. 1, no. 3, pp. 113–123, 2007.

[18] D. Philippon, M.-I. De Barros-Bouchet, T. Le Mogne, O. Lerasle, A. Bouffet, and J.-M. Martin, "Role of nascent metallic surfaces on the tribochemistry of phosphite lubricant additives," *Tribology International*, vol. 44, no. 6, pp. 684–691, 2011.

[19] M. De Barros-Bouchet, M. C. Righi, D. Philippon, S. Mambingo-Doumbe, T. Le-Mogne, J. Martin, and A. Bouffet, "Tribochemistry of phosphorus additives: experiments and first-principles calculations," *RSC Advances*, vol. 5, no. 61, pp. 49270–49279, 2015.

[20] Y. Yamamoto and F. Hirano, "Effect of different phosphate esters on frictional characteristics," *Tribology International*, vol. 13, no. 4, pp. 165–169, 1980.

[21] D. A. Shirley, "High-resolution x-ray photoemission spectrum of the valence bands of gold," *Physical Review B*, vol. 5, no. 12, p. 4709, 1972.

[22] F. Gao, P. V. Kotvis, and W. Tysoe, "The frictional properties of thin inorganic halide films on iron measured in ultrahigh vacuum," *Tribology Letters*, vol. 15, no. 3, pp. 327–332, 2003.

[23] M. Langell and G. Somorjai, "The composition and structure of oxide films grown on the (110) crystal face of iron," *Journal of Vacuum Science and Technology*, vol. 21, no. 3, pp. 858–866, 1982.

[24] R. T. Sanchez, E. Curt, C. Volzone, R. Mercader, and A. Cavalieri, "Study of $Fe(II)$ oxidation in ground magnetite," *Materials research bulletin*, vol. 25, no. 5, pp. 553–561, 1990.

[25] G. Allen and K. Hallam, "Characterisation of the spinels mxco1- x$Fe_2O_4(M = Mn, FeorNi)$ using x-ray photoelectron spectroscopy," *Applied surface science*, vol. 93, no. 1, pp. 25–30, 1996.

[26] X. Wu, P. Cong, H. Nanao, I. Minami, and S. Mori, "Tribological behaviors of 52100 steel in carbon dioxide atmosphere," *Tribology Letters*, vol. 17, no. 4, pp. 925–930, 2004.

[27] D. Philippon, M.-I. De Barros-Bouchet, O. Lerasle, T. Le Mogne, and J.-M. Martin, "Experimental simulation of tribochemical reactions between borates esters and

steel surface," *Tribology Letters*, vol. 41, no. 1, pp. 73–82, 2011.

[28] P. Redhead, "Thermal desorption of gases," *vacuum*, vol. 12, no. 4, pp. 203–211, 1962.

[29] T. S. Rufael, J. D. Batteas, and C. Friend, "The influence of surface oxidation on the reactions of methanol on *Fe* (110)," *Surface Science*, vol. 384, no. 1-3, pp. 156–167, 1997.

[30] C. E. Myers, H. F. Franzen, and J. W. Anderegg, "X-ray photoelectron spectra and bonding in transition-metal phosphides," *Inorganic Chemistry*, vol. 24, no. 12, pp. 1822–1824, 1985.

[31] Y. Barbaux, M. Dekiouk, D. Le Maguer, L. Gengembre, D. Huchette, and J. Grimblot, "Bulk and surface analysis of a $Fe - PO$ oxydehydrogenation catalyst," *Applied Catalysis A: General*, vol. 90, no. 1, pp. 51–60, 1992.

[32] J. Grosseau-Poussard, B. Panicaud, F. Pedraza, P. Renault, and J.-F. Silvain, "Iron oxidation under the influence of phosphate thin films," *Journal of applied physics*, vol. 94, no. 1, pp. 784–788, 2003.

[33] G. K. Marasinghe, M. Karabulut, C. Ray, D. Day, M. G. Shumsky, W. B. Yelon, C. H. Booth, P. G. Allen, and D. K. Shuh, "Structural features of iron phosphate glasses," *Journal of non-crystalline solids*, vol. 222, pp. 144–152, 1997.

[34] M. Nooney, T. Murrell, J. Corneille, E. Rusert, L. Hossner, and D. Goodman, "A spectroscopic investigation of phosphate adsorption onto iron oxides," *Journal of Vacuum Science & Technology A: Vacuum, Surfaces, and Films*, vol. 14, no. 3, pp. 1357–1361, 1996.

[35] C. Wagner and G. Muilenberg, *Handbook of x-ray photoelectron spectroscopy : a reference book of standard data for use in x-ray photoelectron spectroscopy*. Physical Electronics Division, Perkin-Elmer Corp., Eden Prairie, Minn., 1979.

[36] H. Adams, B. P. Miller, P. V. Kotvis, O. J. Furlong, A. Martini, and W. T. Tysoe, "In situ measurements of boundary film formation pathways and kinetics: dimethyl and diethyl disulfide on copper," *Tribology Letters*, vol. 62, no. 1, p. 12, 2016.

[37] H. Adams, B. P. Miller, O. J. Furlong, M. Fantauzzi, G. Navarra, A. Rossi, Y. Xu, P. V. Kotvis, and W. T. Tysoe, "Modeling mechanochemical reaction mechanisms," *ACS applied materials & interfaces*, vol. 9, no. 31, pp. 26531–26538, 2017.

[38] B. P. Miller, P. V. Kotvis, O. J. Furlong, and W. T. Tysoe, "Relating molecular structure to tribological chemistry: borate esters on copper," *Tribology Letters*, vol. 49, no. 1, pp. 21–29, 2013.

[39] M. C. Righi, S. Loehlé, M. de Barros Bouchet, D. Philippon, and J. Martin, "Trimethyl-phosphite dissociative adsorption on iron by combined first-principle

calculations and xps experiments," *RSC Advances*, vol. 5, no. 122, pp. 101162–101168, 2015.

[40] C. A. Tolman, "Electron donor-acceptor properties of phosphorus ligands. substituent additivity," *Journal of the American Chemical Society*, vol. 92, no. 10, pp. 2953–2956, 1970.

[41] Y.-K. Han, J. Yoo, and T. Yim, "Why is tris (trimethylsilyl) phosphite effective as an additive for high-voltage lithium-ion batteries," *Journal of Materials Chemistry A*, vol. 3, no. 20, pp. 10900–10909, 2015.

[42] A. Murase and T. Ohmori, "Tof-sims analysis of phosphate-type lubricant additives adsorbed on friction surfaces of ferrous materials," *Surface and Interface Analysis: An International Journal devoted to the development and application of techniques for the analysis of surfaces, interfaces and thin films*, vol. 31, no. 2, pp. 93–98, 2001.

[43] N. Gosvami, J. Bares, F. Mangolini, A. Konicek, D. Yablon, and R. Carpick, "Mechanisms of antiwear tribofilm growth revealed in situ by single-asperity sliding contacts," *Science*, vol. 348, no. 6230, pp. 102–106, 2015.

[44] J. Zhang and H. Spikes, "On the mechanism of zddp antiwear film formation," *Tribology Letters*, vol. 63, no. 2, p. 24, 2016.

[45] A. Riga, J. Cahoon, and W. Pistillo, "Organophosphorus chemistry structure and performance relationships in fzg gear tests," *Tribology Letters*, vol. 9, no. 3-4,

pp. 219–225, 2001.

[46] M. Najman, M. Kasrai, and G. Bancroft, "Chemistry of antiwear films from ashless thiophosphate oil additives," *Tribology Letters*, vol. 17, no. 2, pp. 217–229, 2004.

[47] D. Sung and A. J. Gellman, "Thermal decomposition of tricresylphosphate isomers on *Fe*," *Tribology Letters*, vol. 13, no. 1, pp. 9–14, 2002.

[48] E. Osei-Agyemang, S. Berkebile, and A. Martini, "Decomposition mechanisms of anti-wear lubricant additive tricresyl phosphate on iron surfaces using dft and atomistic thermodynamic studies," *Tribology Letters*, vol. 66, no. 1, p. 48, 2018.

[49] H. L. Adams, M. T. Garvey, U. S. Ramasamy, Z. Ye, A. Martini, and W. T. Tysoe, "Shear-induced mechanochemistry: pushing molecules around," *The Journal of Physical Chemistry C*, vol. 119, no. 13, pp. 7115–7123, 2015.

Chapter 7

Adsorption and Reaction of Trimethyl and Triethyl Phosphites on Fe_3O_4 by Density Functional Theory

7.1 Introduction

Lubricant additives are mixed with a base oil of commercial lubricants to improve the frictional and anti-wear properties of the sliding interface by forming a tribochemically formed layer [1]. Compounds containing phosphorus, such as phosphate and phosphite esters are used to lubricate Fe (III) oxide surfaces where phosphate films are formed during the tribological process [2–6]. The chemistry of triethyl phosphite (TEPi) and trimethyl phosphite (TMPi) has been investigated previously on oxidized iron surfaces in ultrahigh vacuum (UHV), Chapter 6. It is reported that the phosphite esters adsorb onto a thin Fe_3O_4 film grown on an iron substrate by electron donation from the substrate to the phosphorus atom, leading to a binding energy that increases in the order TMPi>TEPi [7], and correlates well with the location of the vacant LUMO

energy. Phosphite esters decompose on an iron oxide surface via a sequential P–O bond scission to form adsorbed alkoxy species, which then react rapidly on the surface either by hydrogen addition to form the corresponding alcohol or by hydrogen abstraction to yield an aldehyde. Because the alcohol and aldehyde form simultaneously, this suggests that the hydrogen required to form the alcohol derives from the alkoxy dehydrogenation to form the aldehyde. The phosphate esters desorb molecular at relatively low temperatures (~290 K) leading to estimated desorption energies from a Redhead analysis of ~67 (0.69 eV) for TEPi and ~71 (0.73 eV) kJ/mol for TMPi [8]. Note that the decomposition products referred to above desorb at up to ~600 K, so that there are more strongly bound species on the surface that remain to much higher temperatures. In this Chapter, adsorption energies of phosphite esters and their decomposition products are theoretically calculated using density functional theory and correlated with the experimental results. The calculations are performed on a Fe_3O_4 substrate to compare as closely as possible to the experimental conditions, where the surface chemistry was studied on a film of this oxide grown on an iron substrate.

7.2 Theoretical Method

Vienna ab initio simulation package, VASP, density functional theory (DFT) calculations were performed using the projector augmented wave (PAW) method [9, 10]. The

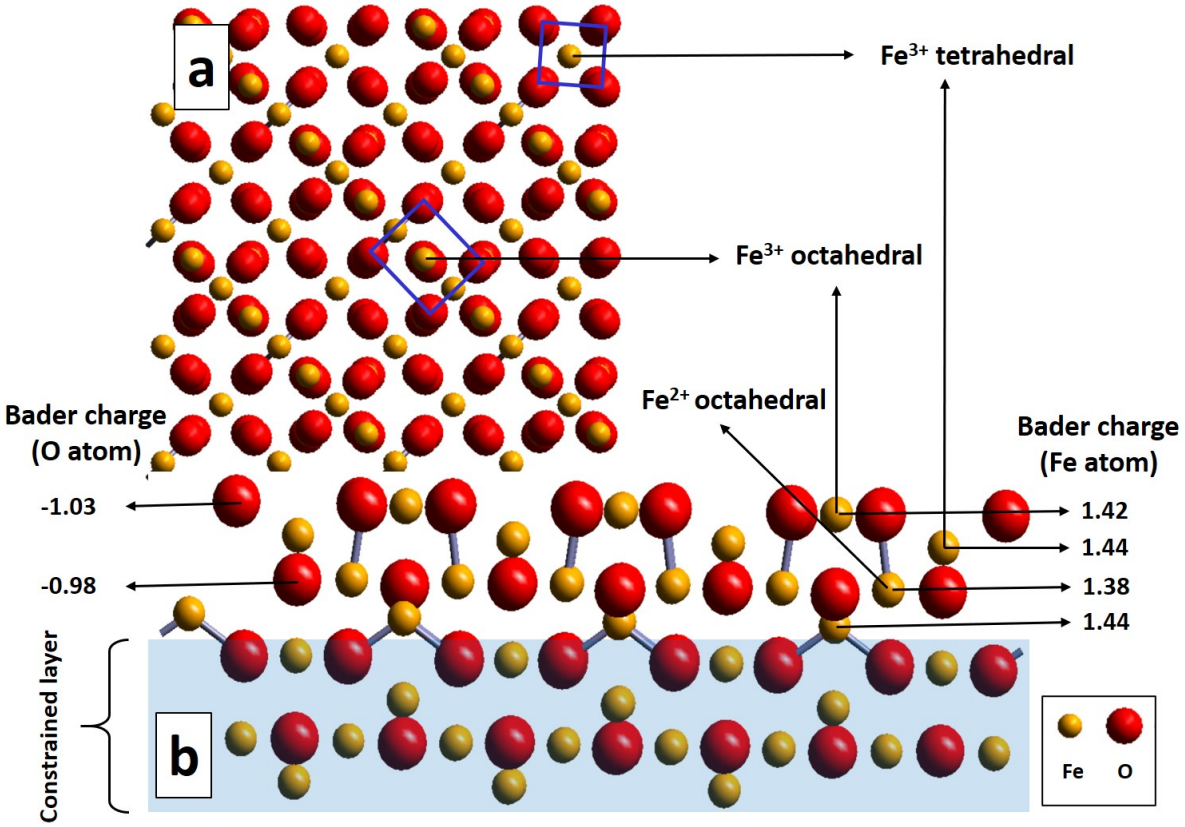

FIGURE 7.1: a) Top and b) side views of the Fe_3O_4 slab used for adsorption of phosphite ester molecules, where the bottom shaded part of the iron oxide slab is constrained.

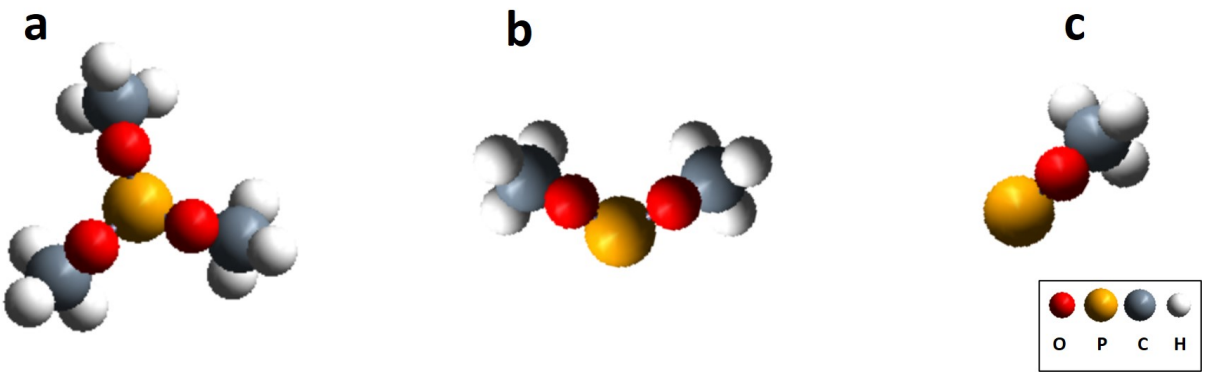

FIGURE 7.2: Geometric models of a) trimethyl phosphite, b) dimethyl phosphite and c) monomethyl phosphite.

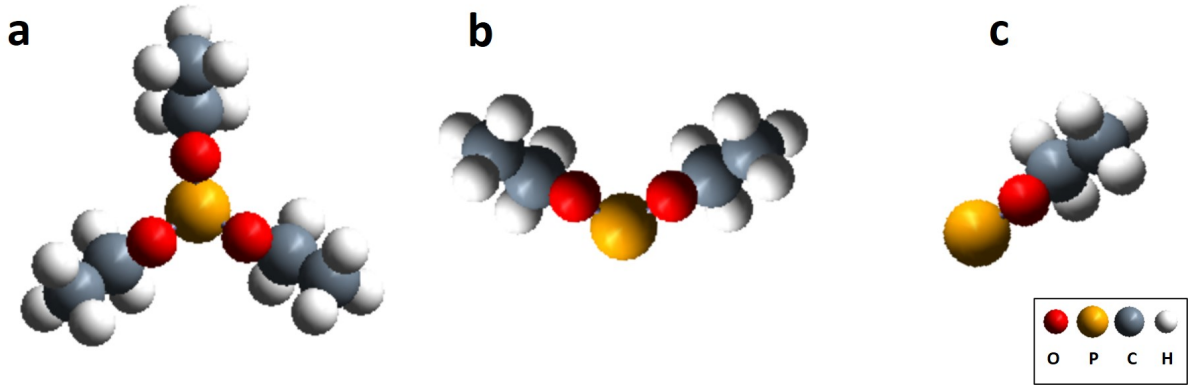

FIGURE 7.3: Geometric models of a) triethyl phosphite, b) diethyl phosphite and c) monoethyl phosphite.

exchange-correlation potential was described using the generalized gradient approximation of Perdew, Burke and Ernzerhof (PBE). A cutoff of 400 eV was used for the plane wave basis set [11–13], and the wave functions and electron density were converged to within 1×10^{-5} eV. The Brillouin zone was sampled with a MonkhorstPack grid of $1 \times 1 \times 1$ for phosphite molecules in the vacuum and a $6 \times 6 \times 1$ MonkhorstPack grid was set for the Fe_3O_4 slab alone, and for molecules adsorbed on the Fe_3O_4 surface. Geometric relaxations were converged when the force was less than 0.05 eV/Å on all unrestricted atoms. The bottom two layers (Figure 7.1) of iron and oxygen of Fe_3O_4 slab were held stationary in all calculations. Spin polarized calculations were carried out whenever an iron oxide slab is in use. Also van der Waals (VDW) forces were included in all calculations. The outermost octahedral Fe^{3+} [14] ions (Figure 7.1 (b)) on the Fe_3O_4 slab have equivalent charges, i.e. + 1.42 electron, which were calculated by a grid-based Bader analysis [15]. The phosphites molecules were adsorbed

with the phosphorous atom located on top of a Fe ion. The initial trial structures of the phosphite ester molecules were constructed using the coordinates from energy-minimized 3-D structures obtained using ChemDraw 13.0, and the Fe_3O_4 (Materials ID: mp-19306) POSCAR [16] file was downloaded from Materials Project. The initial downloaded Fe_3O_4 cell was further enlarged by $2 \times 2 \times 1$ in the X, Y, and Z directions. Adsorption energies were calculated using the equation 7.1.

$$E_{ads} = E_{(molecule\ +\ Fe_3O_4\ slab)} - E_{Fe_3O_4\ slab} - E_{gas-phase\ molecule} \tag{7.1}$$

where, E_{ads} is the adsorption energy, $E_{(molecule\ +\ Fe_3O_4\ slab)}$ is the energy of the Fe_3O_4 slab with a molecular adsorbate, $E_{Fe_3O_4\ slab}$ is energy of the Fe_3O_4 slab and, $E_{gas-phase\ molecule}$ is energy of intact molecule or alkoxy group removed phosphite molecule.

7.3 Results

7.3.1 Adsorption of Trimethyl Phosphite on Fe_3O_4

The energies of trimethyl phosphite, dimethyl phosphite and monomethyl phosphite, shown in Figure 7.2, were calculated using a Monkhorst-Pack grid of $1 \times 1 \times 1$. The energies of a Fe_3O_4 slab alone and these molecules adsorbed on a Fe_3O_4 slab were calculated by using a Monkhorst Pack grid of $6 \times 6 \times 1$. DFT calculations were performed

using, VASP, and once the calculations were converged, Eqn. 7.1 was used to calculate the adsorption energy of TMPi, dimethyl phosphite and monomethyl phosphite. The final calculated adsorption energies, including van der Waals (VDW) forces are summarized in Table 7.1. The adsorption geometries are depicted in Figure 7.4.

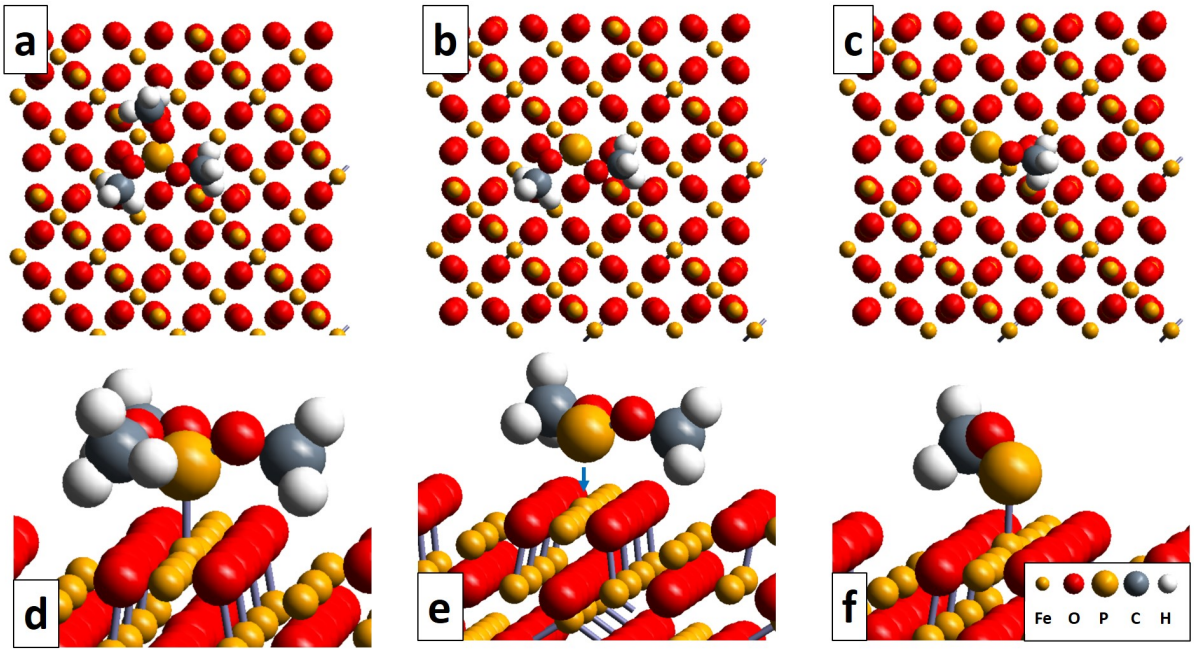

FIGURE 7.4: Geometric models of adsorbed trimethyl phosphite (a - top view, d - magnified section of side view), dimethyl phosphite (b - top view, e - magnified section of side view), and monomethyl phosphite (c - top view, f - magnified section of side view) on Fe_3O_4.

Since the trimethyl phosphite reacts to gives dimethyl phosphite and an adsorbed methyl species, the energy of dimethyl phosphite and a co-adsorbed methoxy species was calculated and was found to be 2.87 eV more stable than the trimethyl phosphite alone. The calculated energy of monomethyl phosphite and a co-adsorbed methoxy

Phosphite ester	Binding Energy/eV (Alkyl = CH_3)	Binding Energy/eV (Alkyl = C_2H_5)
Trialkyl phosphite	-1.91	-1.72
Dialkyl phosphite	-2.16	-2.15
Monoalkyl phosphite	-2.72	-2.66
Phosphorus	-3.61	-3.61

TABLE 7.1: Adsorption energies of trimethyl phosphite, dimethyl phosphite and monomethyl phosphite adsorbed on Fe_3O_4 calculated by implementing the Vienna ab initio simulation package, VASP, density functional theory (DFT). The structures include van der Waals (VDW) forces.

species was found to be 2.78 eV more stable than dimethyl phosphite. A similar calculation was carried out for adsorbed phosphorus and a methoxy, which was found to be 2.81 eV more stable than monomethyl phosphite on Fe_3O_4. This indicates that a co-adsorbed methoxy has a binding energy of ~2.82 eV on the oxide surface.

Phosphite ester	P (δ^+) electron (gas-phase)	P (δ^+) electron (adsorbed)	Fe (δ^+) electron (gas-phase)	Fe (δ^+) electron (adsorbed)
Trimethyl phosphite	1.53	2.39	1.42	1.20
Dimethyl phosphite	1.41	1.57	1.42	1.22
Monomethyl phosphite	0.65	0.93	1.42	1.04
Phosphorus	0.00	0.11	1.42	1.04

TABLE 7.2: Grid-based Bader charge analysis of P and Fe atoms calculated for trimethyl phosphite, dimethyl phosphite and monomethyl phosphite in vacuum and when adsorbed on Fe_3O_4.

The grid-based Bader charges of the atoms were calculated for the gas-phase and adsorbed structures shown in Fig. 7.4 The partial electronic charges (δ^+) on the P and Fe atoms are summarized in the Table 7.2. A decrease in δ^+ on the P atom is observed

Phosphite ester	O (δ^-) electron (gas-phase)	O (δ^-) electron (adsorbed)	C (δ^+) electron (gas-phase)	C (δ^+) electron (adsorbed)
Trimethyl phosphite	-1.03±0.00	-1.25±0.02	0.23±0.01	0.37±0.02
Dimethyl phosphite	-1.25±0.00	-1.24±0.02	0.41±0.00	0.34±0.07
Monomethyl phosphite	-1.19±0.00	-1.22±0.00	0.35±0.00	0.37±0.00

TABLE 7.3: Grid-based Bader charge analysis of O and C atoms calculated for trimethyl phosphite, dimethyl phosphite and monomethyl phosphite in vacuum and when adsorbed on Fe_3O_4.

when there are fewer methoxy groups on the gas-phase molecules where, by definition, the charge on an isolated phosphorus atom is zero. This due to the large electronegativity of the oxygen in the alkoxy group that tends to withdraw electrons from the phosphorus. A similar trend is seen for molecular fragments adsorbed on Fe_3O_4 where the value of δ^+ on P increases are the methyl groups are removed, but the positive charges are larger than for the corresponding gas-phase fragments. The δ^+ charge on the Fe ion on the bare oxide is +1.42 electrons, but δ^+ of Fe atom decreases after the fragments in the same order as the increase in positive charge on the phosphorus. This indicates that there is charge transfer to the iron from the phosphorus which contradicts the hypothesis mentioned in Chapter 6 [8], where the predicted charge transfer was from iron to phosphorus. The charge on oxygen and carbon atoms were calculated and are summarized in Table 7.3. Again, some charge is transferred from the carbon to the more electronegative oxygen.

7.3.2 Adsorption of Triethyl Phosphite on Fe_3O_4

Similar DFT calculations were carried out of ethoxy-containing phosphite esters, starting with triethyl phosphite and then calculating the energies of the reaction products found experimentally, namely diethyl phosphite, monoethyl phosphite, and phosphorus. Note that the binding of phosphorus was discussed in the previous section and is the common final product for all phosphite esters on iron oxide surfaces. The equilibrium structures of triethyl phosphite (TEPi), diethyl phosphite and monoethyl phosphite are shown in Figure 7.3, where the structures and energies of the free molecules were calculated VASP with a Monkhorst Pack grid of $1 \times 1 \times 1$ in vacuum. The energies and structures of triethyl phosphite (TEPi), diethyl phosphite and monoethyl phosphite adsorbed on a Fe_3O_4 slab calculated using VASP using a $6 \times 6 \times 1$ Monkhorst-Pack grid. After convergence, Eqn. 7.1 was used to calculate the adsorption energies. The calculated binding energies are summarized in Table 7.1 and the final adsorption geometries are shown in Figure 7.5. The final structures are very similar to those found for TMPi-derived species, discussed in the previous section.

Since the triethyl phosphite reacts to give diethyl phosphite and an adsorbed ethyl species, the energy of diethyl phosphite and a co-adsorbed ethoxy species was calculated and was found to be 2.63 eV more stable than the triethyl phosphite alone. The calculated energy of monoethyl phosphite and a co-adsorbed ethoxy species was found

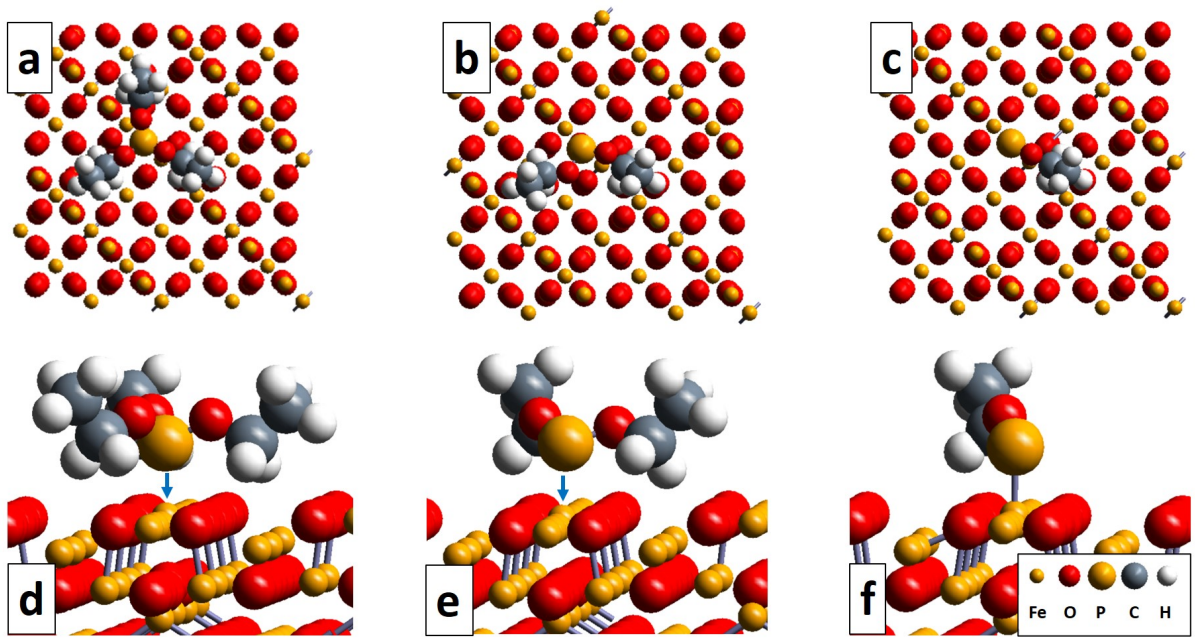

FIGURE 7.5: Geometric models of adsorbed triethyl phosphite (a - top view, d - magnified section of side view), diethyl phosphite (b - top view, e - magnified section of side view), and monoethyl phosphite (c - top view, f - magnified section of side view) on Fe_3O_4.

to be 2.93 eV more stable than diethyl phosphite. A similar calculation was carried out for adsorbed phosphorus and an ethoxy, which was found to be 2.86 eV more stable than monoethyl phosphite on Fe_3O_4. This indicates that a co-adsorbed ethoxy has a binding energy of ~2.80 eV on the oxide surface.

The grid-based Bader charges of atoms were calculated for triethyl phosphite (TEPi), diethyl phosphite, and monoethyl phosphite where the molecules were adsorbed via the phosphorus to Fe ions in the top layer of the Fe_3O_4 slab, in a similar way to the methoxy-containing phosphite esters. The partial electronic charge (δ^+) of the P atoms and Fe ions are summarized in the Table 7.4. A decrease in δ^+ on the P atom is as the

ethoxy groups are removed and the charges on the adsorbate and the substrate are essentially identical to those found for methoxy-containing phosphite esters. The charge on oxygen and carbon atoms were calculated and are summarized in Table 7.5. Where, some charge is transferred from the carbon to the more electronegative oxygen.

Phosphite ester	P (δ^+) electron (gas-phase)	P (δ^+) electron (adsorbed)	Fe (δ^+) electron (gas-phase)	Fe (δ^+) electron (adsorbed)
Triethyl phosphite	2.14	2.35	1.42	1.21
Diethyl phosphite	1.40	1.58	1.42	1.23
Monoethyl phosphite	0.64	0.92	1.42	1.04
Phosphorus	0.00	0.11	1.42	1.04

TABLE 7.4: Grid-based Bader charge analysis of P and Fe atoms calculated for triethyl phosphite, diethyl phosphite, and monmethyl phosphite in vacuum and when adsorbed on Fe_3O_4.

no. of ethoxy groups	O (δ^-) electron (gas-phase)	O (δ^-) electron (adsorbed)	C1 (δ^+) electron (gas-phase)	C1 (δ^+) electron (adsorbed)	C2 (δ^-) electron (gas-phase)	C2 (δ^-) electron (adsorbed)
3	-1.25±0.00	-1.25±0.00	0.41±0.01	0.39±0.03	-0.06±0.03	-0.04±0.01
2	-1.24±0.00	-1.23±0.02	0.43±0.02	0.40±0.00	-0.06±0.05	-0.02±0.02
1	-1.19±0.00	-1.21±0.00	0.37±0.00	0.46±0.00	-0.02±0.00	-0.03±0.00

TABLE 7.5: Grid-based Bader charge analysis of O, C1 and C2 atoms calculated for a for triethyl phosphite, diethyl phosphite, and monoethyl phosphite on Fe_3O_4.

Phosphite ester	TMPi Experimental E_{act}/eV	TMPi ΔH/eV	TEPi Experimental E_{act}/eV	TEPi ΔH/eV
Trialkyl phosphite	0.93	3.10	0.93	3.23
Dialkyl phosphite	1.34	3.38	1.24	3.31
Monoalkyl phosphite	1.59	3.68	1.48	3.75

TABLE 7.6: Activation energies estimated by Redhead analysis from experimentally observed data [Chapter 6] and the calculated change in enthalpy (ΔH) trialkyl phosphite, dialkyl phosphite, and monoalkyl phosphite adsorbed on Fe_3O_4 calculated by implementing Vienna ab initio simulation package, VASP, density functional theory (DFT). The structures are converged by considering Van der Waals (VDW) forces.

7.4 Discussion

The surface chemistry of phosphite esters has been studied on Fe_3O_4 films in ultrahigh vacuum so that the experimental and theoretical systems are essentially identical, and it should therefore be possible to compare them directly. It was found that trimethyl phospite reacted sequentially to form methanol and formic acid while triethyl phospite reacted to form ethanol and acetic acid. The simultaneous formation of the alcohol and aldehyde was interpreted as being limited to the rate at which alkoxy group was thermally removed from the phosphite ester. This, therefore enabled the activation energy of each of the steps to be measured from the peak desorption temperature of the simultaneous formation of the alcohol and aldehyde using the Redhead equation [17] from the experimental data [8] and the results are summarized in Table 7.6.

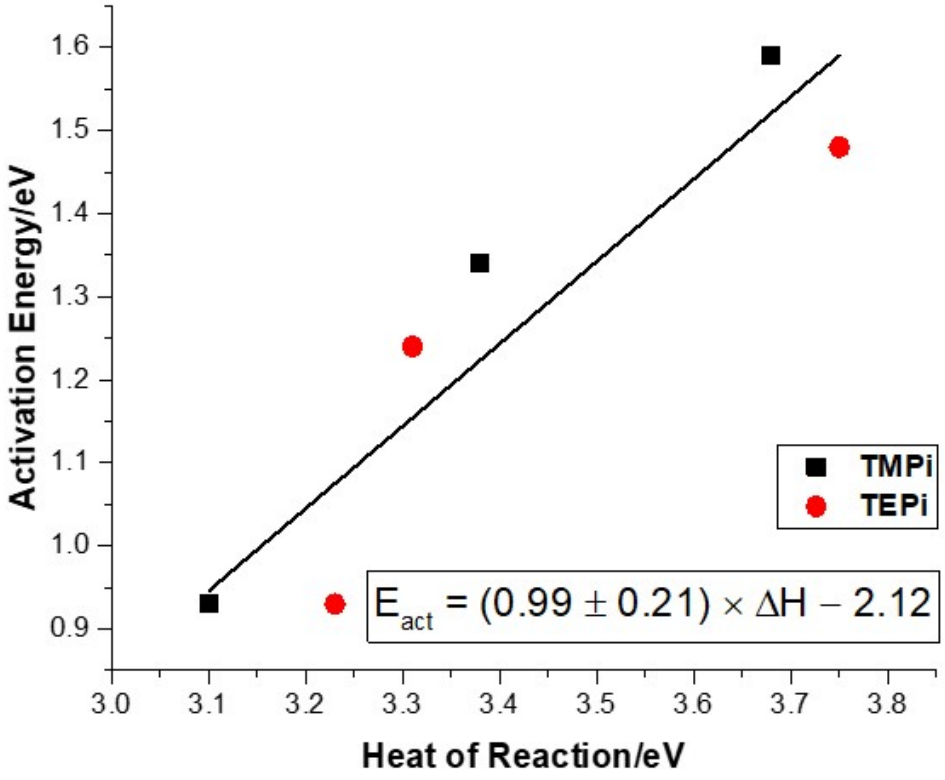

FIGURE 7.6: Bronsted-Evans-Polanyi plot for alkoxy group removal elementary reaction (thermally induced) of TMPi (■) and TEPi (●), the change in P-O bond scission activation energies (E_{act}) are estimated from Redhead analysis from the experimental results and enthalpy changes (ΔH) are calculated from the DFT calculated adsorption energies.

Some molecular desorption of TMPi and TEPi was found on thin Fe_3O_4 films grown on polycrystalline iron at relatively low temperatures desorption activation energies estimated to be ~71 kJ mol^{-1} (0.74 eV) and ~67 kJ mol^{-1} (0.69 eV) respectively using a Redhead analysis [17] with a usual value of the pre-exponential factor of 1×10^{13} s^{-1}. Since they correspond to molecular desorption, the desorption activation energy is

likely to be close to the heat of adsorption, but these values are much lower than the calculated heat of adsorption values (Table 7.1). This implies that these low-temperature desorption states are not isolated molecular species. It may be that the lateral interaction at high coverage sufficiently lowers the heat of adsorption to allow the molecules to desorb at low temperatures. This may be due to direct intermolecular interactions. However, binding of the phosphite esters to the surface results in significant charge transfer between the adsorbate and substrate. This will also influence the change on iron ions at adjacent sites and reduce the heat of adsorption. It is also noted that the heat of adsorption of the trialkyl phosphite must be larger than the reaction energy, otherwise it would desorb before reacting and thus implies that the heat of adsorption must be larger than ~0.93 eV.

However it has been found that reaction activation energies and heat of reaction are often linearly correlated and are known as Evans-Polanyi relations [18–20], where the activation energy, E_{act}, varies with heat of reaction, ΔH, as $E_{act} = E_{act}(0) - \alpha \Delta H$, where $0<\alpha<1$. The heats of reaction can be calculated from the heats of adsorption, assuming that the reaction sequences is $P(OR)_3 \rightarrow P(OR)_2 + OR \rightarrow P(OR) + OR \rightarrow P + OR$, where R = CH_3- or C_2H_5-. As indicated above, the heat of adsorption of a co-adsorbed methoxy and ethoxy group on the Fe_3O_4 surface are 2.82 and 2.80, which yield the reaction energies given in Table 7.6. The resulting plots of the experimental activation energy versus the heats of reaction calculated from density functional theory is shown in Fig.

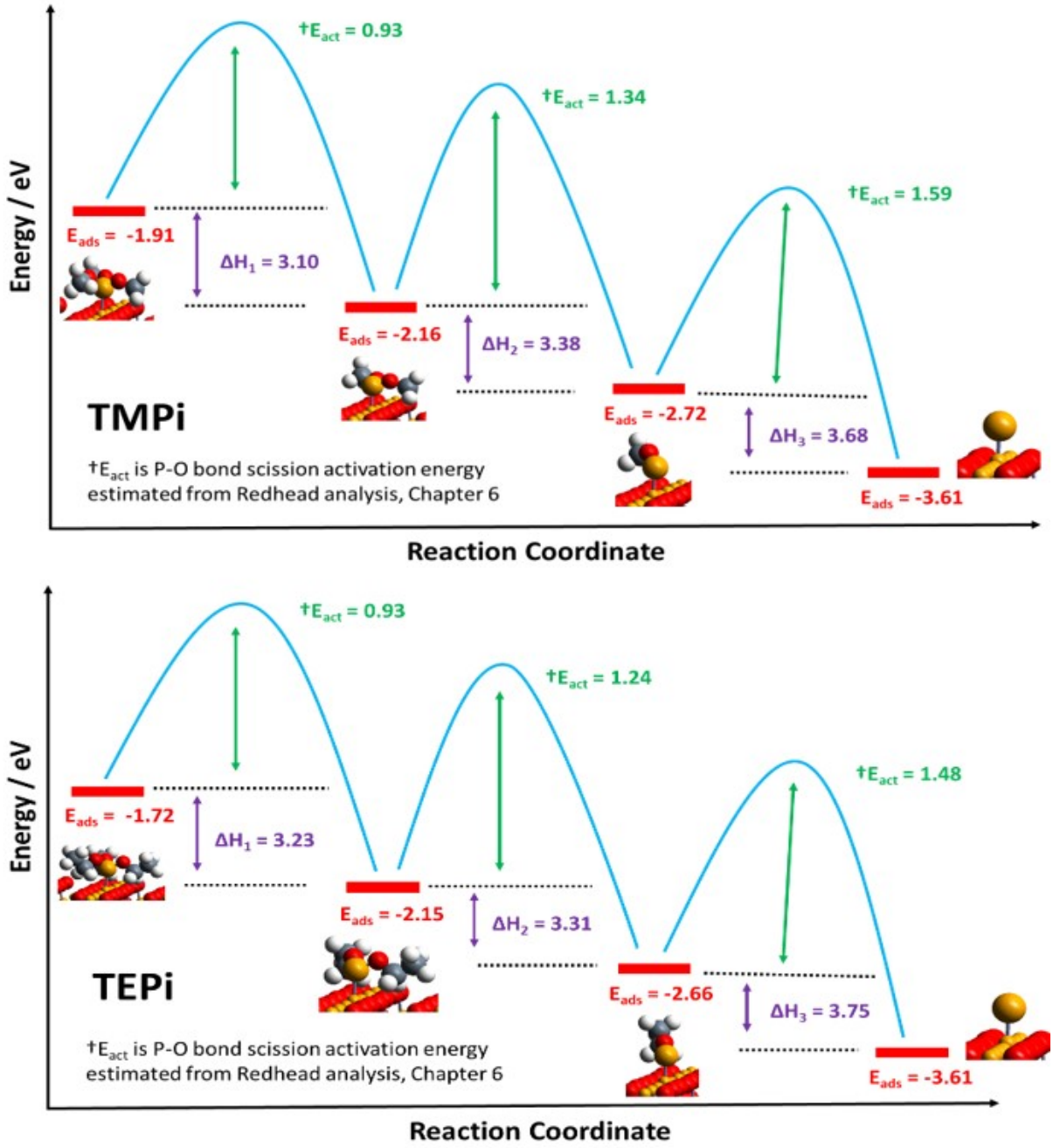

FIGURE 7.7: DFT calculated adsorption energy profiles of TMPi (top) and TEPi (bottom), where activation energy ($\dagger E_{act}$), adsorption energy (E_{ads}) and reaction enthalpy (ΔH) are shown for the reaction sequence found on Fe_3O_4 slab.

7.6. This shows a good linear correlation, in accord with the Evans-Polanyi relations and confirms that the phosphate esters decompose on an iron oxide surface by a sequential removal of the alkoxide groups, which react rapidly to give an approximately equimolar mixture of the corresponding alcohol and aldehyde. The DFT calculated adsorption energy profiles of trialkyl phosphite, dialkyl phosphite, monoalkyl phosphite and phosphorus atom adsorbed on Fe_3O_4 are shown in Figure 7.7, where alkyl = CH_3- (for TMPi) or C_2H_5- (for TEPi).

It is clear that the activation energy increases with the number of alkoxy species removed from the surface that gives rise to a step-wise removal in a temperature-programmed desorption experiment that enables the activation energy to be measured for each step. The trend in surface charges provide some insights into this behavior; δ^+ on octahedral Fe^{3+} decreases when the alkoxy groups are removed and finally phosphorus is left on the surface to form iron phosphate tribofilm [8, 21, 22].

7.5 Conclusions

It is thus demonstrated that the adsorption energies of TMPi and TEPi molecules calculated by implementing the Vienna ab initio simulation package, VASP, DFT are different, and observed adsorption energies are greater on TMPi compared to TEPi. Grid-based Bader charge analysis suggests that phosphite esters adsorb on Fe_3O_4 surface

via P atom by donating electrons to octahedral Fe^{3+} atom, where the P atom becomes more electropositive when adsorbed. It is evident that P atom donates electrons to the Fe atom, where Fe atom is attached to more electronegative oxygen atoms. The BEP plot shows that the E_{act} and ΔH are linearly correlated and transition state resembles to the final state.

References

[1] T. Mang and W. Dresel, *Lubricants and lubrication*. Wiley-VCH, Weinheim; New York; Chichester, 2001.

[2] A. Gauthier, H. Montes, and J. Georges, "Boundary lubrication with tricresylphosphate (tcp). importance of corrosive wear," *ASLE TRANSACTIONS*, vol. 25, no. 4, pp. 445–455, 1982.

[3] Y. Yamamoto and F. Hirano, "The effect of the addition of phosphate esters to paraffinic base oils on their lubricating performance under sliding conditions," *Wear*, vol. 78, no. 3, pp. 285–296, 1982.

[4] D. G. Placek and S. G. Shankwalkar, "Phosphate ester surface treatment for reduced wear and corrosion protection," *Wear*, vol. 173, no. 1-2, pp. 207–217, 1994.

[5] E. Forbes, "The load-carrying action of organo-sulphur compounds—a review," *Wear*, vol. 15, no. 2, pp. 87–96, 1970.

[6] M. Najman, M. Kasrai, G. Bancroft, and A. Miller, "Study of the chemistry of films generated from phosphate ester additives on 52100 steel using x-ray absorption spectroscopy," *Tribology Letters*, vol. 13, no. 3, pp. 209–218, 2002.

[7] Y.-K. Han, J. Yoo, and T. Yim, "Why is tris (trimethylsilyl) phosphite effective as an additive for high-voltage lithium-ion batteries?," *Journal of Materials Chemistry*

A, vol. 3, no. 20, pp. 10900–10909, 2015.

[8] R. Rana and W. Tysoe, "Tribochemical mechanisms of trimethyl and triethyl phosphite on oxidized iron in ultrahigh vacuum," *Tribology Letters*, vol. 67, no. 3, p. 93, 2019.

[9] G. Kresse and D. Joubert, "From ultrasoft pseudopotentials to the projector augmented-wave method," *Physical Review b*, vol. 59, no. 3, p. 1758, 1999.

[10] P. E. Blöchl, "Projector augmented-wave method," *Physical Review B*, vol. 50, no. 24, p. 17953, 1994.

[11] G. Kresse and J. Hafner, "Ab initio molecular dynamics for liquid metals," *Physical Review B*, vol. 47, no. 1, p. 558, 1993.

[12] G. Kresse and J. Furthmüller, ""efficient iterative schemes for ab initio total-energy calculations using a plane-wave basis set," phys. rev. b, vol. 54, pp. 11169-11186," 1996.

[13] G. Kresse and J. Furthmüller, "Efficient iterative schemes for ab initio total-energy calculations using a plane-wave basis set," *Physical Review B*, vol. 54, no. 16, p. 11169, 1996.

[14] D. Santos-Carballal, A. Roldan, R. Grau-Crespo, and N. H. de Leeuw, "A *DFT* study of the structures, stabilities and redox behaviour of the major surfaces of

magnetite Fe_3O_4," *Physical Chemistry Chemical Physics*, vol. 16, no. 39, pp. 21082–21097, 2014.

[15] W. Tang, E. Sanville, and G. Henkelman, "A grid-based bader analysis algorithm without lattice bias," *Journal of Physics: Condensed Matter*, vol. 21, no. 8, p. 084204, 2009.

[16] K. Persson, "Materials data on Fe_3O_4 (sg:227) by materials project," 1 2015. An optional note.

[17] P. Redhead, "Thermal desorption of gases," *vacuum*, vol. 12, no. 4, pp. 203–211, 1962.

[18] H. Eyring and M. Polanyi, "Über einfache gasreaktionen," *Z. Phys. Chem. B*, vol. 12, pp. 279–311, 1931.

[19] R. A. Van Santen, M. Neurock, and S. G. Shetty, "Reactivity theory of transition-metal surfaces: a brønsted- evans- polanyi linear activation energy- free-energy analysis," *Chemical Reviews*, vol. 110, no. 4, pp. 2005–2048, 2009.

[20] J. Cheng, P. Hu, P. Ellis, S. French, G. Kelly, and C. M. Lok, "Brønsted- evans-polanyi relation of multistep reactions and volcano curve in heterogeneous catalysis," *The Journal of Physical Chemistry C*, vol. 112, no. 5, pp. 1308–1311, 2008.

[21] N. Gosvami, J. Bares, F. Mangolini, A. Konicek, D. Yablon, and R. Carpick, "Mechanisms of antiwear tribofilm growth revealed in situ by single-asperity sliding contacts," *Science*, vol. 348, no. 6230, pp. 102–106, 2015.

[22] J. Zhang and H. Spikes, "On the mechanism of $ZDDP$ antiwear film formation," *Tribology Letters*, vol. 63, no. 2, p. 24, 2016.

Curriculum Vitae

RESEARCH INTERESTS

Surface Science, Tribology, Material Science.

EDUCATION

2016–2020 **Ph.D., Physical Chemistry**, *University of Wisconsin-Milwaukee*.
Concentrations: Surface Science; Tribology.
Dissertation Title: Understanding Mechanochemical Processes on Surfaces Measured in Ultrahigh Vacuum. Advisor: Professor Wilfred T. Tysoe.

2010–2012 **M.Sc., Physical Chemistry**, *Tribhuvan University*, Nepal.
Minor: Inorganic Chemistry, Organic Chemistry.

2008–2010 **B.Sc., Chemistry**, *Tri-Chandra College, Tribhuvan University*, Nepal.
Minor: Zoology, Botany.

EXPERIENCE

2016–2020 **Graduate Research/Teaching Assistant**, *University of Wisconsin-Milwaukee*.
Undergraduate Course Taught: CHEM 102, 103, 104, and 105.

2012–2015 **Lecturer**, *Himalaya College of Engineering*, Nepal.
Undergraduate Courses Taught: Chemistry.

2011–2012 **Lecturer**, *Malpi Institute*, Nepal.
A/AS Level Courses Taught: Chemistry(9701).

2006–2007 **School Teacher**, *Babylon National School, Kathmandu*, Nepal.
Courses Taught: Science.

2005–2006 **School Teacher**, *Canvas English Boarding School, Kathmandu*, Nepal.
Courses Taught: Science.

SELECTED PUBLICATIONS

1 Rana, Resham and Tysoe, Wilfred. Tribochemical Mechanisms of Trimethyl and Triethyl Phosphite on Oxidized Iron in Ultrahigh Vacuum. *Tribology Letters* **67**(3), 93, 2019.

2 Rana, Resham, et al. Kinetic Mechanism for the Mechanochemical Formation of Metastable Phases from the Reaction between Sulfur and Copper. *Manuscript in-preparation.*

3 Rana, Resham, et al. Tribochemical Reaction Pathways of Carboxylic Acid Monolayers on Copper in Ultrahigh Vacuum. *Manuscript in-preparation.*

4 Rana, Resham, et al. Adsorption and Reaction of Trimethyl and Triethyl Phosphites on Fe_3O_4 by Density Functional Theory. *Manuscript in-preparation.*

SELECTED TALKS AND PRESENTATIONS

2020 Kinetics of Mechanochemical Formation of Metastable Tribolayer from the Reaction between Copper and Sulfur, *Gordon Research Symposium: Tribology*, Lewiston, ME, US. (Postponed due to pandemic)

2019 Investigation of Sulfur Transport and Thiolate Decomposition on Copper, *Regional AVS Prairie Chapter Symposium, University of Illinois at Urbana-Champaign*, Urbana, IL, USA.

2019 Sulfur Transport Kinetics: Sulfur into the Bulk and Back to Surface, *Spring Research Symposium, University of Wisconsin- Milwaukee*, Milwaukee, WI, USA.

2018 Study of Reaction and Lubrication Trialkyl Phosphites on an Oxidized Iron in Ultrahigh Vacuum, *Regional AVS Prairie Chapter Symposium, University of Chicago*, Chicago, IL, USA.

2018 Reaction of Triethyl Phosphite on an Oxidized Iron Surface in Ultrahigh Vacuum: Temperature-Programmed Desorption and X-ray Photoelectron Spectroscopy Analysis, *Spring Research Symposium, University of Wisconsin- Milwaukee*, Milwaukee, WI, USA.